Metocean Climate Study
Offshore Newfoundland & Labrador

STUDY MAIN REPORT
Volume 1: Full Data Summary Report

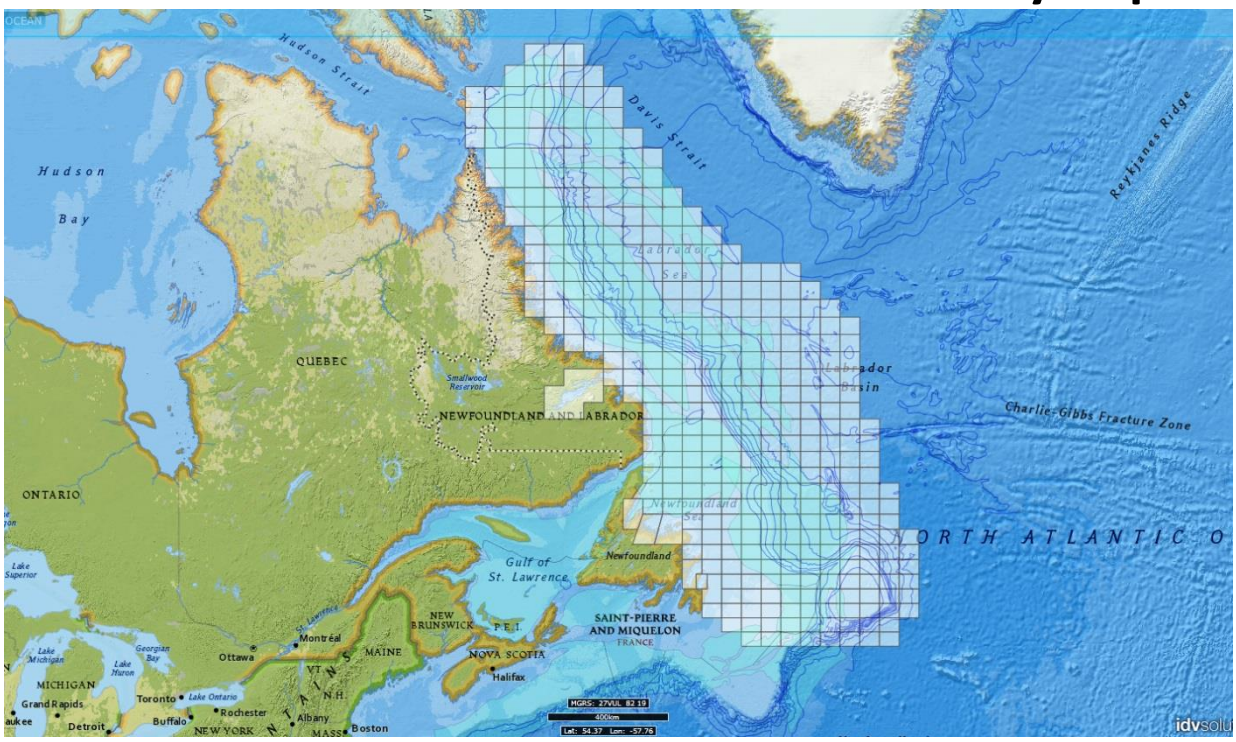

Prepared for:
Nalcor Energy Oil and Gas

Prepared by:
C-CORE

Reviewed & Edited by:
Bassem Eid, Ph.D.

May 2015

DISCLAIMER

All of the material contained on the website and the material contained herein ("information") are provided without warranty of any kind, whether express or implied, for information purposes only, and is not to be relied upon by any party. All implied warranties, including, without limitation, implied warranties of merchantability, fitness for a particular purpose, and non-infringement, are hereby expressly disclaimed. Links and references to any other websites are provided for information only and listing shall not be taken as endorsement of any kind. Nalcor Energy – Oil and Gas Inc. is not responsible for the content or reliability of the linked websites and does not endorse the content, products, services, or views expressed within them.

Nalcor Energy – Oil and Gas Inc. accepts no liability for any action taken as a result of reliance of any party upon the information. The taking of any action upon reliance upon the information is expressly prohibited. Under no circumstances will Nalcor Energy – Oil and Gas Inc. be liable to any person or business entity for any damages or remedy of any kind whether direct, indirect, special, incidental, consequential, or other damages based on any use of the information or any others website which is linked, including, without limitation, any lost profits, business interruption, or loss of programs, or information, even if Nalcor Energy – Oil and Gas Inc. has been specifically advised of the possibility of such damages.

ACKNOWLEDGEMENTS

This report (Volume 1 and 2) and associated cell reports were prepared by C-CORE for Nalcor Energy – Oil and Gas Inc.

C-CORE Study Team & Contribution:
Tony King (Project Manager & Icebergs)
Robert David Briggs (Currents & compilation of Cell Reports)
Grant Parr (Wind and Waves)
Robert Burton (Pack Ice)
Andrew Cuff (Icebergs – Satellite image analysis)
Perry Moore (Icing & Fog)
Martin Richard (Icing & Fog)
Kashfi Habib (Icebergs – aerial reconnaissance data)
Mark Howell (Icebergs- Satellite Image Analysis)
Janaka Deepakumara (Icebergs – Satellite Image Analysis)
Kelly Dodge (Icebergs – Satellite Image Analysis)
Sue Carter (Icebergs – Satellite Image Analysis)
Carl Howell (Icebergs – Aerial Reconnaissance Data)
Pradeep Bobby (Icebergs – Aerial Reconnaissance Data)

Technical Review, QA/QC, Reports Compilation & Editing
Dr. Bassem Eid, B. Eid Holdings Inc.
Martha Muzychka, Technical Writer, Praxis Communications

Nalcor Study & Management Team
Erin Gillis, Nalcor Study Lead
Mike White, Nalcor (NESS Team Lead)
Keith Drover, Nalcor Study Advisor
Greg Fleming, Nalcor Study Advisor
Richard Wright, Nalcor Exploration manager
Holli Green, Nalcor Office Administrator

EXECUTIVE SUMMARY

Offshore oil and gas exploration, development, and operations as well as other marine activities are significantly affected by the environmental and climate conditions. With an accurate description of the operating environment, drilling rigs, ships, production platforms, and other marine structures can operate safely in these areas of interest. For offshore exploration and development, an environmental baseline is needed as well as extensive engineering data. These projects require vast multi-dimensional, geospatial, and long temporal data coverage with easy access to interested parties.

In 2013, Nalcor announced the mapping of three newly defined sedimentary basins off the Labrador coast (the Henley, Chidley, and Holton Basins) as well as the extension of the previously defined Hawke Basin. This mapping was based on the regional 2D seismic surveys conducted by Nalcor, Petroleum Geo-services (PGS) and TGS Geophysical in 2011 and 2012. These newly defined sedimentary basins are located primarily in deep water in the Labrador Sea, off the east coast of Newfoundland and Labrador, Canada. To date, there has been no regional study of the metocean conditions offshore Newfoundland and Labrador. As part of Nalcor's exploration strategy, a metocean study would be considered a crucial piece of information in an area of frontier exploration. Nalcor commissioned C-CORE to provide the most comprehensive and accurate meteorological and oceanographic data set to characterize the metocean environment, covering topics such as winds, waves, currents, vessel icing, visibility (fog), pack ice, icebergs and ice islands, changes in conditions expected due to climatic change, and comparisons with other frontier regions. Various data sources were reviewed, evaluated, and verified for their suitability, coverage (spatial and temporal), accuracy and reliability. Only the most suitable data sets have been selected in this study.

The study area extends from 45.5^{o} N to 63^{o} N latitude, and from 42^{o} W to 65^{o} W longitude, covering the entire Labrador Sea and Northern Grand Banks, Flemish Pass, and Flemish Cap areas. The study area is divided into 391 grid cells, mostly one degree longitude by half degree latitude blocks, with each cell covering an average area of 3,760 square kilometres. Data summaries for metocean parameters are available for each cell and for the region.

There is a significant amount of data associated with each of the metocean parameters covered in this study. To facilitate the use of such vast data sets, Nalcor developed a web-based, interactive Database Management and Geographic Information System (DBM&GIS), called NESS (Nalcor Exploration Strategy System), which includes the above referenced metocean data as well as other geographic and geophysical information of the Newfoundland and Labrador offshore. The NESS program allows scientists, engineers, managers, and operators easy access to, and use of, the geospatial data for exploration, planning, design, production, and operations of offshore oil and gas resources with reduced risk and uncertainties.

This report (Volume 1) provides detailed descriptions of the metocean data sources, data process and analyses, and statistical summaries. Volume 2 provides regional metocean climatological summaries and trends, as well as comparisons with other frontier exploration regions of similar characteristics. More details and statistical summaries for each of the 391 cells are provided in separate cell reports. These reports are also available in NESS as PDF files, which can be viewed or downloaded from NESS as needed.

TABLE OF CONTENTS

Metocean Climate Study
Offshore Newfoundland & Labrador

STUDY MAIN REPORT
Volume 1: Chapter 1 – Introduction

Prepared for:
Nalcor Energy Oil and Gas

Prepared by:
C-CORE

Reviewed & Edited by:
Bassem Eid, Ph.D.

May 2015

CHAPTER 1 – INTRODUCTION

TABLE OF CONTENTS

LIST OF FIGURES

1 INTRODUCTION

1.1 BACKGROUND

In 2013, Nalcor announced the mapping of three newly defined sedimentary basins off the Labrador coast (the Henley, Chidley, and Holton Basins) as well as the extension of the previously defined Hawke Basin (Figure 1-1). This mapping was based on the regional 2D seismic surveys conducted by Nalcor, Petroleum Geo-services (PGS) and TGS Geophysical in 2011 and 2012. These newly defined sedimentary basins are located primarily in deep water in the Labrador Sea, off the east coast of Newfoundland and Labrador, Canada. To date, there has been no regional study of the metocean conditions offshore Newfoundland and Labrador. As part of Nalcor's exploration strategy, a metocean study would be considered a crucial piece of information in an area of frontier exploration. Nalcor initiated a regional metocean study over the Labrador Sea, Northern Grand Banks, Flemish Pass, and Flemish Cap (Figure 1-1).

There is a perception that offshore Newfoundland and Labrador is a challenging environment, but also that the Labrador Sea is essentially an arctic environment. However, conditions vary substantially, and to date, there has been no comprehensive characterization of the region as a whole. The intent of this metocean study is to provide the most complete and accurate data regarding the meteorological and oceanographic conditions in the study area, including sea ice and icebergs.

C-CORE (2007) characterized the portion of the Labrador Shelf between 54°N and 58°N, and showed that iceberg and pack ice frequency decreased substantially off the Labrador Shelf going into deeper water. However, the emphasis of that study was development of gas reserves on the Labrador Shelf; characterizing the deep-water regions off the shelf was not a priority at that time. The Canada-Newfoundland and Labrador Offshore Petroleum Board (C-NLOPB) has funded a number of Strategic Environmental Assessment (SEA) studies covering areas such as the Labrador Shelf (Sikumiut, 2008), Orphan Basin (LGL, 2003), and Eastern Newfoundland (AMEC, 2014), but these tend to focus more on regulatory or environmental issues (mammals, seabirds, fish, oil spills, etc.) and these studies do not address metocean or ice conditions in sufficient detail for decision making regarding potential exploration activities in the entire study area.

The Canadian Ice Service (CIS) published Sea Ice Climatic Atlas, East Coast 1981-2010 (CIS, 2013), which addresses pack ice conditions in most of the study area (the northern half of the Labrador Shelf is on the CIS website under Sea Ice Climatic Atlas for Northern Canadian Waters, 1981-2010). While these reports show the decreasing pack ice presence over the deepwater sedimentary basins off the Labrador Shelf, the combined 30-year analysis does not address changes in the pack ice regime over time. There is no comprehensive iceberg climatology for the region. The Panel for Energy Research and Development (PERD) iceberg sighting database (PERD, 2013) gives iceberg-sighting locations for the region, but this information alone does not define iceberg frequency and is useful only qualitatively. The available metocean studies, typically prepared for industry for development studies, generally analyze wind and wave data for a single point near the site of interest, but they do not consider regional variations in parameters, nor do they compare conditions to a known baseline.

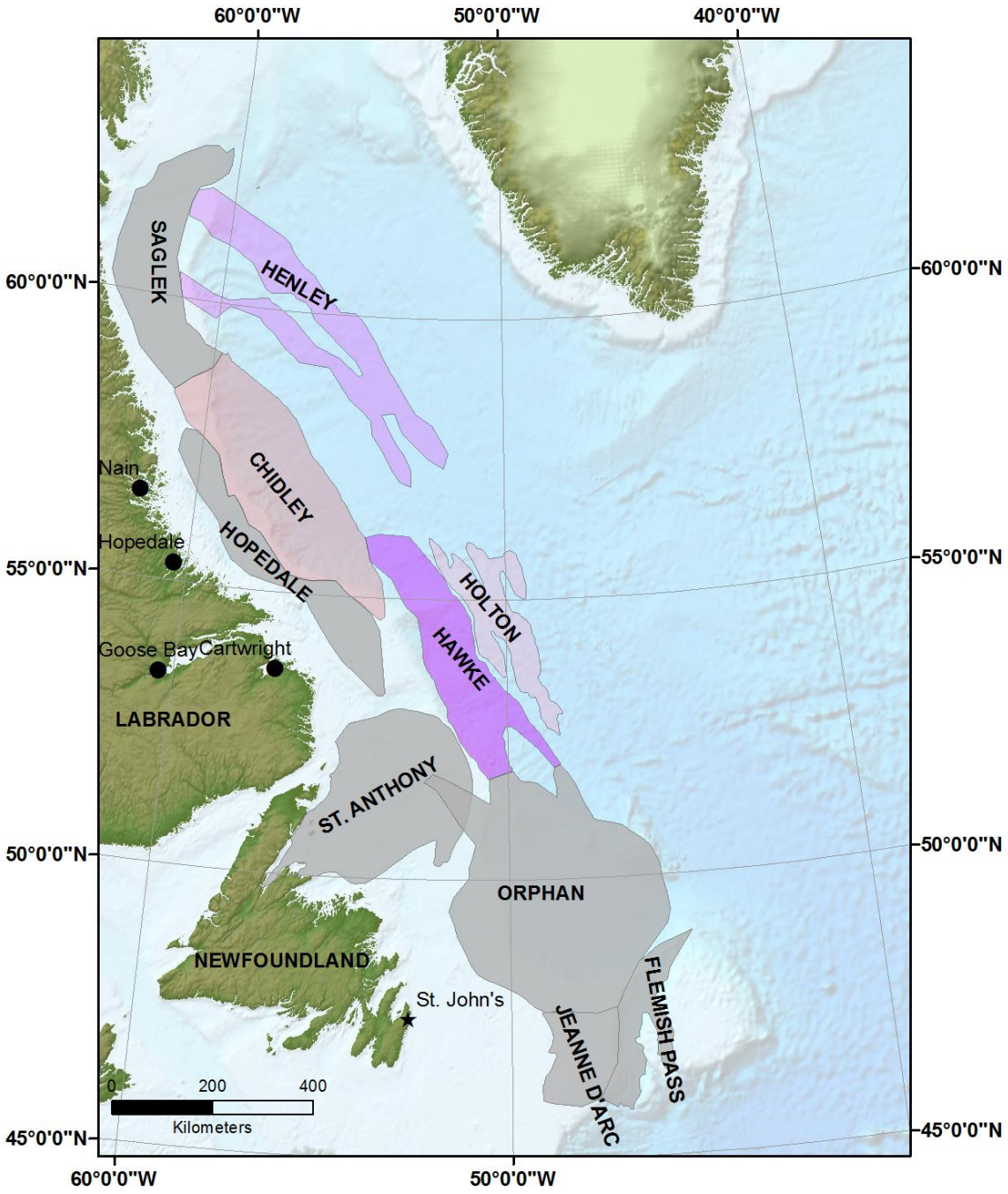

Figure 1-1 Sedimentary basins offshore Newfoundland and Labrador

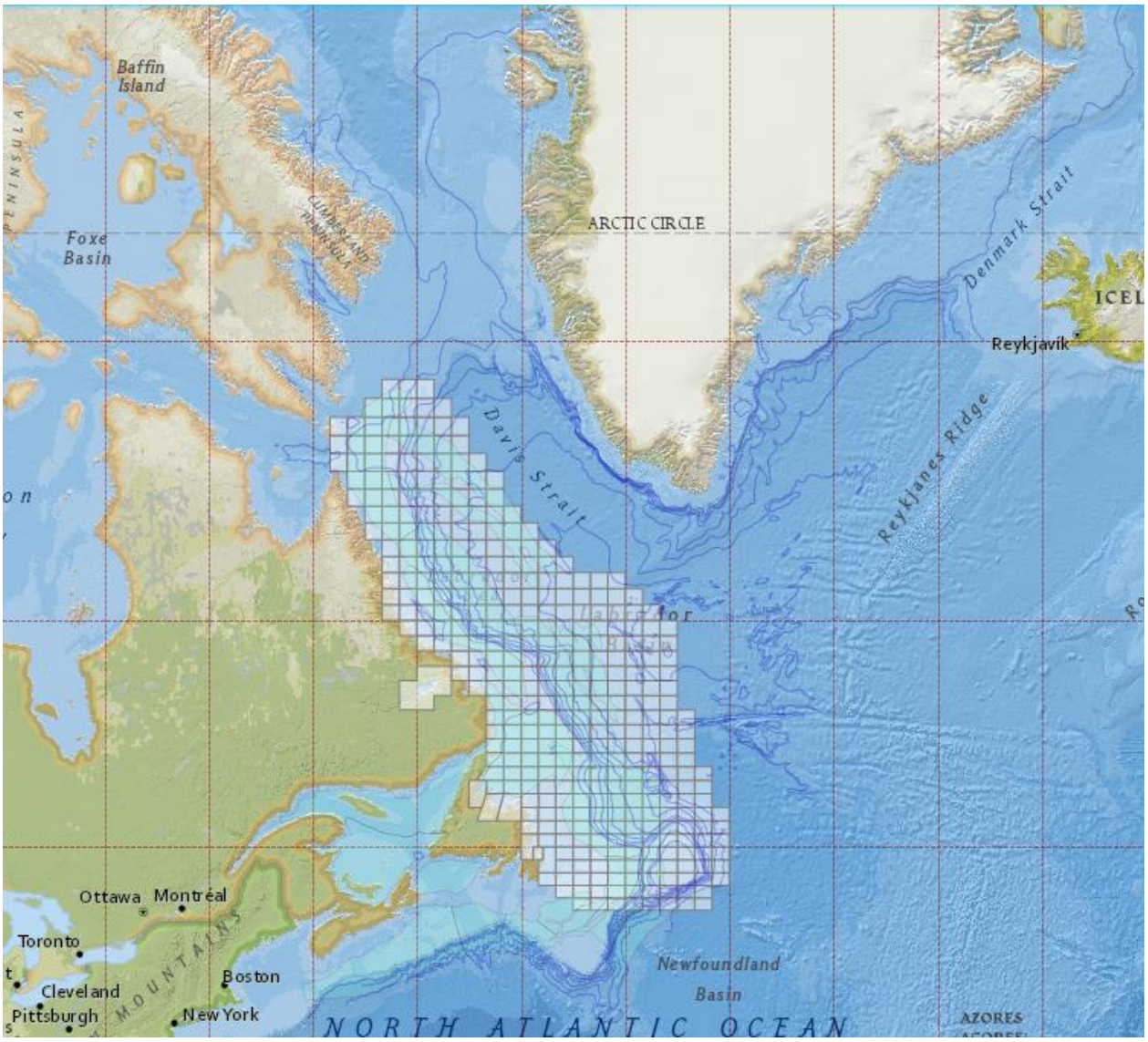

Figure 1-2 Study Area (with Grid & Bathymetry) – North West Atlantic Ocean Map

1.2 STUDY SCOPE AND OBJECTIVES

Nalcor Energy Oil and Gas Inc. has commissioned C-CORE to conduct this metocean study, with the objective to provide the most comprehensive and complete database using the most recent and accurate data sources covering the offshore areas of Labrador and the Newfoundland east coast. This report represents Volume 1 of the Metocean Study Report. It provides regional summaries of meteorological and physical oceanographic conditions in the study area over the offshore sedimentary basins including Saglek, Henley, Chidley, Hopedale, Hawke, Holton, St. Anthony, Orphan, Jeanne d'Arc, and Flemish Pass (Figure 1-1).

In addition, Nalcor is making results from other selected studies (pore pressure analysis and rock physics) available to industry to increase scientific knowledge over a frontier exploration area. This metocean study is yet another source of information that interested parties may look to when defining the risks associated with an exploration program in the Newfoundland and Labrador offshore environment.

To facilitate the use of this vast data set, Nalcor Energy has developed a web-based, interactive database or Geographic Information System, called NESS (Nalcor Exploration Strategy System), which includes the metocean data presented in this report as well as other geographic and geophysical data of the sedimentary basins in the study area.

The objectives of this study are to:

- Characterize regional metocean conditions (winds, waves, currents, visibility, vessel icing, pack ice, icebergs and ice islands) in the specified area of interest and influence of environmental changes on such conditions; and
- Compare these conditions to those in other analogous internationally explored regions (i.e., East and West Greenland, North Sea, Barents Sea, Canadian Beaufort Sea, Chukchi Sea, Kara Sea, Caspian Sea, and Sakhalin Island as well as the Grand Banks and Orphan Basin).

The overall goal of this study is to provide the most comprehensive, extensive, and accurate metocean data set (both geospatial and temporal extent) that is easily accessible by all interested parties.

1.3 STUDY AREA & DATA COVERAGE

The study area extends from 45.5^{O} N to 63^{O}N latitude, and from 42^{O}W to 65^{O}W longitude, covering the entire Labrador Sea and Northern Grand Banks, Flemish Pass and Flemish Cap (Figure 1-2). The study area was divided into 391 grid cells (mostly one degree longitude by half degree latitude blocks) as shown in Figure 1-3. As shown, the study area covers a large area of offshore Newfoundland and Labrador, with variable geographical, geophysical, and meteorological and oceanographic characteristics. It may be divided into two main regions:

- The Labrador Sea, which can be divided into three distinctive areas:
  - The Labrador Continental Shelf (from the coastline up to 200 m water depth)
  - The Labrador Shelf Slope (from 200 m to 1000 m)
  - Deep water offshore (the Labrador Basin).

  The above areas include six sedimentary basins: Saglek, Hopedale, Chidley, Henley, Holton, and Hawke.

- The Newfoundland offshore areas:
  - Newfoundland Sea – (includes St. Anthony and Orphan Basins)
  - The Grand Banks of Newfoundland (includes Jeanne d'Arc Basin)
  - Flemish Pass (includes Flemish Pass Basin)
  - Flemish Cap.

As shown in the following sections of this report, the metocean characteristics of these areas are quite diversified.

Vast data sources and data coverage of metocean parameters have been compiled and analyzed for the following parameters: wind, wave, current, vessel icing, visibility (fog), sea ice (pack ice), and icebergs and ice islands.

The Study Report is presented in two volumes:

VOLUME 1 – Full Data Summary Report (this report)

VOLUME 2 – Regional Trends, Influence of Environmental Changes and Comparisons with Other Regions

This report covers the following parameters/topics with each provided as a stand-alone chapter:

- Bathymetry: Chapter 2
- Winds: Chapter 3
- Waves: Chapter 4
- Currents: Chapter 5
- Icing: Chapter 6
- Visibility (Fog): Chapter 7
- Pack Ice: Chapter 8
- Icebergs & Ice Islands: Chapter 9

Detailed data analysis results (statistical summaries) are provided for each cell in separate Cell Reports with a total of 391 cell reports available.

The above reports are uploaded into the NESS as digital PDF files, which can be easily accessed, viewed, and printed directly from the NESS portal website.

Figure 1-3 Study Area with grid cells showing the offshore sedimentary basins

1.4 NESS SOFTWARE SYSTEM

1.4.1 NESS General Functional Specifications

The Nalcor Exploration Strategy System (NESS) provides an easy to use, yet powerful application for the presentation and analysis of data related to the oil and gas resources in Newfoundland and Labrador. The system integrates many unique data sets containing spatial information and uses a map as the focal point of the user. With NESS, data can be displayed, queried, and results exported depending on the needs of the end user. The Metocean Study consists of a large-scale, unique data set which NESS helps present (Figure 1-4).

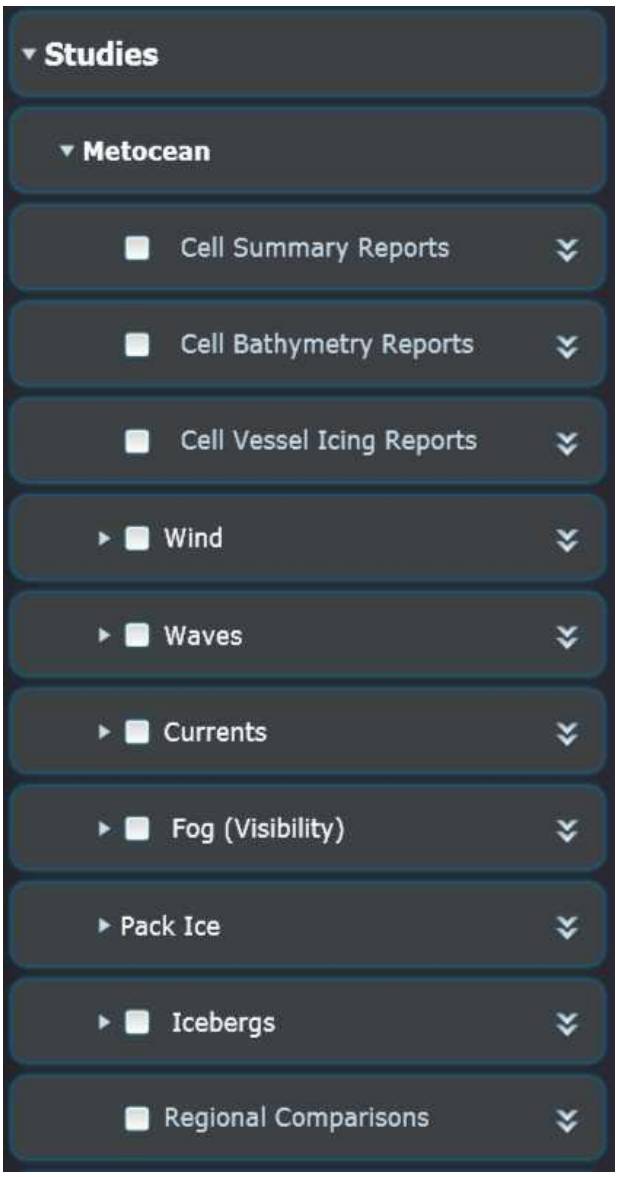

Figure 1-4 Metocean FEEDS within the NESS program

Each main FEED represents a unique task of the Metocean study, where the data are categorized by time and geography (e.g., wind, waves, currents, etc.). Each main FEED contains a report for each of the 391 cells contained within the study area, as well as data records that can be further analyzed using filters within the application. For example, the Wind FEED contains monthly records for each month of the year from 1954-2013, resulting in 276,000 records.

Displaying and analyzing tens or hundreds of thousands of records within NESS is managed by filter settings applied by the user. Filters are easy to use controls defining the criteria that must be met by the records to be made available. A common set of filters is available for each FEED, and these are:

Start Year: Records must have a year value greater than or equal to this value

End Year: Records must have a year value lower than or equal to this value

Period: Records must be for a month or season, which is a collection of months as follows:

- Winter = 1,2,3
- Spring = 4,5,6
- Summer = 7,8,9
- Fall = 10,11,12
- Annual = 1 to 12

Cells Contain: Values are aggregated for each cell over the defined range of years and period. Options are:

- The Largest Value For Year(s)/Period Per Cell
  - This returns the maximum value, which may occur in more than one year
- The Average Value For Year(s)/Period Per Cell
  - This returns the average value for each cell over the range of years for the defined period

Available Cells: This defines the number of cells to be used, which limits the spatial extent of available records. All feeds, with the exception of Pack Ice, have a range of one to 391, where one is the Northern- and Westernmost cell and 391 is the Southern- and Easternmost cell. Pack Ice cells range from one to 9774, where one is the Northern- and Westernmost cell and 9774 is the Southern- and Easternmost cell. The Pack Ice task split each cell into 25 sub-cells to display a more accurate distribution of the Pack Ice task throughout the grid, especially in areas of the shelf/slope break.

Once filters are applied, the results are available immediately. These filtered results can be viewed on the map portion of the interface, or in the list of filtered results (Figure 1-5), which can then be easily sorted.

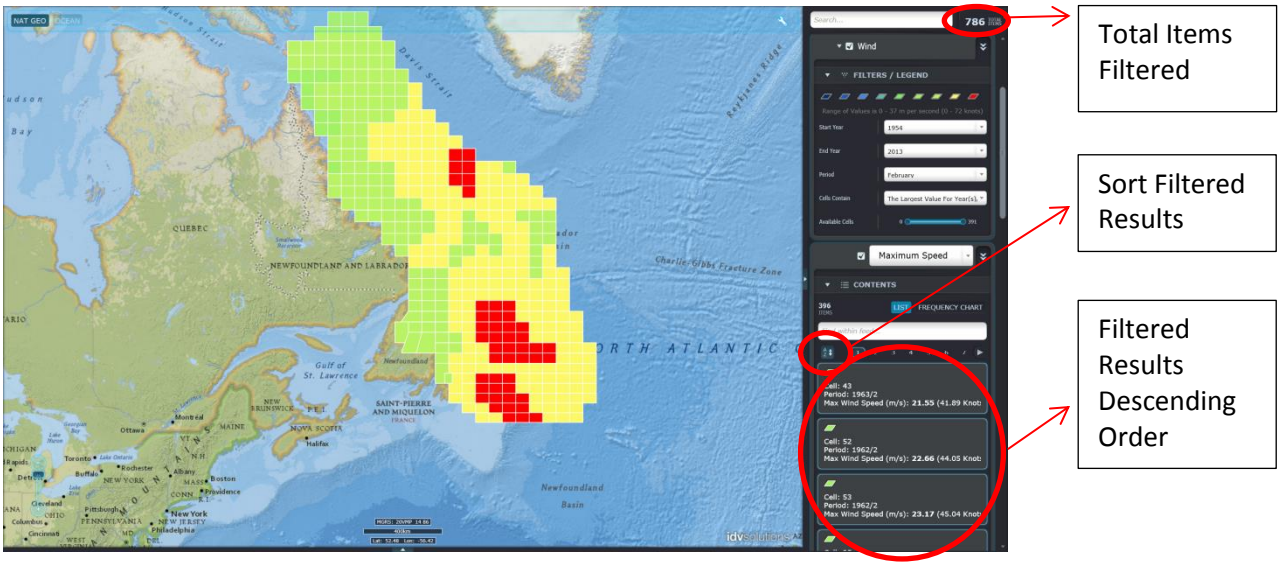

Figure 1-5 Filtered results from a NESS query

The example shown above in Figure 1-5 represents Maximum Wind Speed in the month of February from 1954 to 2013. The map display indicates wind values visually (colour-coded as per scale on the top of display window), while the numerical results can be found by hovering the mouse over each cell block on the map or looking at the filtered results in the lower right hand side of the page in the filters tab. The corresponding cell report can also be viewed by clicking on the selected cell.

As well as a static map visual of the data, NESS is also able to animate the metocean FEEDS. This is a powerful visualization tool for the vast metocean data sets as you can set a filter for a specific FEED and play the results to get an idea of how the metocean data are changing over time (e.g., year to year, month to month, or season to season).

Overall, the NESS software allows for quick, easy visualization of the vast metocean data set, allowing all users to analyze easily the metocean conditions offshore Newfoundland and Labrador. For more information on the operation of the NESS software, please view the NESS how-to videos located on the Nalcor Energy Exploration website (http://www.nalcorenergy.com/oil-and-gas.asp).

1.4.2 NESS Table of Contents

STUDIES

> Metocean

- Metocean Full Report (combined PDF file of Volume 1 and Volume 2 of the Study Reports)
- Cell Summary Reports
- Cell Bathymetry Reports
- Cell Vessel Icing Reports (this is the only data on Icing)
- **Wind** (wind speed at 10 m above MSL)
  - Period covered: 1954 – 2013

- Filters/legend:
  - Monthly, Seasonal (summer, fall, winter, spring), and Annual
    - The Average Value for Year(s) Period Per Cell
    - The Largest Values for Years (s) Period Per Cell
      - Mean Speed; and
      - Maximum Speed
- Advanced Wind – Animate Mean Speed & Animate Maximum Speed

➢ **Waves** (Significant Wave Height)
- Period covered: 1954 – 2013
- Filters/legend:
  - Monthly, Seasonal (summer, fall, winter, spring), and Annual
    - The Average Value for Year(s) Period Per Cell
    - The Largest Values for Years (s) Period Per Cell
      - Mean Significant Wave Height; and
      - Maximum Significant Wave Height
- Advanced Waves – Animate Mean and Maximum Sig wave height

➢ **Currents** (current velocity – flow rate)
- Period covered: 2003 – 2012
- Filters / legend:
  - Monthly, Seasonal (summer, fall, winter, spring), and Annual
    - The Average Value for Year(s) Period Per Cell
    - The Largest Values for Years (s) Period Per Cell
      - Current Magnitude @2 metres
      - Current Magnitude @10 metres
      - Current Magnitude @100 metres
      - Current Magnitude @500 metres
      - Current Magnitude @1/3 of depth from 500m to seabed
      - Current Magnitude @2/3 of depth from 500m to seabed
- Advanced Currents – Animate Current Flow Rate

➢ **Fog (Visibility)**
- Period Covered : 1979 – 2013
- Filters/Legend:
  - Monthly, Seasonal (summer, fall, winter, spring), and Annual
    - The Average Value for Year(s) Period Per Cell
    - The Largest Values for Years (s) Period Per Cell
      - Average Visibility < 1 KM (Hrs of Daylight with Visibility <1KM)
      - Average Visibility < 2 KM (Hrs of Daylight with Visibility <2KM)
      - Average Visibility < 5 NM (Hrs of Daylight with Visibility <5NM)
- Advanced Fog – Animate Visibility (< 1 KM; < 2 KM; < 5 NM)

- **Pack Ice**
  - Period Covered: 1984 – 2013
    - Monthly, Seasonal (summer, fall, winter, spring), and Annual
      - The Average Value for Year(s) Period Per Cell
      - The Largest Values for Years (s) Period Per Cell
        - Mean Concentration
        - Maximum Concentration
  - Advanced Pack Ice – Animate Mean and Max count per year

  Note: due to the very large volume of pack ice data, only monthly summaries are provided (i.e., no seasonal and annual filters). Also the filters apply to one year up to 5 years duration for each query. However, animation can cover the entire 30 year period.

- **Icebergs**
  - Data Coverage: 1998 – 2014
  - Filters / Legend
    - Monthly, Seasonal (summer, fall, winter, spring), and Annual
      - The Average Value for Year(s) Period Per Cell
      - The Largest Values for Years (s) Period Per Cell
        - Icebergs Count (number of icebergs in each cell)
        - Other summaries (aerial density, mean drift, size distribution) are provided in the cell report for each cell
  - Advanced Icebergs – Animate Counts

- **Regional Comparisons (Harshness)**
  - Comparisons with Other Regions (monthly comparisons of pack ice, wind, and waves) for each cell
  - Harshness Index (for the study area, and for each cell including comparison with other regions)

Note: The Bathymetry data are included under Tab **"Licenses / Basins – Boundaries**."

1.5 REFERENCES

AMEC Environment & Infrastructure. (2014). Eastern Newfoundland Strategic Environmental Assessment. Report prepared for the Canada-Newfoundland and Labrador Offshore Petroleum Board (C-NLOPB), February.

Canadian Ice Service (CIS). (2010). Sea Ice Climactic Atlas, East Coast 1981-2010. Ottawa: Environment Canada.

C-CORE (2007). Location, Environmental and Other Factors Influencing Exploration and Development of Labrador Gas, C-CORE Report R 06 088-525 V2, Prepared for Atlantic Canada Opportunities Agency (ACOA), May.

LGL Limited. (2003). Orphan Basin Strategic Environmental Assessment. Report SA767. Report prepared for the Canada-Newfoundland and Labrador Offshore Petroleum Board (C-NLOPB), November.

PERD. (2013). PERD Iceberg Sighting Database Update 2013. Prepared by BMT Fleet Rechnologu Limited for National Research Council Canada, Reference: 7909FR (Rev 00), March.

Sikumiut Environment Management Limited. (2008). Strategic Environmental Assessment Labrador Offshore Area. Project No. P 064. Report prepared for the Canada-Newfoundland and Labrador Offshore Petroleum Board (C-NLOPB), August.

Metocean Climate Study
Offshore Newfoundland & Labrador

STUDY MAIN REPORT
Volume 1: Chapter 2 – Bathymetry

Prepared for:
Nalcor Energy Oil and Gas

Prepared by:
C-CORE

Reviewed & Edited by:
Bassem Eid, Ph.D.

May 2015

CHAPTER 2 – BATHYMETRY

TABLE OF CONTENTS

LIST OF FIGURES

2 BATHYMETRY

The bathymetry for the study region is shown in Figure 2-1. The bathymetry layer was acquired from the publically available General Bathymetric Chart of the Oceans (GEBCO), a global 30 arc-second grid largely generated by combining quality-controlled ship depth soundings with interpolation between sounding points guided by satellite-derived gravity data. However, in areas where they improve on the existing grid, we have included data sets generated by other methods. This data set was used to generate bathymetry charts for each of the study area cells for inclusion in the appendices. An example is shown in Figure 2-2.

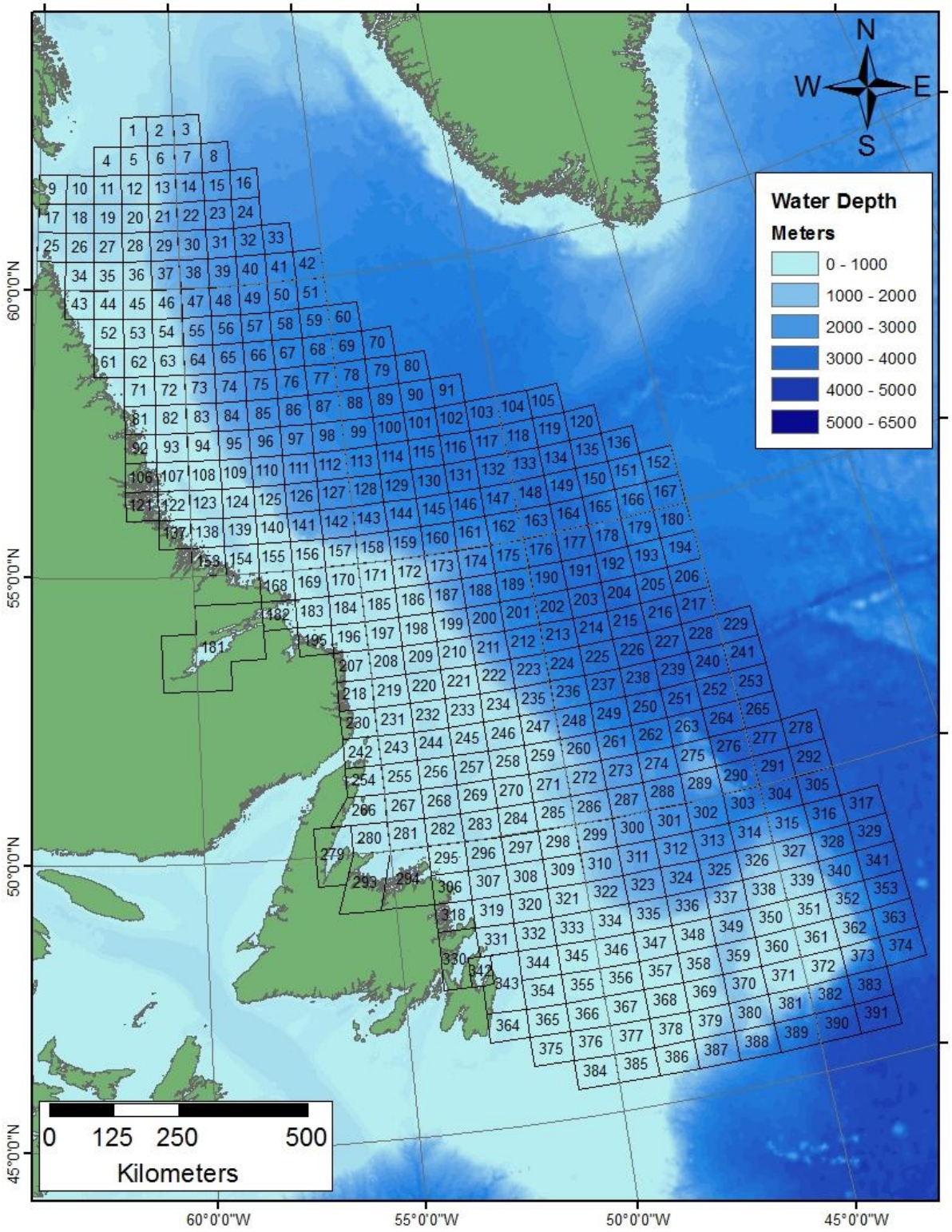

Figure 2-1 Study area with bathymetry

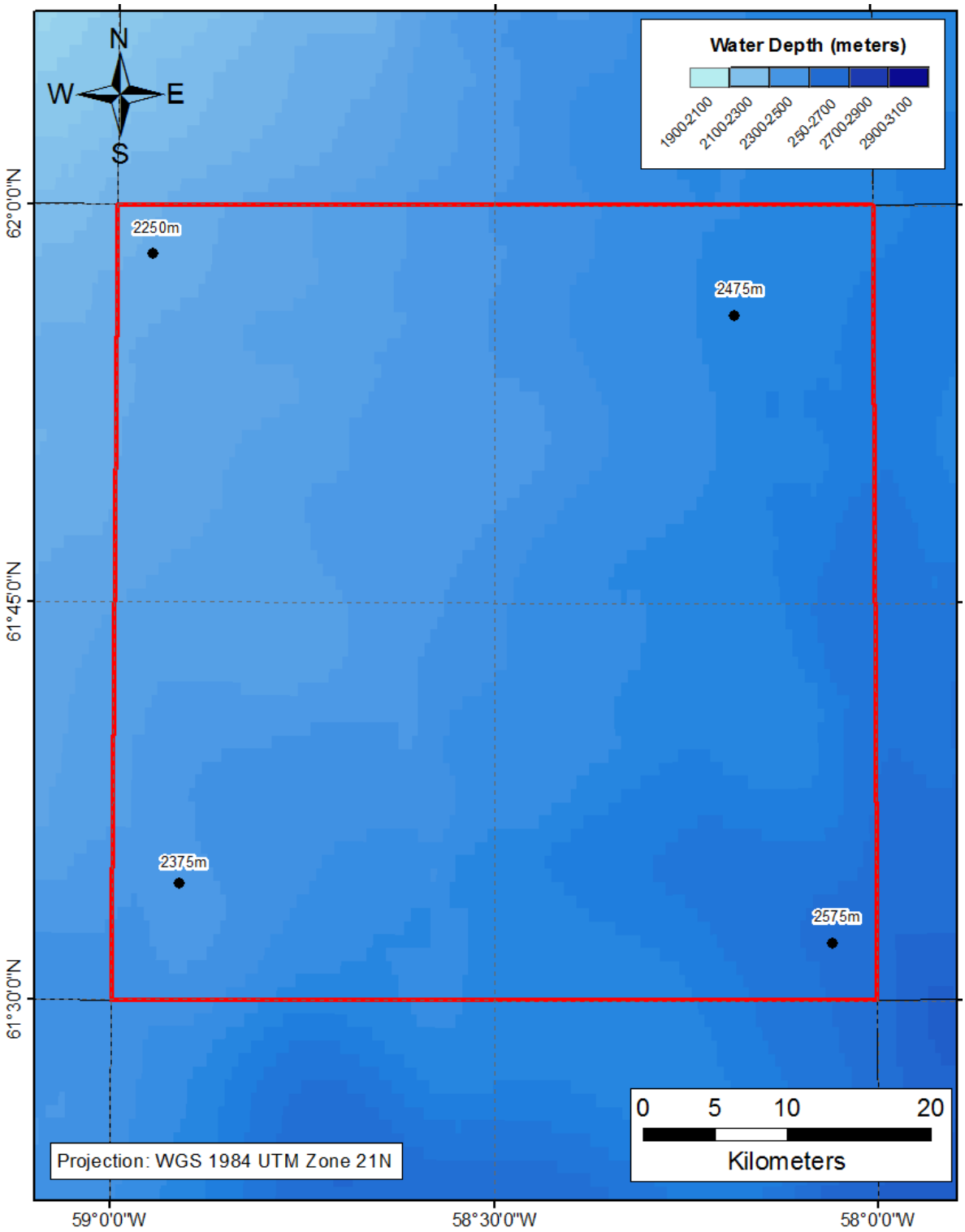

Figure 2-2 Bathymetry chart for Cell 15

Metocean Climate Study
Offshore Newfoundland & Labrador

STUDY MAIN REPORT
Volume 1: Chapter 3 – Winds

Prepared for:
Nalcor Energy Oil and Gas

Prepared by:
C-CORE

Reviewed & Edited by:
Bassem Eid, Ph.D.

May 2015

CHAPTER 3 – WINDS

TABLE OF CONTENTS

LIST OF FIGURES

LIST OF TABLES

3 WINDS

3.1 DATA SOURCE

The primary source for wind data is the MSC50 data set (Swail, Cardone, Ferguson, Gummer, Harris, Orelup, and Cox, 2006). The MSC50 database is a hindcast wind and wave data set for offshore Canadian waters, which was developed by Oceanweather Inc. for Meteorological Services of Canada (MSC) Environment Canada.

The data set contains either hourly or three-hour recordings of wind and wave values for 60 years from 1954 to 2013. Wind speed is provided as the one-hour average of effective neutral wind in metres per second (m/s) at 10 m above mean sea level (MSL). Wind direction is provided as the direction that the wind is blowing from, clockwise from north in degrees. The MSC50 data are presented for a number of geographic points; generally in 0.5 degree resolution for northern areas and 0.1 degree resolution for southern areas such as the Grand Banks (see Figure 3-1).

3.2 DATA PROCESSING

Data points from the MSC50 course grid (0.5 degree resolution) were used throughout the area of interest. This meant only values at 0.5 degree grid were used. The remaining points, as well as the points in the northern area, are present on the cell boundaries as can be seen in Figure 3-1. All cells, except those on the boundaries of the region, are surrounded by six MSC50 grid points. The time series of wind and wave values were available every three hours for the entire 60-year data set for each of the six MSC50 grid points around each cell. To get a single magnitude value of wind and wave parameters representing the entire cell, the maximum of each of these six values was taken at each time step in the time series. The new time series of maximum values was then used for the analyses. For direction of wind and wave, the vector average of the six MSC50 points was used. For the high-resolution MSC50 points, data were presented every hour instead of every three hours as was done in the low-resolution areas. To account for this, every third value in the high-resolution data set was used.

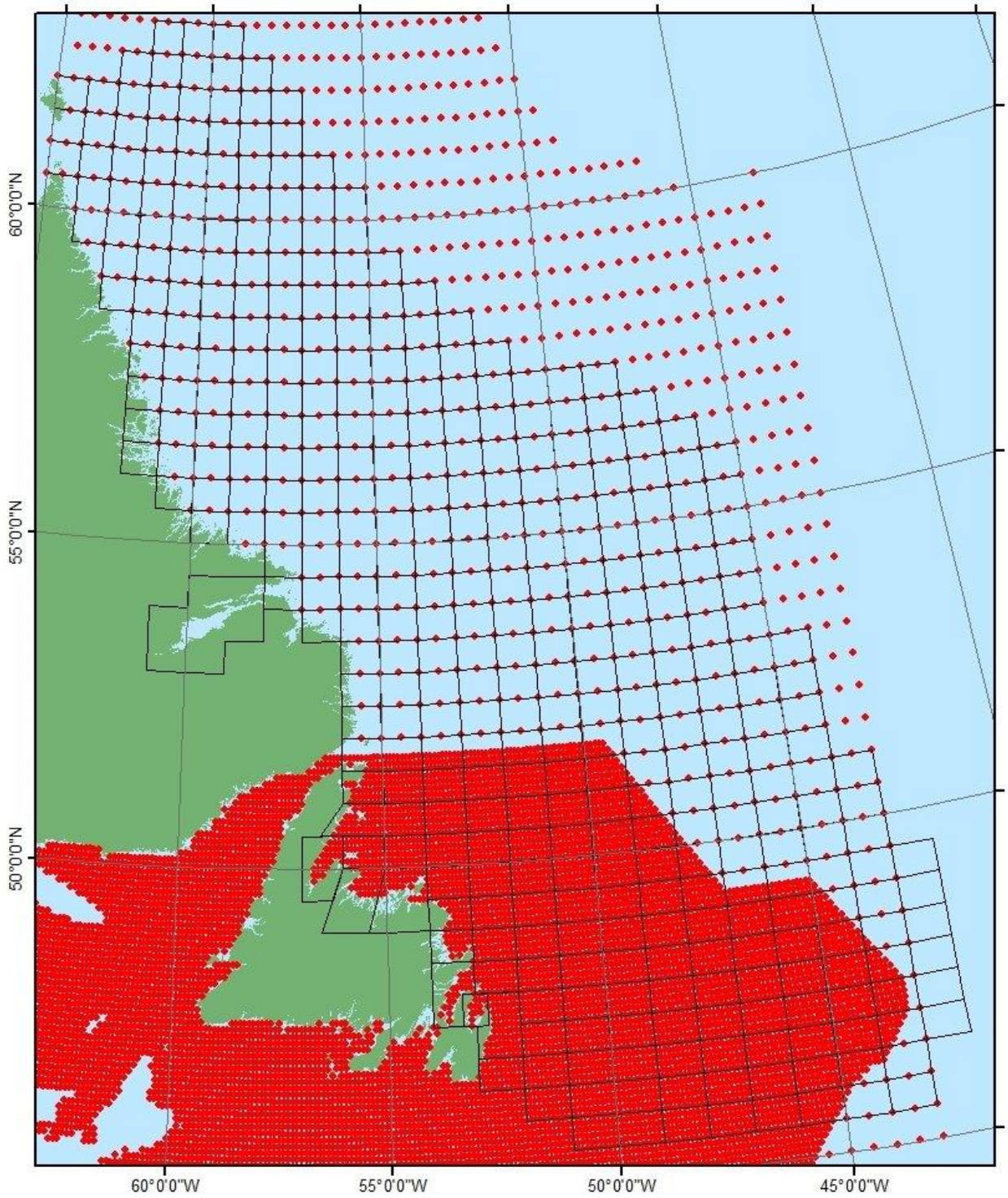

Figure 3-1. Nalcor study area with MSC50 grid points (red)

3.3 Extreme Value Analysis

The full 60 years of MSC50 hindcast data have been used to provide a description of wind for each cell. The 10, 25, 50, and 100-year return period extreme wind speeds were determined. Data are broken down by month to account for monthly and seasonal trends. The 10, 25, 50, and 100-year return period values were determined using a peak over threshold extreme value analysis. The peak value is determined as any event greater than the threshold value, and any other peak must separate it by at least 48 hours. The threshold was set to give a minimum of 50 storm events over the course of the 60 years for each month, with peak wind events within 48 hours of a local maximum excluded. Thresholds were set at a high value first, and then lowered in increments of 0.5 m/s until the minimum number of storm events was reached.

The storm event wind speeds were approximated with a shifted Weibull distribution, and the wind speeds at the appropriate probability level for 10, 25, 50, and 100-year return periods were determined from the Weibull parameters. The distribution was shifted by an amount equal to the threshold for that month. An example output table for Cell 110 of 10, 25, 50, and 100-year extreme wind speeds by month is shown in Table 3-1. Note that these are one-hour average wind speeds, not gusts. Extreme values of wind speed for the remaining cells are given in the cell reports. Since the data for all months and grid cells were assumed to follow the same distribution, some months for some cells may provide data that do not fit the distribution perfectly, resulting in inaccuracy in the extreme values.

Table 3-1. Cell 110 - Extreme wind speeds by return period

Cell: 110 56.75°N 57.5°W		Wind Speed Extremes by Return Period												
		Jan	Feb	Mar	Apr	May	Jun	Jul	Aug	Sep	Oct	Nov	Dec	Annual
WS (m/s)	10 Year	25.6	24.9	23.6	21.3	19.7	17.7	15.5	17.1	21.4	23.2	25	26.3	27.9
	25 Year	27.1	26.8	26	22.6	21.4	19.3	16.8	18.5	23.6	24.9	27.3	28.4	29.4
	50 Year	28.2	28.2	27.9	23.5	22.7	20.5	17.7	19.5	25.2	26.3	29.1	30	30.6
	100 Yr.	29.2	29.6	29.8	24.5	24	21.8	18.6	20.5	26.9	27.5	30.9	31.6	31.8

3.4 Statistical Analysis

3.4.1 Summary Table

A table summarizing the wind speed has been provided for each cell. An example for cell 110 is provided in Table 3-2. The parameters as defined in the table are:

Mean – scalar mean of all wind speeds in time series

St. Dev. – standard deviation of all wind speeds in time series

Median – median of all wind speeds in time series

P90 – 90th percentile of all wind speeds in time series

Max. – maximum value of all wind speeds in time series

Dom. Dir. – dominant (most frequent) direction of wind in 10 degree bins

Table 3-2. Cell 110 - Wind speed summary

Cell: 110 56.75°N 57.5°W		Summary Table - Wind Speed												
		Jan	Feb	Mar	Apr	May	Jun	Jul	Aug	Sep	Oct	Nov	Dec	Annual
Wind Speed (m/s)	Mean	11.3	10.5	9.9	8.5	6.9	6	5.4	6	7.8	9.2	10.3	11.3	8.6
	St. Dev.	4.3	4.1	4	3.7	3.4	3.1	2.8	3	3.5	3.8	3.9	4.2	4.2
	Median	11	10.2	9.6	8.1	6.4	5.6	5	5.6	7.4	8.9	10	11.1	8.1
	P90	17	15.8	15.3	13.7	11.4	10.1	9.2	9.9	12.3	14.3	15.6	16.8	14.4
	Max.	28.3	27.8	26.9	24.2	22.5	21.6	19.1	18.5	24.9	26.2	28.3	29.7	29.7
	Dom. Dir.	295	295	305	325	315	315	135	305	295	305	285	295	295

3.4.2 Histograms

Histograms of wind speed have been provided for each cell. An example has been provided for cell 110 in Figure 3-2.

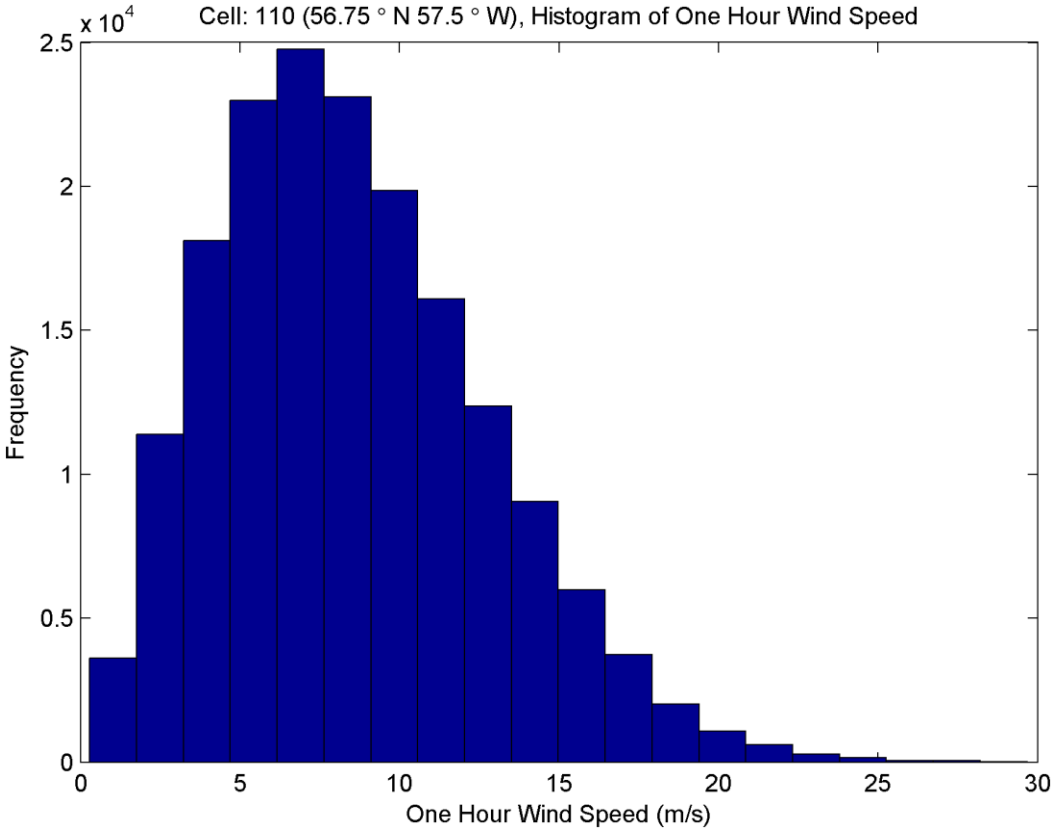

Figure 3-2. Cell 110 – Histogram of one hour wind speed

3.4.3 Probability of Exceedance

Probabilities of exceedance for wind speeds are shown in Table 3-3 for Cell 110. The numerical values represent the proportion of time (from 0 to 1) that the wind speeds meet or exceed the values listed in each row. The data are presented monthly with a color scale representing the more likely cases. Cases

with a zero listed as the probability and the squares shaded cyan (blue) represent cases in which the probability was less than 0.0005 (rounded to zero). Cases with an unshaded square and a zero value displayed mean that wind speeds above that value did not occur in the hindcast data set. Values for the 391 cells are given in the cell reports.

Table 3-3. Cell 110 – Wind speed and probability of exceedance by month

Cell: 110 56.75°N 57.5°W		Wind Speed - Probability of Exceedance by Month											
		Jan	Feb	Mar	Apr	May	Jun	Jul	Aug	Sep	Oct	Nov	Dec
Wind Speed (m/s)	2	1	1	1	0.999	0.995	0.991	0.982	0.992	0.998	1	1	1
	4	0.994	0.99	0.979	0.958	0.885	0.825	0.767	0.84	0.934	0.977	0.993	0.996
	6	0.942	0.921	0.89	0.823	0.674	0.576	0.505	0.584	0.775	0.874	0.925	0.954
	8	0.825	0.786	0.741	0.62	0.435	0.333	0.273	0.334	0.552	0.696	0.781	0.844
	10	0.67	0.61	0.555	0.411	0.243	0.16	0.114	0.157	0.328	0.486	0.591	0.681
	12	0.503	0.426	0.374	0.243	0.118	0.065	0.033	0.059	0.171	0.299	0.396	0.506
	14	0.338	0.26	0.219	0.128	0.051	0.025	0.009	0.022	0.075	0.158	0.239	0.329
	16	0.198	0.134	0.112	0.059	0.019	0.008	0.002	0.005	0.032	0.074	0.128	0.184
	18	0.099	0.063	0.05	0.021	0.008	0.002	0	0.001	0.014	0.03	0.053	0.092
	20	0.045	0.028	0.019	0.007	0.003	0	0	0	0.005	0.011	0.023	0.042
	22	0.018	0.013	0.007	0.002	0	0	0	0	0.002	0.004	0.009	0.019
	24	0.006	0.004	0.002	0	0	0	0	0	0.001	0.002	0.004	0.008
	26	0.003	0.001	0.001	0	0	0	0	0	0	0	0.001	0.003
	28	0.001	0	0	0	0	0	0	0	0	0	0	0.001
	30	0	0	0	0	0	0	0	0	0	0	0	0

3.4.4 Wind Roses

In order to quantify the frequency and strength of winds by direction, a series of plots, similar to Figure 3-3 have been created. Wind direction is provided as the direction that the wind is blowing from, clockwise from north in degrees. Winds are broken down into 10-degree bins. The radial length of each bin represents the frequency and the distribution of colors on each bar represents the frequency of winds speeds corresponding to the legend. Wind rose plots for each cell for each month are given in the cell reports.

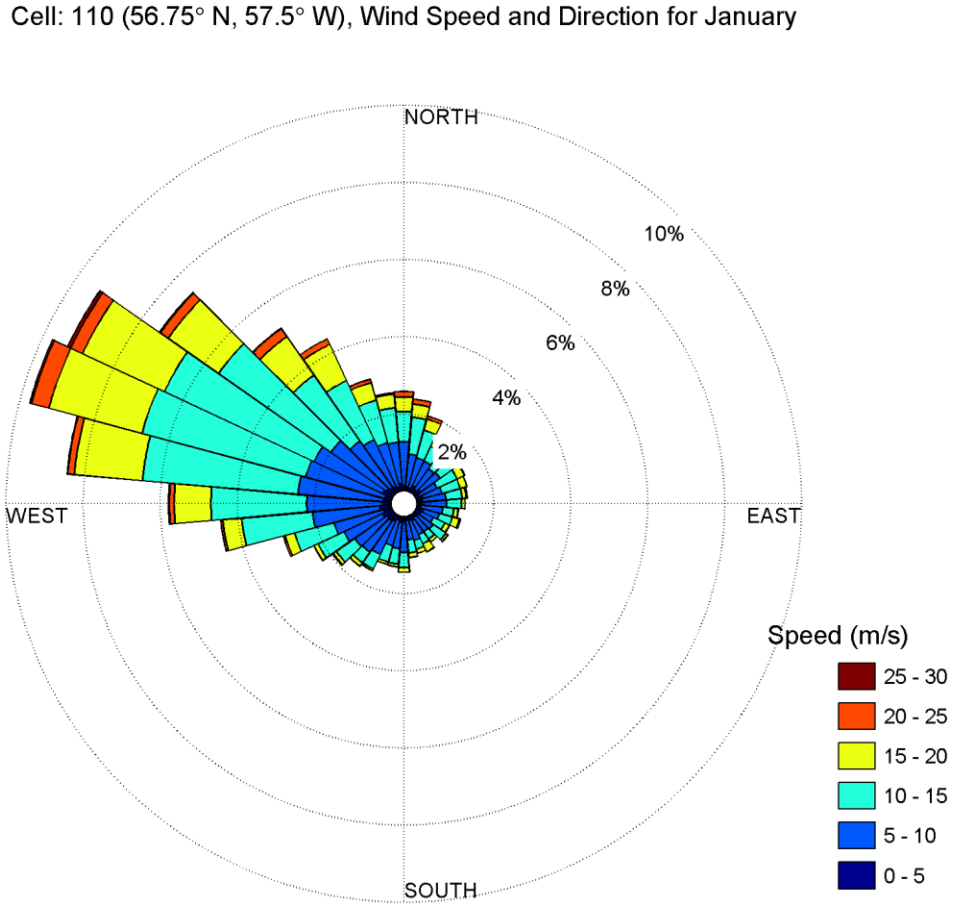

Figure 3-3. Wind rose for cell 110 for January

3.5 REGIONAL OVERVIEW

To gain an understanding of how winds vary over the entire study region, a series of seasonal and annual contour plots have been created. The annual plots for mean, maximum, and 100-year return period extreme wind speed are shown in Figure 3-4 to Figure 3-6. The figures show that the winds are more severe over the Grand Banks and the Flemish Pass and Cap than elsewhere. These differences are likely due to the increased occurrence of hurricanes (extra tropical storms) on the Grand Banks originating from the southern Caribbean region. The winds appear less severe closer to shore as well as further north in the newly identified hydrocarbon basins.

Figure 3-7 to Figure 3-9 show the seasonal variation of mean, maximum, and 100-year return period extreme wind speed. Seasons are defined according to the accepted convention with winter, spring, summer and fall covering December to February, March to May, June to August, and September to November, respectively. Other seasonal summaries covered in this report use the same convention. The contour maps clearly show that winter has the most severe winds and summer the least severe. Fall and spring fall between the two extremes and spring is slightly less severe than fall in most areas.

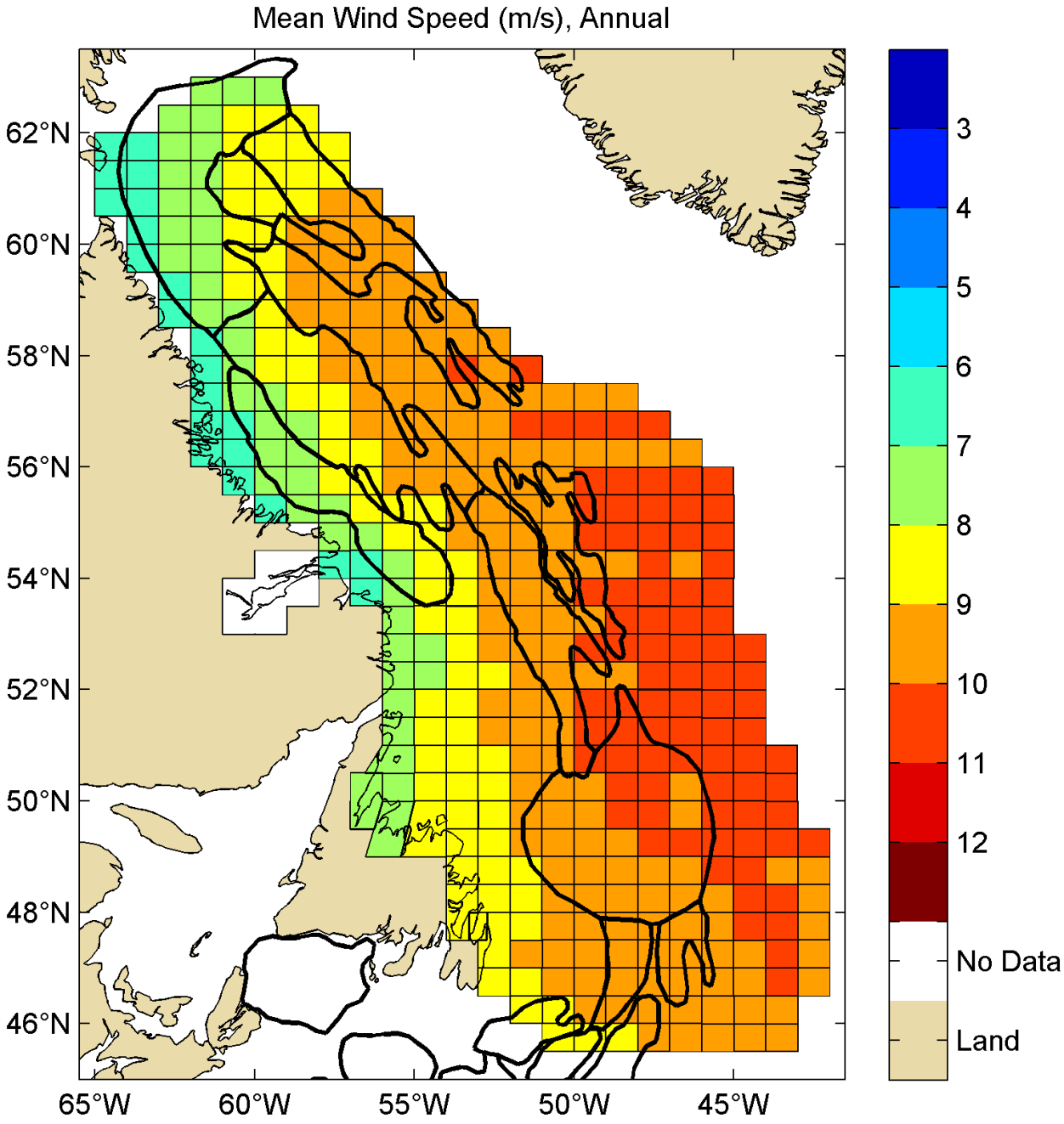

Figure 3-4. Regional overview of annual mean wind speed (m/s)

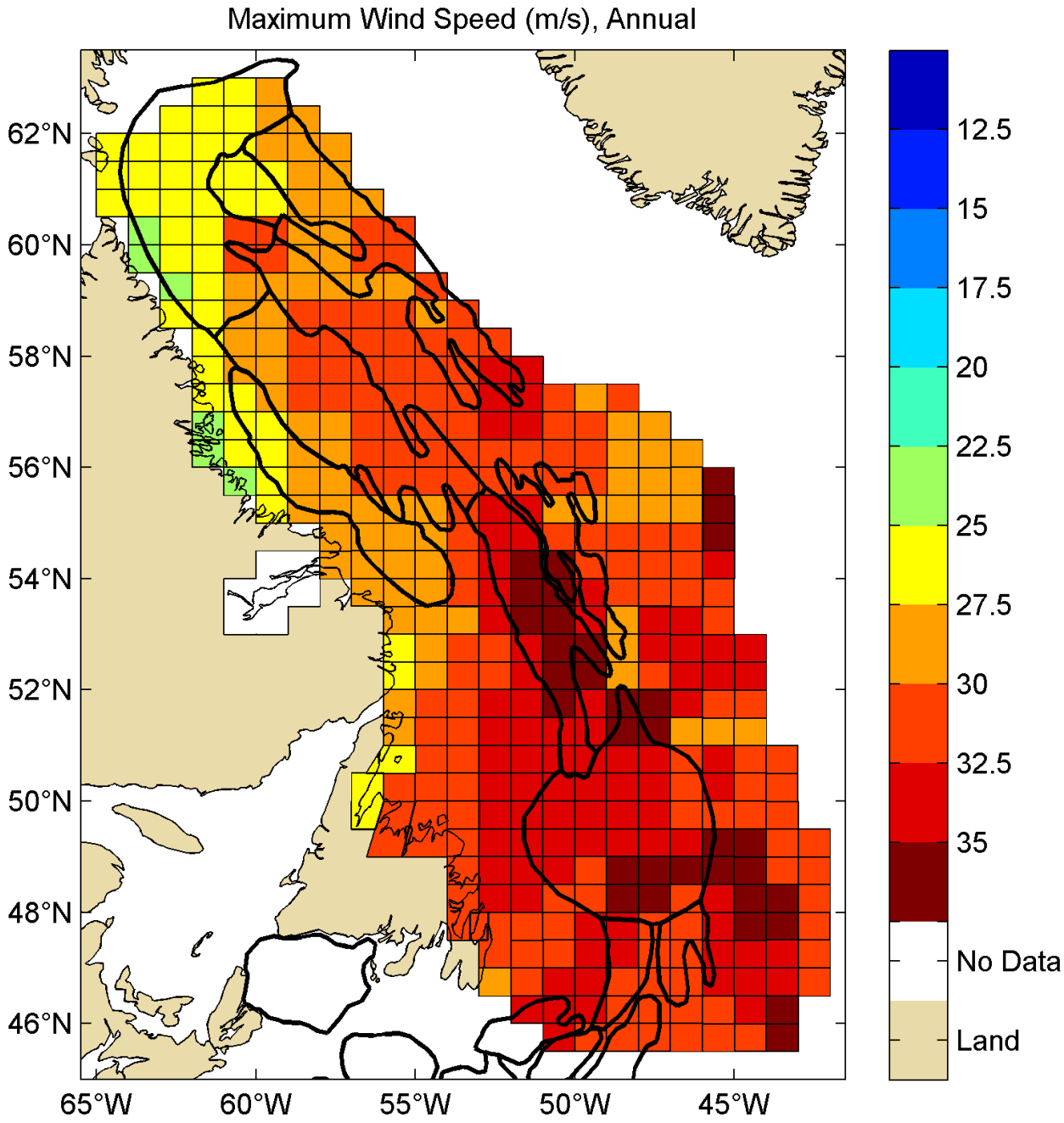

Figure 3-5. Regional overview of maximum wind speed (m/s) in MSC50 data set

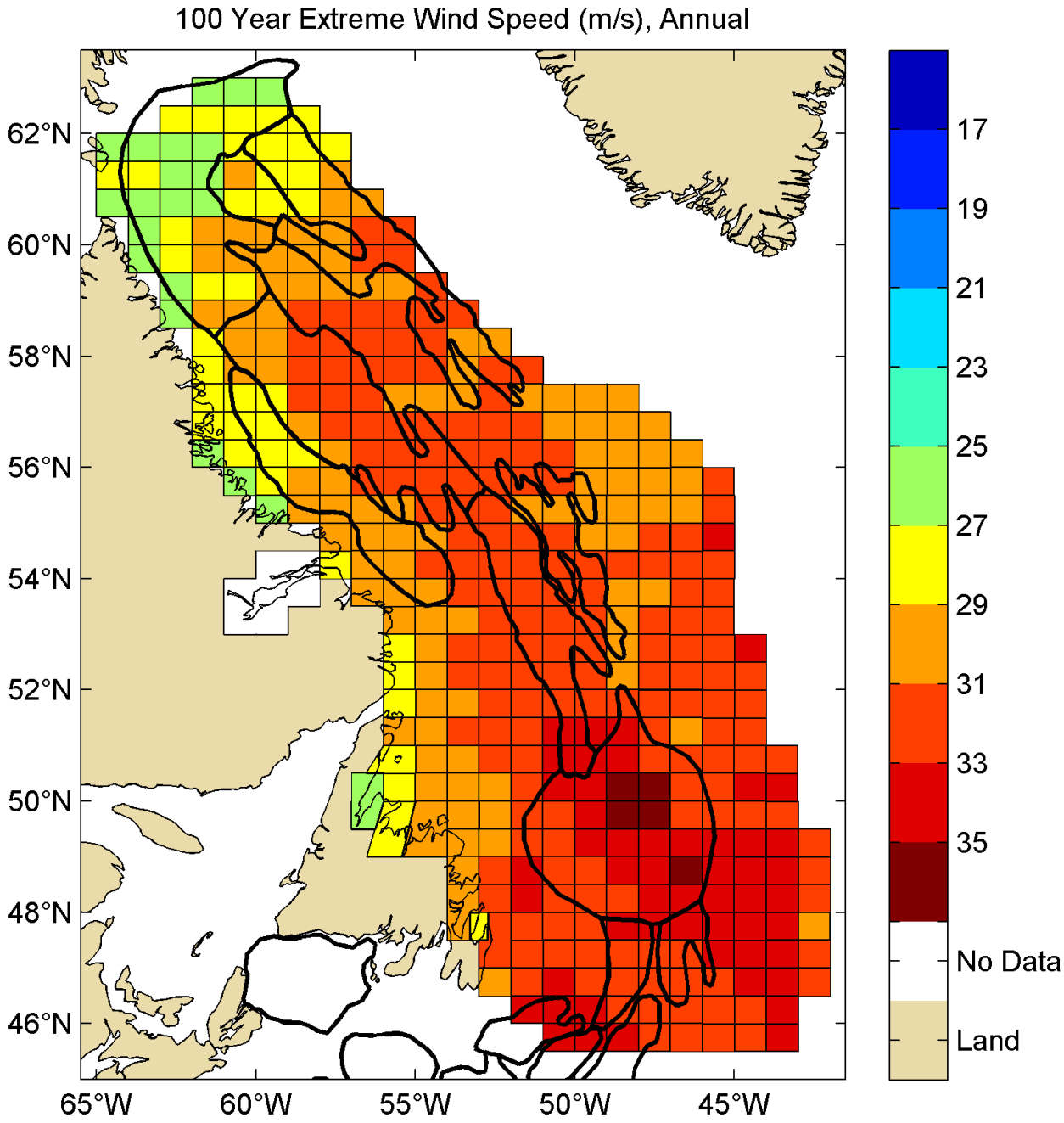

Figure 3-6. Regional overview of 100-year return period maximum wind speed (m/s)

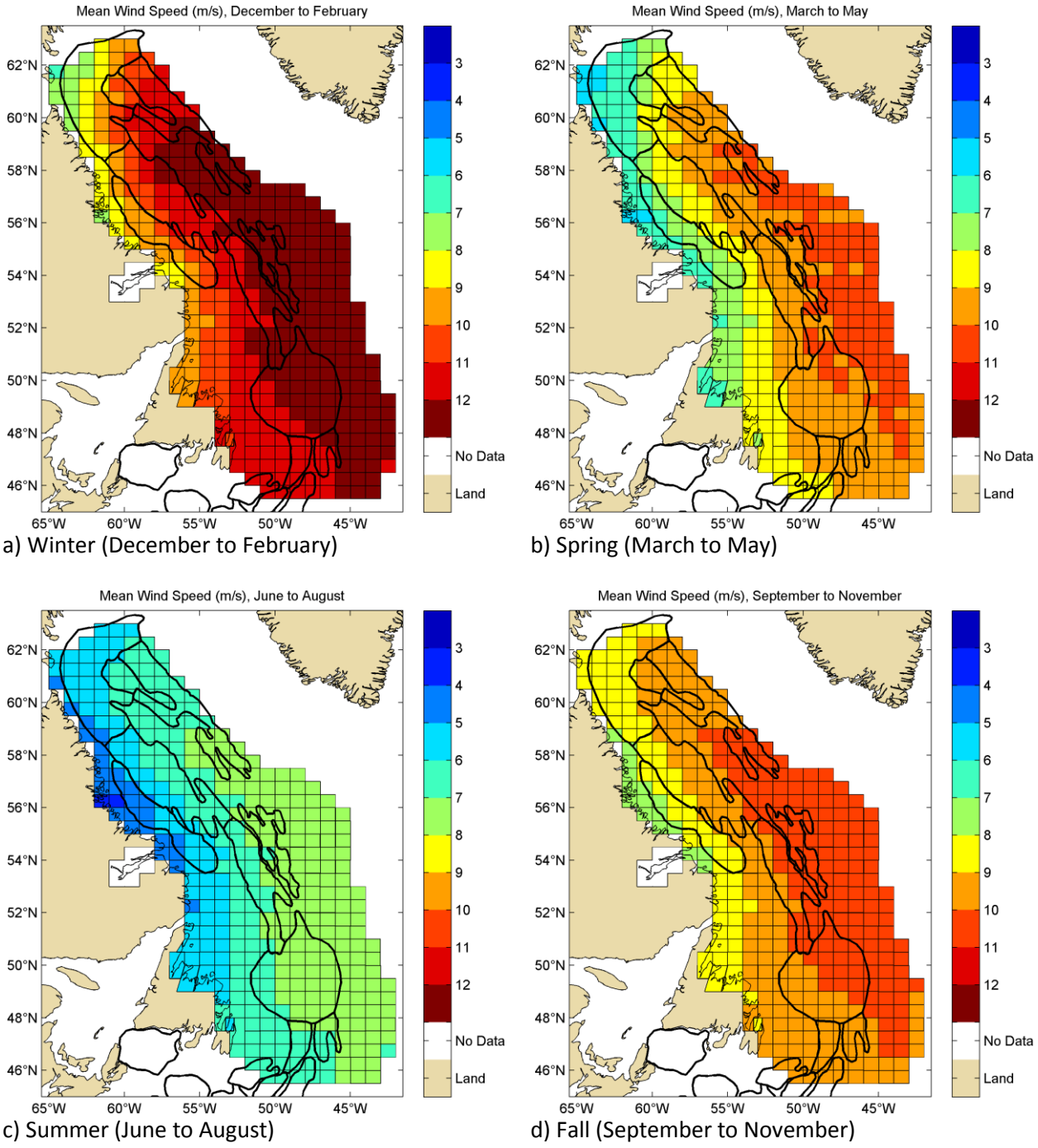

a) Winter (December to February)

b) Spring (March to May)

c) Summer (June to August)

d) Fall (September to November)

Figure 3-7. Seasonal overviews of mean wind speed (m/s) for (a) winter, (b) spring, (c) summer and (d) fall

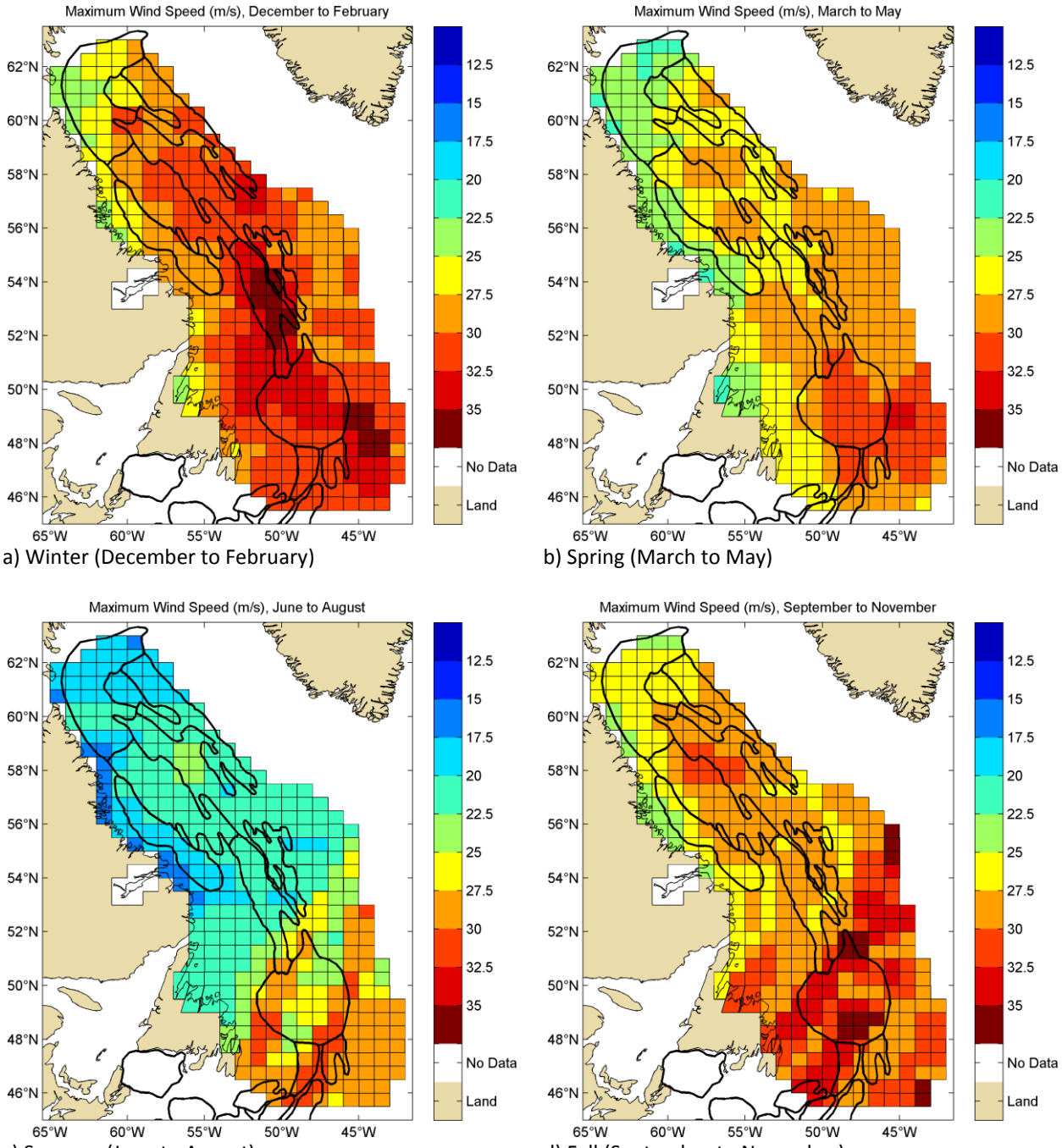

a) Winter (December to February)

b) Spring (March to May)

c) Summer (June to August)

d) Fall (September to November)

Figure 3-8. Seasonal overviews of maximum wind speed (m/s) for (a) winter, (b) spring, (c) summer and (d) fall

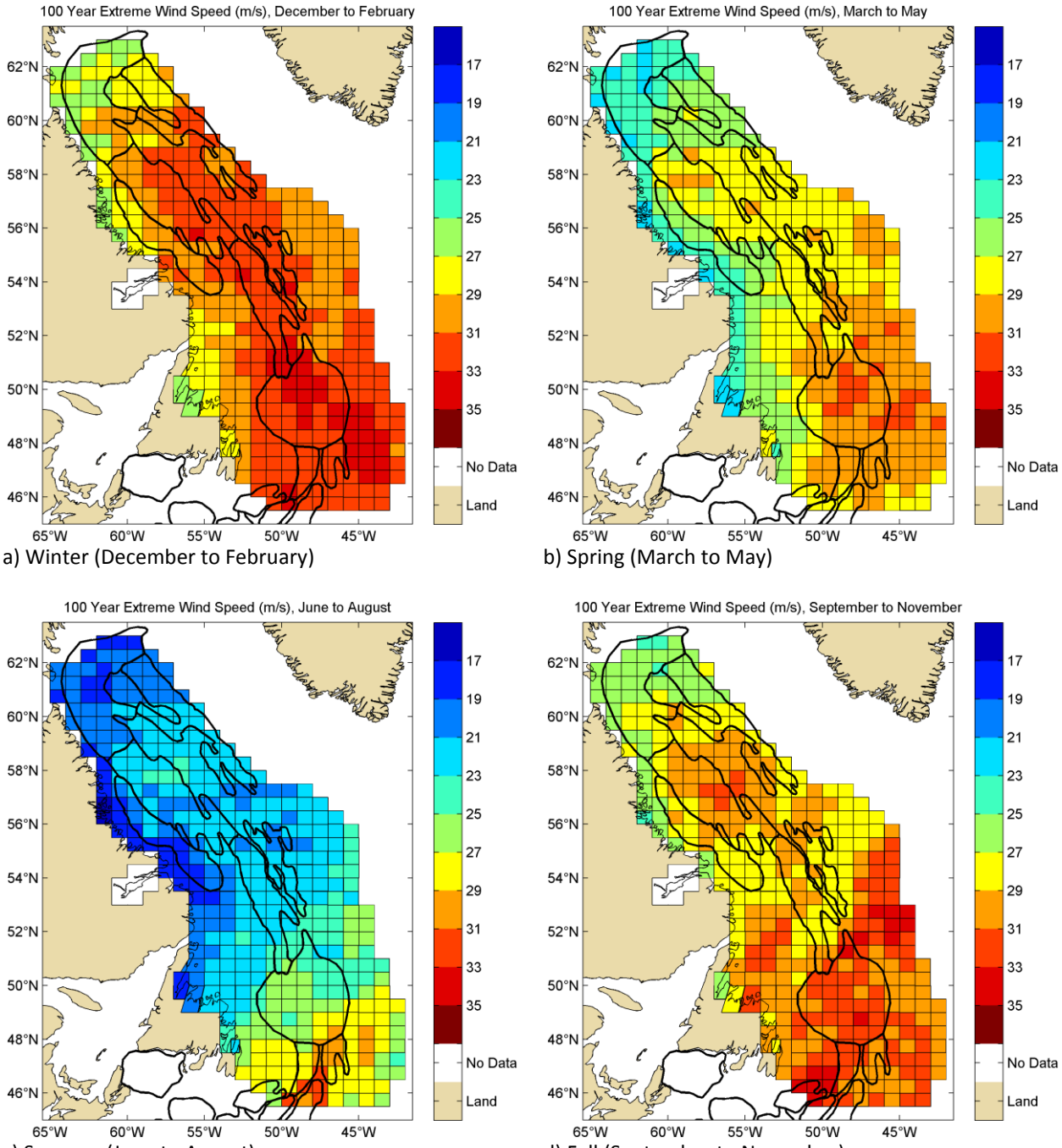

a) Winter (December to February)

b) Spring (March to May)

c) Summer (June to August)

d) Fall (September to November)

Figure 3-9. Seasonal overviews of 100-year return period maximum wind speed (m/s) for (a) winter, (b) spring, (c) summer and (d) fall

3.6 REFERENCES

Swail, V.R., Cardone, V.J., Ferguson, M., Gummer, D.J., Harris, E.L., Orelup, E.A. and Cox, A.T. (1996). The MSC50 Wind and Wave Reanalysis. 9th International Workshop on Wave Hindcasting and Forecasting, September 25-29, Victoria, B.C., Canada.

Metocean Climate Study
Offshore Newfoundland & Labrador

STUDY MAIN REPORT
Volume 1: Chapter 4 – Waves

Prepared for:
Nalcor Energy Oil and Gas

Prepared by:
C-CORE

Reviewed & Edited by:
Bassem Eid, Ph.D.

May 2015

CHAPTER 4 – WAVES

TABLE OF CONTENTS

LIST OF FIGURES

LIST OF TABLES

4 WAVES

4.1 DATA SOURCE

As with the wind analysis, the primary source for wave data is the MSC50 dataset (Swail et al., 2006). The MSC50 dataset is a wind and wave hindcast dataset for offshore waters. It contains either hourly or three hour recordings of wind and wave values for 60 years from 1954 to 2013. Wave height values are provided as significant wave heights in metres. Additional parameters for wave characteristics such as peak spectral period of the total spectrum (in seconds) and vector mean direction of total spectrum (to which waves are travelling, clockwise from north in degrees) are provided in the dataset, and used for additional analyses. The MSC50 data are presented for a number of geographic points, generally in 0.5 degree resolution for northern areas and 0.1 degree resolution for southern areas such as the Grand Banks.

4.2 DATA PROCESSING

Data points from a 0.5 degree resolution grid were used throughout the area of interest. This meant that in the 0.1 degree resolution area, most points were omitted. The remaining points, as well as the points in the northern area, are present on the cell boundaries as can be seen in Figure 4-1. Six MSC50 grid points surround all cells, except those on the boundaries of the region. The time series of wind and wave values were available every three hours for the entire 60-year dataset for each of the six MSC50 grid points around each cell. To get a single magnitude value of wind and wave parameters representing the entire cell, the maximum of each of these six values was taken at each time step in the time series. The new time series of maximum values was then used for the analyses. For direction of wind and wave, the vector average of the six MSC50 points was used. For the high-resolution MSC50 points, data were presented every one hour instead of every three as done in the low-resolution areas. To account for this, every third value in the high-resolution data set was used.

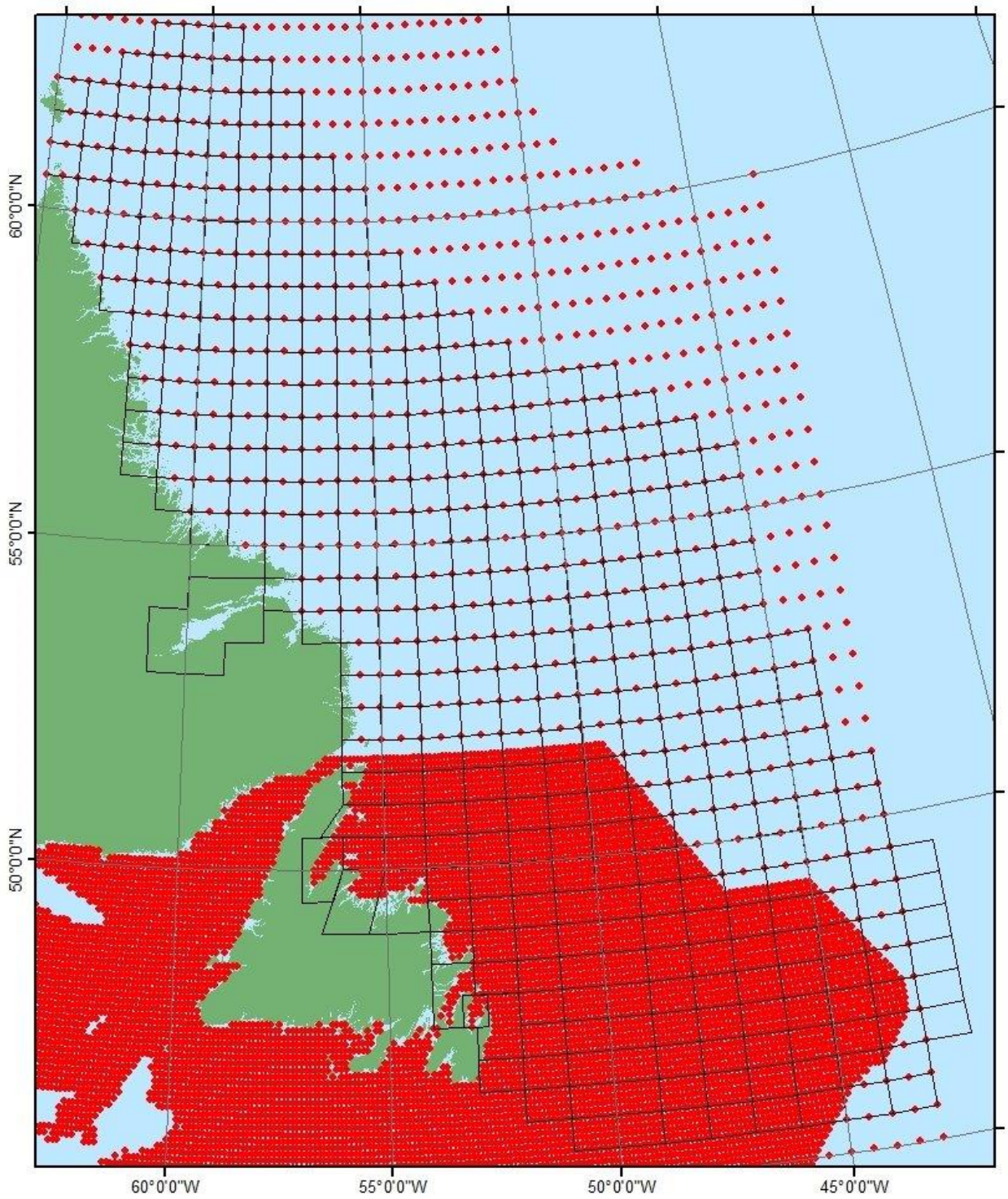

Figure 4-1. Nalcor study area with MSC50 grid points (red)

4.3 EXTREME VALUE ANALYSIS

Significant wave heights for 10, 25, 50, and 100-year return periods have been determined using a peak over threshold method. The threshold was set to give a minimum of 50 storm events over the course of the 60 years for each month, season, or year. Peak wave events within 48 hours of a local maximum were excluded. The storm event significant wave heights were approximated using a shifted exponential distribution. The distribution was shifted by an amount equal to the threshold for that month and the wave heights at the appropriate probability level for 10, 25, 50, and 100-year return periods was determined. Note: since the data for all months and grid cells were assumed to follow the same distribution, some months for some cells may provide data that do not fit the distribution perfectly, resulting in inaccuracy in the extreme values. The exponential distribution provided the best overall fit to the data.

The 10, 25, 50, and 100-year return period values assume sea ice will remain constant and are based upon the last 60 years of data (1954-2013). With reduced sea ice in some areas, winter design wave heights values may increase due to increased exposure.

Table 4-1 shows an example output of extreme significant wave heights for cell 110. Values for the remaining sites are given in the cell reports.

Table 4-1. Cell 110 - Extreme significant wave heights by return period

Cell: 110 56.75°N 57.5°W		Significant Wave Height Extremes by Return Period												
		Jan	Feb	Mar	Apr	May	Jun	Jul	Aug	Sep	Oct	Nov	Dec	Annual
Hs (m)	10 Year	10.3	10.1	9.5	7.8	6.2	5.3	4.3	5	7.7	9.4	10.7	10.9	11.6
	25 Year	11.5	11.6	10.8	8.9	7.2	6.1	4.9	5.7	9	10.7	12.3	12	12.3
	50 Year	12.4	12.8	11.8	9.7	7.9	6.6	5.4	6.3	10	11.7	13.4	12.9	12.9
	100 Yr.	13.3	13.9	12.8	10.5	8.6	7.2	5.8	6.8	10.9	12.7	14.6	13.7	13.5

4.4 STATISTICAL ANALYSIS

4.4.1 Summary Table

Each cell has a table summarizing the significant wave heights Table 4-2 provides an example for cell 110. The parameters, as defined in the table, are:

Mean – scalar mean of all significant wave heights in time series

St. Dev. – standard deviation of all significant wave heights in time series

Median – median of all significant wave heights in time series

P90 – 90th percentile of all significant wave heights in time series

Max. – maximum value of all significant wave heights in time series

Dom. Dir. – dominant (most frequent) direction of waves (FROM) in 10 degree bins

Table 4-2. Cell 110 - Significant wave height summary

Cell: 110 56.75°N 57.5°W		Summary Table - Wave												
		Jan	Feb	Mar	Apr	May	Jun	Jul	Aug	Sep	Oct	Nov	Dec	Annual
Sig. Wave Height (m)	Mean	2.5	2.4	2.2	2	1.4	1.4	1.3	1.5	2.1	2.7	3.1	3.2	2.1
	St. Dev.	2.1	1.9	1.8	1.5	1.1	0.9	0.7	0.7	1	1.3	1.5	2	1.6
	Median	2.4	2.3	2.1	1.9	1.4	1.3	1.2	1.3	1.8	2.4	2.8	3	1.8
	P90	5.3	4.8	4.6	3.9	2.8	2.5	2.1	2.4	3.3	4.4	5.1	5.7	4.2
	Max.	12.2	11.2	13.1	10.2	8.5	8.3	5.3	5.7	9.6	11.2	12.2	12.2	13.1
	Dom. Dir.	325	335	355	5	95	115	125	125	335	345	325	315	335

4.4.2 Wave Time Series

Time series plots show the entire 60 year wave record including when sea ice was present with respect to a threshold. Figure 4-2 shows an example for Cell 110 with a threshold of four metres (4 m). White areas represent times when the hindcast did not provide wave height values due to the presence of ice (waves are assumed to be zero). Green areas represent wave heights below the threshold (in this case four metres) for three days or more; yellow areas represent wave heights below the threshold for three days or less; and red areas represent wave heights above the threshold.

A decline in the white areas of the time series plot, representing ice, can be seen from the 1970s and 1980s to the last decade. This is a common trend across most cells. It means that ice conditions have been less severe since 2000, and that more events with waves above four metres have occurred in that time frame.

The cell reports contain figures for the remaining sites in addition to plots with a threshold of six metres.

Figure 4-2. Cell 110 - Time series of wave heights above 4 m threshold

4.4.3 Histograms

Histograms of significant wave height and period have been provided for each cell. Examples have been provided for cell 110 in Figure 4-3 and Figure 4-4.

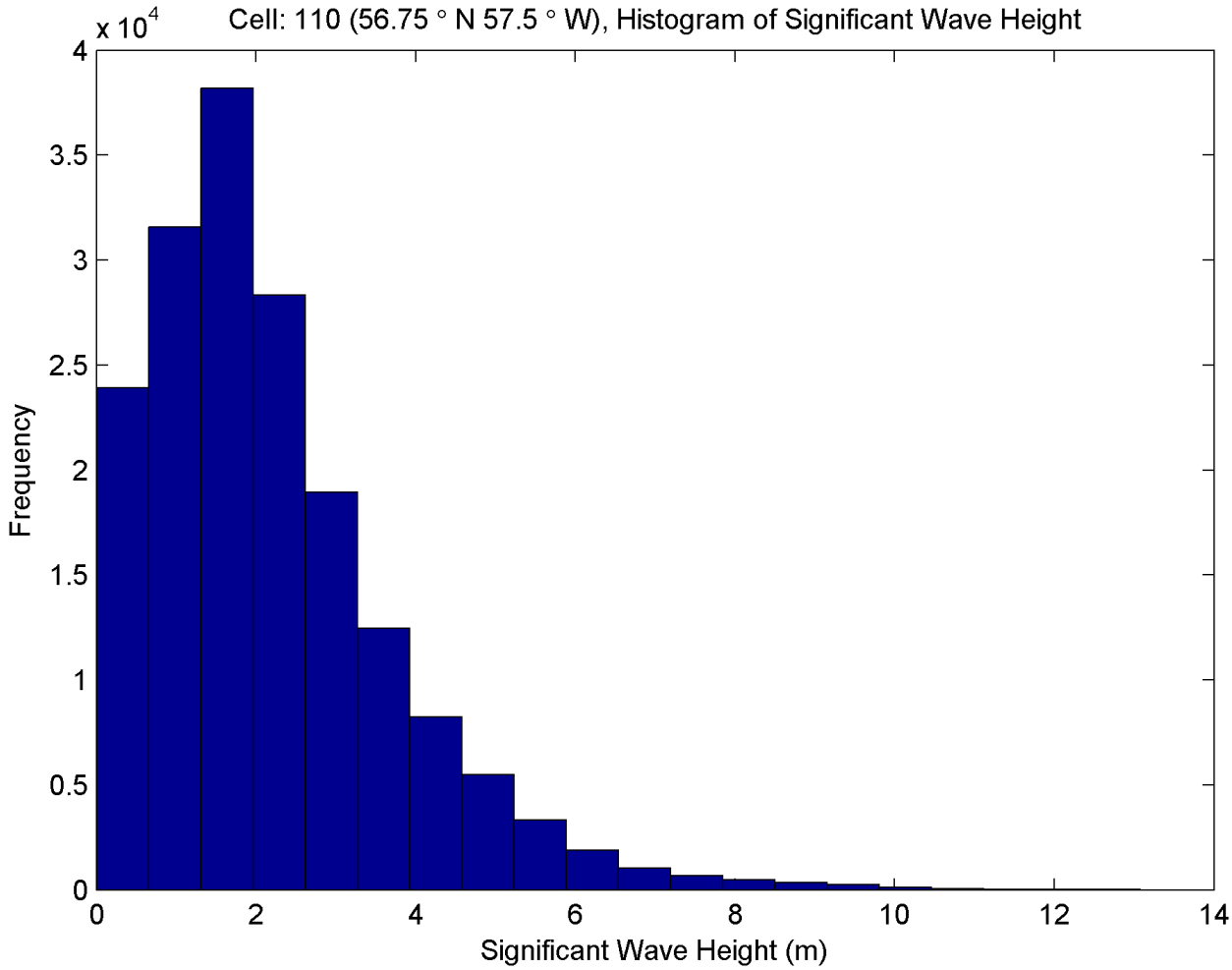

Figure 4-3. Cell 110 – Histogram of significant wave height

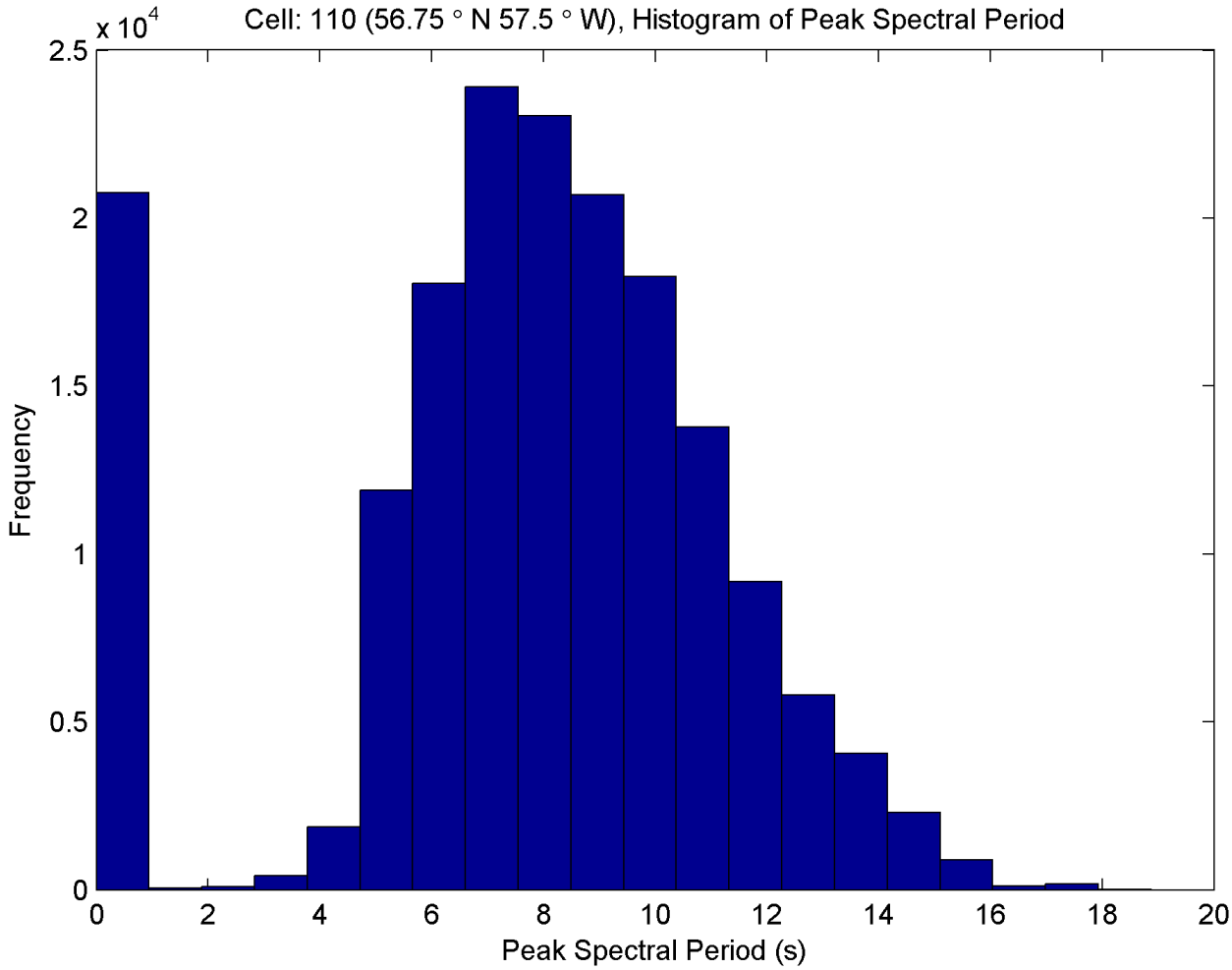

Figure 4-4. Cell 110 – Histogram of peak spectral period

4.4.4 Probability of Exceedance Tables

The probability of exceedance for significant wave heights is shown in Table 4-3 for Cell 110 and in Table 4-4 for peak period. Values for the remaining cells are given in the cell reports. The numerical values represent the proportion of time (from 0 to 1) that the wave heights meet or exceed the values listed in each row. The data are presented monthly with a color scale representing the more likely cases. Cases with a zero listed as the probability and the squares shaded cyan (blue) represent instances in which the probability was less than 0.0005 (0.05%). This is due to rounding. Cases with an unshaded square and a zero value displayed mean that wind speeds above that value did not occur in the hindcast dataset.

Table 4-3. Cell 110 – Significant wave height probability of exceedance by month

Cell: 110 56.75°N 57.5°W		Significant Wave Height - Probability of Exceedance by Month											
		Jan	Feb	Mar	Apr	May	Jun	Jul	Aug	Sep	Oct	Nov	Dec
Sig. Wave Height (m)	1	0.704	0.772	0.741	0.752	0.672	0.669	0.627	0.721	0.932	0.978	0.991	0.881
	2	0.578	0.564	0.535	0.45	0.25	0.191	0.123	0.172	0.427	0.653	0.766	0.755
	3	0.384	0.334	0.306	0.212	0.081	0.051	0.02	0.04	0.146	0.303	0.436	0.511
	4	0.23	0.181	0.155	0.09	0.025	0.014	0.003	0.01	0.048	0.135	0.233	0.302
	5	0.125	0.089	0.072	0.032	0.008	0.003	0	0.003	0.02	0.058	0.106	0.156
	6	0.06	0.041	0.031	0.011	0.003	0.001	0	0	0.009	0.026	0.045	0.078
	7	0.029	0.022	0.014	0.005	0.001	0	0	0	0.004	0.011	0.022	0.039
	8	0.014	0.012	0.006	0.003	0	0	0	0	0.002	0.006	0.013	0.023
	9	0.006	0.006	0.003	0.001	0	0	0	0	0.001	0.002	0.006	0.011
	10	0.002	0.001	0.001	0	0	0	0	0	0	0.001	0.002	0.003
	11	0.001	0	0	0	0	0	0	0	0	0	0.001	0.001
	12	0	0	0	0	0	0	0	0	0	0	0	0
	13	0	0	0	0	0	0	0	0	0	0	0	0
	14	0	0	0	0	0	0	0	0	0	0	0	0

Table 4-4. Cell 110 – Peak spectral period probability of exceedance by month

Cell: 110 56.75°N 57.5°W		Peak Spectral Period - Probability of Exceedance by Month											
		Jan	Feb	Mar	Apr	May	Jun	Jul	Aug	Sep	Oct	Nov	Dec
Peak Spectral Period (s)	1	0.717	0.799	0.766	0.816	0.783	0.866	0.961	0.983	1	1	1	0.883
	2	0.717	0.799	0.766	0.816	0.783	0.866	0.958	0.983	1	1	1	0.883
	3	0.717	0.799	0.766	0.816	0.783	0.866	0.952	0.983	1	1	1	0.883
	4	0.715	0.797	0.764	0.811	0.781	0.863	0.933	0.978	0.999	1	1	0.883
	5	0.707	0.784	0.748	0.785	0.758	0.831	0.883	0.929	0.98	0.99	0.994	0.881
	6	0.676	0.732	0.704	0.722	0.677	0.711	0.705	0.755	0.867	0.912	0.939	0.849
	7	0.611	0.653	0.629	0.628	0.552	0.547	0.494	0.53	0.703	0.788	0.822	0.773
	8	0.531	0.556	0.534	0.502	0.413	0.378	0.297	0.329	0.497	0.618	0.669	0.656
	9	0.435	0.444	0.418	0.356	0.268	0.219	0.155	0.176	0.311	0.439	0.508	0.509
	10	0.335	0.333	0.304	0.226	0.147	0.105	0.091	0.1	0.184	0.278	0.341	0.367
	11	0.23	0.236	0.202	0.123	0.066	0.049	0.053	0.058	0.091	0.152	0.2	0.252
	12	0.155	0.16	0.113	0.059	0.027	0.029	0.04	0.042	0.057	0.075	0.113	0.148
	13	0.098	0.108	0.07	0.036	0.016	0.023	0.024	0.028	0.033	0.047	0.062	0.083
	14	0.05	0.06	0.036	0.018	0.007	0.014	0.012	0.014	0.012	0.019	0.028	0.047
	15	0.01	0.019	0.012	0.004	0.003	0.006	0.004	0.007	0.003	0.003	0.005	0.008
	16	0.002	0.001	0	0	0.002	0.003	0.002	0.005	0.002	0.001	0.001	0.001
	17	0.001	0	0	0	0.001	0.002	0.001	0.005	0.001	0.001	0	0
	18	0	0	0	0	0	0	0	0	0	0	0	0
	19	0	0	0	0	0	0	0	0	0	0	0	0

4.4.5 Duration of Significant Wave Height Below Specified Threshold

A certain time period with sea states below a certain value may be required to conduct an operation. The likelihood of significant wave heights below certain thresholds for varying periods (in days) has been calculated using the MSC50 data. An example is shown in Figure 4-5. The *x*-axis represents the duration of days below the threshold, the *y*-axis represents the probability of exceeding this value, and the various colored lines represent different wave height threshold values. The probability of exceedance in this case refers to the number of days, not the sea state. For example, the probability of getting sea states below four m for five days or more in January is about 1x10-1 (10%). As the threshold significant wave increases, so does the probability. A full set of plots for each site and month are given in the cell reports.

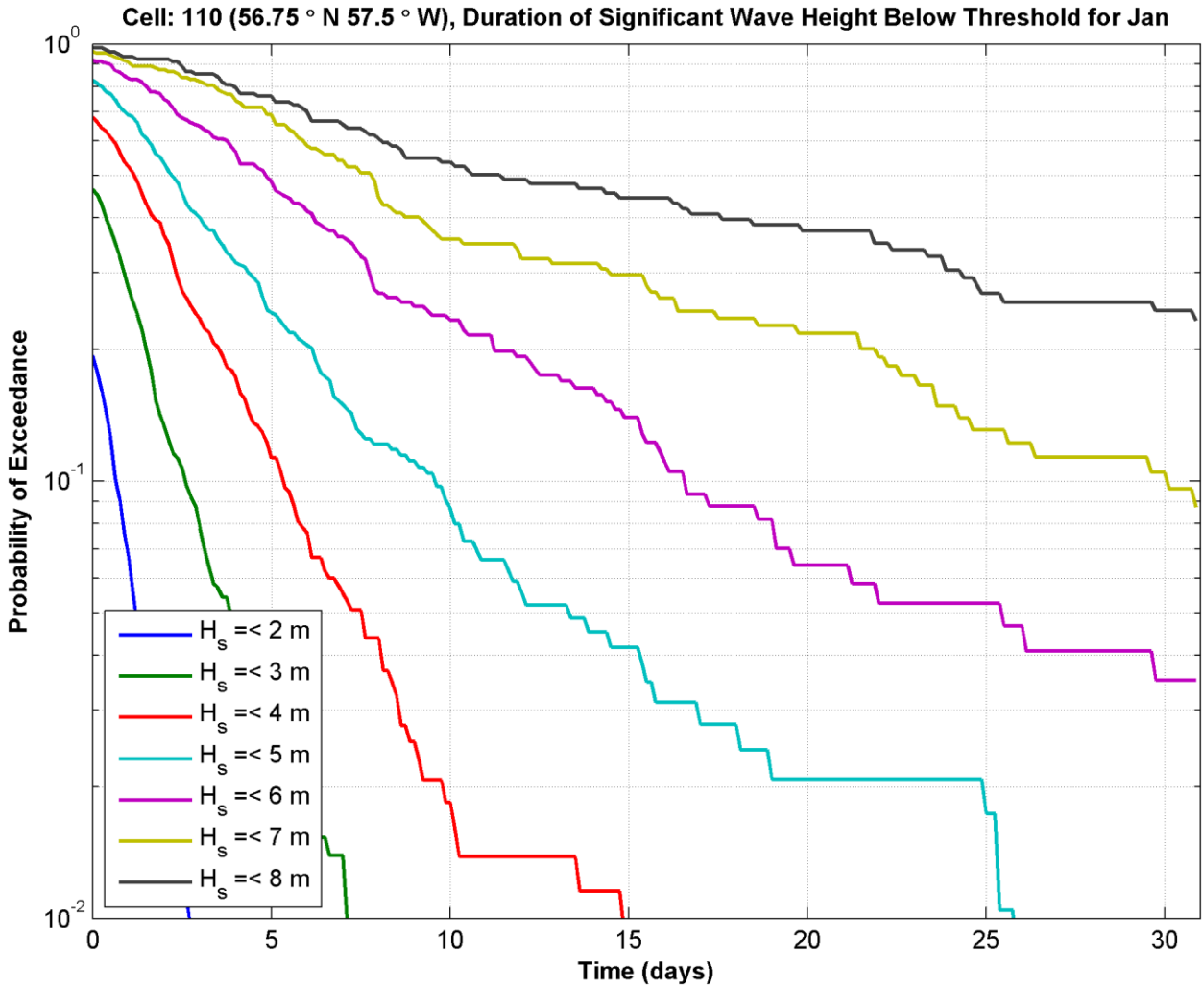

Figure 4-5. Cell 110 – duration of significant wave height below threshold for January

4.4.6 Joint Probability of Significant Wave Height and Period

The joint probability distribution of significant wave heights and wave period are shown in Table 4-5 for Cell 110 for January. The columns are broken down into wave height bins and the rows are broken down into wave period bins. The percentage of time that each bin occurs over the course of the 60 years is shown in the cell. A corresponding color scheme is used to highlight the frequency of occurrence for the cells, with purple values being the highest and cyan (blue) being the lowest. The plots often show a high chance of waves with zero to one m wave height and zero to one-second period, this often indicates that ice was present in winter months, but may simply represent a very calm sea state when ice is not present. Joint probability distributions for each cell and month are shown in the cell reports.

Table 4-5. Cell 110 – Significant wave height and period joint distribution for January

Cell: 110 56.75°N 57.5°W		Significant Wave Height and Period - Joint Probability Distribution for January														
		Sig. Wave Height (m)														
		0-1	1-2	2-3	3-4	4-5	5-6	6-7	7-8	8-9	9-10	10-11	11-12	12-13	13-14	14-15
Wave Period (s)	0-1	28.34	0	0	0	0	0	0	0	0	0	0	0	0	0	0
	1-2	0	0	0	0	0	0	0	0	0	0	0	0	0	0	0
	2-3	0	0	0	0	0	0	0	0	0	0	0	0	0	0	0
	3-4	0.054	0.007	0	0	0	0	0	0	0	0	0	0	0	0	0
	4-5	0.034	0.464	0.02	0	0	0	0	0	0	0	0	0	0	0	0
	5-6	0.067	0.806	0.672	0.007	0	0	0	0	0	0	0	0	0	0	0
	6-7	0.054	0.659	3.858	0.255	0	0	0	0	0	0	0	0	0	0	0
	7-8	0	0.706	3.125	3.777	0.114	0	0	0	0	0	0	0	0	0	0
	8-9	0	0.423	1.559	4.22	2.07	0.074	0	0	0	0	0	0	0	0	0
	9-10	0	0.249	1.64	2.305	3.656	1.082	0.054	0	0	0	0	0	0	0	0
	10-11	0	0.464	1.539	1.788	2.466	3.185	0.941	0.054	0.007	0	0	0	0	0	0
	11-12	0	0.612	1.667	1.532	1.27	1.653	1.606	0.699	0.141	0.013	0	0	0	0	0
	12-13	0	0.349	1.465	1.156	0.974	0.853	0.753	0.679	0.484	0.161	0.06	0	0	0	0
	13-14	0	0.329	1.512	1.042	0.954	0.773	0.504	0.175	0.235	0.161	0.101	0.013	0.007	0	0
	14-15	0	0.148	1.089	1.337	0.793	0.847	0.571	0.302	0.161	0.235	0.074	0.087	0.034	0	0
	15-16	0	0.04	0.134	0.276	0.208	0.141	0.108	0.074	0.02	0	0	0.007	0.02	0	0
	16-17	0	0.034	0.094	0.121	0.047	0.034	0.02	0.027	0.027	0	0	0	0	0	0
	17-18	0	0.02	0.06	0.054	0	0	0	0.027	0	0	0	0	0	0	0
	18-19	0	0	0	0	0	0	0	0	0	0	0	0	0	0	0
	19-20	0	0	0	0	0	0	0	0	0	0	0	0	0	0	0

4.4.7 Wave Rose

To quantify the frequency and strength of waves by direction, a series of plots, similar to Figure 4-6 have been created. Wave direction is the vector mean direction of total spectrum (the direction from which waves are coming, clockwise from North in degrees). Waves are broken down into 10-degree bins. The radial length of each bin represents the frequency and the distribution of colors on each bar represents the frequency of significant wave heights corresponding to the legend. Wave rose plots are given in the cell reports for each cell for each month.

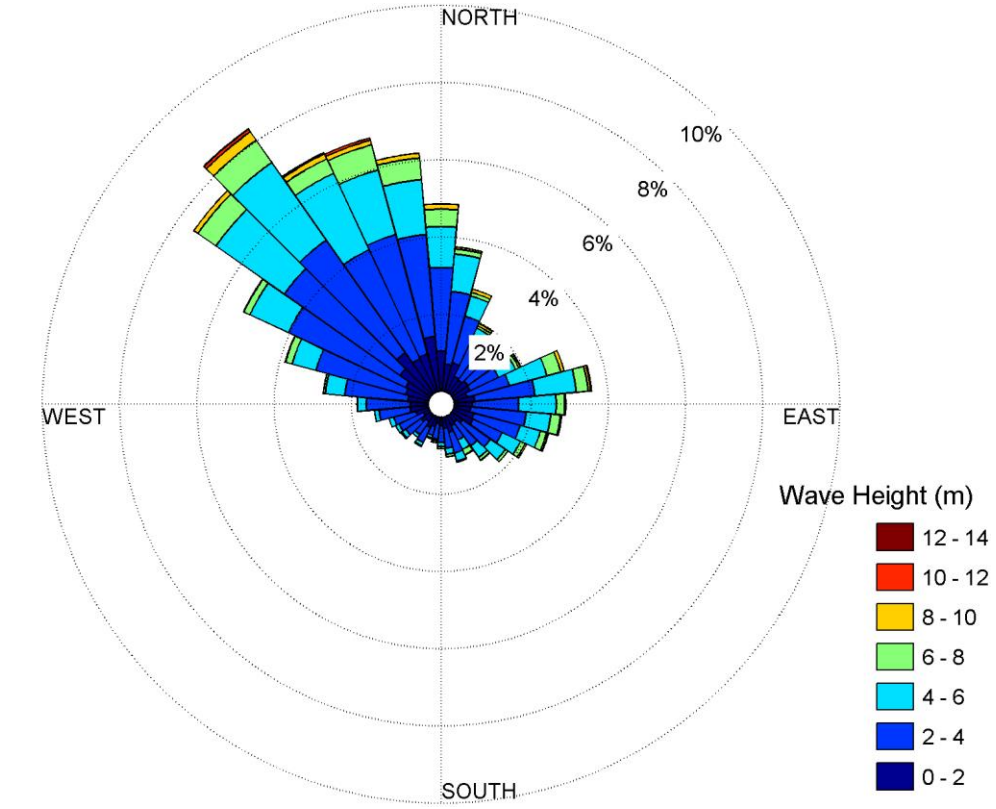

Figure 4-6. Wave rose for cell 110 for January

4.5 REGIONAL OVERVIEW

To gain an understanding of how waves vary over the entire study region, a series of seasonal and annual contour plots have been created. Figure 4-7 to Figure 4-9 show the annual plots for mean, maximum, and 100-year return period extreme significant wave height. The figures show that the waves are more severe over the Grand Banks and Flemish Pass/Flemish Cap than elsewhere and less severe closer to shore. These differences are likely due to the increased occurrence of hurricanes tracking from the southern Caribbean region to the Grand Banks, and less fetch near shore for wave generation.

Figure 4-10 to Figure 4-12 show the seasonal variation of mean, maximum, and 100-year return period extreme significant wave height. Winter provides the most severe waves in the offshore, while areas close to the coast are sheltered by ice presence. It can be seen that wave severity varies significantly by season, with much less severe sea states in summer.

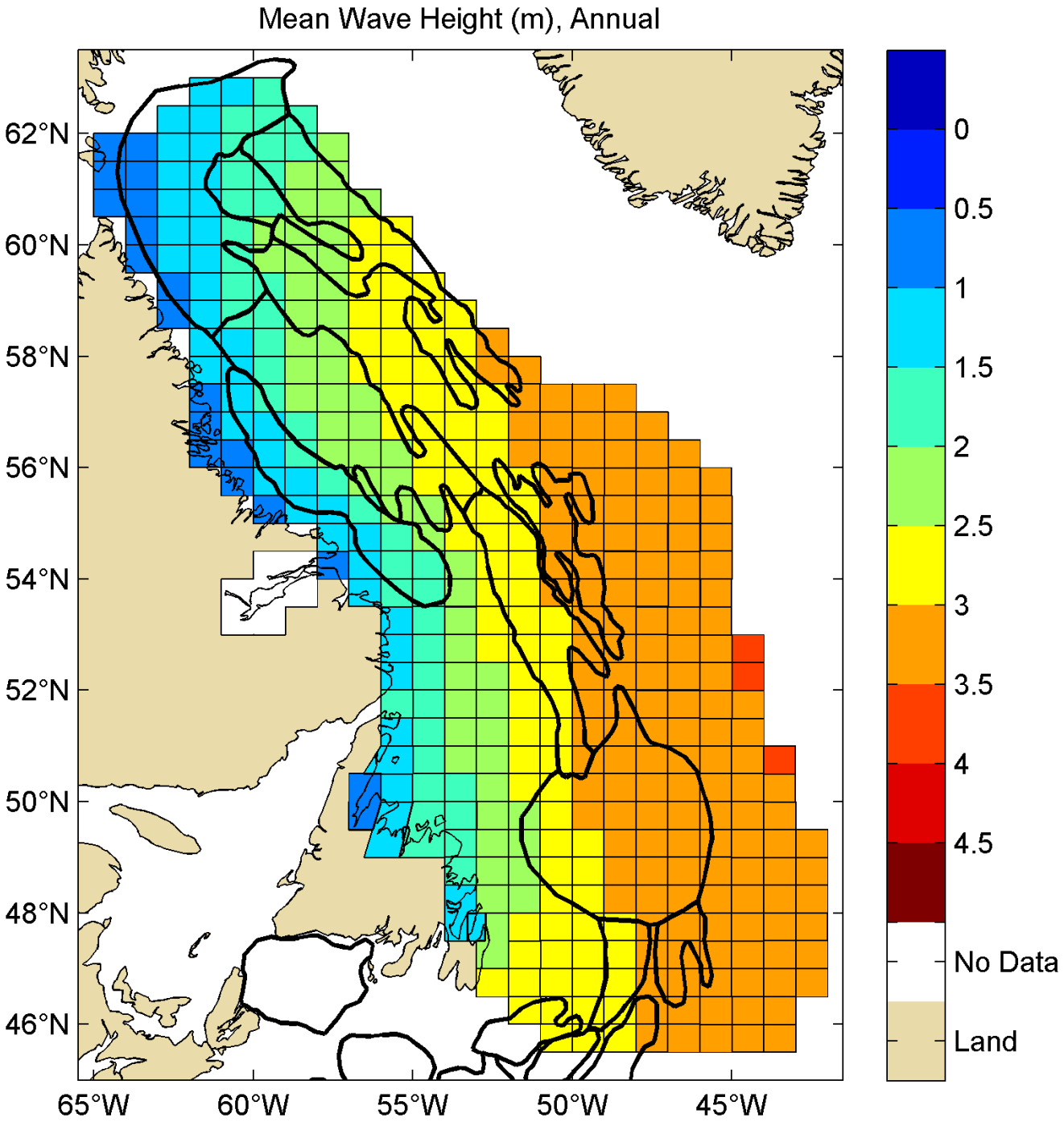

Figure 4-7. Regional overview of annual mean significant wave heights (m)

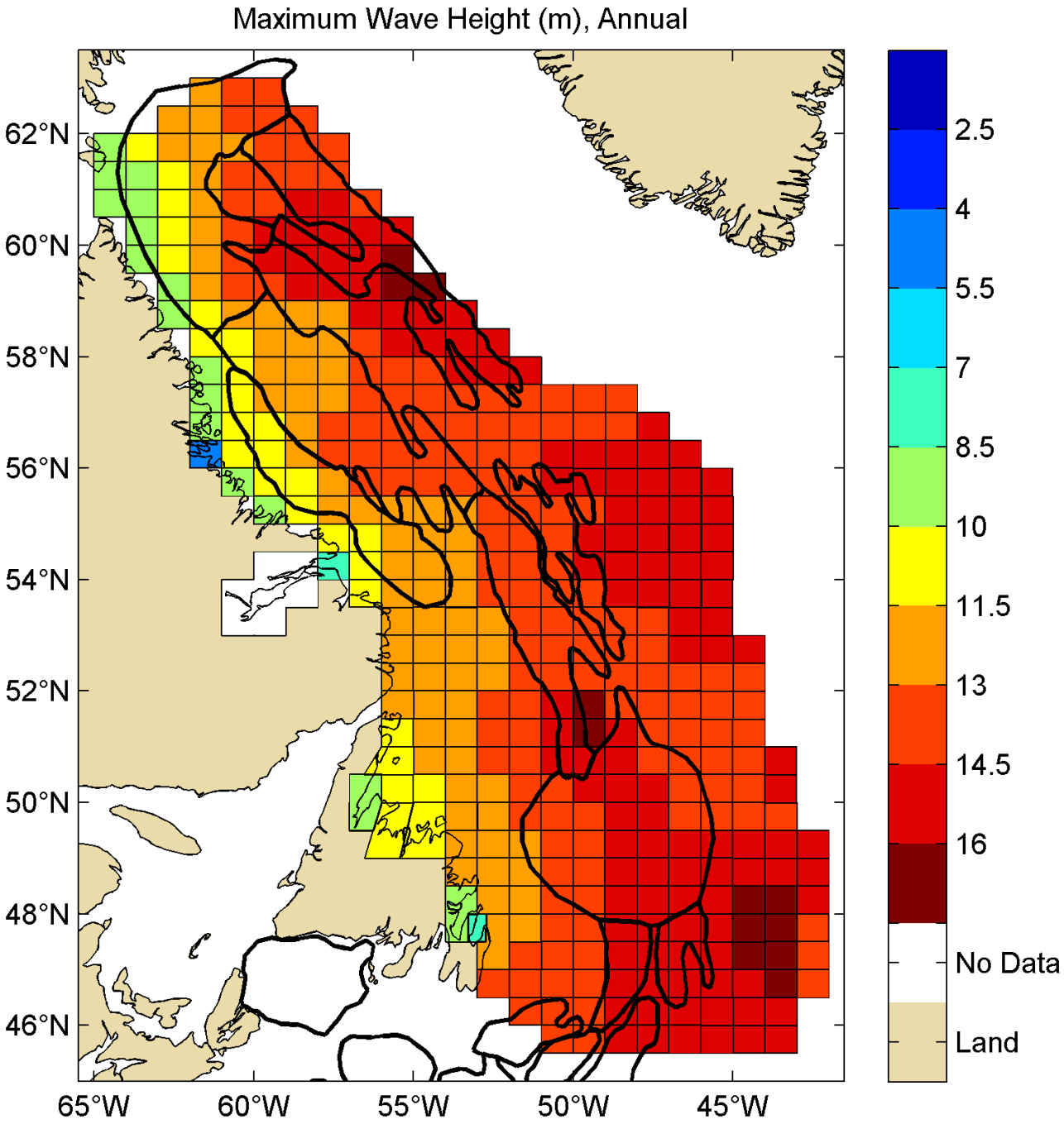

Figure 4-8. Regional overview of maximum significant wave heights (m) in MSC50 dataset

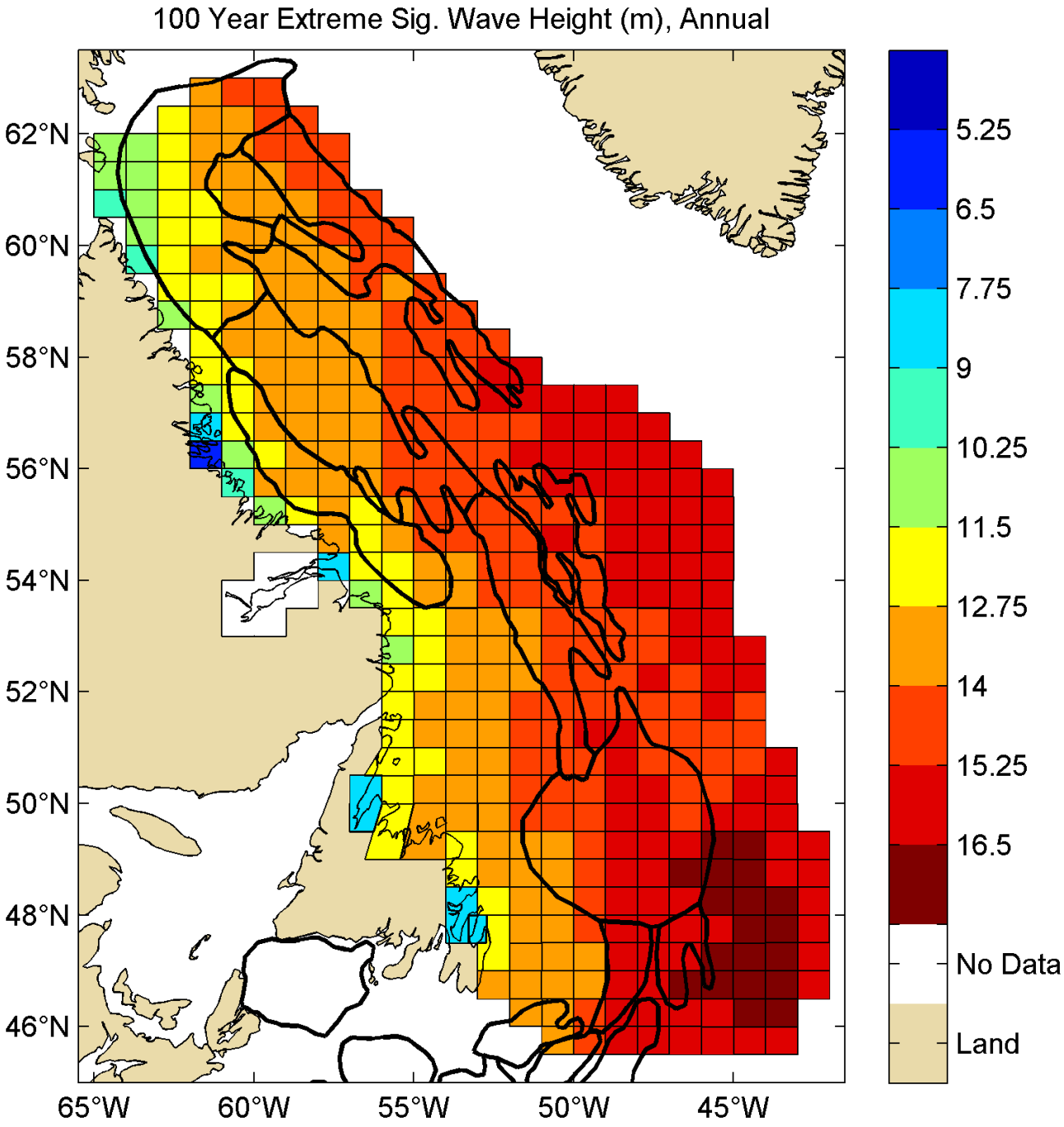

Figure 4-9. Regional overview of 100-year return period significant wave heights (m)

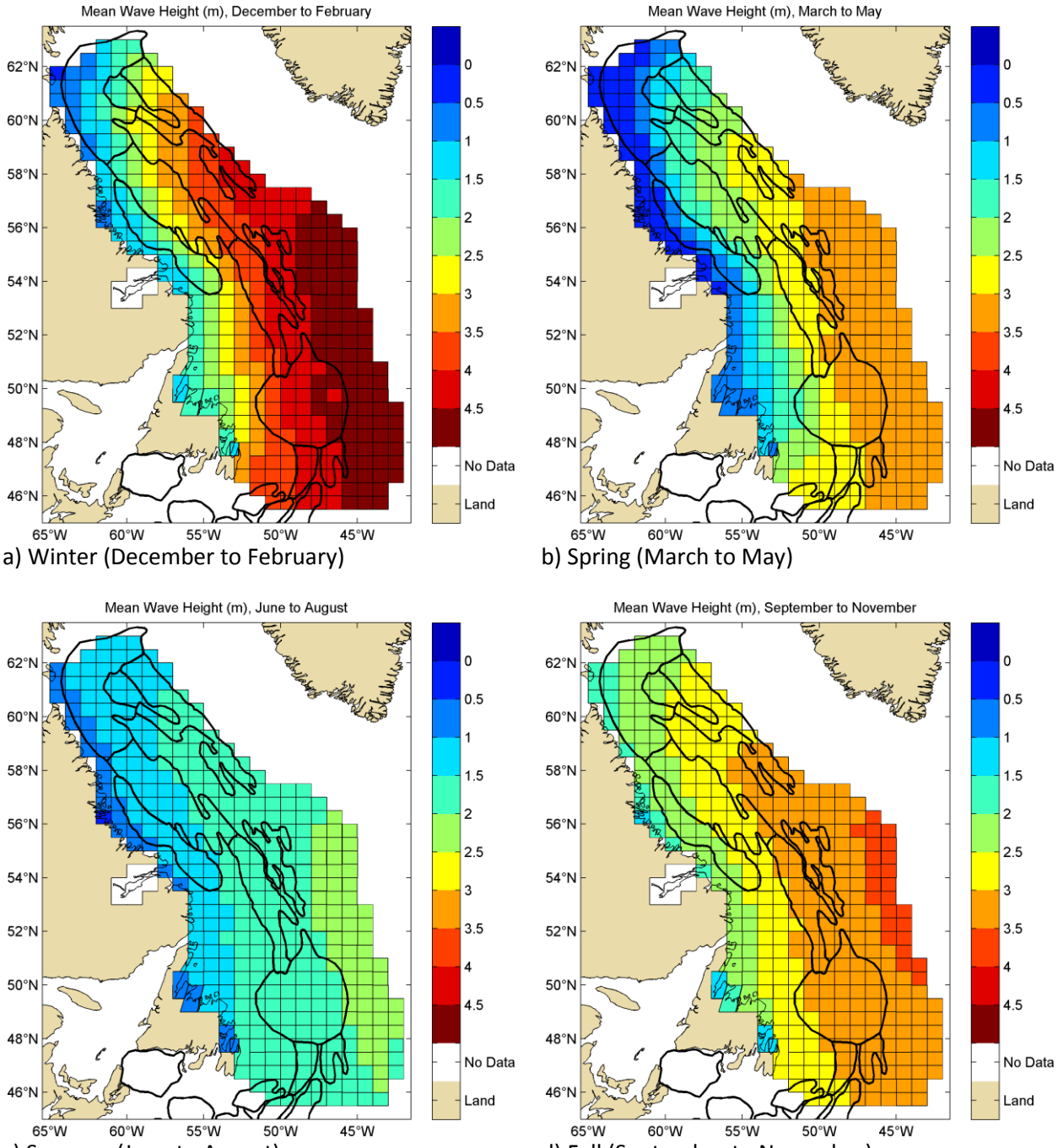

a) Winter (December to February)

b) Spring (March to May)

c) Summer (June to August)

d) Fall (September to November)

Figure 4-10. Seasonal overviews of mean significant wave heights (m) for (a) winter, (b) spring, (c) summer and (d) fall

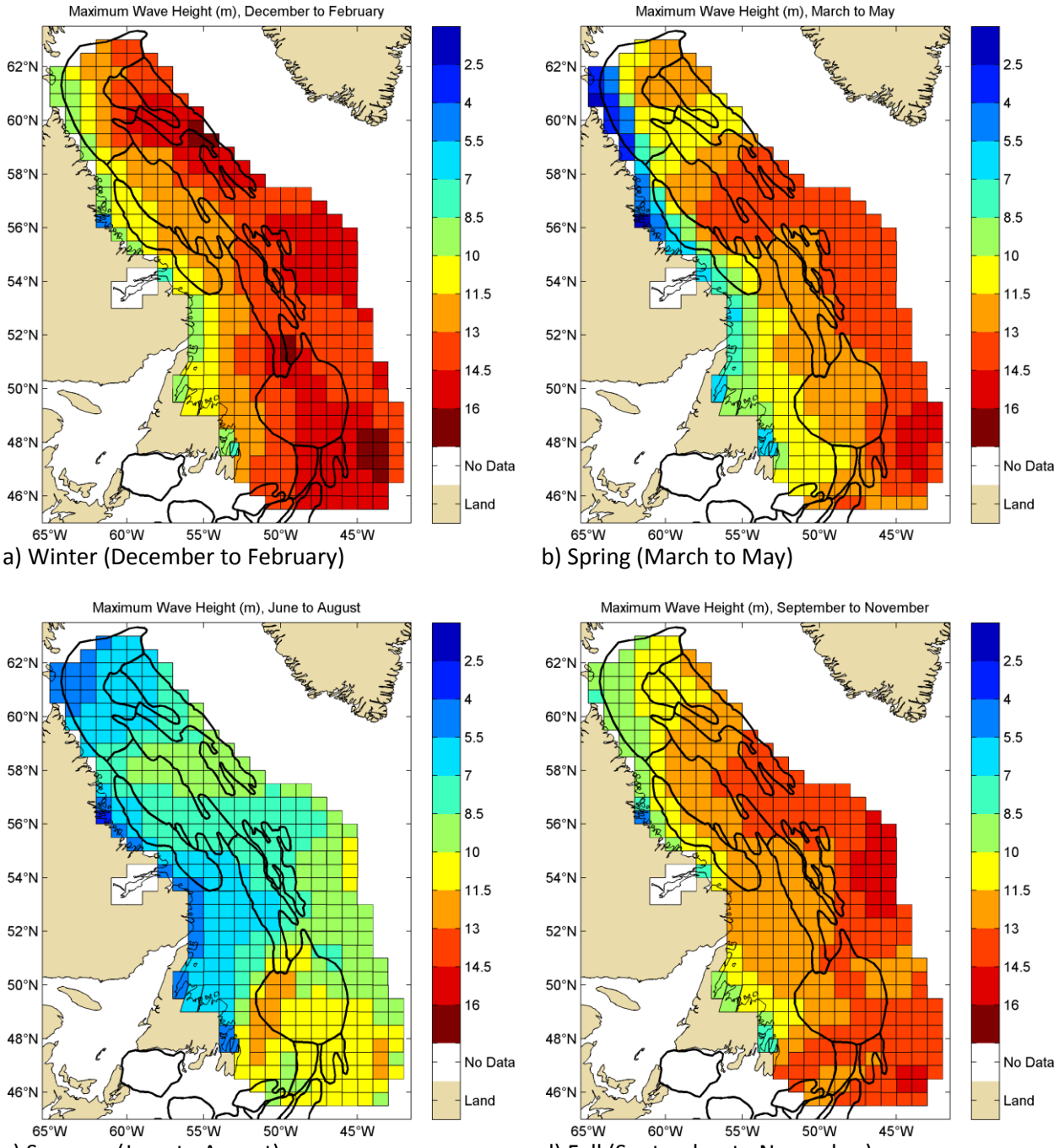

a) Winter (December to February)

b) Spring (March to May)

c) Summer (June to August)

d) Fall (September to November)

Figure 4-11. Seasonal overviews of maximum significant wave heights (m) for (a) winter, (b) spring, (c) summer and (d) fall

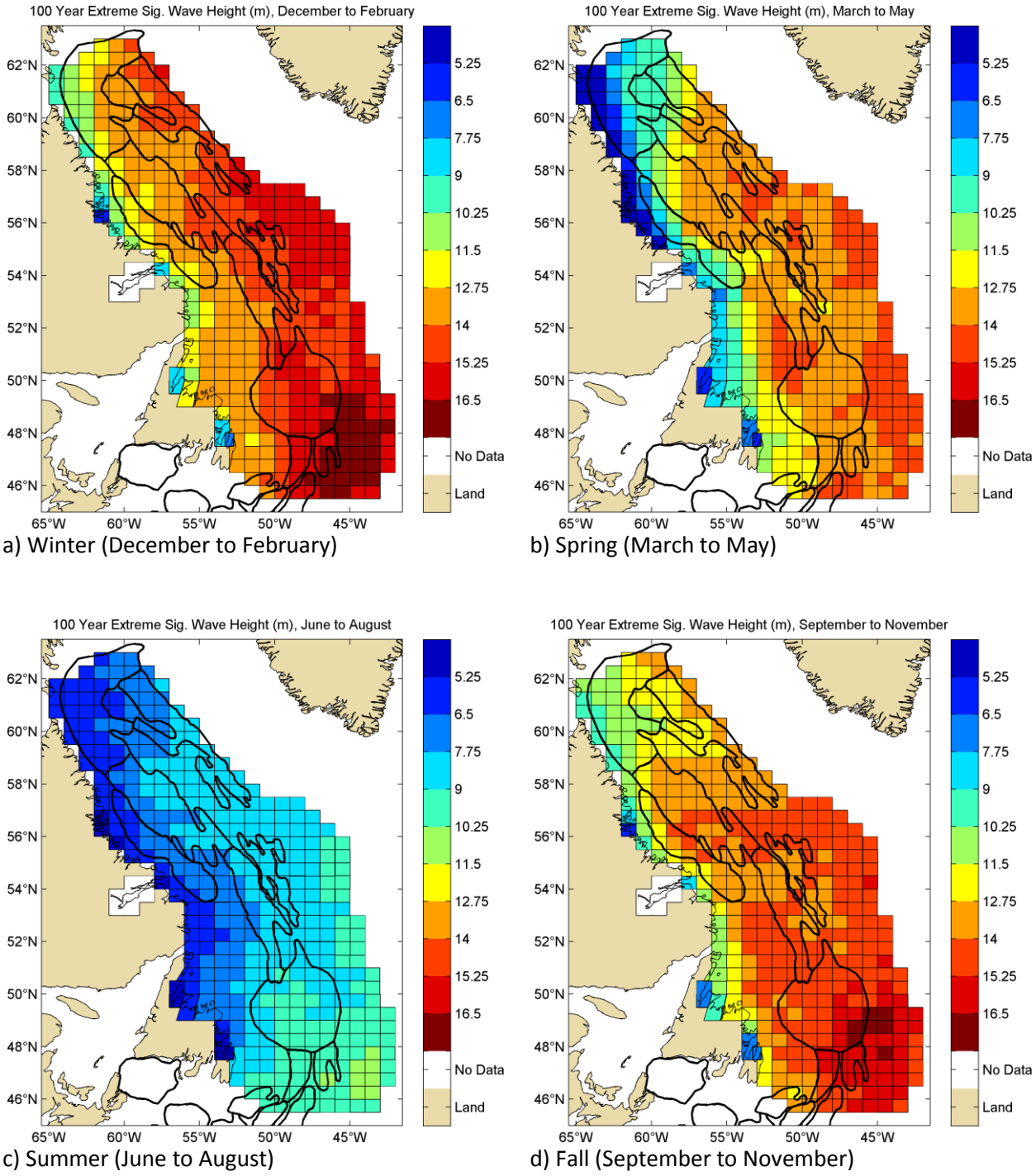

a) Winter (December to February)

b) Spring (March to May)

c) Summer (June to August)

d) Fall (September to November)

Figure 4-12. Seasonal overviews 100-year return period significant wave heights (m) for (a) winter, (b) spring, (c) summer and (d) fall

4.6 REFERENCES

Swail, V.R., Cardone, V.J., Ferguson, M., Gummer, D.J., Harris, E.L., Orelup, E.A. and Cox, A.T. (1996). The MSC50 Wind and Wave Reanalysis. Ninth International Workshop on Wave Hindcasting and Forecasting, September 25-29, Victoria, B.C., Canada.

Metocean Climate Study
Offshore Newfoundland & Labrador

STUDY MAIN REPORT
Volume 1: Chapter 5 – Currents

Prepared for:
Nalcor Energy Oil and Gas

Prepared by:
C-CORE

Reviewed & Edited by:
Bassem Eid, Ph.D.

May 2015

CHAPTER 5 CURRENTS

TABLE OF CONTENTS

LIST OF FIGURES

LIST OF TABLES

LIST OF ACRONYMS

BIO	Bedford Institute of Oceanography, Fisheries and Oceans Canada
CECOM	Canadian East Coast Ocean Model
NETCDF	Network Common Data Form
DFO	Department of Fisheries and Oceans

5 CURRENTS

5.1 DATA SOURCE

Current data were provided by Dr. Yongsheg Wu of Bedford Institute of Oceanography (BIO), Fisheries and Oceans Canada (DFO), which was derived from the Canadian East Coast Ocean Model (CECOM) model. CECOM is a dynamically and thermodynamically coupled ice-ocean model developed and maintained by researchers at the Bedford Institute of Oceanography. The ocean component is based on the Princeton Ocean Model and the ice model is a multi-category ice component. The model has been employed in numerous studies including basin-scale and shelf circulations, operational ocean forecasting, seasonal variation of ice cover, deep convection, wave-current coupling and surface trajectory, optical heating of the upper ocean, and storm-induced changes in phytoplankton distribution (Yao, Tang, & Peterson, 2000; Tang et al., 2008; Wu, Tang, & Dunlap, 2010).

The overlap between the Nalcor study area grid domain and the CECOM model domain is shown in Figure 5-1. The model resolution is 0.1o x 0.1° with a 21-level generalized σ (sigma) co-ordinate grid in the vertical (i.e., the vertical spacing is proportional to the water depth with a greater concentration of data points toward the surface). The depths of interest for this study were defined to be 2 m, 10 m, 20 m, 100 m, 500 m, one-third of depth from 500 m to seabed, two-thirds of depth from 500 m to seabed, and the last data point above seabed (whatever that depth might be for the study cell under consideration). For data points deeper than 600 m, current data are presented from these depth levels: 2 m, 10 m, 20 m, 100 m, 500 m, one-third of depth from 500 m to seabed, two-thirds of depth from 500 m to seabed, and the last data point above seabed. For data points shallower than 600 m, data are presented from whichever levels are available from the 2 m, 10 m, 20 m, 100 m, and 500 m depth levels, and the last data point above the seabed; for example, if the depth of water for a grid cell is 250 m, data are extracted for 2 m, 10 m, 20 m, 100 m, and the last data point above the seabed.

The data analyzed for this study have a temporal range from January 2003 to August 2012 with a 30-minute resolution. The CECOM data set has a spatial domain that covers nearly 98% of the Nalcor study area. Two cells – 390 and 391 – on the southern boundary fall outside the spatial domain. Six cells – 181, 279, 293, 294, 330, and 342 – are located over bays and inlets such as Lake Melville, Labrador and White Bay, Newfoundland, and which are too small for the model to resolve. These anomalous cells can be seen in Figure 5-1.

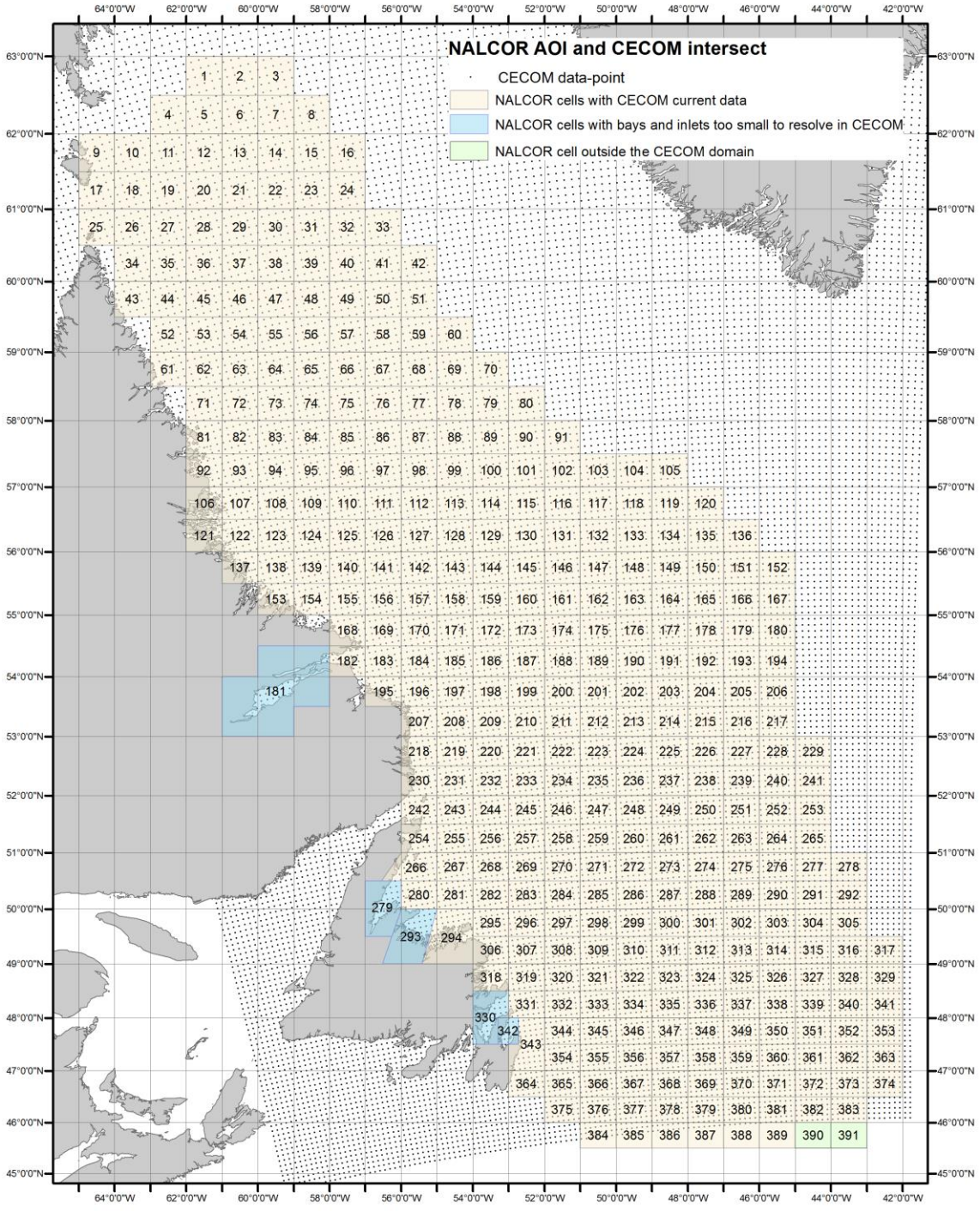

Figure 5-1. Map showing intersection of Nalcor grid cells, CECOM data-points, and anomalous cells

5.2 Data Processing Methodology

The CECOM data were delivered in the NETCDF format. There is one NETCDF file per year of data and each file is approximately 80 GBytes. The data were extracted and processed as described in Table 5-1; however, for each Nalcor grid cell, current data were extracted from the CECOM data-point nearest to the centroid of the grid cell. Once extracted, the current data were summarized and presented on a cell-by-cell basis in separate cell reports. Each cell report represents the data summaries in form of maps, depth-profile plots, time-series plots, current rose plots, and tables of mean, standard deviation, and Extreme Value Analysis data. Representative plots and tables from Cell 110, and a description of any detailed processing steps used to generate them, are presented in Sections 5.3, 5.4, and 5.5. A regional overview is presented in Section 5.6.

Table 5-1 Processing methodology for CECOM current data set

Step	Description	Comment/Notes
1	For each Nalcor grid-cell, find the centre of the Nalcor grid cell and find the nearest CECOM data point.	Cells without associated CECOM data-cell because the Nalcor cell is outside the CECOM domain: 390, 391
2	From the grid-cell to data-point association generated in step one, extract the current data from the associated CECOM data-point for each Nalcor grid cell.	Cells with an associated CECOM data-cell but zero data because CECOM considers the cell land or is too small to resolve: 181, 279, 293, 330, 342
3	For each Nalcor associated CECOM data-point, interpolate from the vertical sigma co-ordinate grid onto a vertical grid of 1 m resolution	Linear interpolation was used to generate the interpolated data set.
4	From the extracted CECOM data and the interpolated data, generate the summary maps, depth-profile plots, the time-series plots, and the rose plots, then compute and populate the mean, standard deviation and extreme value analysis table. Output all the images as PNG files.	Images/data are only generated for cells/depth levels where there are data. Pre-defined list : 2 m, 10 m, 20 m, 100 m, 500 m, depth, at 1/3 of 500 m to seabed, 2/3 of 500 m to seabed and the deepest data-point. if depth is less than 600 m everything except 1/3 to deep and 2/3 to deep is produced if depth less than 500 m whichever levels can be produced are produced except for 1/3 to deep and 2/3 to deep, i.e., if depth is 450 m then 2 m, 10 m, 20 m, 100 m and the deepest data point are extracted
5	From the interpolated data, generate the regional summaries	Cells without data, either from being outside the domain or masked as land, are included but marked as -9999
6	From the interpolated data, generate the NESS data-structure.	Cells without data, either from being outside the domain or masked as land, are included but marked as -9999

5.3 Statistical Analysis Results

5.3.1 Depth Profiles

Sample depth-profile plots are shown in Figure 5-2. The depth-profile plots display mean-monthly magnitudes, maximum-monthly magnitudes, and mean-monthly direction throughout the water

column. The current direction notation follows the traditional method of 0° being a north flowing current; that is, the current flows northwards, and working clockwise, 90° being an easterly flowing current, 180° being a southerly current, and 270° being a westerly current. In the sample plot, the current has an approximate general direction of 135°; that is, a current flowing to the south-east.

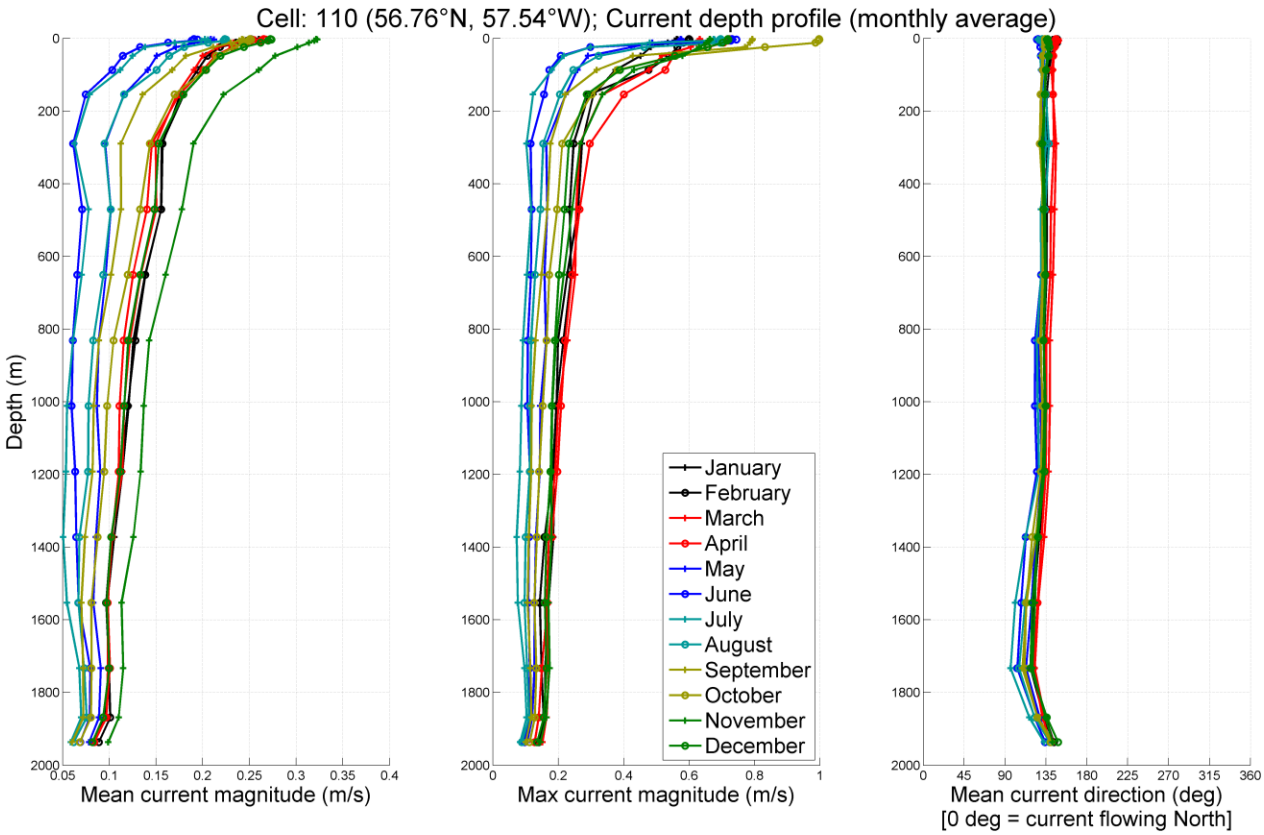

Figure 5-2. Sample depth profile plots for cell 110 showing monthly average of current magnitude (left), monthly maximum current magnitude (center) and monthly average of current direction (right)

Scalar averaging (Bailey, 2000) has been used to compute the monthly mean magnitude. Vector averaging was used to compute the monthly mean direction. The justification for this choice being that scalar averaging is more conservative in computing magnitudes whereas vector averaging more accurately represents the mean direction. Mean-monthly signifies that all the data for each unique month in the data set are averaged; that is, mean January data are the mean of all the January data for each year in the data set. The maximum-monthly is computed similarly; that is, maximum January data are the maximum current magnitude for all the January data for each year.

Monthly averaging was chosen as it enables the viewer to appreciate the variability of the current at depth over the course of a year without swamping the plots. The upper data point is extracted from the two metre depth-level data; all data below this point are directly extracted from the CECOM data set for that grid point. This merging was performed to avoid excessively shallow/thin depth levels in grid cells

where the water is shallow; i.e., grid cells with shallow bathymetry will have sigma-coordinates than can approach centimetre resolution close to the surface susceptible to unrepresentative behavior from the air-surface interface (hence the upper two metre depth limit).

Note: The scales on the *x*-axis of the magnitude plots might be different (identical scales would compress the presented data losing distinction between the temporal variability).

5.3.2 Time Series

Sample time-series plots are shown in Figure 5-3, with current magnitude data presented in the upper plot and current direction in the lower. For each grid cell, a time-series figure has been produced at each pre-defined depth level.

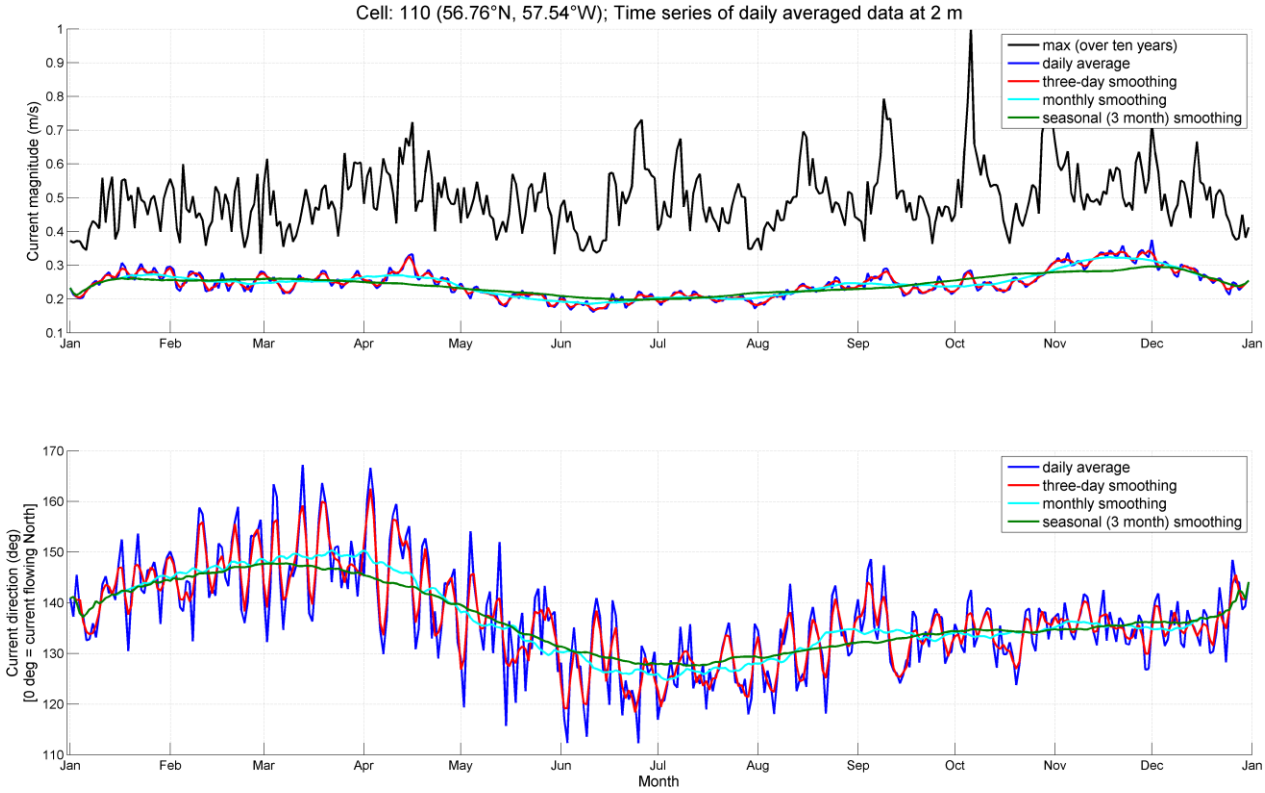

Figure 5-3. Sample time-series plot for cell 110 at 2 m depth

Averaging follows the same logic as described in Section 5.3.1, except the averaging time-period is over a daily (24 hour) period. The three-day, monthly, and seasonal (three month) running averages are computed from the daily mean magnitude and mean direction. The maximum is computed as the maximum current magnitude for each identical day in the data set; that is, the maximum current over all the first of Januarys, the maximum current for all the second of Januarys, and so on. The three different sampling windows allow the viewer to appreciate the differing temporal variability of the data.

5.3.3 Current Rose

Sample current roses are shown in Figure 5-4. For this analysis, the full temporal range of the CECOM model was averaged for each season at each depth for each grid cell. The seasons are defined as: Winter (December, January, February); Spring (March, April, May); Summer (June, July, August); and Fall (September, October, November). In the sample figure, the current is predominantly flowing in southeast direction, with little variability over the course of the four seasons. This aligns with the current directions seen in the sample depth plots and time-series plots (Figure 5-2 and Figure 5-3). Note: the magnitude legend is dependent on magnitude range of data analyzed for each rose (i.e., the range presented is not constant for all current roses).

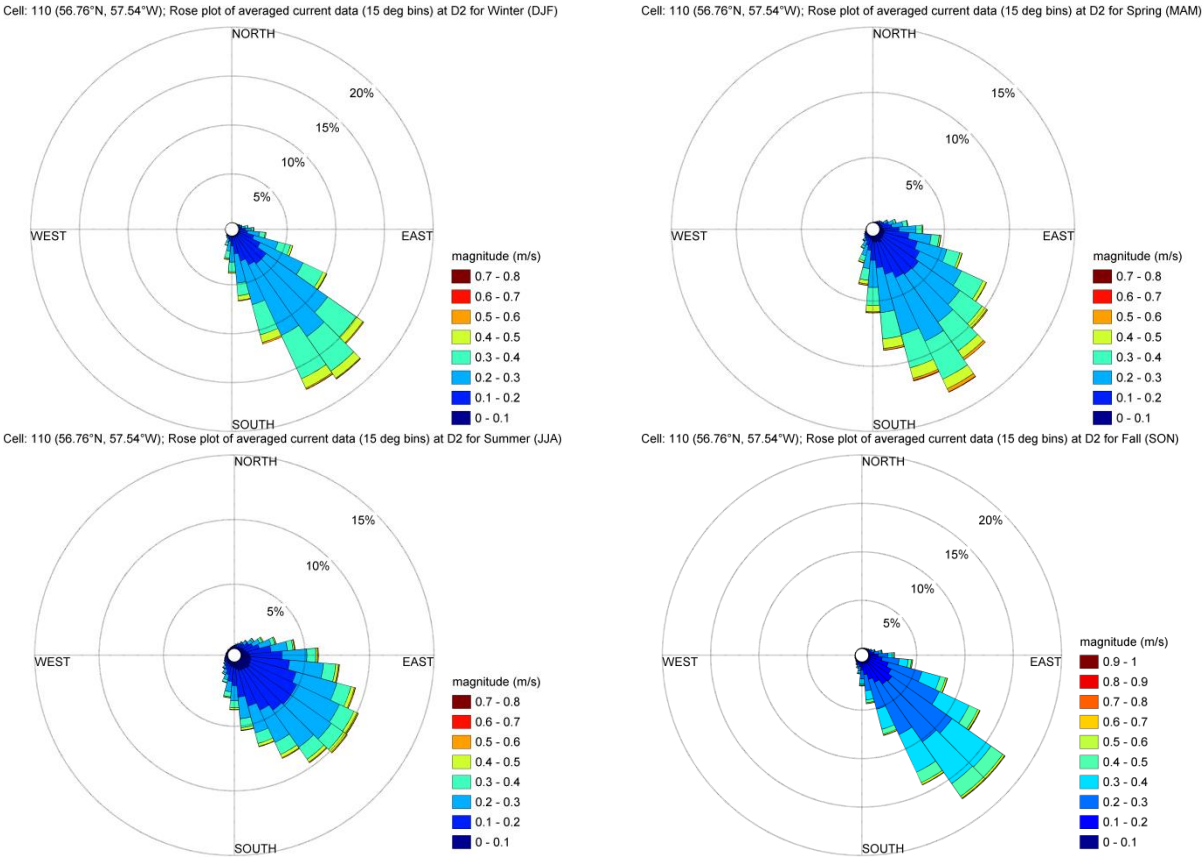

Figure 5-4. Sample seasonal current roses for cell 110 at 2 m depth

5.4 STATISTICAL SUMMARIES

Mean, Max, and Standard Deviation Tables show mean monthly, maximum monthly, and monthly standard deviations of current speed extracted for study area cell 110. These are presented for each cell in the cell reports for each level sample present for each grid cell. The monthly mean is computed as described in Section 5.3.1. The yearly mean is computed similarly to the monthly, but the data were not segregated into months. Maximum values and standard deviations are computed from the derived magnitudes.

5.5 EXTREME VALUE ANALYSIS (EVA)

Extreme Value Analysis (EVA) was performed to estimate a current magnitude for each grid cell, for each month, at each depth level over a 10-year and a 100-year return period. Table 5-5 shows a sample of the 100-year EVA data. The following steps were performed to compute the EVA data for each month:

1. For each grid cell, for each depth level, the maximum values per day per month were extracted.
2. This data set of maximum values was fitted to a lognormal distribution from which maximum likelihood estimate (MLE) parameters were obtained. The lognormal distribution was analyzed to give the best fit for the current data set. This best fit analysis was based on a visual inspection of the distributions that are commonly used in EVA analysis and the fit to the lognormal distribution is shown in Figure 5-5.
3. The MLE parameters were then used to generate a log-normal inverse cumulative distribution function from which estimates for the one-in-10-years and one-in-100-years current magnitudes were computed. The yearly EVA value was computed as for monthly, but the data were not segregated into monthly bins.

The accuracy of the EVA estimates is dependent on the fit of the data set to the lognormal distribution. Since the data for the EVA is assumed to follow the same distribution for each cell, some of the EVA estimates may be derived from imperfect fits to the distribution. In these cases, the EVA estimates will be over- or underestimated.

Table 5-2 Sample table of monthly average current magnitudes for cell 110

Cell: 110 56.76°N 57.54°W	Mean current magnitudes (m/s) at selected depth levels (0 indicates magnitude < 0.01 m/s. Colours binned every 0.2 m/s)							
	D2	D10	D20	D100	D500	D981	D1463	D1936
Jan	0.26	0.24	0.22	0.17	0.14	0.12	0.1	0
Feb	0.25	0.22	0.21	0.17	0.14	0.11	0.1	0
Mar	0.25	0.22	0.2	0.17	0.13	0.11	0.1	0
Apr	0.27	0.24	0.22	0.17	0.12	0.11	0.1	0
May	0.21	0.17	0.16	0.11	0.09	0.09	0.09	0
Jun	0.19	0.14	0.12	0.07	0.06	0.06	0.07	0
Jul	0.2	0.14	0.13	0.08	0.07	0.05	0.06	0
Aug	0.22	0.18	0.17	0.11	0.09	0.08	0.07	0
Sep	0.24	0.22	0.19	0.13	0.1	0.08	0.07	0
Oct	0.25	0.24	0.22	0.16	0.12	0.09	0.08	0
Nov	0.32	0.31	0.28	0.22	0.16	0.13	0.11	0
Dec	0.27	0.25	0.23	0.17	0.13	0.11	0.1	0
Year	0.24	0.21	0.19	0.14	0.11	0.1	0.09	0

Table 5-3 Sample table of monthly maximum current magnitudes for cell 110

Cell: 110 56.76°N 57.54°W	Maximum of current magnitudes (m/s) at selected depth levels (0 indicates magnitude < 0.01 m/s. Colours binned every 0.02 m/s)							
	D2	D10	D20	D100	D500	D981	D1463	D1936
Jan	0.56	0.49	0.46	0.3	0.22	0.19	0.16	0
Feb	0.6	0.57	0.55	0.27	0.24	0.19	0.15	0
Mar	0.63	0.61	0.55	0.31	0.25	0.19	0.16	0
Apr	0.72	0.66	0.59	0.38	0.24	0.2	0.16	0
May	0.57	0.43	0.32	0.21	0.16	0.14	0.13	0
Jun	0.73	0.32	0.21	0.15	0.11	0.11	0.11	0
Jul	0.68	0.31	0.21	0.12	0.1	0.08	0.09	0
Aug	0.7	0.48	0.29	0.19	0.13	0.11	0.1	0
Sep	0.79	0.78	0.44	0.21	0.14	0.12	0.11	0
Oct	1	0.87	0.58	0.28	0.17	0.14	0.13	0
Nov	0.66	0.64	0.59	0.32	0.21	0.18	0.17	0
Dec	0.72	0.67	0.58	0.27	0.2	0.18	0.16	0
Year	1	0.87	0.59	0.38	0.25	0.2	0.17	0

Table 5-4 Sample table of monthly standard deviations of current magnitudes for cell 110

Cell: 110 56.76°N 57.54°W	Standard deviation of current magnitudes (m/s) at selected depth levels (0 indicates magnitude < 0.01 m/s. Colours binned every 0.02 m/s)							
	D2	D10	D20	D100	D500	D981	D1463	D1936
Jan	0.08	0.07	0.06	0.03	0.02	0.02	0.02	0
Feb	0.09	0.07	0.06	0.03	0.02	0.02	0.02	0
Mar	0.09	0.08	0.07	0.04	0.03	0.02	0.02	0
Apr	0.11	0.09	0.07	0.05	0.03	0.02	0.02	0
May	0.09	0.06	0.04	0.03	0.02	0.01	0.01	0
Jun	0.1	0.04	0.02	0.02	0.01	0.01	0.01	0
Jul	0.09	0.04	0.02	0.01	0.01	0.01	0.01	0
Aug	0.1	0.05	0.03	0.02	0.01	0.01	0.01	0
Sep	0.1	0.08	0.04	0.02	0.01	0.01	0.01	0
Oct	0.1	0.09	0.06	0.03	0.02	0.01	0.01	0
Nov	0.09	0.08	0.07	0.03	0.02	0.02	0.02	0
Dec	0.09	0.08	0.06	0.03	0.02	0.02	0.02	0
Year	0.1	0.08	0.07	0.05	0.03	0.03	0.02	0

Table 5-5 Sample 100-year Extreme Value Analysis data for cell 110

Cell: 110 56.76°N 57.54°W	Current magnitudes (m/s) for 100 Year Extreme at selected depth levels (0 indicates magnitude < 0.01 m/s. Colours binned every 0.2 m/s)							
	D2	D10	D20	D100	D500	D981	D1463	D1936
Jan	0.75	0.62	0.52	0.31	0.24	0.22	0.18	0
Feb	0.77	0.67	0.57	0.34	0.24	0.21	0.19	0
Mar	0.88	0.77	0.65	0.41	0.29	0.24	0.19	0
Apr	1.01	0.79	0.67	0.42	0.27	0.23	0.17	0
May	0.88	0.5	0.38	0.26	0.18	0.15	0.13	0
Jun	0.86	0.37	0.24	0.15	0.12	0.12	0.11	0
Jul	0.79	0.32	0.23	0.14	0.12	0.09	0.09	0
Aug	0.78	0.46	0.31	0.2	0.14	0.12	0.11	0
Sep	0.8	0.66	0.41	0.23	0.16	0.13	0.12	0
Oct	0.88	0.8	0.49	0.3	0.19	0.16	0.15	0
Nov	0.74	0.7	0.6	0.34	0.23	0.21	0.19	0
Dec	0.81	0.74	0.57	0.32	0.24	0.22	0.2	0
Year	1.07	0.98	0.85	0.69	0.41	0.34	0.23	0

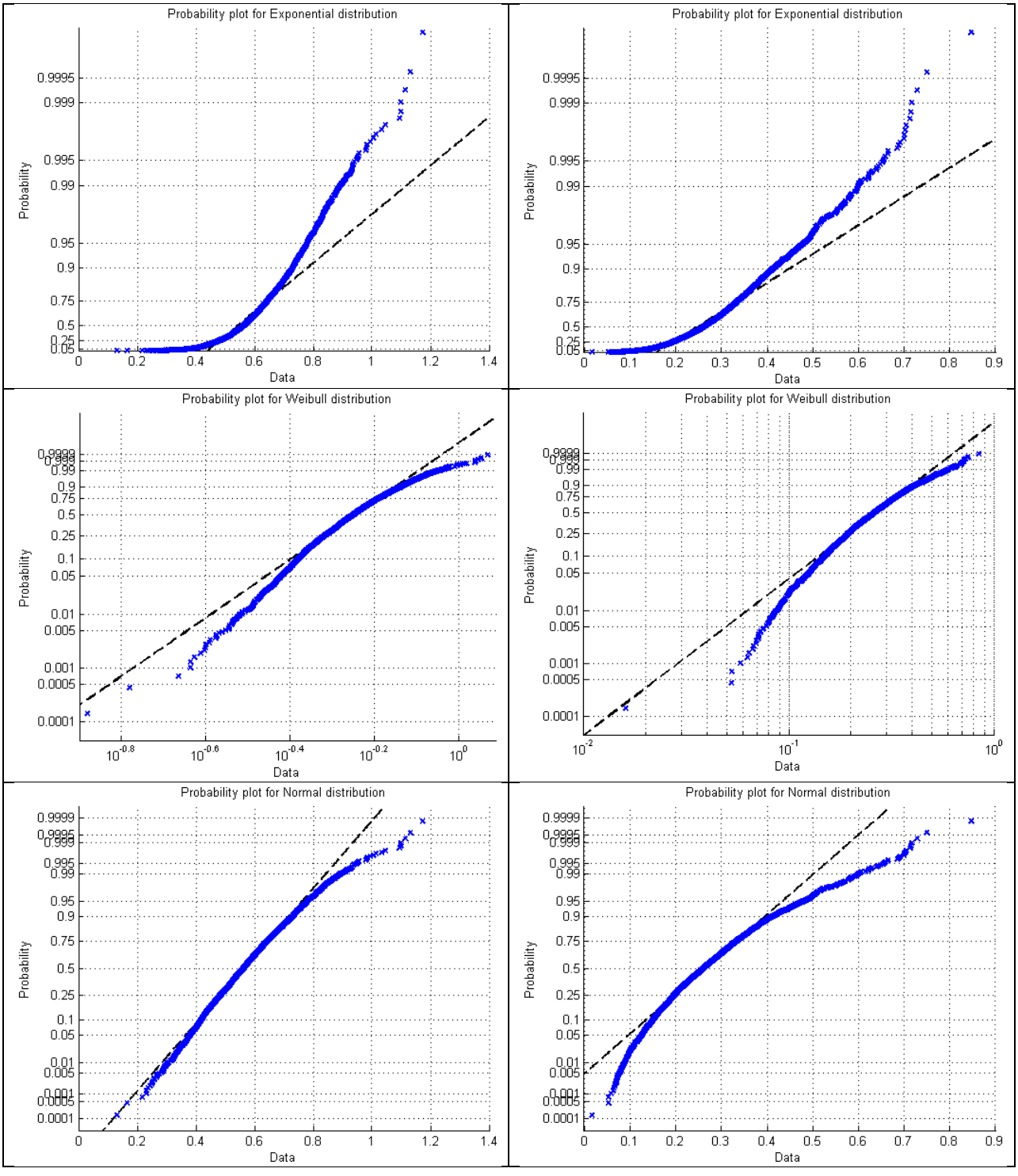
Probability plot for Exponential distribution
Probability
Data
Probability plot for Exponential distribution
Probability
Data
Probability plot for Weibull distribution
Probability
Data
Probability plot for Weibull distribution
Probability
Data
Probability plot for Normal distribution
Probability
Data
Probability plot for Normal distribution
Probability
Data

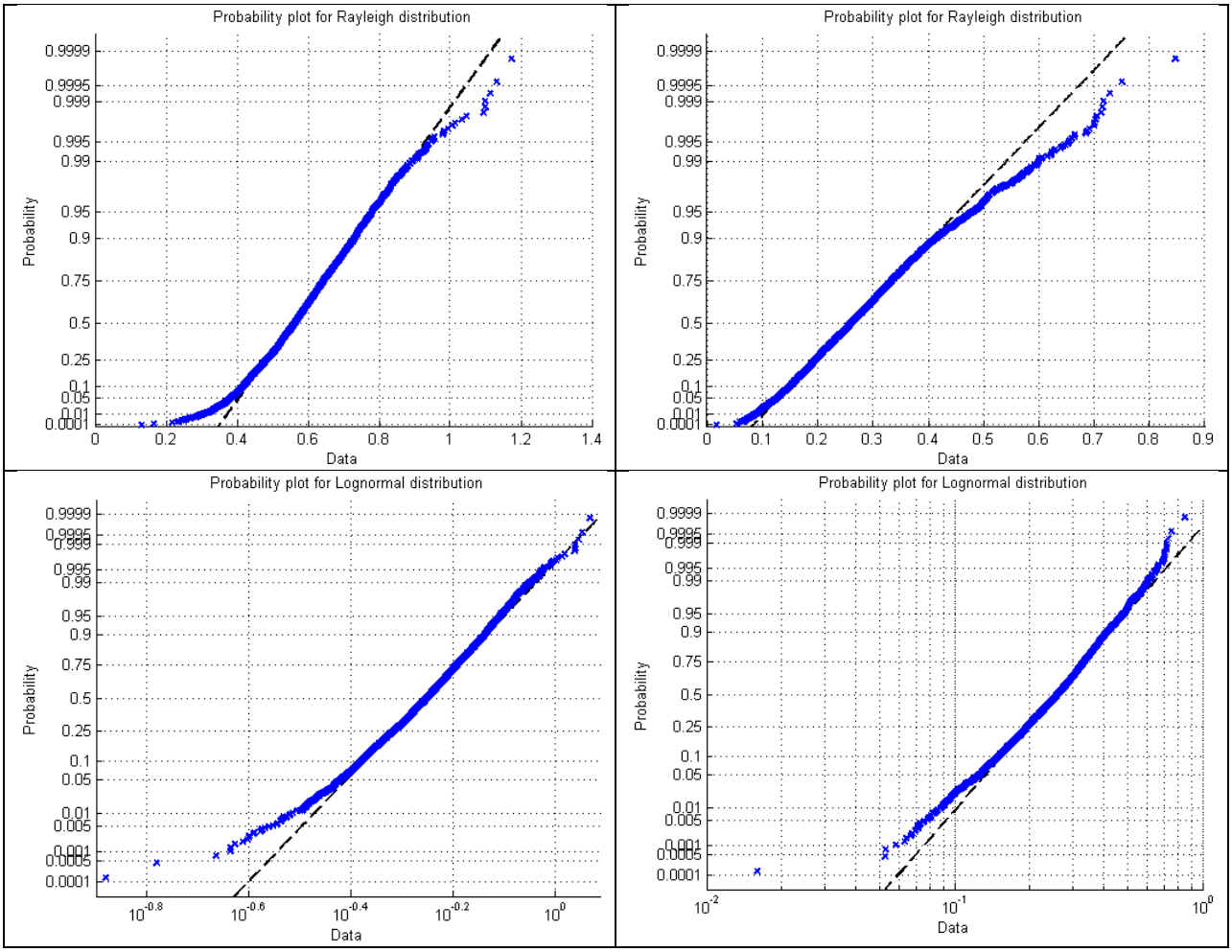

Figure 5-5. Probability plots (blue line) of two sample maximum value data sets cell 141 (left) and cell 368 (right) fitted to the lognormal distribution (the straight dotted line passes through the lower and upper quartiles of the data set and can be used as a guide to judge how well the data follows the distribution)

5.6 REGIONAL OVERVIEW

The regional overview is split into seasonal and annual overviews. Figure 5-6 to Figure 5-10 are seasonal summary maps of the current data set at 2 m, 10 m, 20 m, 100 m, and 500 m. The vectors represent the average seasonal current velocity at those depths; the colour scheme within each cell represents the one-in-100 year seasonal extreme current magnitude. The seasonal extreme magnitude is computed as described in Section 5.5 except on a seasonal basis. Figure 5-11 to Figure 5-15 are annual summaries showing mean, maximum, 10-year, and 100-year EVA values at 2 m, 10 m, 20 m, 100 m, and 500 m. The magnitude and colour schemes are consistent throughout the plots to allow one to make visual inter-comparisons. Any value that is greater than 2 m/s is likely an over-estimation due to a poor fit to the lognormal distribution. As such, the colour scheme is clipped at 2 m/s to increase the resolution of the data displayed without swamping the maps with excess colour gradations.

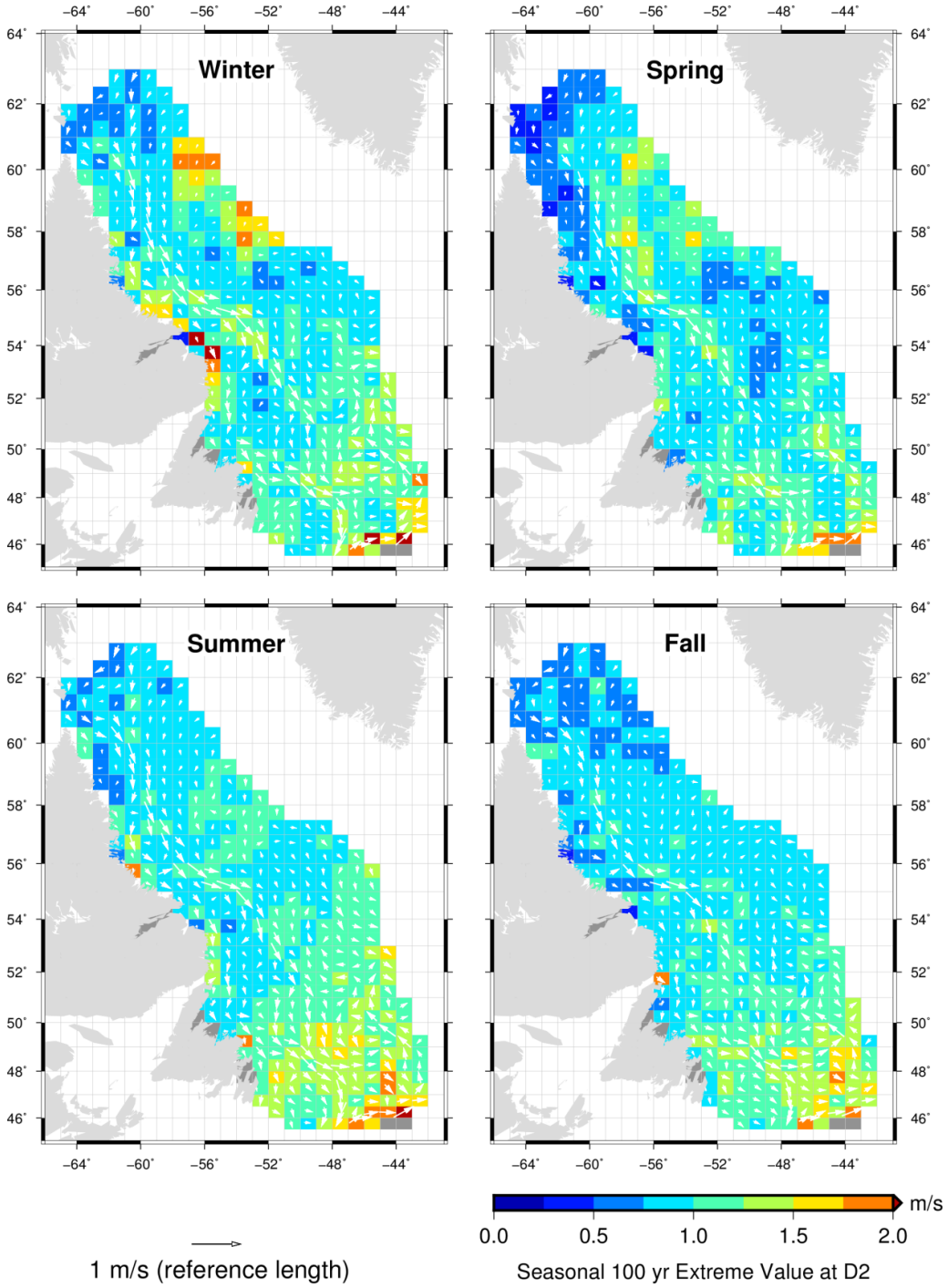

Figure 5-6. Seasonal current summary for 2 m water depth, vectors represent average seasonal currents and the colour map represents 100-year extreme values

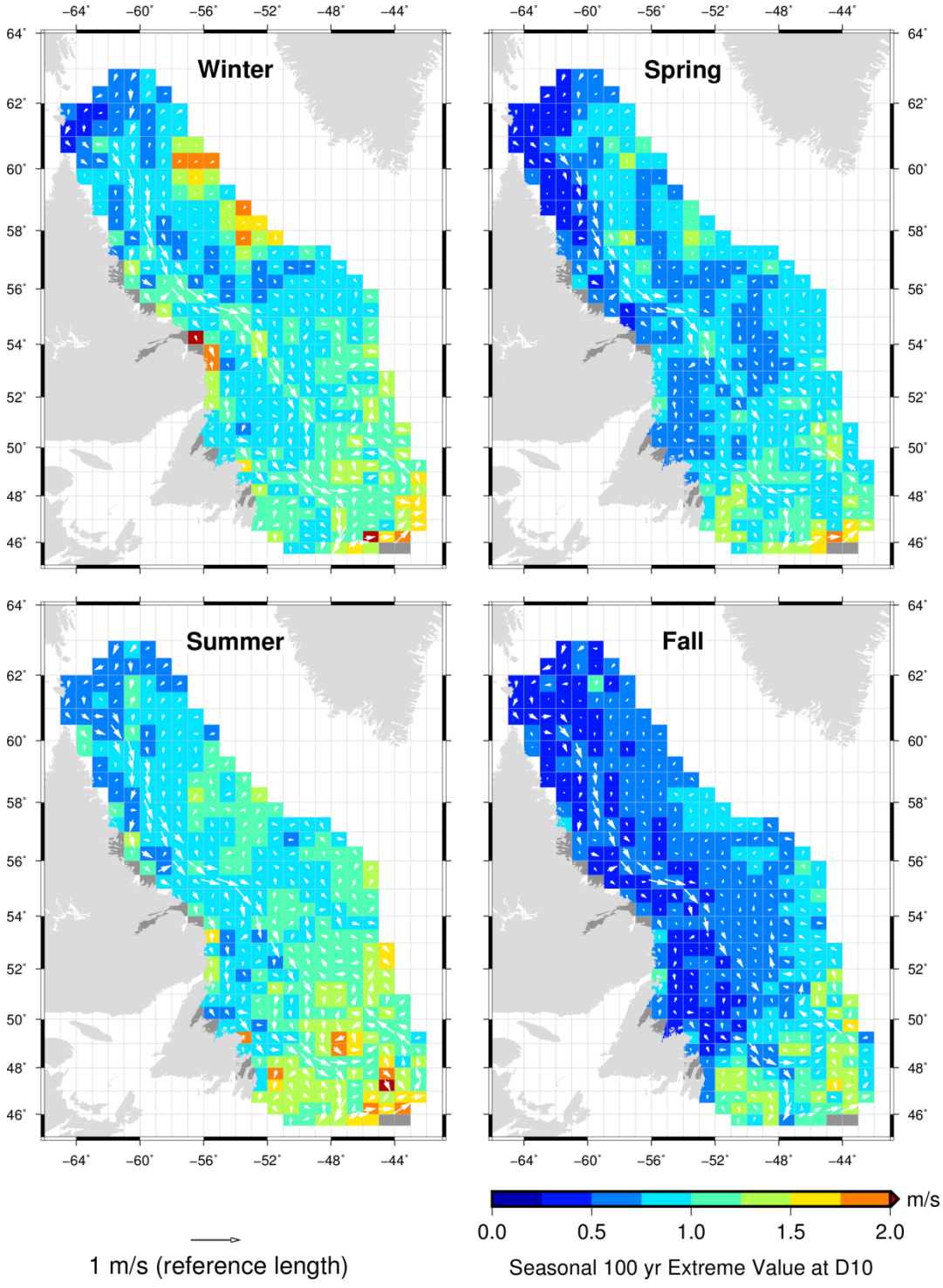

Figure 5-7. Seasonal current summary for 10 m water depth, vectors represent average seasonal currents and the colour map represents 100-year extreme values

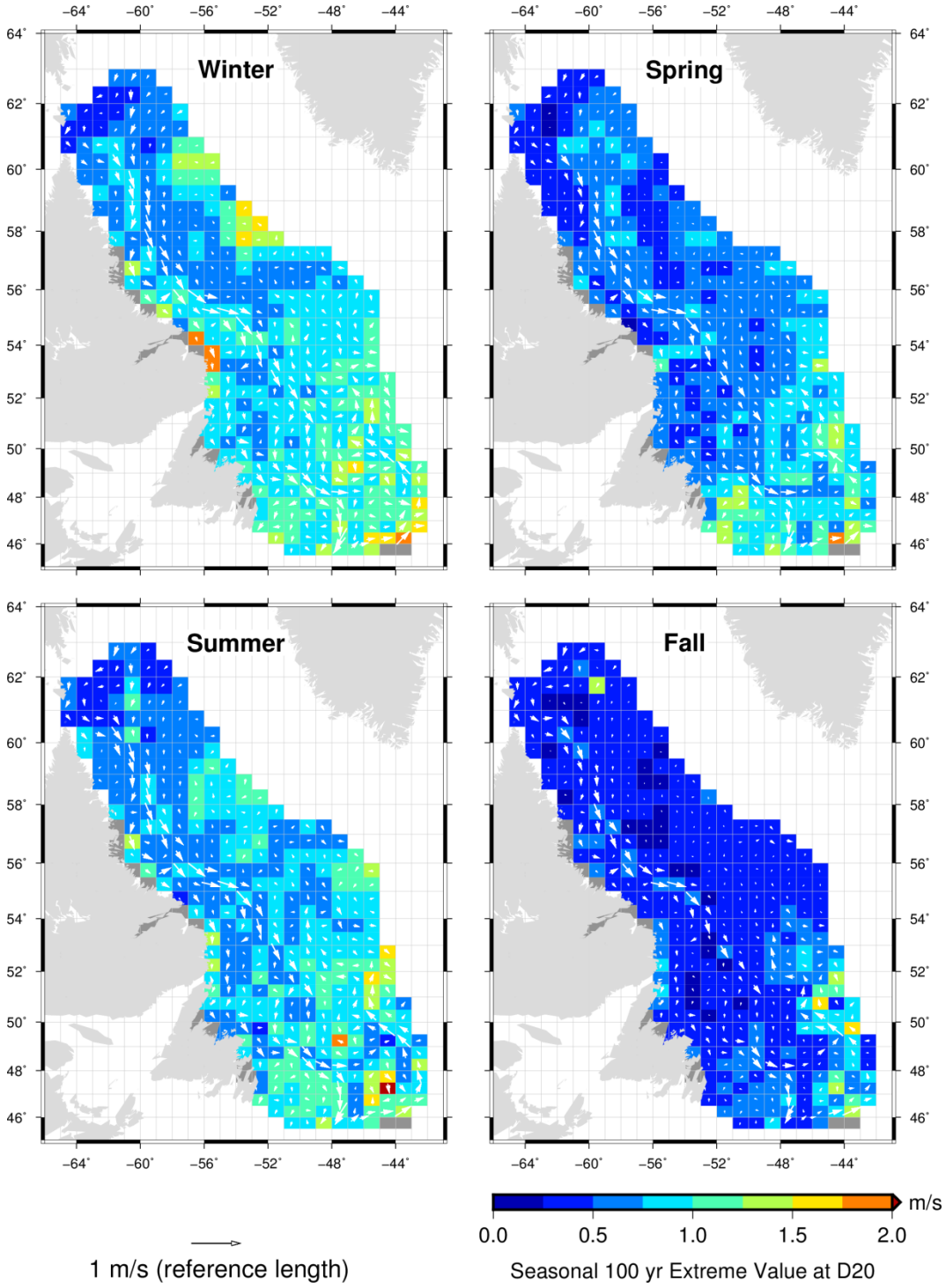

Figure 5-8. Seasonal current summary for 20 m water depth, vectors represent average seasonal currents and the colour map represents 100-year extreme values

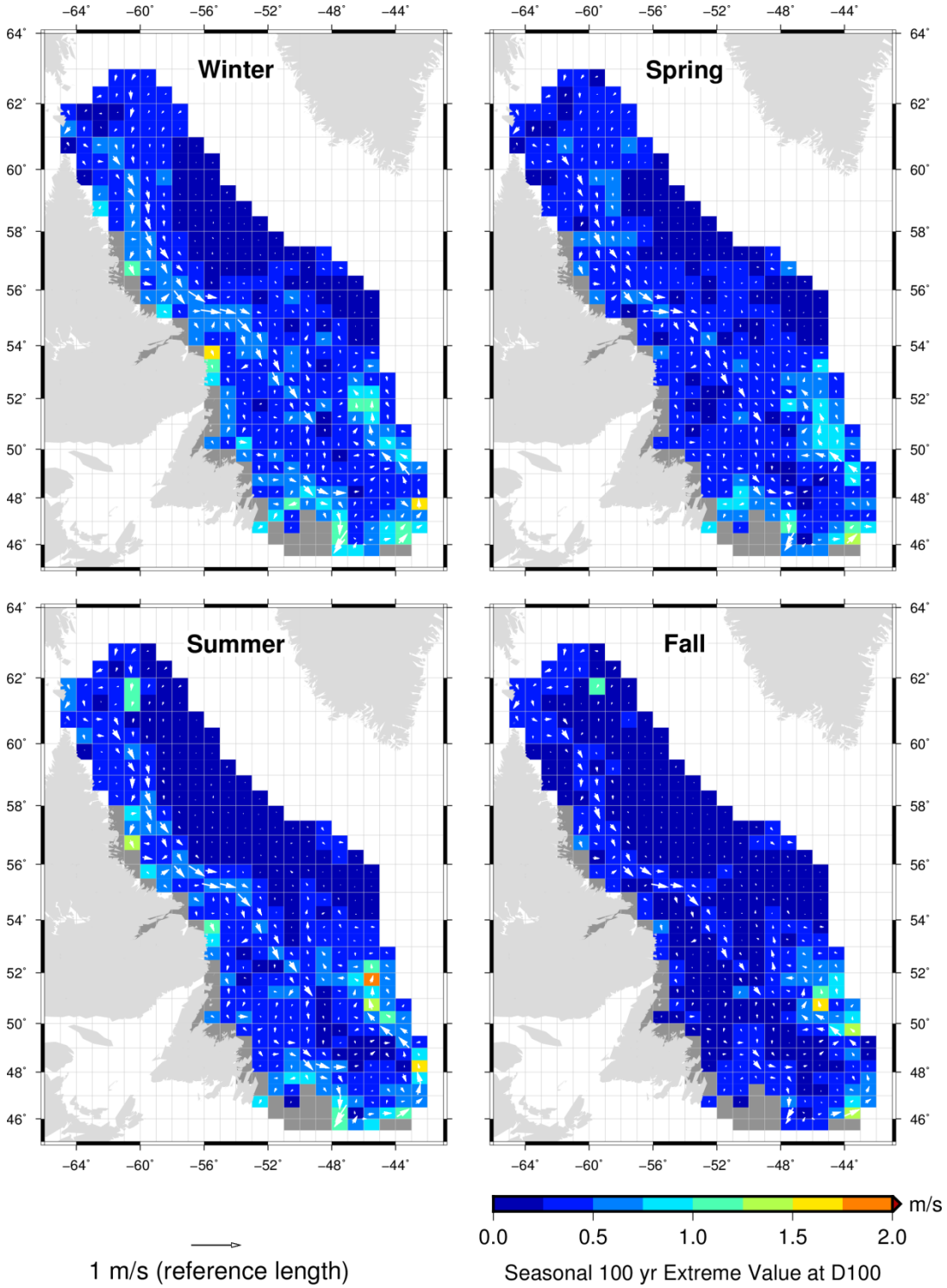

Figure 5-9. Seasonal current summary for 100 m water depth, vectors represent average seasonal currents and the colour map represents 100-year extreme values

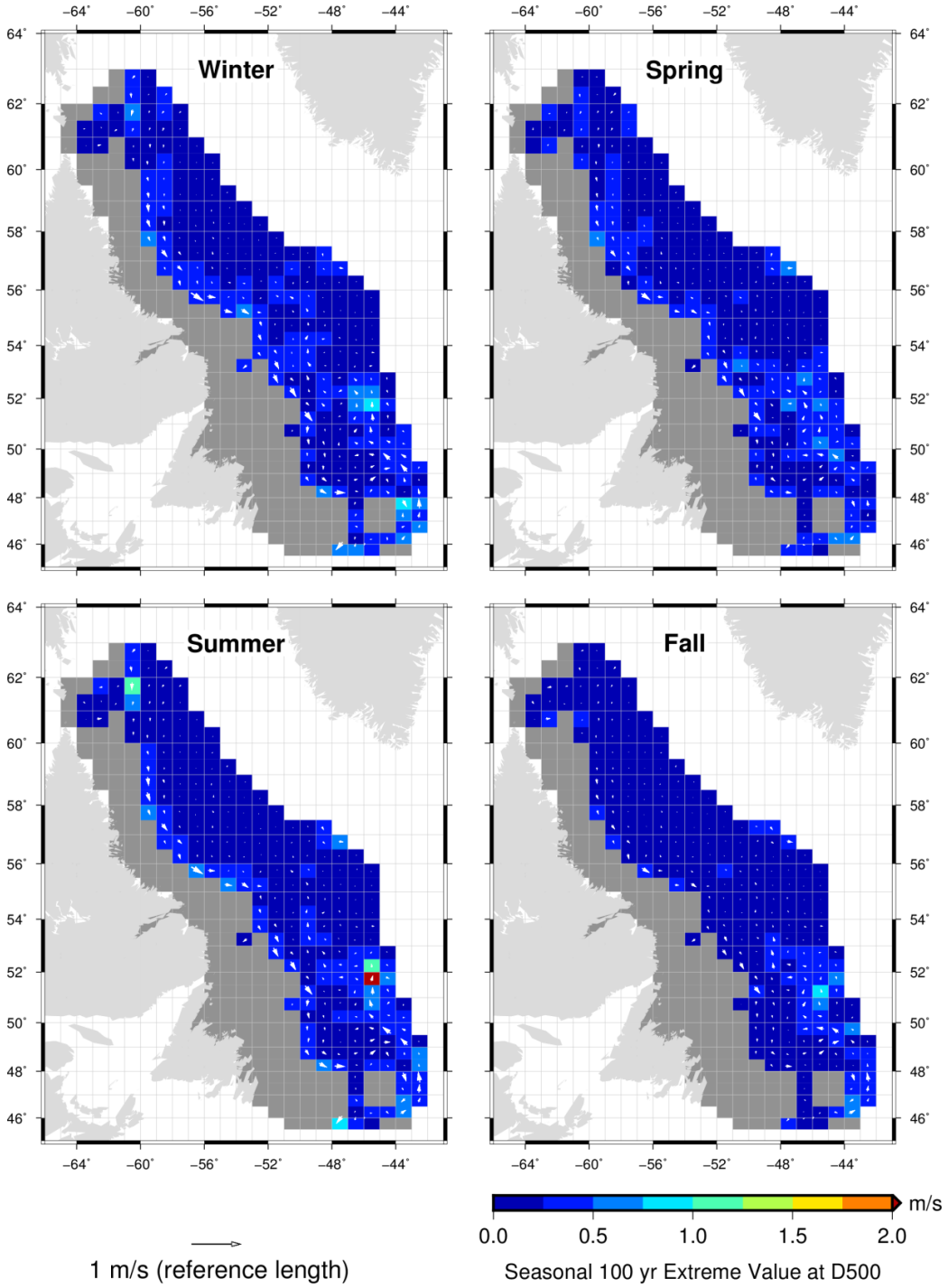

Figure 5-10. Seasonal current summary for 500 m water depth, vectors represent average seasonal currents and the colour map represents 100-year extreme values

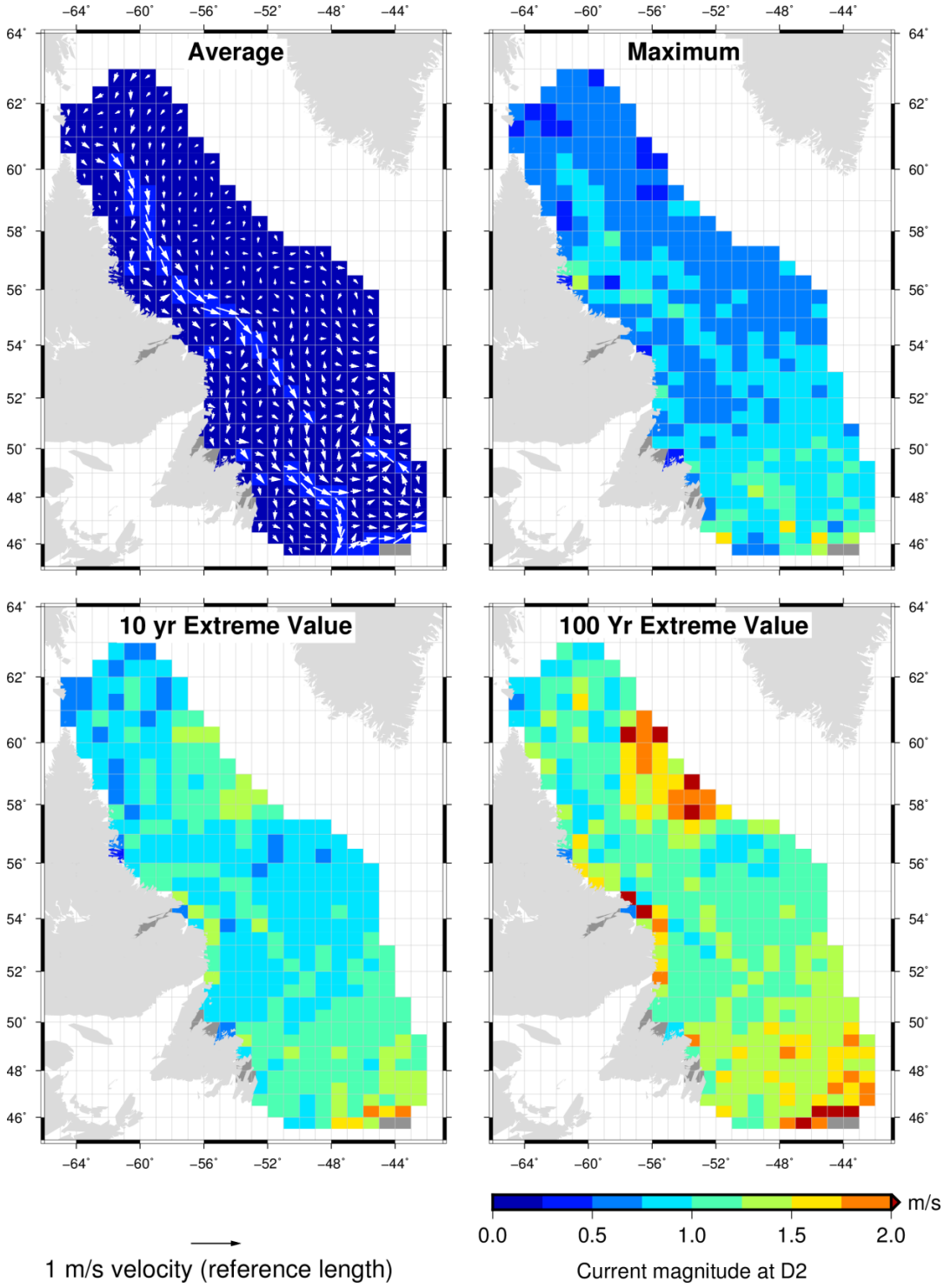

Figure 5-11. Annual current summary for 2 m water depth, vectors in the top-right represent average currents, the colour maps represent the current magnitude for the different data sets as indicated by the sub-plot label.

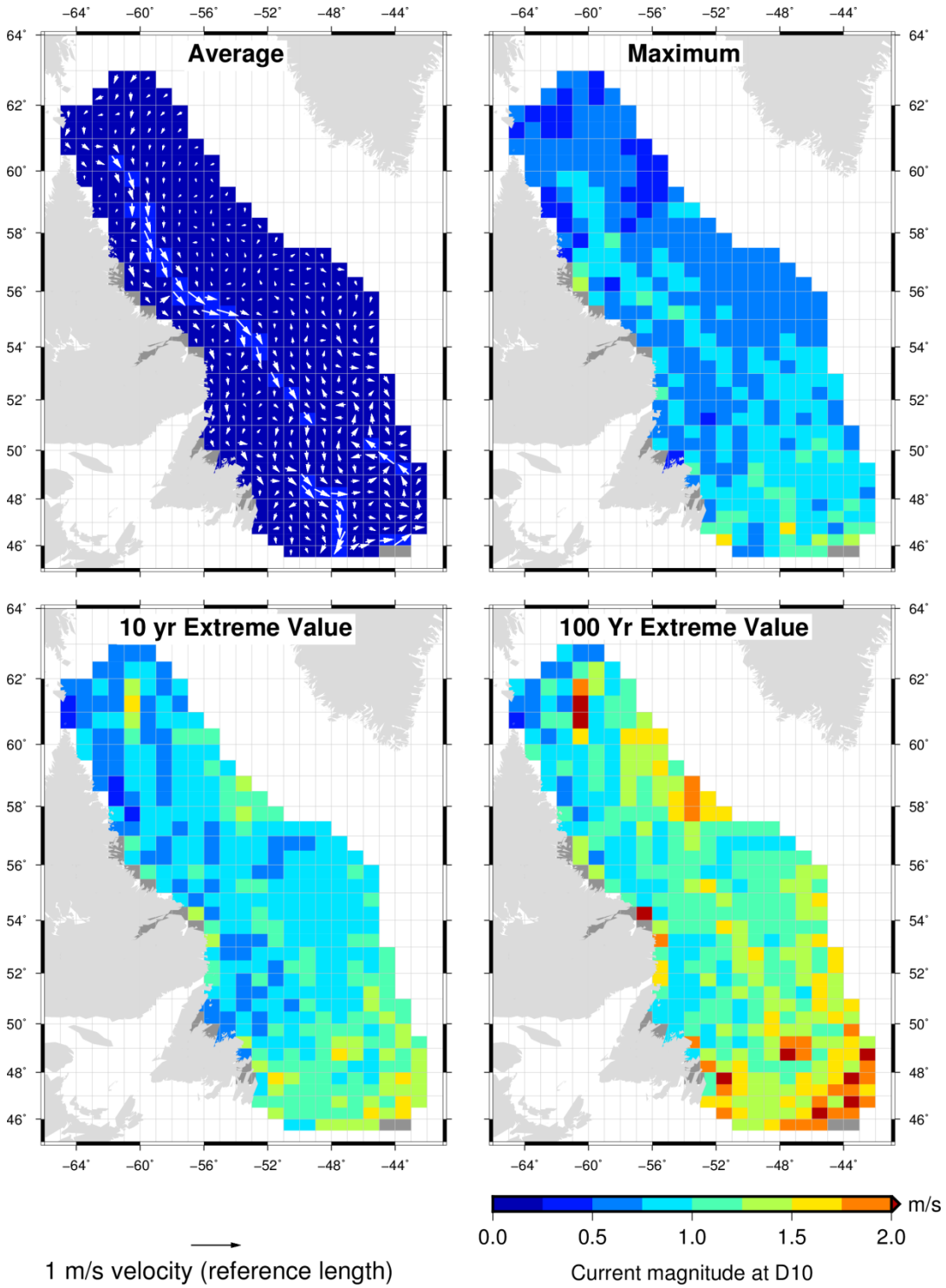

Figure 5-12. Annual current summary for 10 m water depth, vectors in the top-right represent average currents, the colour maps represent the current magnitude for the different data sets as indicated by the subplot label.

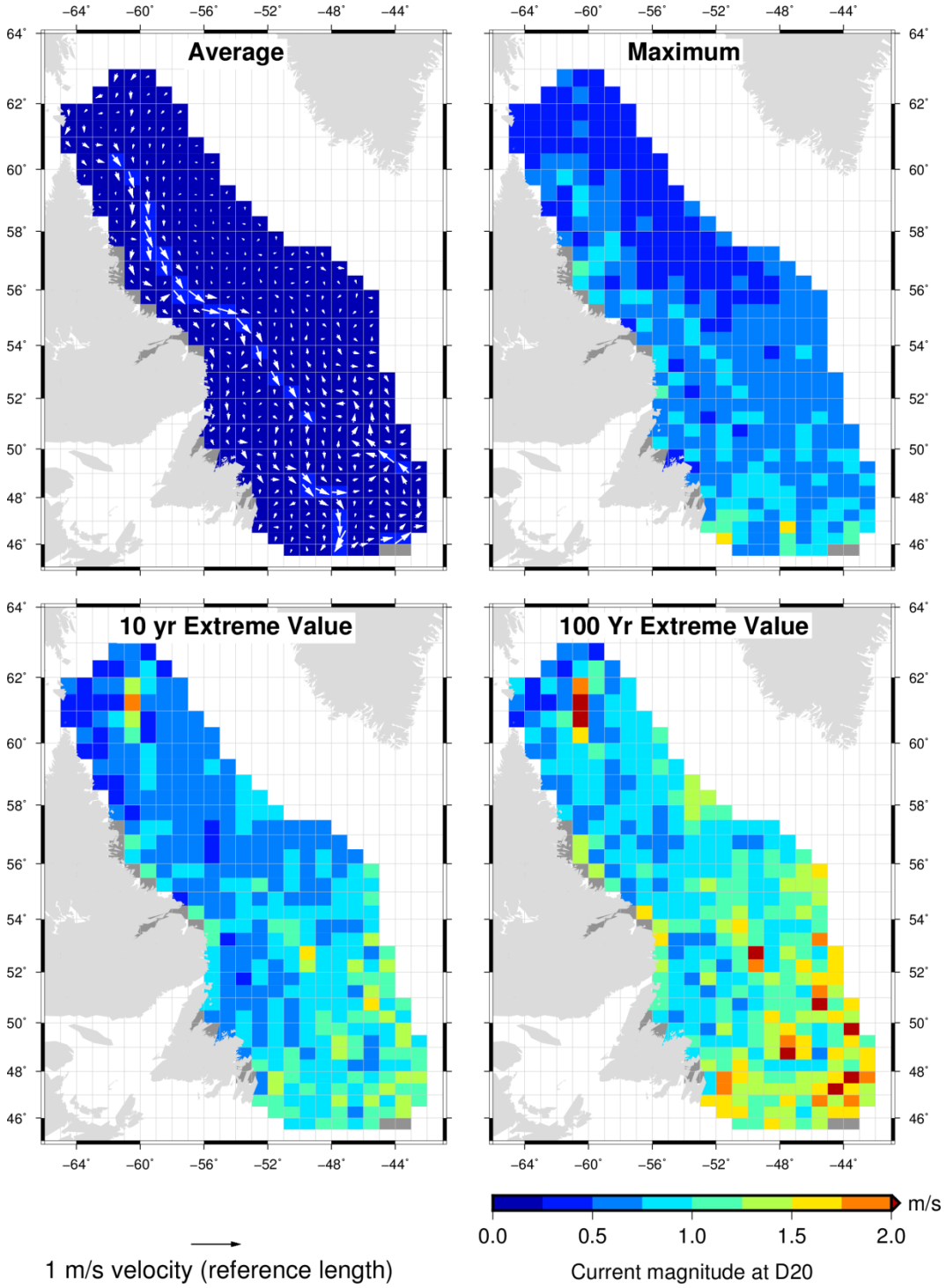

Figure 5-13. Annual current summary for 20 m water depth, vectors in the top-right represent average currents, the colour maps represent the current magnitude for the different data sets as indicated by the subplot label.

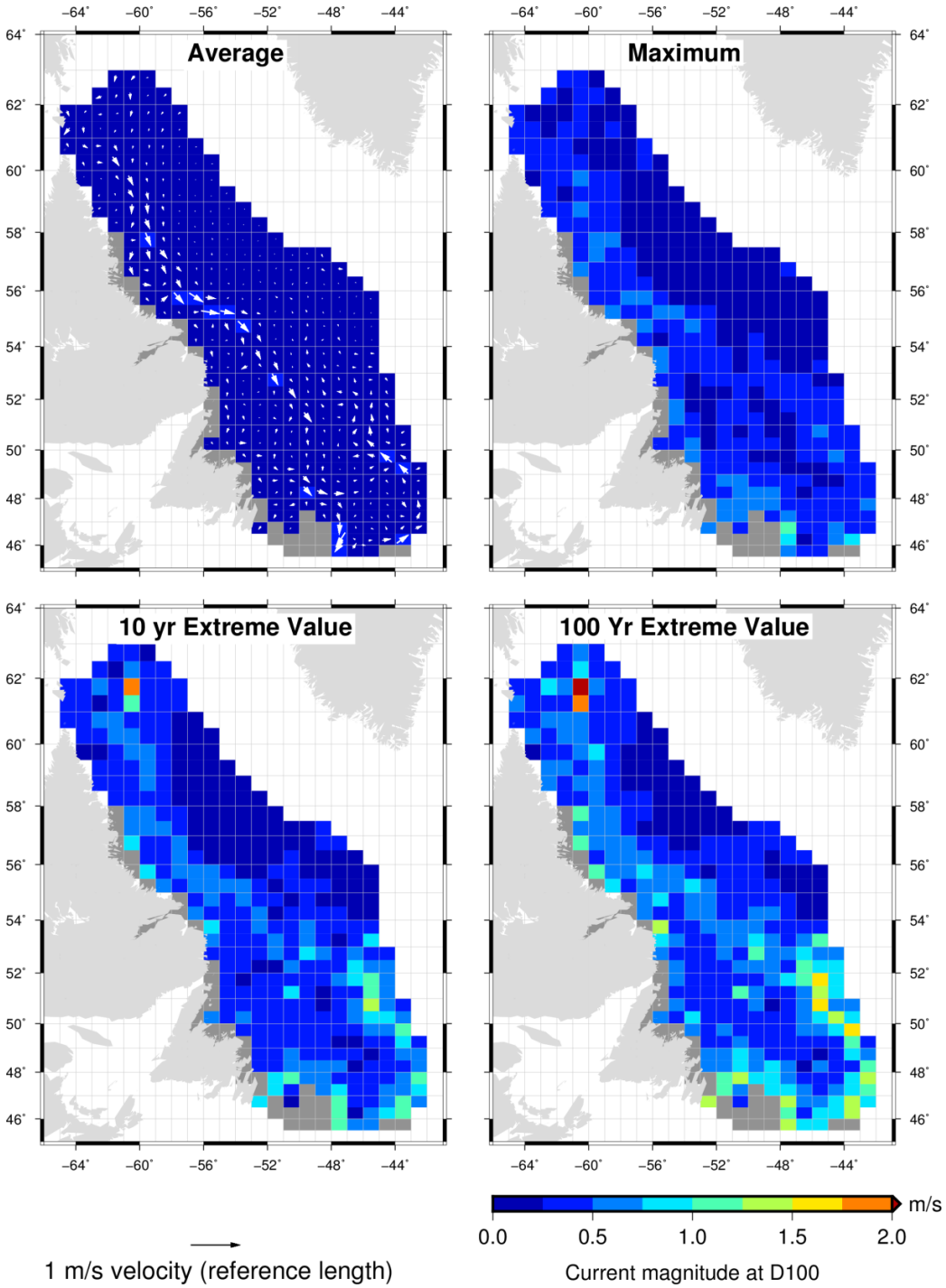

Figure 5-14. Annual current summary for 100 m water depth, vectors in the top-right represent average currents, the colour maps represent the current magnitude for the different data sets as indicated by the subplot label.

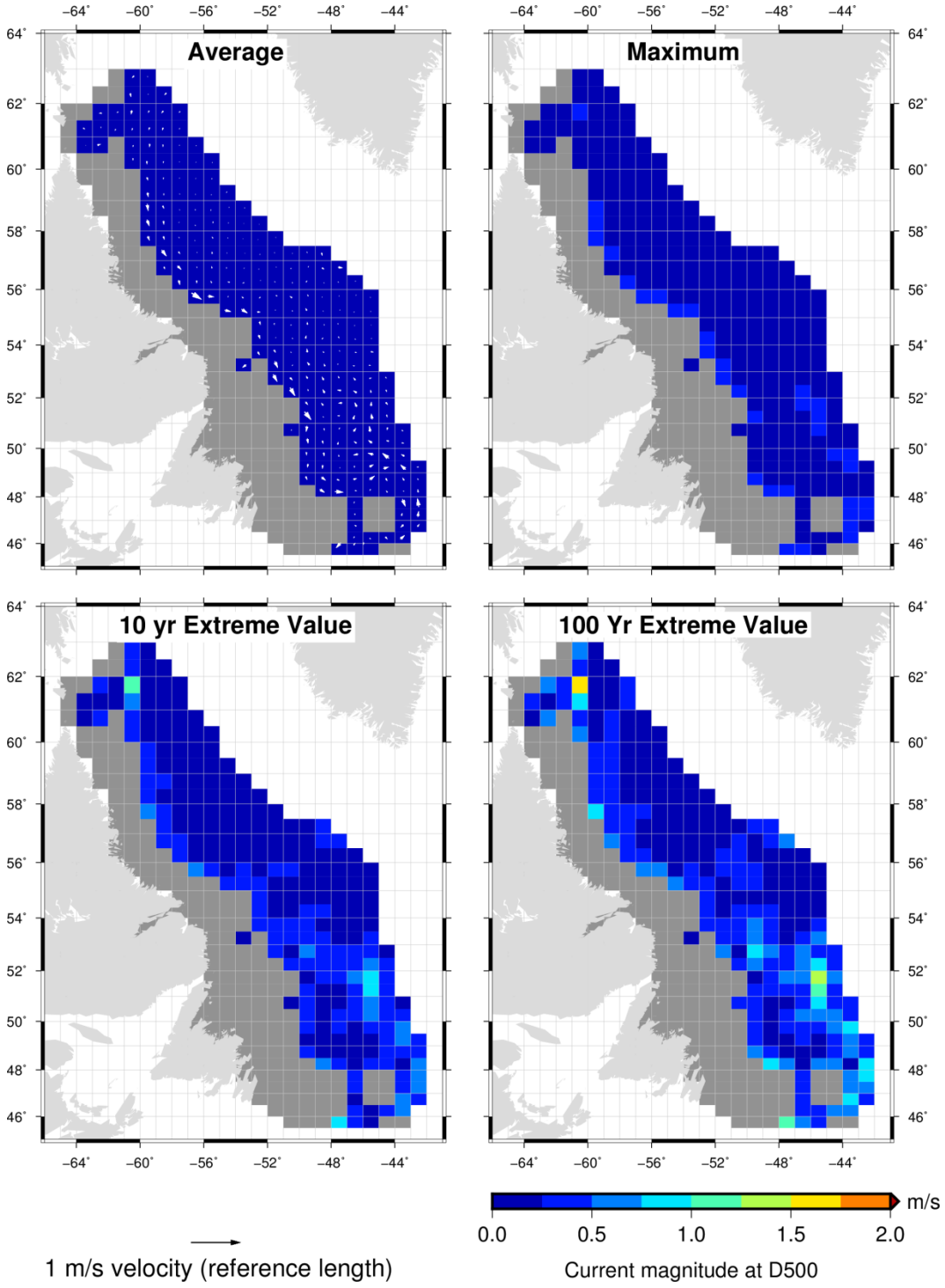

Figure 5-15. Annual current summary for 500 m water depth, vectors in the top-right represent average currents, the colour maps represent the current magnitude for the different data sets as indicated by the subplot label.

5.7 REFERENCES

Bailey, D. T. (2000). Meteorological monitoring guidance for regulatory modeling applications. DIANE Publishing.

Tang, C. L., Yao, T., Perrie, W., Detracey, B., Toulany, B., Dunlap, E., & Wu, Y. (2008). BIO Ice-Ocean and Wave Forecasting Models and Systems For Eastern Canadian Waters. Fisheries and Oceans Canada.

Wu, Y., Tang, C., & Dunlap, E. (2010). Assimilation of sea surface temperature into CECOM by flux correction. Ocean Dynamics, 60(2), 403–412. http://doi.org/10.1007/s10236-010-0266-6

Yao, T., Tang, C., & Peterson, I. (2000). Modeling the seasonal variation of sea ice in the Labrador Sea with a coupled multicategory ice model and the Princeton ocean model. Journal of Geophysical Research: Oceans (1978–2012), 105(C1), 1153–1165.

Metocean Climate Study
Offshore Newfoundland & Labrador

STUDY MAIN REPORT
Volume 1: Chapter 6 – Icing

Prepared for:
Nalcor Energy Oil and Gas

Prepared by:
C-CORE

Reviewed & Edited by:
Bassem Eid, Ph.D.

May 2015

CHAPTER 6 ICING

TABLE OF CONTENTS

LIST OF FIGURES

LIST OF ACRONYMS

CICE	Community Ice CodE (aka Los Alamos Sea Ice Model)
ECMWF	European Centre for Medium-Range Weather Forecasts
ERA	ECMWF Re-Analysis
EUMETSAT	European Organization for the Exploitation of Meteorological Satellites
GHRSST	Group for High Resolution Sea Surface Temperatures
HYCOM	HYbrid Coordinate Ocean Model
ICEMOD	Sea icing prediction model (Horjen and Vefsnmo)
NOAA	National Oceanic and Atmospheric Administration
OSI SAF	Ocean and Sea Ice Satellite Application Facility
OSTIA	Operational Sea Surface Temperature and Sea Ice Analysis
RIGICE	Sea icing prediction model (Roebber and Mitten)
TOPAZ4	Towards an Operational Prediction system for the North Atlantic European Coastal Zones, 4th generation

6 ICING

6.1 BACKGROUND

Icing of vessels and offshore structures can pose concerns for operability and safety. The most serious form of icing affecting marine operations near the surface (ships, buoys, platforms) is from sea spray (Guest, 2005). Accreted ice can reduce stability (especially for small mobile vessels); induce extra weight stress on structural members; cause slipping hazards; block access to and otherwise disable important equipment (Ryerson, 2011); and increase lateral forces from wave-structure interactions due to greater cross-sectional area (Forest, Lozowski and Gagnon, 2005; Kojo, 1984).

The calculation of icing rates is complex. Ice accretion processes are controlled by environmental factors but also depend on the surface, material and shape of the structural member subject to icing accretion. Quantitative procedures to evaluate and forecast vessel icing are limited.

Overland, Pease, Priesendorfer, and Comiskey (1986) developed an empirical method, using icing data on vessels off Alaska, to characterize the severity of sea spray icing events on vessels. An icing predictor index (PR) is calculated from meteorological variables and used as an analogue to the icing rate, according to the following categories: (1) no icing; (2) light icing; (3) moderate icing; (4) heavy icing; and (5) extreme icing. This model was subsequently refined by including extra sets of data from the Labrador Sea to the calibration (Overland, 1990). Compared to alternative models, this method has the advantage of being fairly simple and it has been tested over several decades by the National Oceanic and Atmospheric Administration (NOAA), which produces daily icing predictions for regions prone to icing conditions using this procedure.

More complex models also exist. Chung et al. (1998) and Lozowski, Szilder, and Makkonen (2000) cite early offshore structure icing models by Ashcroft (1985), and Romagnoli (1988), as well as the RIGICE (Roebber and Mitten, 1987; Mitten 1994) and the ICEMOD (Horjen and Vefsnmo 1986a, 1986b; 1987; Horjen, Vefsnmo and Bjerke, 1988) models. The RIGICE model was a simplification of ICEMOD (Forest et al., 2005). RIGICE was modified and tested by Lozowski, Forest, Chung and Szilder (2002) and subsequently refined by Forest et al. (2005). The focus of the model is on spray generation from wave-structure impacts. In RIGICE, the total flux of water hitting the platform, including spray from wind shear off wave crests and atmospheric precipitation as well as wave structure collisions (based on wind speed and direction, wave height and frequency) are calculated and heat transfer fluxes are used to predict the ice accretion, using the boundary layer model of Makkonen (1985) for a cylindrical column.

Jones and Andreas (2009) and Jones and Andreas (2012) describe a model for sea spray icing on fixed offshore structures. Their model begins with a characterization of the spray cloud as a function of wind speed and air temperature, as well as, the theoretical icing rate on a cylinder. Heat balance is neglected in the model because of the rapid cooling involved. Sea spray flux from whitecaps was calculated using a function from Fairall et al., (1994) after consideration of several theoretical models (Andreas, 2002).

Hansen (2012) developed a predictive icing model for offshore structures and vessels. The model considered wind-induced spray from whitecaps after Jones and Andreas (2012), as well as spray from wave impacts, after Lozowski et al., (2000), along with a thermodynamic model for the icing process and an application to polygon-based vessel geometry.

6.2 ANALYSIS APPROACH

This study uses the approach described in Overland et al. (1986) and Overland (1990) to assess the occurrence and severity of sea spray icing events at each cell block between years 1985-2012. The model is briefly presented here.

The thermodynamic balance between latent heat released from ice growth, heat loss from cooling the water (cooling of the seawater to the freezing point, runoff from the vessel of a portion of the cooled water), and the transfer of heat away from the surface (by convection of sensible heat, evaporative heat flux, and radiative cooling) determines the maximum ice accretion rate on a surface. This can be written as (Jessup, 1985; in Overland et al., 1986):

$$L_i\rho_i\frac{dh_i}{dt} + f\rho_w\frac{dh_w}{dt}c_w(T_w - T_f) + (1-f)\rho_w\frac{dh_w}{dt}c_w(T_w - T_{runoff}) = C_H\rho_a c_a U\left[(T_f - T_a) + \eta(e_s - 0.9e_a)\right] + \sigma\left(T_f^4 - \epsilon_a T_a^4\right) \quad (6\text{-}1)$$

in which

- ρ_i, ρw. and ρa. are the densities of the ice, water and air respectively;
- T_f, Tw. and Ta. are the temperatures of the saline water at the freezing point, seawater and air respectively;
- $Trunoff$. is the average temperature of runoff leaving the vessel;
- f is the fraction of impinging seawater remaining on the vessel and available for freezing;
- Li. is the latent heat of freezing of saline water;
- cw. and ca. are the specific heat of seawater and air respectively;
- hi. and hw. are the thickness of accreted ice and impinged seawater respectively;
- CH. is a heat transfer coefficient;
- U is the wind speed;
- es. and ea. are the vapor pressure of saturated and ambient air, respectively;
- η is a constant (~16 °C kPa-1);
- σ is the Stefan-Boltzmann constant; and
- ϵa. is the emissivity of the air (0.5 to 1.0; with higher values for fog and overcast conditions).
- The following assumptions are made (Overland et al., 1986):
- The difference between Tf. and Ta. is used instead of between Tf. and T_w;
- The temperature of the impinging water is near T_w;
- The dependency between the sensible heat flux and the wind speed is linear (which is appropriate for very turbulent boundary layers – Kraus, 1972); and
- The water on the deck must be at the freezing point before icing can occur (i.e., $T_{runoff} \approx T_f$; this implies that f can also be interpreted as a freezing fraction).

Based on these assumptions, Equation (6-1) becomes:

$$\frac{dh_i}{dt} = \frac{C_H\rho_a c_a U\left[(T_f - T_a) + \eta(e_s - 0.9e_a)\right] + \sigma\left(T_f^4 - \epsilon_a T_a^4\right)}{L_i\rho_i\left(1 + \frac{c_w}{L_i f}(T_w - T_f)\right)}. \quad (6\text{-}2)$$

It is assumed the most important factor in determining the icing rate is the sensible heat flux from the icing surface to the air (Overland et al., 1986) and that the basic functional form for the dependence of icing rate on meteorological variables is (Overland et al., 1986):

$$\frac{d h_i}{dt} \propto PR \equiv \frac{U(T_f - T_a)}{1 + \Phi(T_w - T_f)} \quad (6\text{-}3)$$

where PR is the icing predictor and $\Phi \equiv c_w/(Li.f)$. The numerator of Equation (6-3) represents sensible heat transfer while the denominator accounts for both the heat removal required to freeze the water (which would then remain accreted as ice) and the cooling of the seawater to the freezing point.

Other environmental variables influencing icing rate (e.g., wave height, relative humidity and radiation) were assumed by Overland et al. (1986) not to sufficiently vary independently from the primary meteorological variables (as in Equation (6-3)) to provide additional predictive skills.

Data for icing events on (1) vessels (fishing vessels, fish processors, tow boats, and Coast Guard vessels) 20-75 m in length navigating in Alaskan waters (see Overland et al., 1986); and (2) from fishing-type vessels in the Labrador Sea (Zakrzewski, Lozowski, and Horjen, 1989, in Overland, 1990), were used to empirically determine the value for Φ. Vessels were assumed to not actively be avoiding icing through heading downwind, moving at slow speeds or avoiding open seas.

Using reanalysis data, this formulation for PR was used to calculate the expected intensity of sea spray icing events at each of the grid cells between years 1985-2012. Note that Calculated values of PR are related to the expected icing rate and severity, according to the following categories (Guest, 2005; Overland et al., 1986; Overland, 1990):

$PR \leq 0$:	no icing
PR between 0 and 22:	light icing (icing rate <0.7 cm/hour)
PR between 22 and 53:	moderate icing (icing rate between 0.7-2.0 cm/hour)
PR between 53 and 83:	heavy icing (icing rate between 2.0-4.0 cm/hour)
$PR > 83$:	extreme icing (icing rate >4.0 cm/hour).

6.3 Input Data

To implement the model, data from different environmental reanalysis products were used. These are briefly presented below.

6.3.1 TOPAZ4

Towards an Operational Prediction System for the North Atlantic European Coastal Zones, 4th generation (TOPAZ4) (Sakov et al., 2012) was developed at the Nansen Environmental and Remote Sensing Center in Norway, which runs the Hybrid Coordinate Ocean Model (HYCOM), (Bleck, 2002), and was coupled with a modified version of the Community Ice CodE (aka Los Almos sea ice model), CICE (Hunke, Lipscomb, Turner, Jeffery and Elliott, 2013) sea ice model) which produces an estimate of ocean circulation in the North Atlantic and of sea-ice variability in the Arctic. TOPAZ has an advanced component of data assimilation, which uses an Ensemble Kalman filter. The European Centre for

Medium-Range Weather Forecasts (ECMWF) Re-analysis (ERA-Interim) provides ocean-surface forcing from 6h atmospheric fluxes. TOPAZ4 has a quasi-homogeneous grid that covers the North Atlantic and Arctic with 11-16 km resolution and 22 vertical layers. TOPAZ, operational since January 2003 and a reanalysis product which covers the 1990-2010 period, is also available via the MyOcean Project (http://www.myocean.eu/).

6.3.2 OSTIA

To supplement data from TOPAZ4, data from the Operational Sea Surface Temperature and Sea Ice Analysis (OSTIA) system were used. The OSTIA system is run by the Met Office (UK) and is available via the MyOcean Project (http://www.myocean.eu/). The system provides gap-free maps of sea surface temperatures (SST) at a horizontal resolution of up to 0.05° (~6 km). The data is constructed using in situ sensors and satellite data from both infra-red and micro-wave radiometers (Stark, Donlon, Martin and McCulloch, 2007). Satellite data from the Group for High Resolution Sea Surface Temperatures (GHRSST) is incorporated and assessed for individual sensor bias (at 0.25°) by comparing data against reference databases and in situ observations. These differences are entered in an optimal interpolation procedure to produce gridded fields of bias in each sensor (Donlon et al., 2012). Ice concentration data from the European Organization for the Exploitation of Meteorological Satellites' (EUMETSAT) Ocean and Sea Ice Satellite Application Facility (OSI SAF) are also provided as part of the OSTIA product.

6.3.3 ERA-Interim Reanalysis

ERA-Interim is a global atmospheric reanalysis (Dee et al., 2011) produced by the ECMWF. The ERA-Interim product offers global coverage at a horizontal resolution up to 0.125 degree. The reanalysis is available from 1979 to the present time, minus two months. Parameters delineated by 37 pressure levels are available. Weather, ocean-wave, and land-surface conditions are classified by 3h surface parameters while conditions in the troposphere and stratosphere are captured by 6h upper-air parameters. ERA-Interim uses an advanced 12h-4D variation analysis data assimilation procedure.

6.4 Calculation Procedure and Comments

Equation (6-3) was used to calculate PR, which is used as an analogue of the intensity of sea spray icing events. Reanalysis environmental data were acquired for the years between 1985 and 2012, inclusively. The following variables were used:

- Sea surface temperature (T_w): OSTIA data set
- 10 m height wind speed (U): ERA-Interim data set
- 2 m height air temperature (T_a): ERA-Interim data set
- Sea surface salinity (S): TOPAZ data set.

The sea surface salinity (S) was used to calculate the salinity-dependent freezing point of seawater (T_f). For the 1985-1989 time period, the modelled salinity was not available. A freezing temperature of -1.8°C was assumed for these years. For all variables, the daily averaged value was used to calculate a daily PR-value.

An upper threshold on the sea ice concentration was used to determine whether sea spray generation (and therefore icing) was possible or not, based on the assumptions that the presence of sea ice reduces the area of open water available for spray generation and that waves are damped by the presence of sea ice. Note, the value at which the threshold on sea ice concentration must be set is not clear. In Jones and Andreas (2013), a value of 15% was used. This has also been used in the present work.

An interpretive analysis of the results is not provided in this document; however, the reader must be aware of a few important points. The icing severity and probability estimates provided were produced using an algorithm developed for sea spray icing on vessels. Multiple factors can influence the amount of icing produced under given environmental conditions, such as the vessel length, speed, relative heading, and the dimensions of the members exposed to the spray. It is generally acknowledged, for example, that the icing from sea spray will increase for vessels traveling at higher speed (Guest, 2005). Lower icing rates are expected if the vessel is heading downwind or is in less severe sea states (Overland et al., 1986). There are also large variations of icing accumulations, depending on the geometry and location of the structural member on which icing is considered. In Overland (1990) for example, it is reported that ice accumulation on isolated structures such as cranes can be more than twice as heavy as that which occurs on flat horizontal surfaces (greater exposure to conditions favorable to enhancing heat loss – greater wind speeds – and greater encounter rate with spray droplet – less sheltered).

On offshore structures, because they are mainly stationary, sea spray is generated from whitecaps on the ocean surface (Guest, 2005; Jones and Andreas, 2009). Because the structures are larger and higher than vessels, the ice accretion will differ as a function of the relative height from the sea surface as the water droplets hit and freeze on the structure. As pointed out in Jones and Andreas (2009), these types of structures also tend to be relatively open at the water level in contrast with ships (which could impact the icing rate and accumulations). The vertical distribution of the spray cloud is important, as well as the size distribution of the droplets, which determines the rate of cooling of the droplet (Overland, 1990).

6.5 RESULTS

Figure 6-1 shows the calculated icing severity (using a 15% sea ice concentration threshold), as a time series for each year between 1985 and 2012, as a function of the Julian day. Figure 6-2 also shows the calculated icing predictor, here as a function of Julian day for years 1985-2012, calculated using a 15% sea ice concentration threshold. The sea ice concentration threshold is used to determine whether sea spray (and thus icing) is possible or not. For sea ice concentration greater than the threshold, icing is assumed not to happen. The gray dots represent the PR-value of each day (note that there can be many zero values overlapping); the black line is the average for each day; the blue, red, and green lines are the 25th, 75th, and 50th percentiles of each day, respectively. All lines were smoothed using a five-day moving average filter and a uniform weight function. The icing severity classes are determined as described at the end of Section 6.2.

Figure 6-3 shows the proportion of years with conditions conducive to icing, per degree of severity (i.e., light, moderate, heavy and extreme), as a function of Julian day for years 1985-2012, calculated using a 15% sea ice concentration threshold. All lines were smoothed using a five-day moving average filter and a uniform weight function. Figure 6-4 is a bar chart that shows the average number of days per month with conditions conducive to icing for each month, per category, for the period 1985-2012.

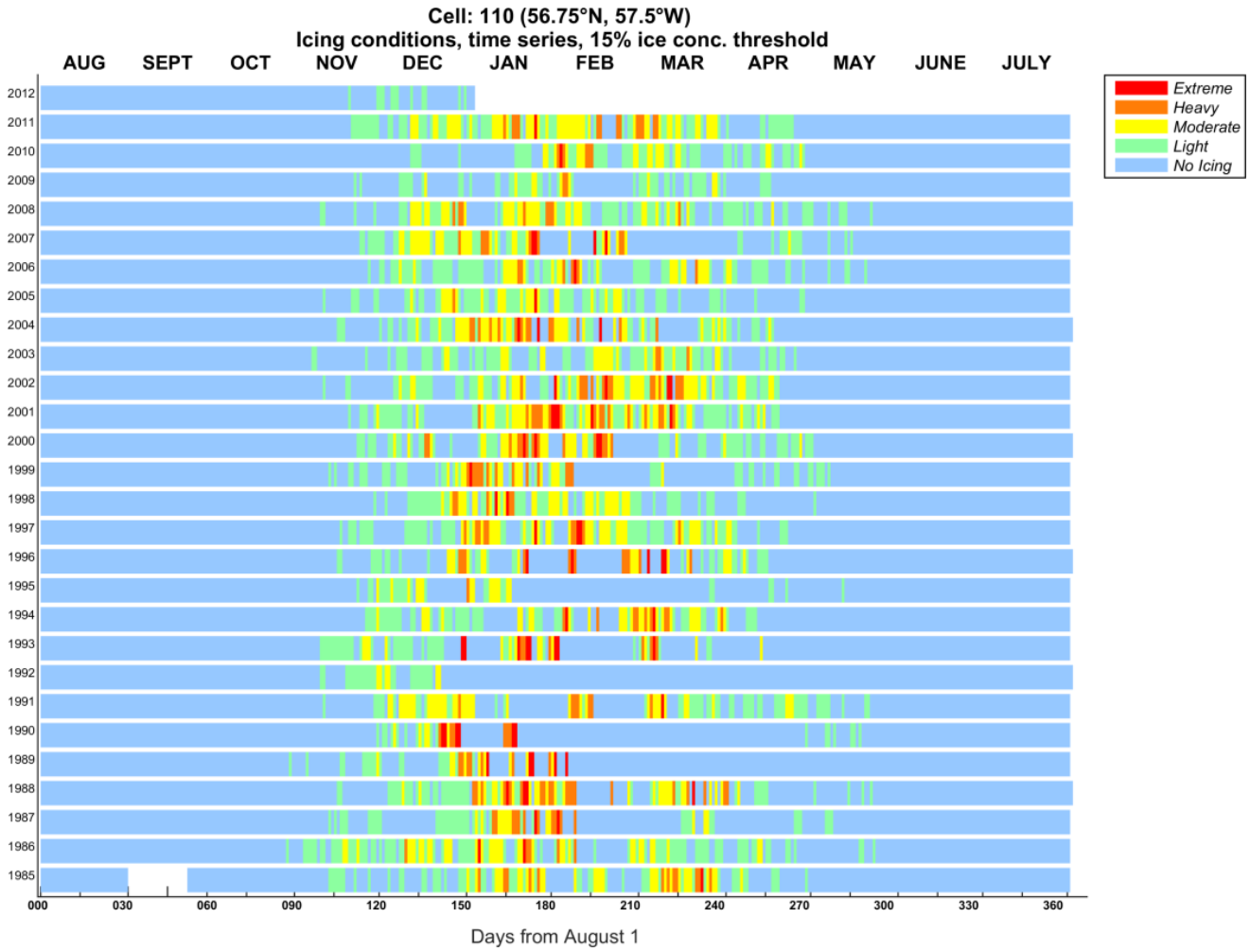

Figure 6-1. Time series of icing severity for years 1985-2012 for cell 110

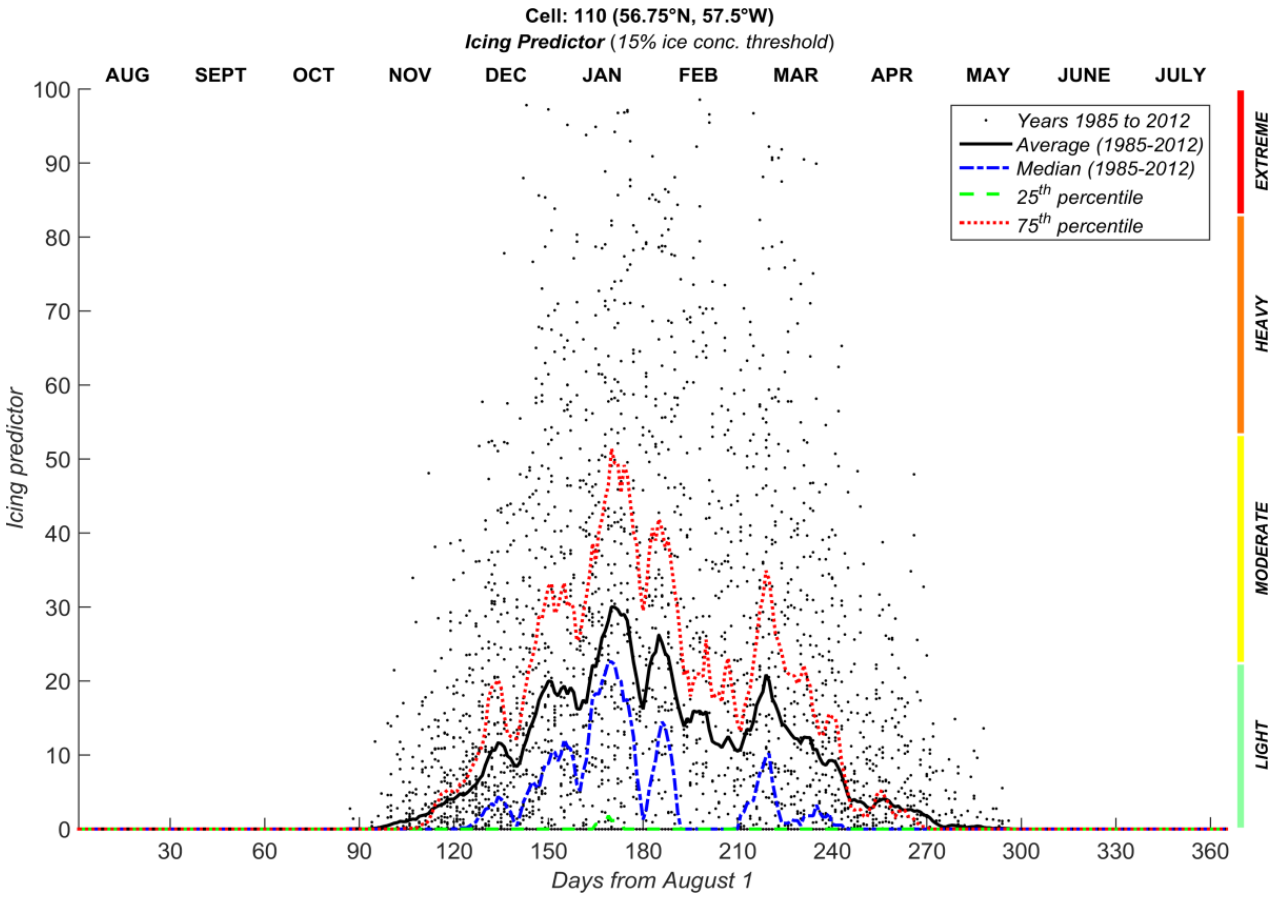

Figure 6-2. Statistics of probability of icing (along with the associated icing intensity) as a function of Julian day for years 1985-2012 for cell 110

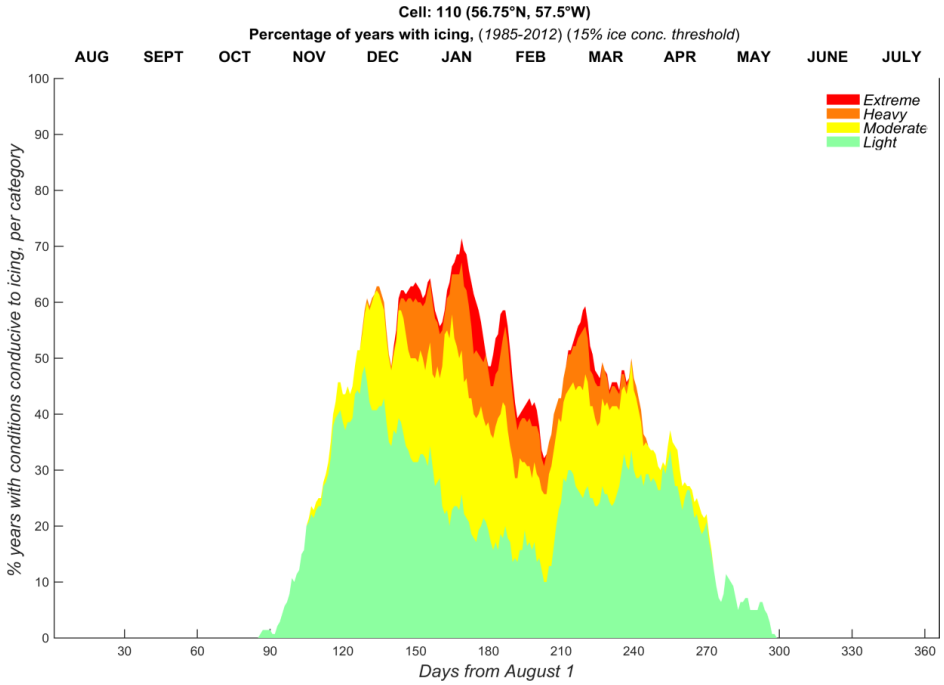

Figure 6-3. Proportion of years with conditions conducive to icing, per degree of severity, as a function of Julian day for years 1985-2012 for cell 110

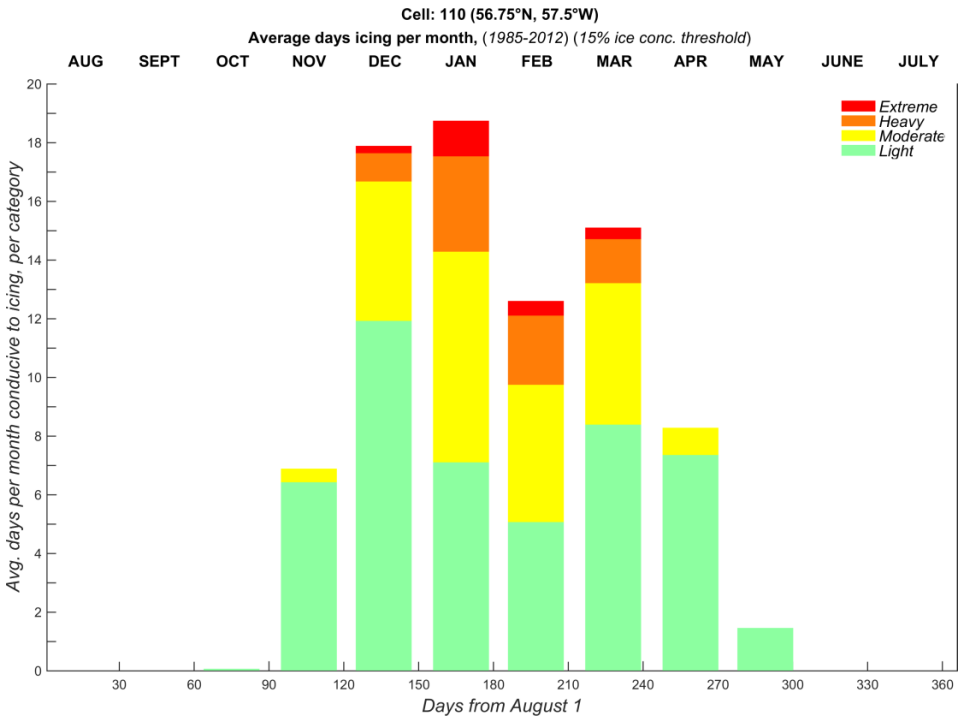

Figure 6-4. Average number of days per month with conditions conducive to icing, per degree of severity, as a function of Julian day for years 1985-2012 for cell 110

6.6 REGIONAL OVERVIEW

Figure 6-5 to Figure 6-7 show the monthly spatial distribution of the percentage of days with light or moderate icing conditions calculated for the 1985-2012 period. Most light or moderate icing events occur during the months of December to May in areas where ice concentration is low enough to allow for sea spray to form. The coastal areas of Labrador and the Chidley and Henley Basins seem prone to icing events, while the Holton and Hawke Basins and most of deepwater offshore areas experience this to a lesser extent.

Figure 6-8 to Figure 6-10 show the monthly spatial distribution of the percentage of days with heavy or extreme icing conditions calculated for the 1985-2012 period. As expected, the incidence of heavy or extreme icing is less than light or moderate, but follows a similar spatial pattern. The majority of the heavy or extreme icing is confined to the December to February period, although limited amounts of heavy or extreme icing is also observed in the March to May period.

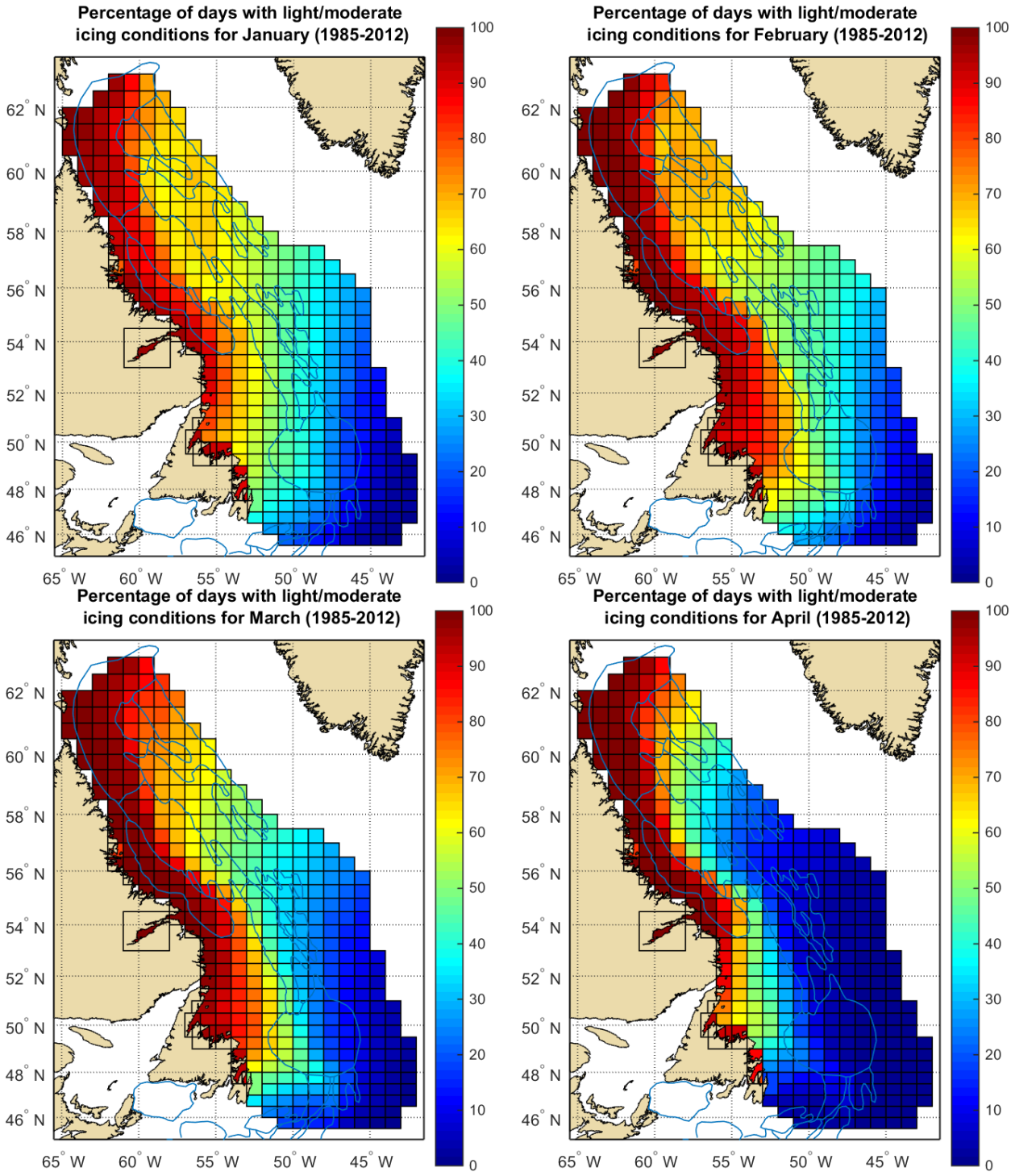

Figure 6-5. Monthly incidence (% of days) of light or moderate icing conditions (January-April, 1985-2012)

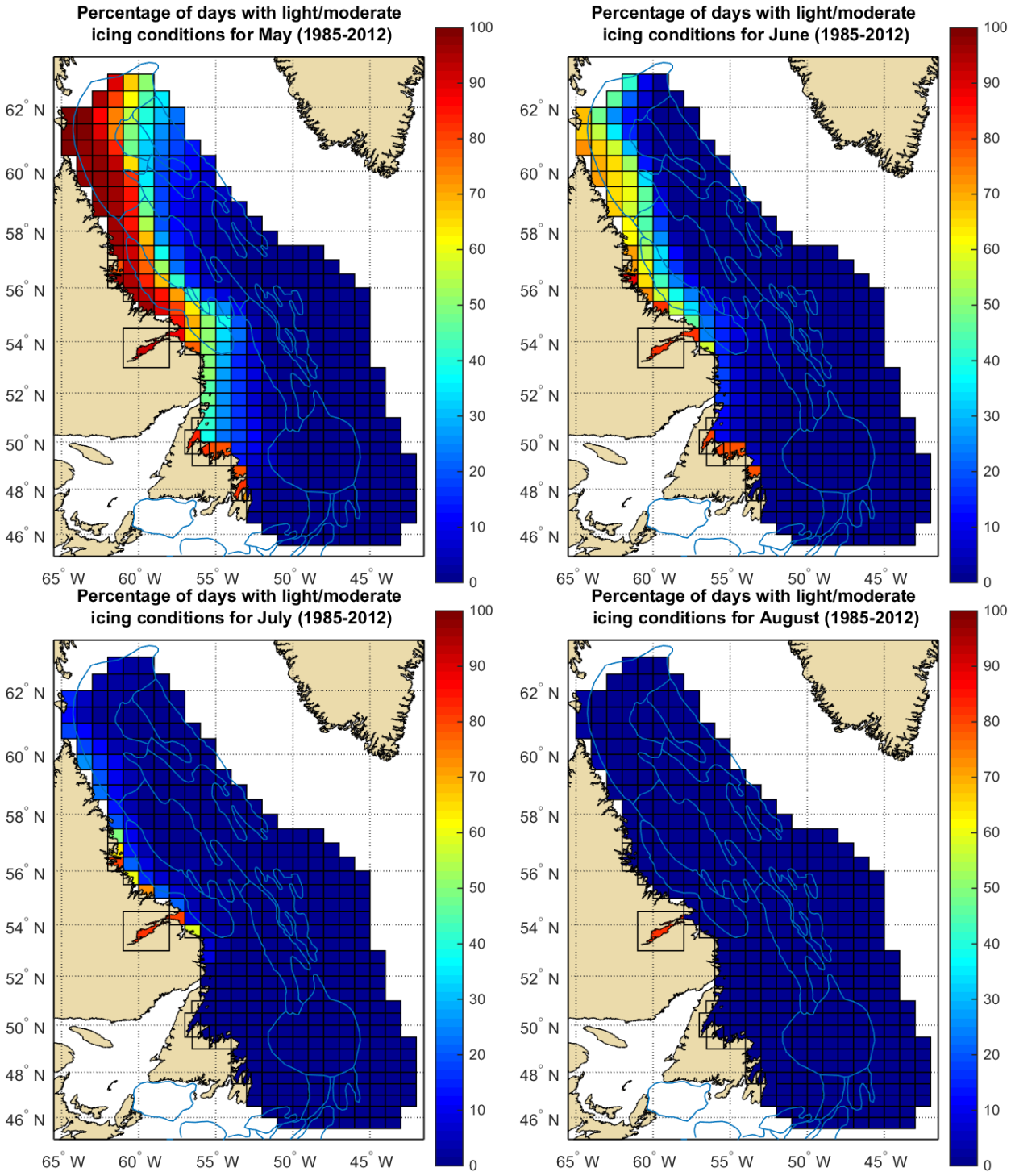

Figure 6-6. Monthly incidence (% of days) of light or moderate icing conditions (May-August, 1985-2012)

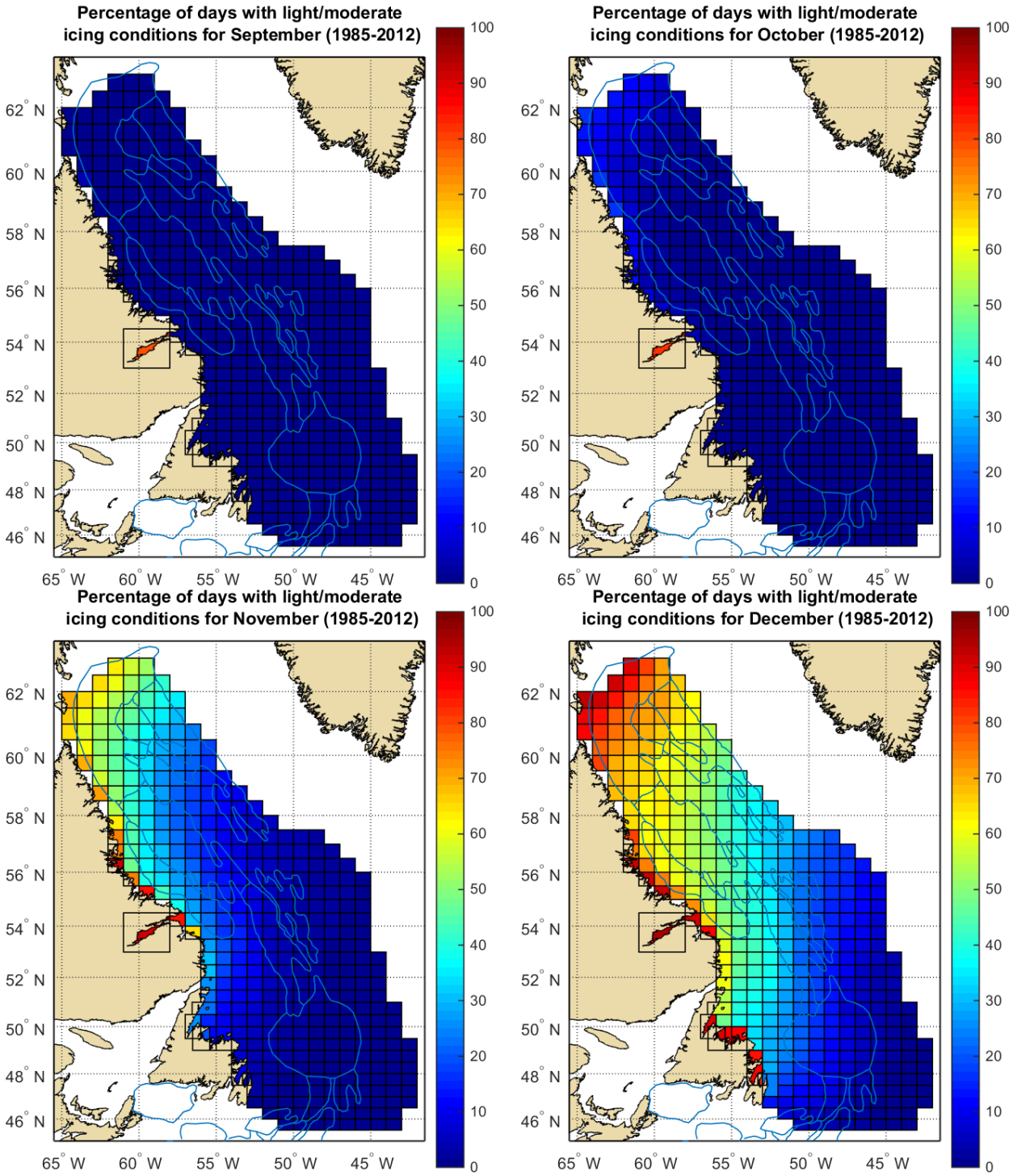

Figure 6-7. Monthly incidence (% of days) of light or moderate icing conditions (September-December, 1985-2012)

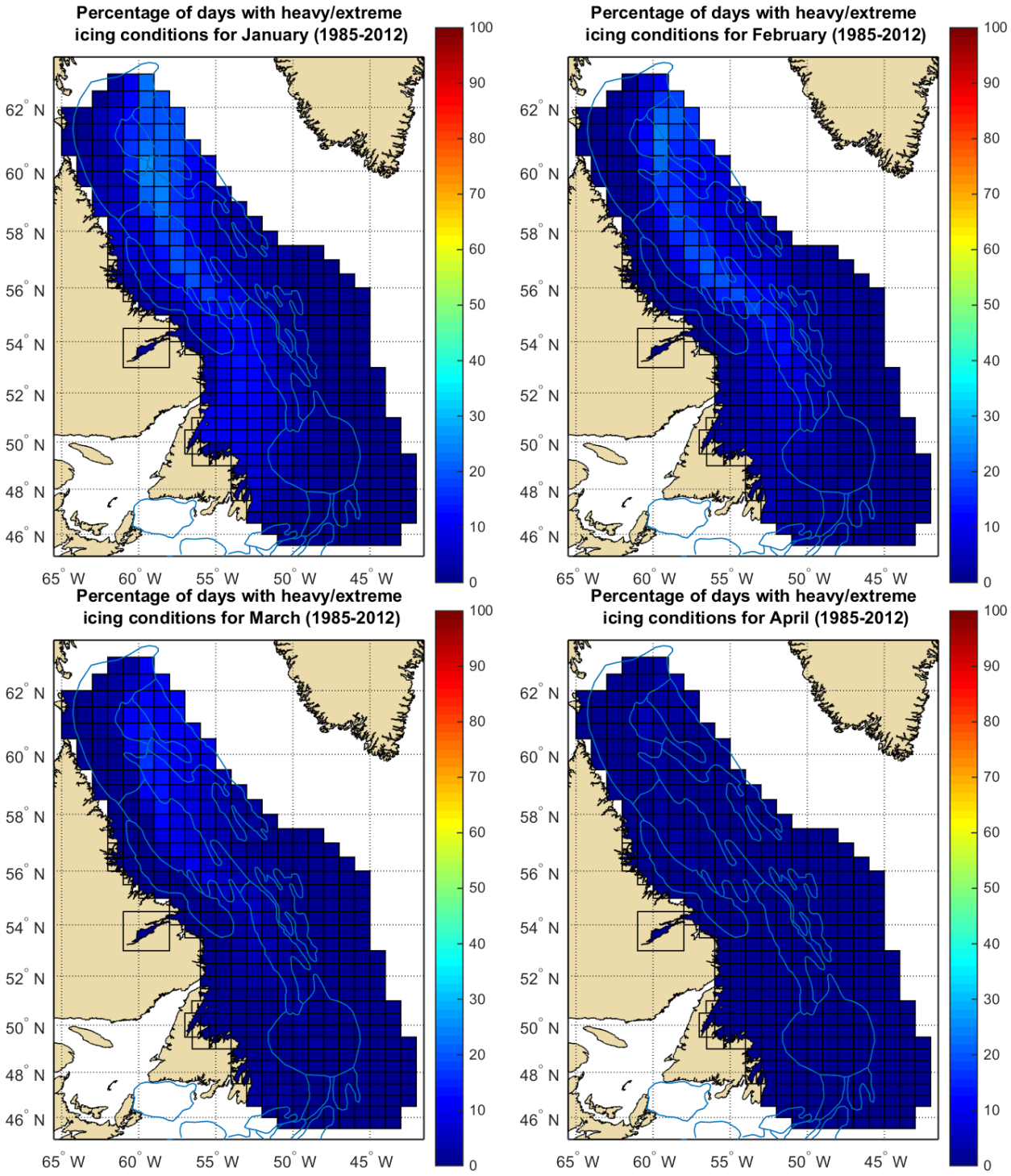

Figure 6-8. Monthly incidence (% of days) of heavy or extreme icing conditions (January-April, 1985-2012)

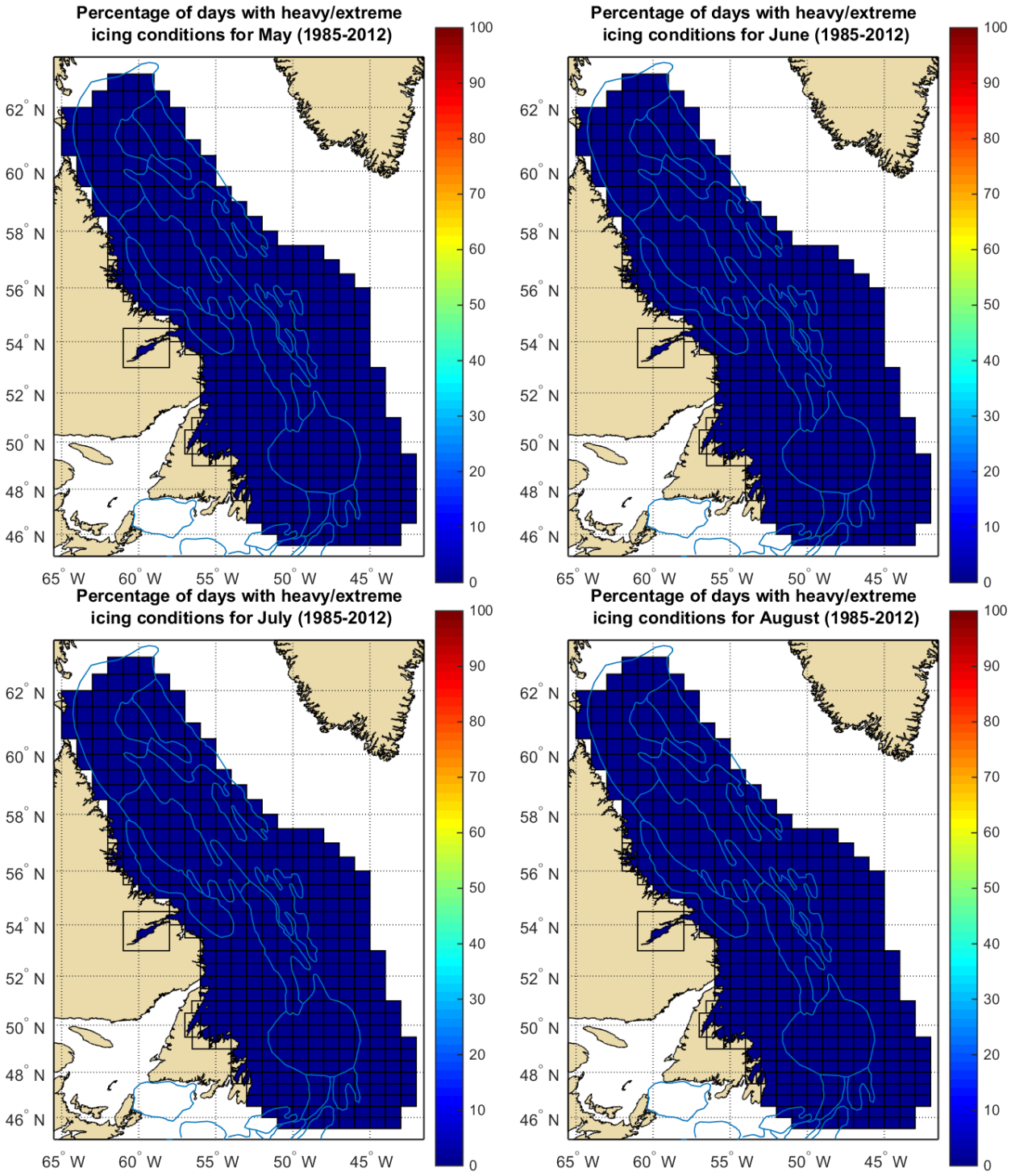

Figure 6-9. Monthly incidence (% of days) of heavy or extreme icing conditions (May-August, 1985-2012)

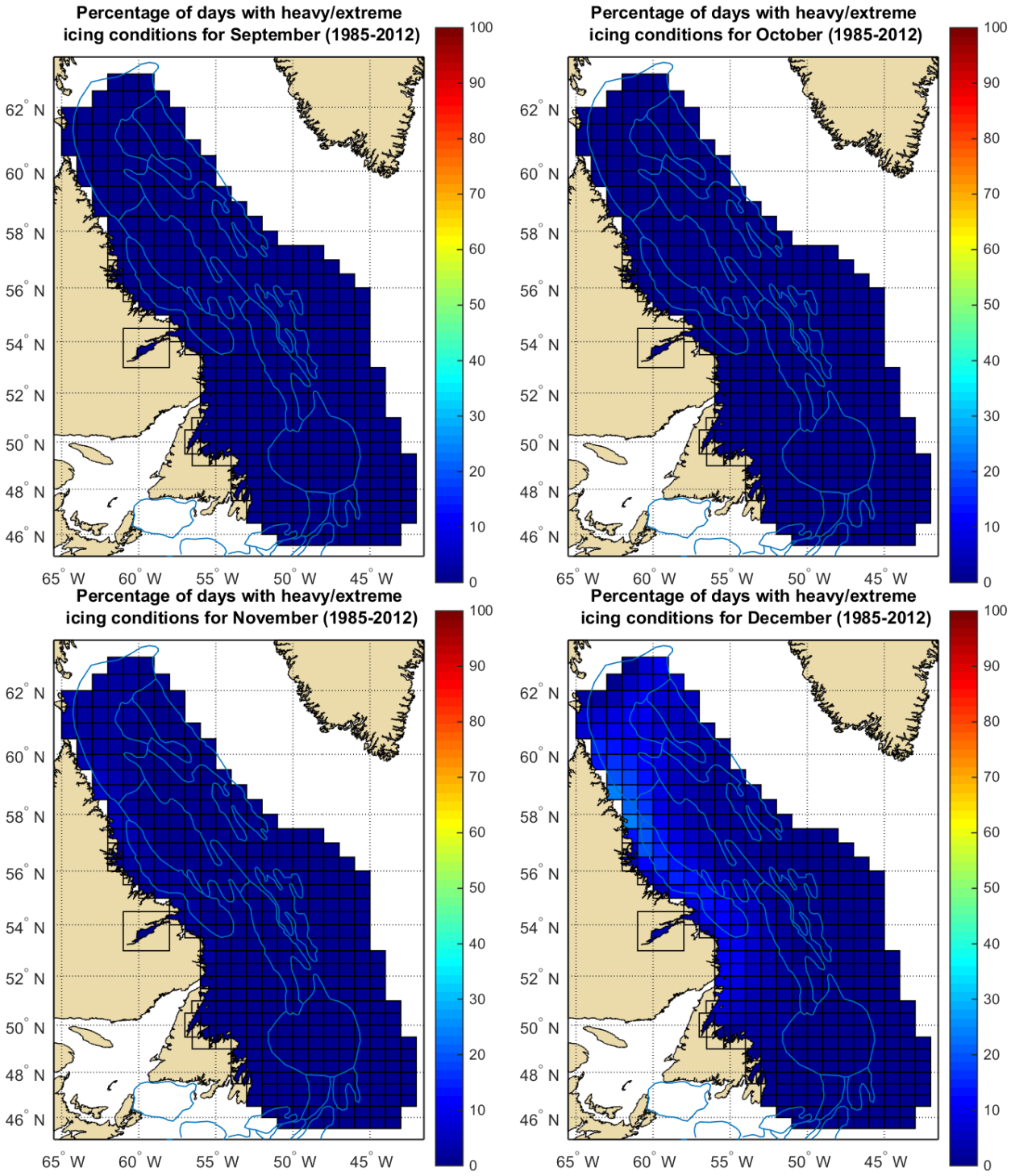

Figure 6-10. Monthly incidence (% of days) of heavy or extreme icing conditions (September-December, 1985-2012)

6.7 REFERENCES

Ashcroft, J. (1985). Potential ice and snow accretion on North Sea rigs and platforms. Marine Technical Note no. 1, British Meteorological Office, Bracknell.

Bleck, R. (2002). An oceanic general circulation model framed in hybrid isopycnic-Cartesian coordinates. Ocean Modelling, 4, 55-88.

Chung, K.K., Forest, T.W., Lozowski, E.P., Gagnon, R., Faulkner, B., Chekhar, M. (1998). Application of New Measurement and Simulartion Methods to Marine Icing on Offshore Structures. Proc. 8th (1998) International Offshore and Polar Engineering Conference, Montreal, Canada, May 24-29, 1998.

Dee, D. P., Uppala, S. M., Simmons, A. J., Berrisford, P., Poli, P., Kobayashi, S., Andrae, U., Balmaseda, M. A., Balsamo, G., Bauer, P., Bechtold, P., Beljaars, A. C. M., van de Berg, L., Bidlot, J., Bormann, N., Delsol, C., Dragani, R., Fuentes, M., Geer, A. J., Haimberger, L., Healy, S. B., Hersbach, H., Hólm, E. V., Isaksen, L., Kållberg, P., Köhler, M., Matricardi, M., McNally, A. P., Monge-Sanz, B. M., Morcrette, J.-J., Park, B.-K., Peubey, C., de Rosnay, P., Tavolato, C., Thépaut, J.-N. and F. Vitart (2011). The ERA-Interim reanalysis: configuration and performance of the data assimilation system. Q.J.R. Meteorol. Soc., 137: 553–597. doi: 10.1002/qj.828.

Donlon, C.J., Martin, M., Stark, J., Roberts-Jones, J., Fiedler, E., and Wimmer, W. (2012). The Operational Sea Surface Temperature and Sea Ice Analysis (OSTIA) system. Remote Sensing of the Environment. doi: 10.1016/j.rse.2010.10.017 2011.

Fairall, C.W., Kepert, J.D. and Holland, G.J. (1994). The effect of sea spray on surface energy transports over the ocean. Global Atmos. Ocean System 2:121-142.

Forest, T.W., Lozowski, E.P., Gagnon, R.E. (2005). Estimating marine icing on offshore structures using ROGICE04. IWAIS XI, Montreal Canada, June 2005.

Guest, P. (2005). Mariners Weather Log – Vessel Icing, NOAA, Vol. 49, No. 3, December 2005, (http://www.vos.noaa.gov/MWL/dec_05/ves.shtml) – accessed in March 2014.

Hansen, E.S. (2012). Numerical modeling of marine icing on offshore structures and vessels. M. Sc. thesis, NTNU Department of Physics, Trondheim, Norway, June 2012.

Horjen, I. and Vefsnmo, S. (1986a). Computer modelling of sea spray icing on marine structures. In Proc. Symp. On Automation for Safety in Shipping and Offshore Operations, Trondheim, Norway (ed. G. Kuo et al.) pp. 315-323. Elsevier.

Horjen, I. and Vefsnmo, S. (1986b). Calibration of ICEMOD – extension to a time-dependent model. Norwegian Hydrodynamic Laboratories Report STF60 F86040.

Horjen, I. and Vefsnmo, S. (1987). Time-dependent sea spray icing on ships and drilling rigs – a theoretical analysis. Norwegian Hydrodynamic Laboratories Report STF60 F87130.

Horjen, I., Vefsnmo, S., and Bjerke, P.L. (1988). Sea spray icing on rigs and supply vessels. ESARC Report no. 15, Norwegian Hydrodynamic Laboratories Report STF60 F88137.

Hunke, E.C., Lipscomb, W.H., Turner, A.K., Jeffery, N. and S. Elliott (2013). CICE: the Los Alamos Sea Ice Model, Documentation and Software User's Manual, Version 5.0, LA-CC-06-012, 115 pp.

Jessup, R.G. (1985). Forecasting techniques for ice accretion on different types of marine structures, including ships, platforms and coastal facilities. Marine Meteorology and Related Oceanographic Activities, Rep. 15, WMO, Canada, 90 pp.

Jones, K.F. and Andreas, E.L. (2009). Sea Spray Icing of Drilling and Production Platforms. ERDC/CRREL TR-09-3, February 2009.

Jones, K.F. and Andreas, E.L. (2012). Sea spray concentrations and the icing of fixed offshore structures. Quarterly Journal of the Royal Meteorological Society, 138, 131-144, January 2012.

Jones, K.F. and Andreas, E.L. (2013). Sea Spray and Icing in the Emerging Open Water of the Arctic Ocean. Progress report to the Office of Naval Research (ONR), Science and Technology (http://www.onr.navy.mil/reports/FY13/agjones.pdf).

Kojo, T.L., 1984. Superstructure icing in the North Chukchi, South Chukchi and Hope Basin areas. Report for the Outer Continental Shelf Environmental Assessment Program Research Unit 519, pp.: 303-360.

Kraus, E.B. (1972). Atmosphere-ocean interaction. Oxford University Press, London, 275 pp.

Lozowski, E.P., Szilder, K. and Makkonen, L. (2000). Computer simulation of marine ice accretion. Phil. Trans. R. Soc. Lond. A, 358, 2811-2845, November 2000.

Lozowski, E.P., Forest, T., Chung, V. and Szilder, K. (2002). Study of marine icing. Institute for Marine Dynamics, National Research Council of Canada, St. John's, NL, Report CR-2002-03, 88pp., 2002.

Makkonen, L. (1985). Heat transfer and icing of a rough cylinder. Cold Regions Science and Techno9logy 10:105-116.

Mitten, P. (1994). Measurement and modelling of spray icing on offshore structures. Final Report to Atmospheric Environment Service of Canada, Contract no. 07SE. KM169-8-7439.

Overland, J.E. (1990). Prediction of vessel icing for near-freezing sea temperatures. Weather and forecasting. Vol . 5, pp.: 62-77.

Overland, J.E., Pease, C.H., Preisendorfer, R.W. and A.L. Comiskey (1986). Prediction of vessel icing. Journal of climate and applied meteorology, Vol. 25, No. 12, pp.: 1793-1806.

Roebber, P. and Mitten, P. (1987). Modelling and measurement of icing in Canadian waters. Canadian Climate Centre Report 87-15.

Romagnoli, R. (1988). Ice growth modeling for icing control purposes of offshore marine units employed by the petroleum industry. In Proc. Int. Association for Hydraulic Research Symposium on Ice, Sapporo, Japan, pp. 486-497.

Ryerson, C.C. (2011). Ice protection of offshore platforms. Cold Regions Science and Technology, 65, 97-110, 2011.

Sakov, P., Counillon, F., Bertino, L., Lisæter, K. A., Oke, P. R., and A. Korablev (2012). TOPAZ4: an ocean-sea ice data assimilation system for the North Atlantic and Arctic. Ocean Sci., 8, 633-656. doi: 10.5194/os-8-633-2012.

Stark, J.D., Donlon, C.J., Martin, M.J. and M.E. McCulloch (2007). OSTIA: An operational, high resolution, real time, global sea surface temperature analysis system. Proc., Oceans 2007, Europe, Aberdeen, Scotland, IEEE, 331–334.

Zakrzewski, W.P., Lozowski, E.P. and I. Horjen (1989). The use of ship icing models for forecasting icing rates on sea-going ships. Proceedings of the 10th international conference on Port and Ocean Engineering Under Arctic Conditions, June 1989, Luleå, Sweden.

Metocean Climate Study
Offshore Newfoundland & Labrador

STUDY MAIN REPORT
Volume 1: Chapter 7 – Visibility (Fog)

Prepared for:
Nalcor Energy Oil and Gas

Prepared by:
C-CORE

Reviewed & Edited by:
Bassem Eid, Ph.D.

May 2015

CHAPTER 7 – VISIBILITY (FOG)

TABLE OF CONTENTS

LIST OF FIGURES

LIST OF ACRONYMS

GFS	Global Forecast System
ISO	International Organization for Standardization
MMAB	Marine Modeling and Analysis Branch (of NCEP)
NARR	North American Regional Analysis
NCEP	National Centers for Environmental Prediction
YYT	St. John's International Airport
UTC	Coordinated Universal Time

7 VISIBILITY (FOG)

7.1 DATA SOURCE AND DATA ANALYSIS

Visibility is defined as the greatest distance at which selected objects can be seen or identified. This section covers only visibility due to fog. Newfoundland and Labrador's coasts are among the regions of the world where fog is the most frequently encountered issue on an annual basis. Fog is defined, technically, as a ground-based cloud layer. There are several types of fogs, classified according to their formation processes (radiation fog, advection fog, terrain-induced fog, rain/post-frontal fog, valley fog, etc.). For Canada's east coast, the two most important types are radiation and advection fogs (Toth et al., 2011).

Radiation fog is caused by overnight infrared cooling of the bottom surface (i.e.,, ground, water, etc.) and the air, until the air reaches the dew point, after which it becomes supersaturated and fog droplets form by condensation. As the fog deepens, less radiative heat escapes to the atmosphere and this slows down the fog formation process. Radiation fog forms and dissipates locally, usually overnight or early morning (when solar radiations are absent), under relatively low wind conditions (< 5 kt; Toth et al., 2011), and usually last a couple of hours.

Advection fog occurs when either (1) warm air moves over a colder surface; or (2) cold air moves over warmer surface. In the first case, the air cools down until condensation occurs (when the dew point is reached). In the second case, when the surface is water, when cold dry air moves over water, evaporation occurs so that the water content in the near-surface air layer is increased. The large vapour pressure gradient created promotes evaporation of the water molecules to the air until saturation is reached. When this happens fast enough so that the air temperature does not change significantly, condensation occurs and fog formation happens. This is common in cold oceans such as those on Canada's east coast. Should the air be cold enough, the evaporated water could also sublimate into small ice crystals. Advection fog occurs in low to moderate wind conditions (less than 10 kt; Toth et al., 2011) and may last up to several days.

The occurrence of fog was estimated using the horizontal visibility data from the North American Regional Reanalysis (NARR) hindcast model produced by the National Centers for Environmental Prediction (NCEP), and US National Oceanographic and Atmospheric Administration (NOAA). Horizontal visibility in NARR is modelled using the approach of NCEP's Marine Modeling and Analysis Branch (MMAB) Global Visibility System, which follows an algorithm developed by Stolinga and Warner (1999). See also: http://polar.ncep.noaa.gov/marine.meteorology/global.visibility/about.gvis.shtml.

In this algorithm, extinguishing coefficients for the various precipitation types are calculated (based on the mass concentration of each type of hydrometeor; that is, cloud liquid water, cloud ice, rain, and snow) and linearly combined to determine a visibility value. Parameters needed to calculate the mass concentration of hydrometeors come from the Global Forecast System (GFS) and include air temperature, relative humidity, surface pressure, synoptic and convective precipitation rates, precipitable water, cloud mixing ratio, categorical rain, freezing rain, ice pellets, and snow. The visibility

data in NARR are available at approximately a 32-km spatial resolution at a three-hour temporal frequency.

Different horizontal visibility thresholds are traditionally associated with weather events for practical purposes. In guidelines provided in the International Organization for Standardization (ISO) 19906:2010(E) standard, the visibility thresholds used are:

- 1 km (≈0.5 nm): generally taken to represent foggy conditions
- 2 km (≈1 nm): denoted for certain regions as snowstorm conditions
- 5 nm (≈9.25 km): limit for which meteorological conditions in the standard are specified for various regions.

A comparison of the horizontal visibility data with the observed visibility at St. John's International Airport has been made. Figure 7-1 shows time series of observed (red) fog events and modelled (blue) low visibility events (visibility <1 km) at St. John's International Airport (YYT) for year 2012. Overall, the modelled data for that year are in reasonable agreement with the observations, with a hit rate (true positive and true negative) of 72.5%, a false alarm rate (false positive) of 9.9%, and a missed rate (false negative) of 17.6%.

7.2 RESULTS

Figure 7-2 presents the percentage of time with horizontal visibility less than one kilometre (km) as a function of time of day and time of year, for data from 1979-2013 at cell 110. For each Julian day and time of day, there were 35 visibility values available (out of the 35 years of available data). The percentage of time is defined as the total number years for a given Julian day and time of day, with low visibility divided by the total number of available years. Time of day is given in Coordinated Universal Time (UTC). Theoretical sunrise and sunset times (as a function of latitude/longitude, given in UTC) are also shown with black lines on the figure. Similar figures are provided for each of the three visibility thresholds at each cell; that is, one km, two km, and five nautical miles (5 nm).

Figure 7-3 shows the percentage of daylight hours per month with low visibility, for each of the three thresholds, for data from 1979-2013 at cell 110. Daylight hours were determined from the sunrise/sunset curves, as presented in Figure 7-2. Figure 7-4 shows the model results using a different format by indicating the mean number of daylight hours with visibility greater than one km for cell 110. Figure 7-5 and Figure 7-6 repeat the previous analysis, based on the total hours per day (i.e., 24-hour period) rather than daylight hours only.

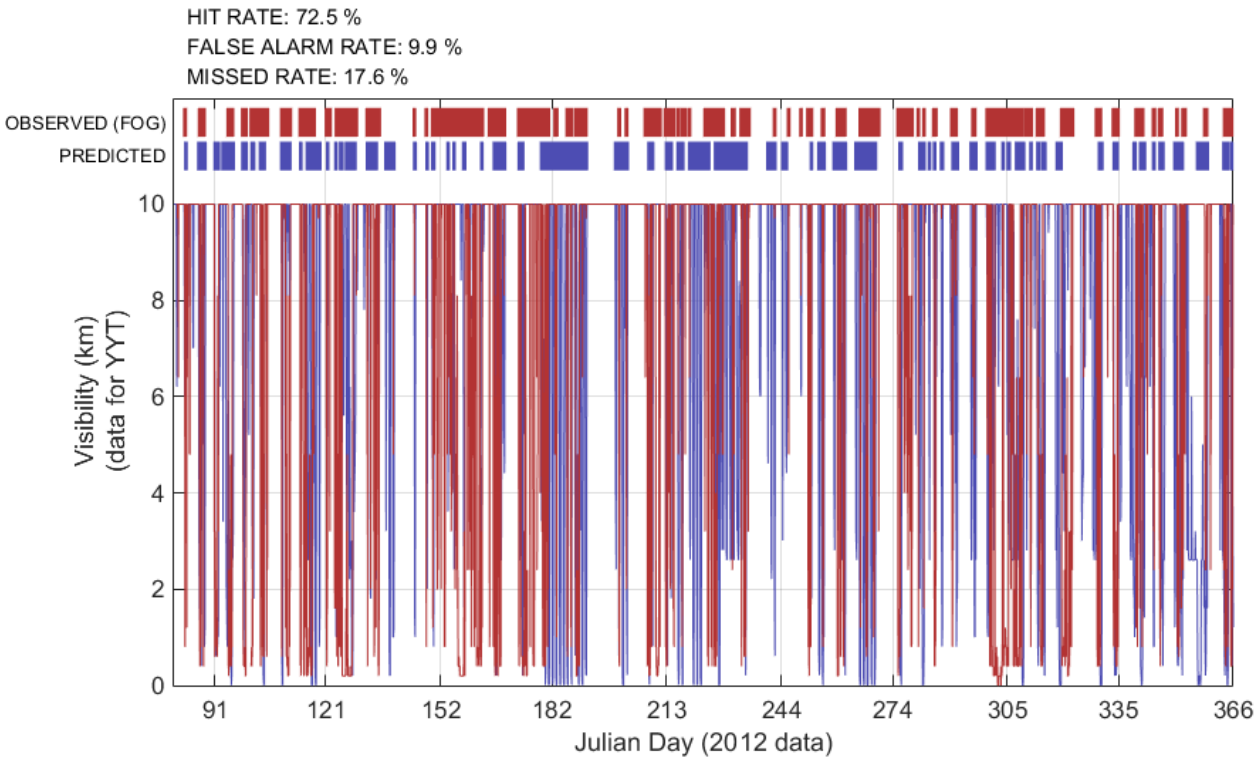

Figure 7-1. Time series of observed (red) fog events and modelled (blue) low visibility events (visibility <1 km) at St. John's International Airport (YYT) for year 2012

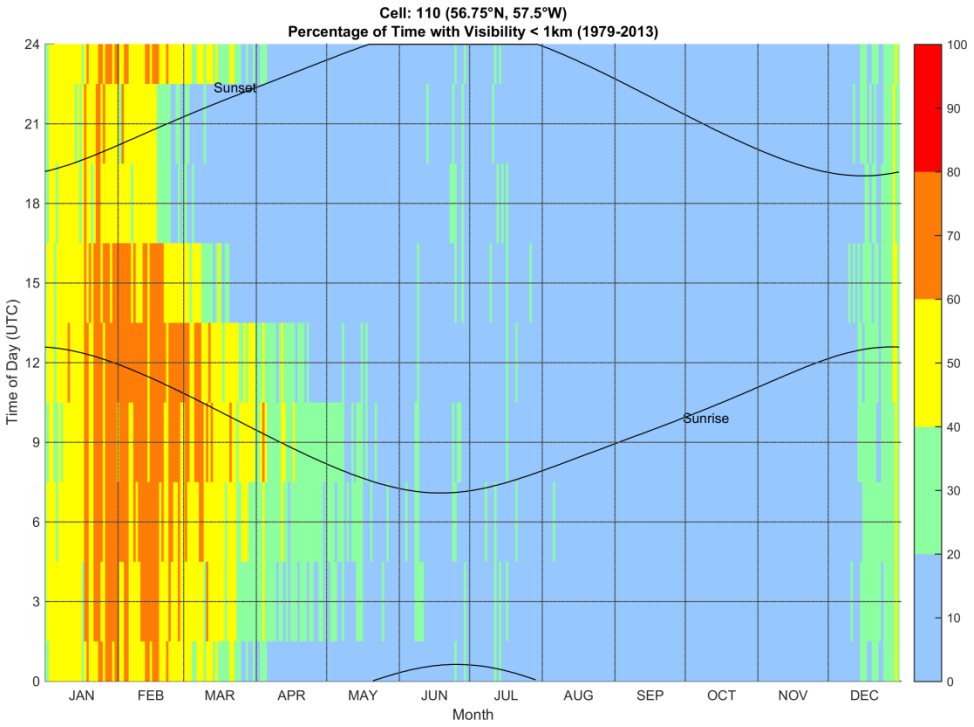

Figure 7-2. Percentage of time with horizontal visibility less than 1 km as a function of time of day and time of year, for data between 1979-2013 at cell 110

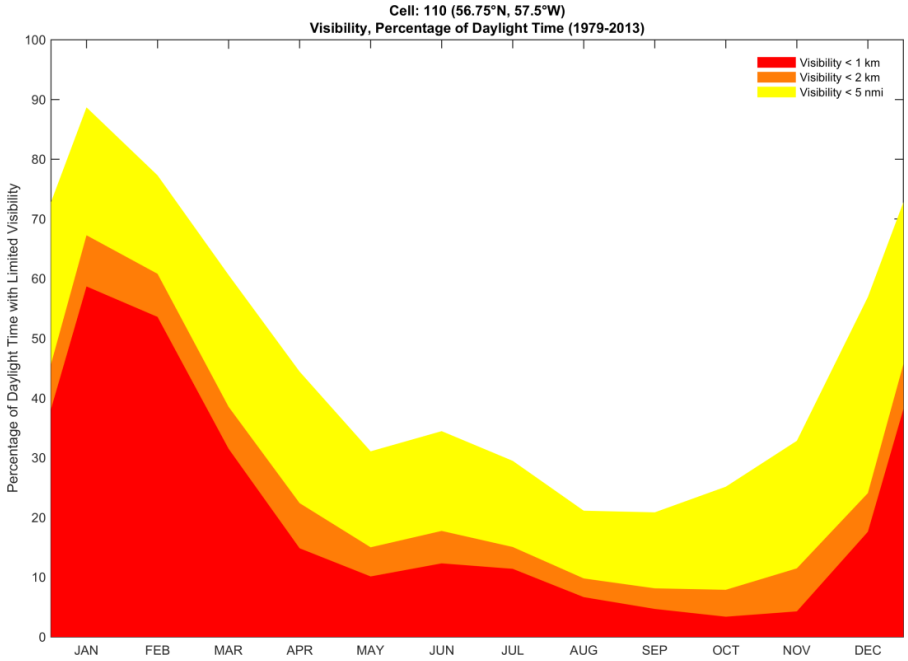

Figure 7-3. Percentage of daylight time per month with low visibility, for each of the three thresholds, for period 1979-2013 at cell 110

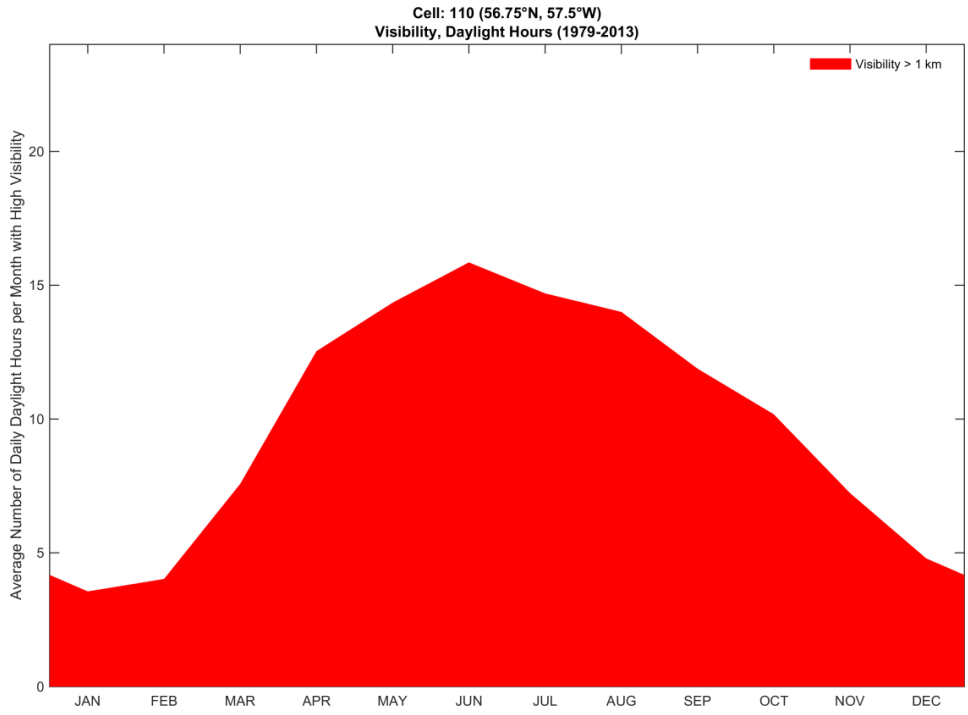

Figure 7-4. Mean daily number of daylight hours with visibility > 1 km in cell 110

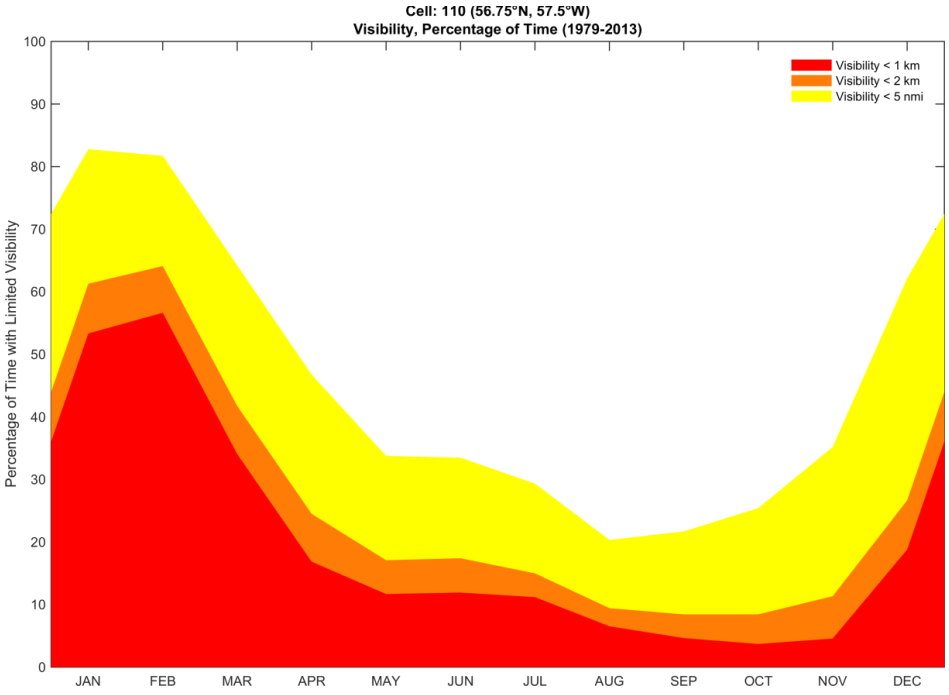

Figure 7-5. Percentage of total time per month with low visibility, for each of the three thresholds, for period 1979-2013 at cell 110

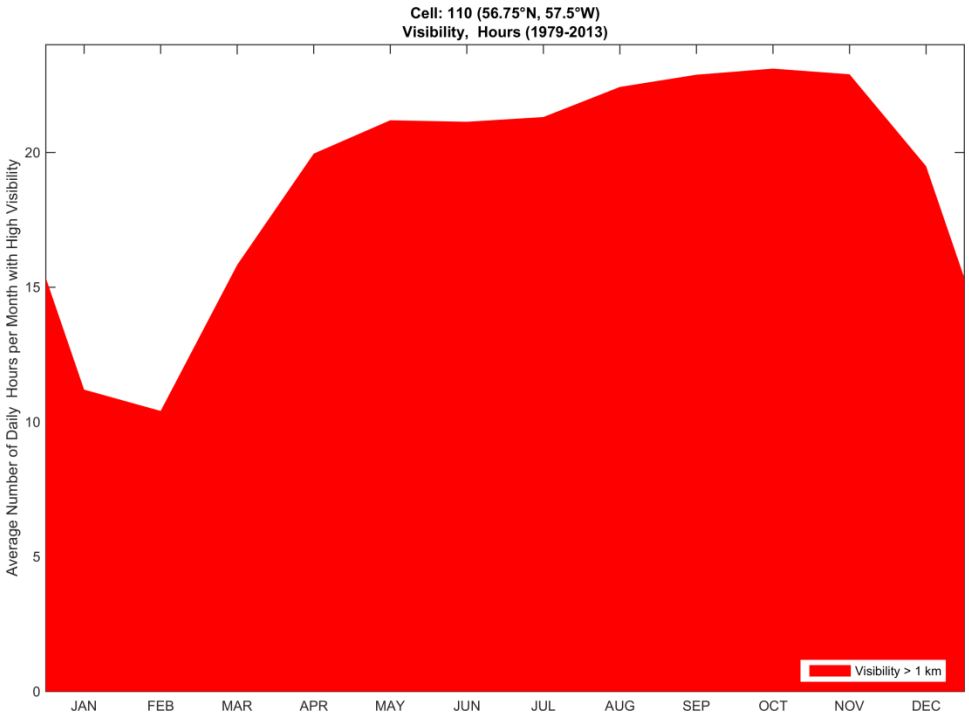

Figure 7-6. Mean daily number of total hours with visibility > 1 km in cell 110

7.3 REGIONAL OVERVIEW

Figure 7-7 to Figure 7-9 show monthly regional trends for percentage of daylight hours with low visibility (< 1 km) for 1979-2013. Regions with low visibility shift from the northern portion of the study area to the south during the year, but are primarily constrained to the areas closer to land, except for the Grand Banks, which is affected spring to fall. In comparison, the deepwater basins in the Labrador Sea are largely unaffected.

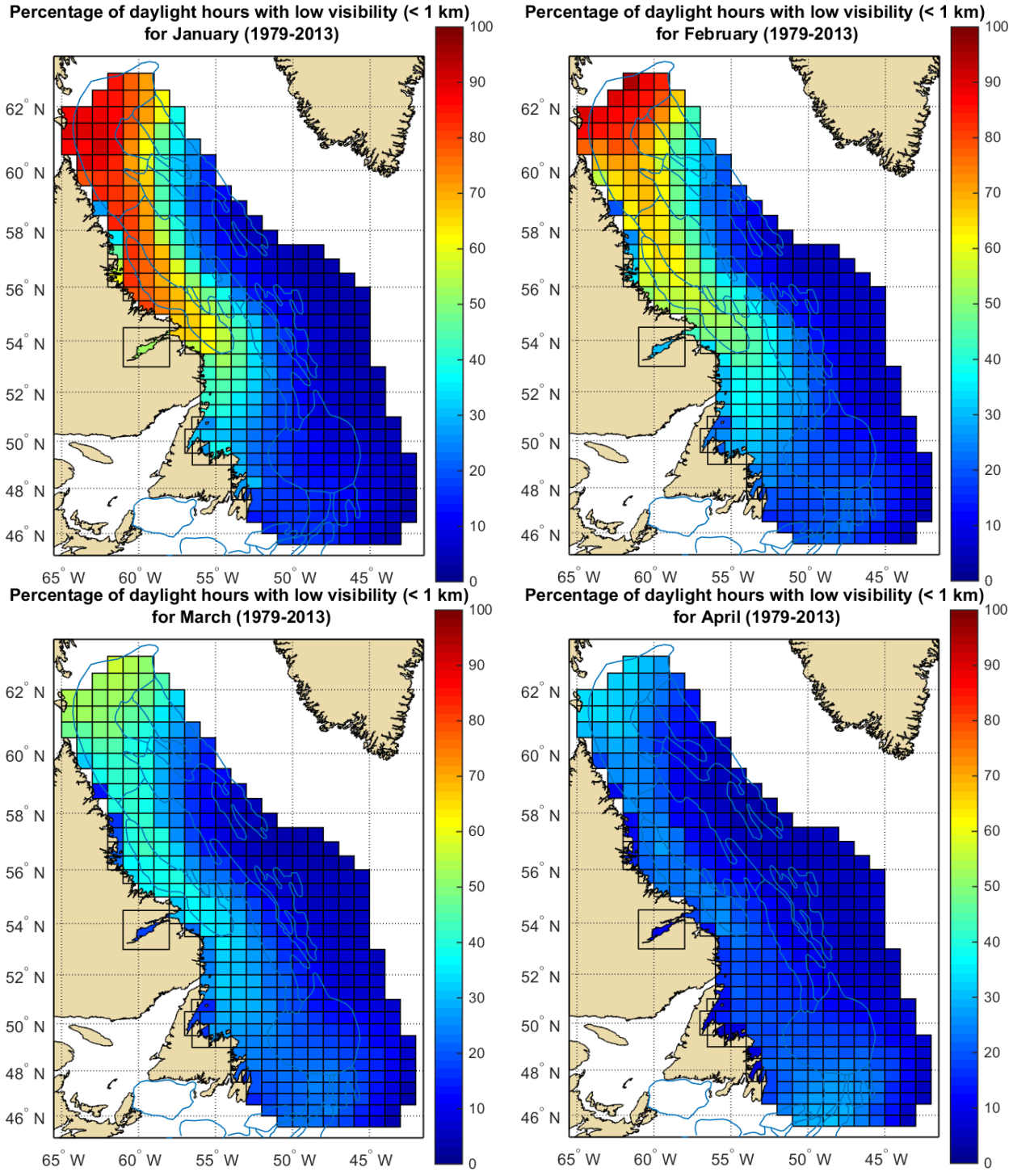

Figure 7-7. Monthly regional trends (January-April) for percentage of daylight hours with low visibility (< 1 km) for period 1979-2013

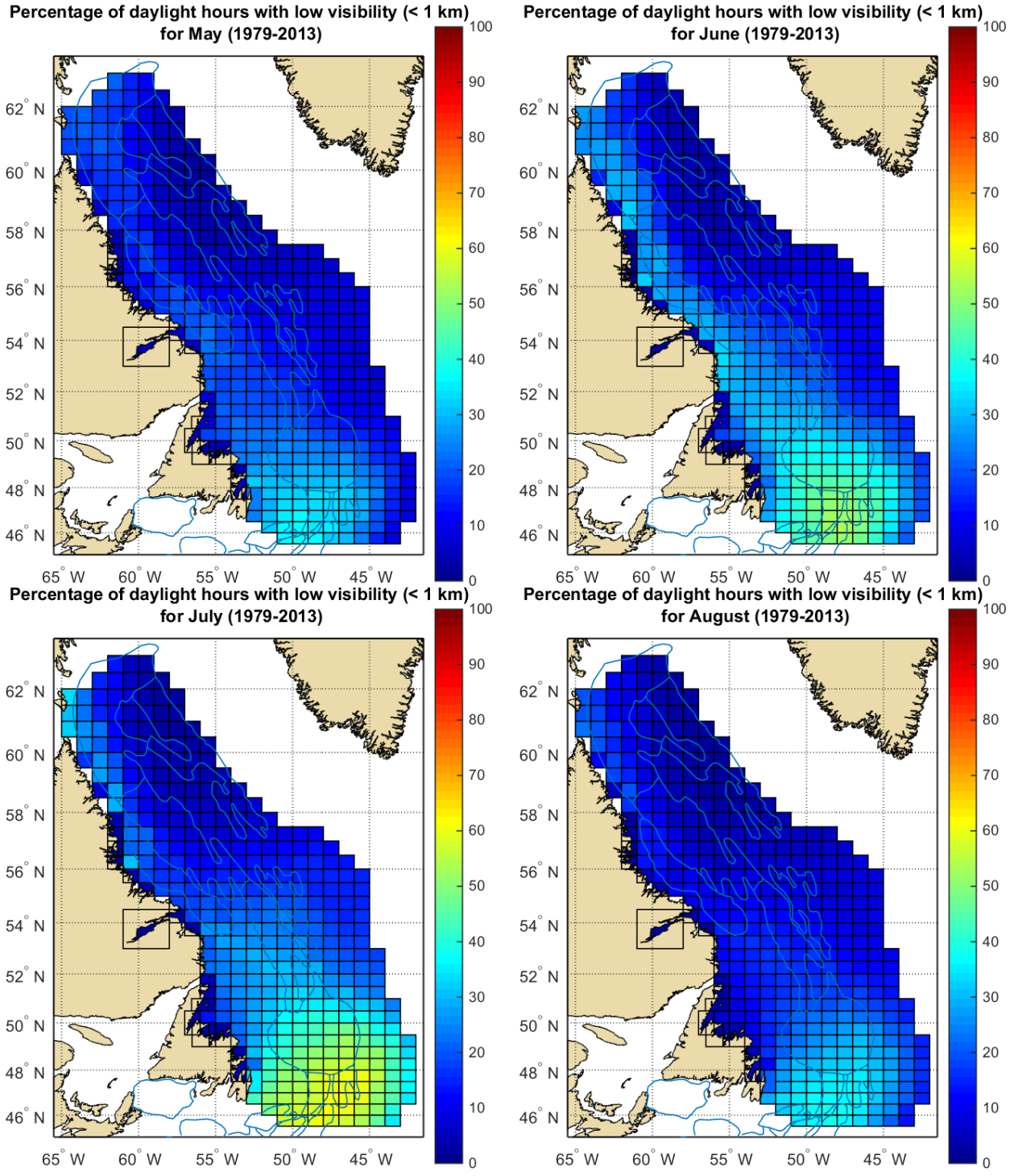

Figure 7-8. Monthly regional trends (May-August) for percentage of daylight hours with low visibility (< 1 km) for period 1979-2013

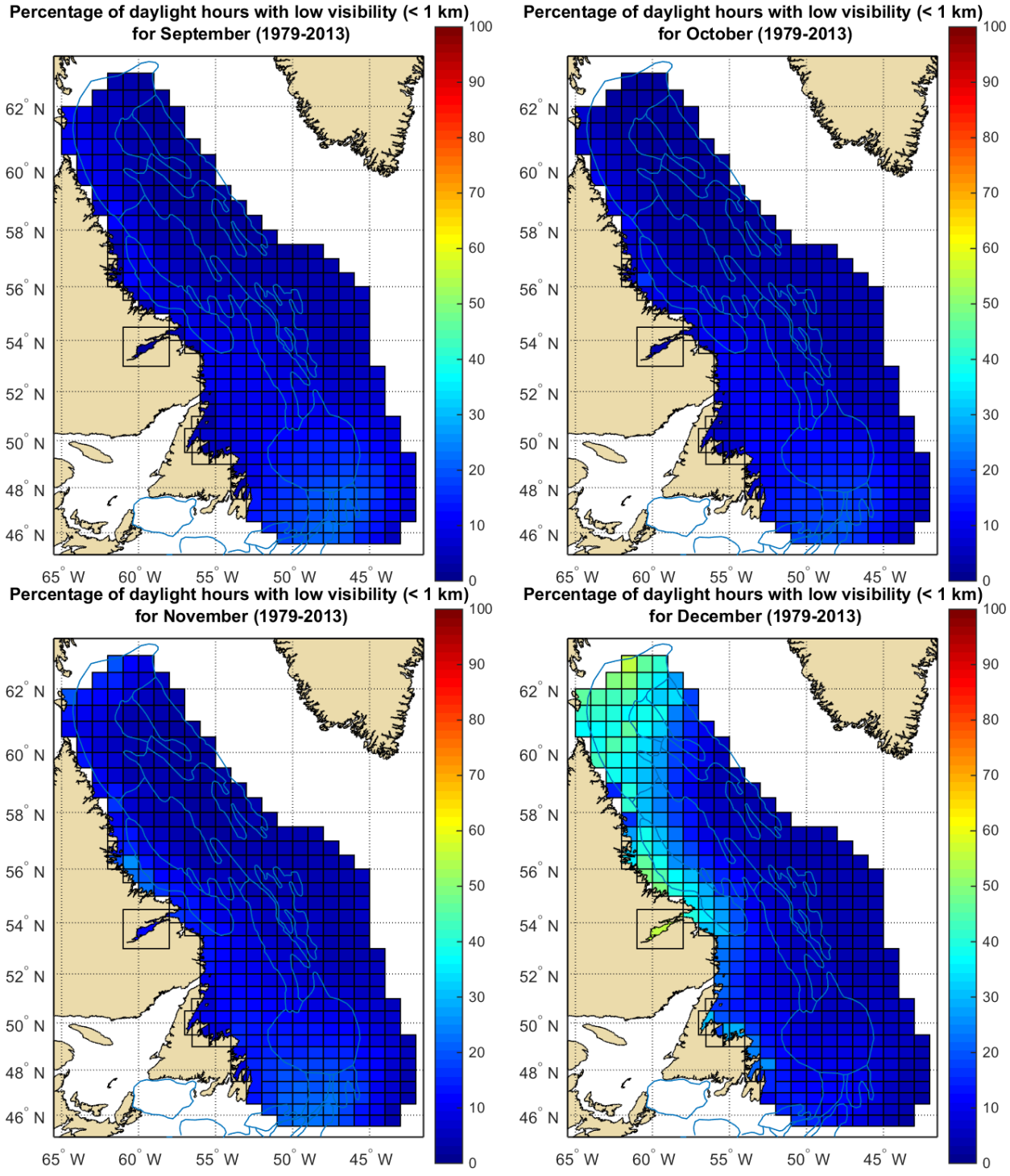

Figure 7-9. Monthly regional trends (September-December) for percentage of daylight hours with low visibility (< 1 km) for period 1979-2013

7.4 REFERENCES

Stolinga, M.T. and T.T. Warner (1999). "Nonhydrostatic, mesobeta-scale model simulations of cloud ceiling and visibility for an East Coast winter precipitation event." Journal of Applied Meteorology. Volume 38: pp. 385-404.

Toth, G., Gultepe, I., Milbrandt, J., Hansen, B., Pearson, G., Fogarty, C. and W. Burrows (2011). The Environment Canada Handbook on Fog and Fog Forecasting. Environment Canada Monograph En56-231/2010, 117 pp.

Metocean Climate Study
Offshore Newfoundland & Labrador

STUDY MAIN REPORT
Volume 1: Chapter 8 – Pack Ice

Prepared for:
Nalcor Energy Oil and Gas

Prepared by:
C-CORE

Reviewed & Edited by:
Bassem Eid, Ph.D.

May 2015

CHAPTER 8 – PACK ICE

TABLE OF CONTENTS

LIST OF FIGURES

LIST OF TABLES

LIST OF ACRONYMS

CD	Consecutive Days
BIO	Bedford Institute of Oceanography, Department of Fisheries and Oceans
CIS	Canadian Ice Service, Environment Canada
GIS	Geographic Information System
IIP	International Ice Patrol
MANICE	Manual of Standard Procedures for observing and Reporting Ice Conditions
MSC	Meteorological Services of Canada (formerly Atmospheric Environment Services (AES))
ND	No Data
NIC	U.S. National Ice Center
OWS	Open Water Season
ULS	Upward Looking Sonar
WMO	World Meteorological Organization

8 PACK ICE

8.1 DATA SOURCE

The size of the study area, as presented in Figure 8-1, required that data for the sea ice (pack ice) analysis be acquired from two sources: Canadian Ice Service (CIS) and the U.S. National Ice Center (NIC). The majority of data was acquired from CIS databases, with NIC databases filling in gaps when available. These databases are primarily based on the analysis of satellite imagery. Within the CIS and NIC databases there are multiple regions providing pack ice data for portions of the study area. Five regions were selected, two from CIS and three from NIC, to provide the most comprehensive coverage of the study area.

The Hudson Bay and East Coast CIS charts were used as the primary sources for the pack ice analysis. The coverage of both regions is shown in Figure 8-1, as well as the overlap between the two regions. For the NIC coverage, data from the South West Greenland Sea, Davis Strait, and Labrador Sea regions were used to provide data for the 15 plus cells toward the northeast not fully covered by CIS, as indicated in Figure 8-1. The NIC charts, unlike CIS, have no overlap and are therefore grouped together as one.

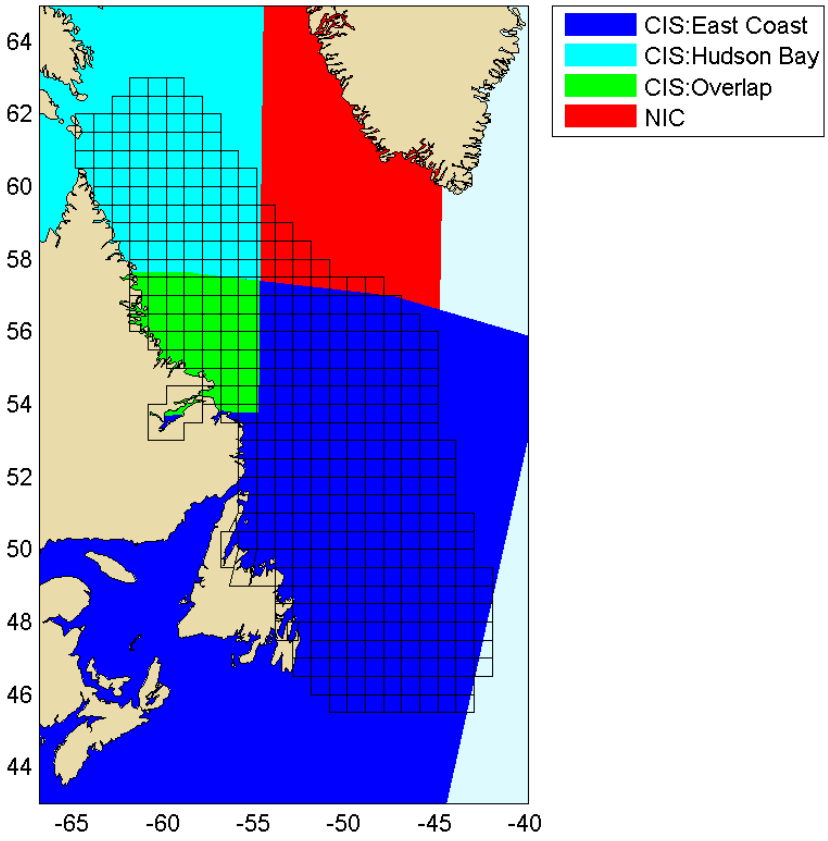

Figure 8-1. CIS and NIC coverage areas

Pack ice data from January 1, 1984 to December 31, 2013 were collected from both data sources according to data availability. The availability of data over the last 30 years varies within each region, as shown in Figure 8-2, ranging from more than 30 years to as few as eight years. The Hudson Bay region has data for all 30 years over its entire coverage area. The coverage of the East Coast region expanded in 1997, and while the majority of this region has data available for more than 30 years, a portion of the region along the northern and eastern perimeter has only 17 years of data, as shown in Figure 8-2.

In the years before the 1997 expansion, ice features extending beyond the coverage area were generally documented by the use of chart inserts; an example of such coverage is shown in Figure 8-3. The South West Greenland Sea and Davis Strait regions have eight years of data coverage, while the Labrador Sea region has 17 years of data. As a result over 98 percent of the study area has data coverage spanning 17 or more years, less than two percent having coverage for eight years, and only about 0.5% of the study area had no available data.

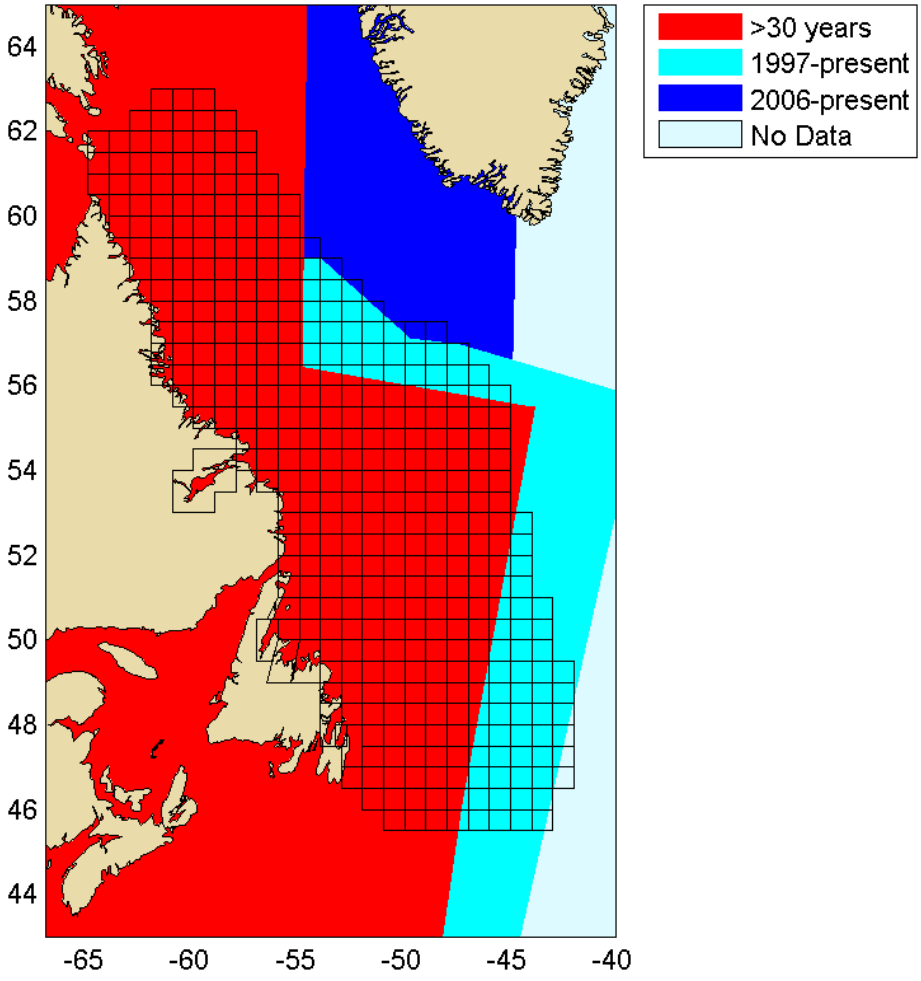

Figure 8-2. Temporal coverage of CIS and NIC data

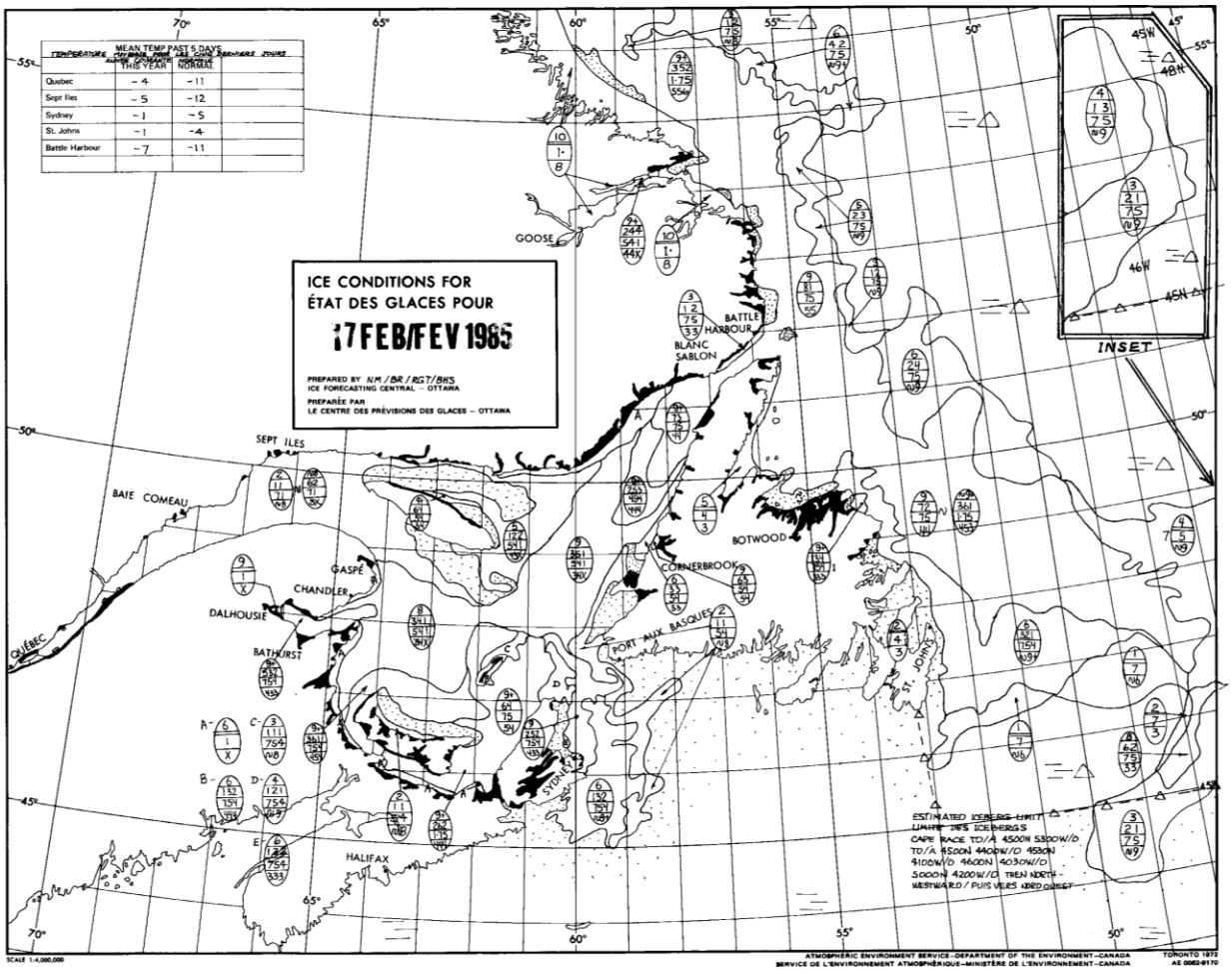

Figure 8-3. Example CIS ice chart showing expanded coverage

Within the NIC archives, ice charts are only available on a weekly basis. However, within the CIS archives, data are available in two formats: weekly regional charts and daily charts. The weekly regional charts are usually produced at weekly intervals during the ice season, with a reduction in frequency during the open water season (OWS). During the period of 1984-2013, the Hudson Bay and East Coast regions averaged 37 and 31 charts per year respectively. An example of a typical weekly regional chart is shown in Figure 8-3. The daily charts are usually produced on a daily basis and cover only a fraction of the area covered by the weekly charts.

The weekly regional charts are produced based on an amalgamation of daily ice charts. The regional charts cover a much larger geographical area as demonstrated in Figure 8-3 and Figure 8-4. As a result of this larger scale, some of the detail contained within the daily charts cannot be included. Additionally, due to limitations in data availability, such as polar orbit frequency of satellites, complete coverage of the region is not possible on a single day. Images collected since the previous regional chart are used to create the next regional chart and now-casting is used to predict ice drift, deterioration, and growth to estimate the ice conditions at the date of the next regional chart. The temporal resolution of the regional charts prevents them from capturing the daily fluctuations in ice coverage, which are present

on daily charts. These daily fluctuations are most prominent at the ice edge; consequently, when investigating regions near the ice edge, one should expect to observe variations between regional and daily charts. While daily charts offer some advantages regarding capturing ice movement over a shorter period of time, weekly charts have been used in the pack ice analysis for two main reasons. First, regional charts are used because daily charts are not available in a GIS-compatible format, and one would require a manual digitization of the charts for analysis. Second, regional charts are available over a much longer time frame, thus enabling a more thorough investigation of pack ice changes over time.

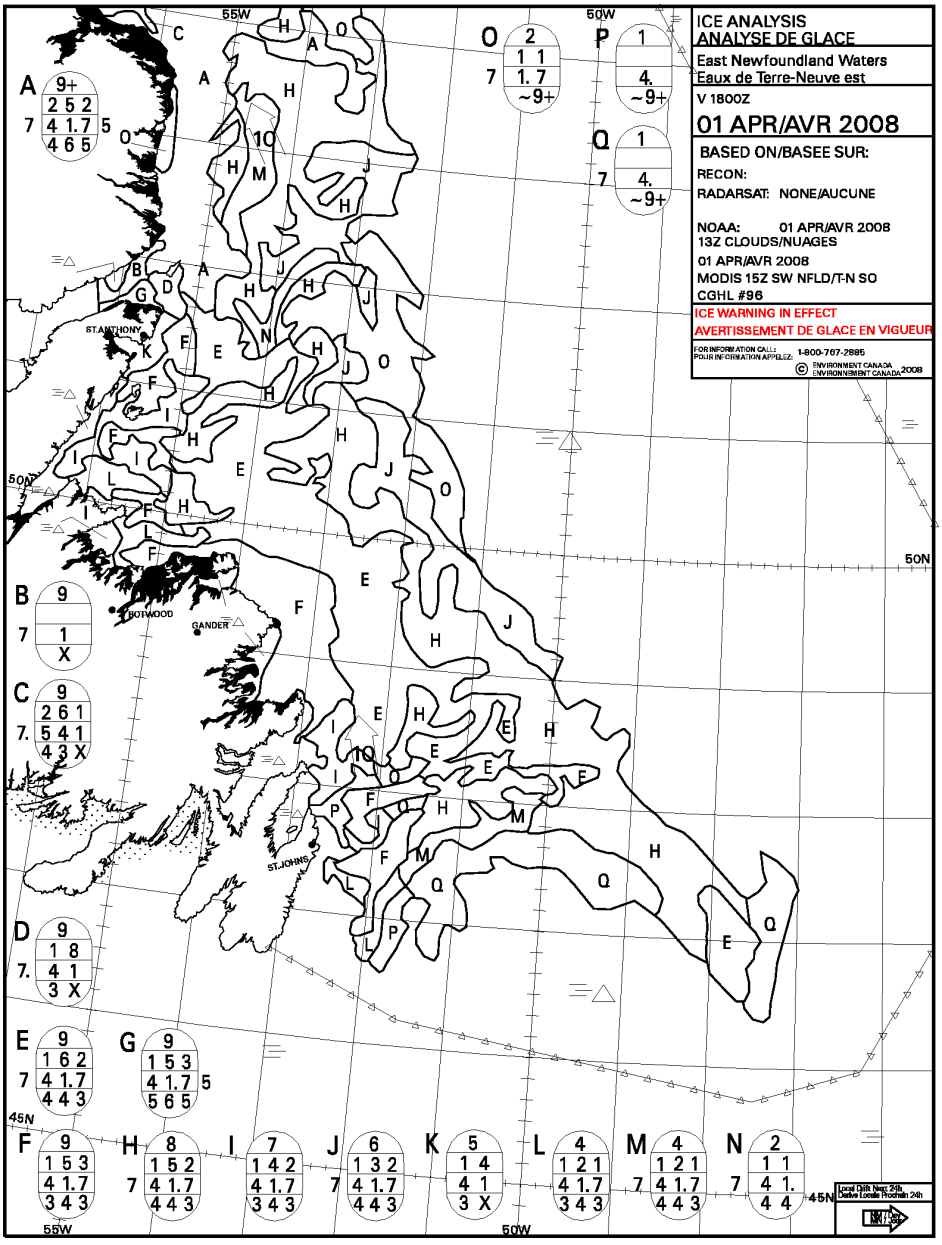

Figure 8-4. Example CIS ice chart showing coverage of daily chart

8.2 DATA PROCESSING

For processing the pack ice data, each study area cell (generally 0.5° latitude by 1° longitude) was segmented into 25 individual grid squares (a 5x5 grid) with each grid square measuring approximately 0.125° latitude by 0.25° longitude. Data were first analyzed on the grid square level and the resultant from each grid square was then processed to obtain results for the cell as a whole. The method of processing was dependent on the data being analyzed.

8.2.1 Time Periods

The data were processed over the following three time periods: 1984-1993, 1994-2003 and 2004-2013. Ice conditions over the last 10 years are of particular interest, as they provide insight into recent ice conditions. Acquiring data from the past 30 years provides opportunity to analyze trends over time, and the analysis can serve as the basis for estimating future ice conditions. Using 10-year windows is considered an appropriate time span to present any possible changes in ice conditions over the past 30 years.

8.2.2 Data Blending

The application of multiple data sources results in areas of overlapping data. Overlapping data occurs when there are overlapping regions within the same source (Hudson Bay [CIS] and East Coast [CIS]), and between sources (Hudson Bay [CIS] and Labrador Sea [NIC]). As to be expected, data within the areas of overlap between CIS and NIC regions do not necessarily mesh properly, resulting in two data points for the same geographic location. Similarly, data within the area of overlap from the Hudson Bay and East Coast regions also result in two data points for the same geographic location. To arrive at a single data point within the areas of overlap requires a blending of data between the two regions.

Data are blended based on a weighted percentage assigned to each cell or group of cells, based on the cell location within a given region. Figure 8-5 displays the weighted percentages employed in the blending of CIS-CIS and CIS-NIC data.

The Hudson Bay and East Coast regions result in an area of overlap spanning approximately from 54.5°N to 57.4°N and extending from the coast of Labrador to approximately 55°E (see Figure 8-2). Typically, the blending of data within this area of overlap is achieved through one of five weightings: 100/0, 67/33, 50/50, 33/67, 0/100, as shown in Figure 8-5.

The available coverage of the NIC data is quite vast, covering the majority of all cells north of 52°N. However, when available, CIS data are given priority, and NIC is primarily used to acquire data for cells outside of the CIS coverage, as shown in Figure 8-1. To help eliminate the possibility of forming sharp transition zones between CIS and NIC coverage, cells next to the NIC region were blended using a 50/50 weighting. All other cells with overlapping NIC/CIS data were weighted as 100% CIS.

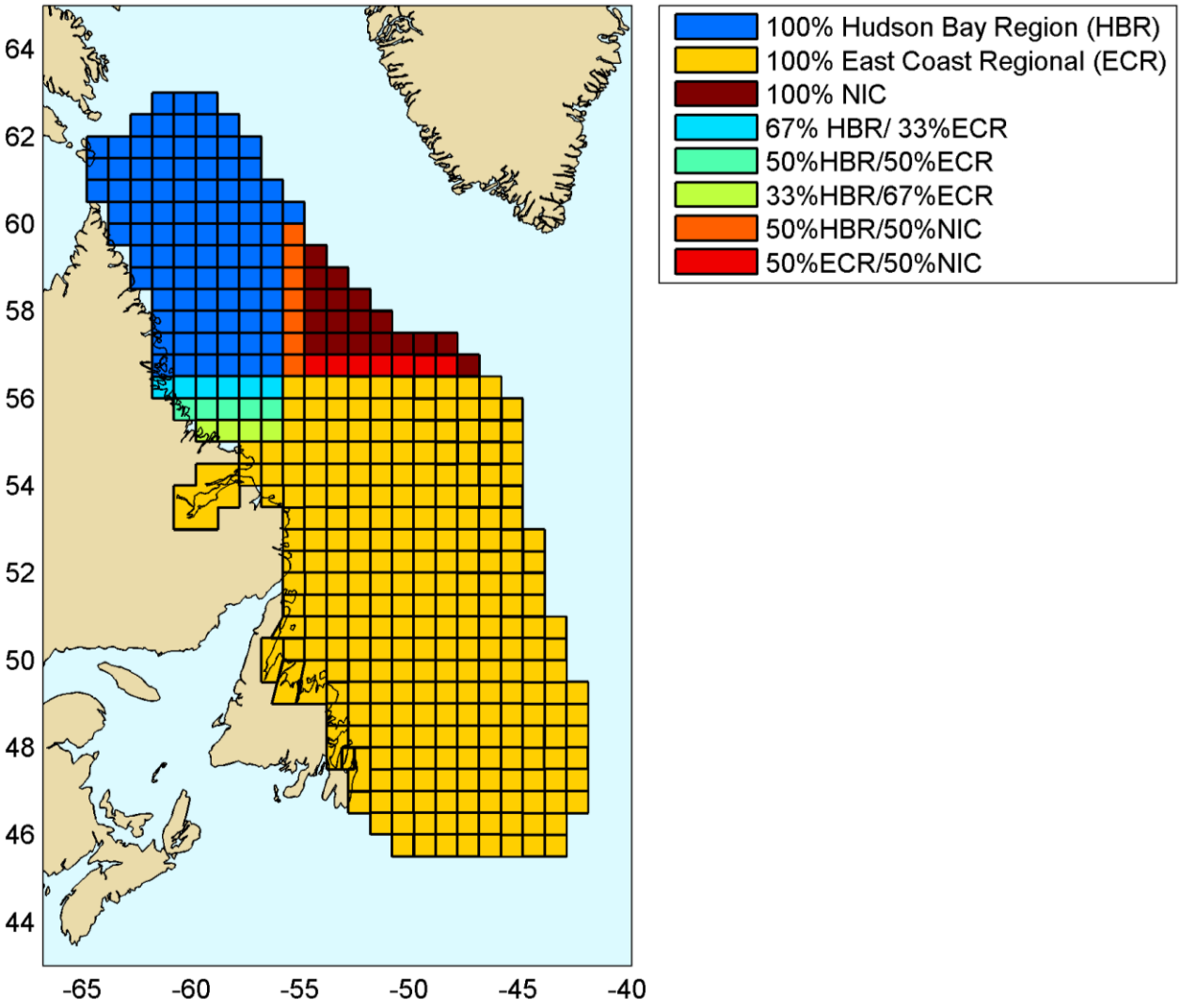

Figure 8-5. Blending scheme for each grid cell

8.2.3 Data Interpolation

Sea ice data for each cell were based on available ice charts from CIS and NIC, generally ranging from zero to four or five charts per month. Generally, months without an ice chart indicate no ice was present. Unprocessed sea ice data are available on an intermittent basis for each cell with the study area. These intermittent concentration data were taken and interpolated over the entire 1984-2013 time period to provide a concentration data point for each day within the 30-year time period. These interpolated data were calculated for each grid square within a given cell, with the cell as a whole being derived from the mean of individual grid squares.

8.2.4 Missing or Non-Applicable Data

The availability of data varies from cell to cell and from year to year. As shown in Figure 8-2, there are a number of cells in which no data (ND) exist during the 1984-2003 time period. As discussed in Section 8.1, ice features extending beyond the pre-1997 chart boundary within the East Coast region were generally covered by the use of chart inserts; however, it is still unknown if ice features wholly defined outside the pre 1997 boundary were documented. Any cells not covered by either an NIC or CIS chart were considered to have no data available for that given date. Cells which are missing data from one or time periods will likely have many figures and tables with entries recorded as No Data or the abbreviation ND. The use of ND can also be applied to data that are not applicable or unusable. Three examples of such unusable or non-applicable data are:

1. ***Mean concentration when present:*** When calculating the mean concentration (when present) of ice exceeding a given threshold, it is possible that no ice exists in concentrations above the selected threshold. For instance, if no ice was recorded over one tenth for a given location, recording the mean concentration for ice ≥ 1/10th as zero tenths seems illogical and therefore such occurrences are recorded as ND (see Table 8-2 for an example).
2. ***Break-up/Freeze-up dates:*** If no ice is present during a given year, the break-up and freeze-up dates for that year would be undefined and therefore would be recorded as ND, as shown in Table 8-4.
3. ***Percentile calculation:*** The calculation of percentiles is based on a ranking of the values associated with a given variable, such as break-up, and are generally calculated over each of the 10-year periods. To provide valuable and meaningful percentile values, any variable on which a percentile is to be based must have a recorded value for each year within the 10-year period, or the percentile is recorded as ND (see Table 8-6).

8.2.5 Pack Ice Background Information

Pack ice information within the CIS and NIC databases are presented using the standard World Meteorological Organization (WMO) code, known as the Egg Code. Within the Egg Code, there are 14 classes or types of pack ice, ranked according to the thickness and age of the ice. These 14 ice types are presented in Table 8-1, ranking from lightest to heaviest.

The analysis of pack ice conditions presented in this report often involves segmenting the types of pack ice into two groups. The first group All Ice includes all 14 types of ice from new ice to multi-year ice. The second group is Old Ice and refers to only the types of ice which have survived at least one melt season, therefore consisting of Old Ice, Second-Year Ice, and Multi-Year Ice as defined in Table 8-1. It should be noted that any occurrences of Old Ice recorded in this report are referring to ice features which have drifted into the study area from further north. All regions of the study area were found to be clear of ice at some point during each of the 30 years studied.

Table 8-1. Pack ice type designations

	Ice type
Lightest	New Ice
	Nilas, Ice rind
	Young Ice
	Grey Ice
	Grey-White Ice
	First-Year Ice
	Thin First-Year Ice
	First Stage Thin First-Year
	Second Stage Thin First-Year
	Medium First-Year Ice
	Thick First-Year Ice
	Old Ice
	Second-Year Ice
Heaviest	Multi-Year Ice

8.2.6 Open Water Versus Ice Free

The term open water, as used within this report, refers to waters in which the concentration of ice is less than one tenth. Conversely, ice free refers to waters in which NO ice is present. As discussed in Section 8.2.2, there is often disagreement between ice charts from different sources and even from different regions within the same source. The CIS commonly uses both the open water and ice free designations within its ice charts, resulting in a distinct line of all known ice, outside of which is open water. The NIC however does not use the open water designation, and instead labels most concentrations that are less than one tenth as ice free. Additionally, due to the large geographic areas covered by the both the CIS and NIC ice charts and bearing in mind that no method of detection performs with 100% accuracy, it is reasonable to assume that some small fragments or trace amounts have gone undetected. For this reason, any areas specified as open water, in particular those regions within NIC coverage including the buffer zones between NIC and CIS, may contain trace amounts of ice. Furthermore, when plotting pack ice concentrations, it is possible to see variations between open water and ice free within a given cell, in particular for cells near the buffer zone between CIS and NIC coverage.

8.3 Pack Ice Analysis for Study Area Cells

Pack ice analysis was performed on a cell-by-cell basis for each of the 391 study area cells. The pack ice analysis provides a number of key characteristics of the pack ice conditions and trends within each cell. These key characteristics generally fit into one of the following categories:

A. Pack ice summary, including
    - Mean and max concentration (when present)
    - Dominant ice type
    - Probability of encountering ice
B. Concentration and probability summaries
C. Concentration time series
D. Break-up/ freeze-up dates and corresponding OWS
E. Number of open water days
F. Probability of open water
G. Number of weeks with ice
H. Occurrence of fast ice.

These key characteristics are presented using an assortment of tables and figures for each individual cell. Where practical, this report uses Cell 110 to provide an example of these various figures and tables used in defining the pack ice conditions of each cell.

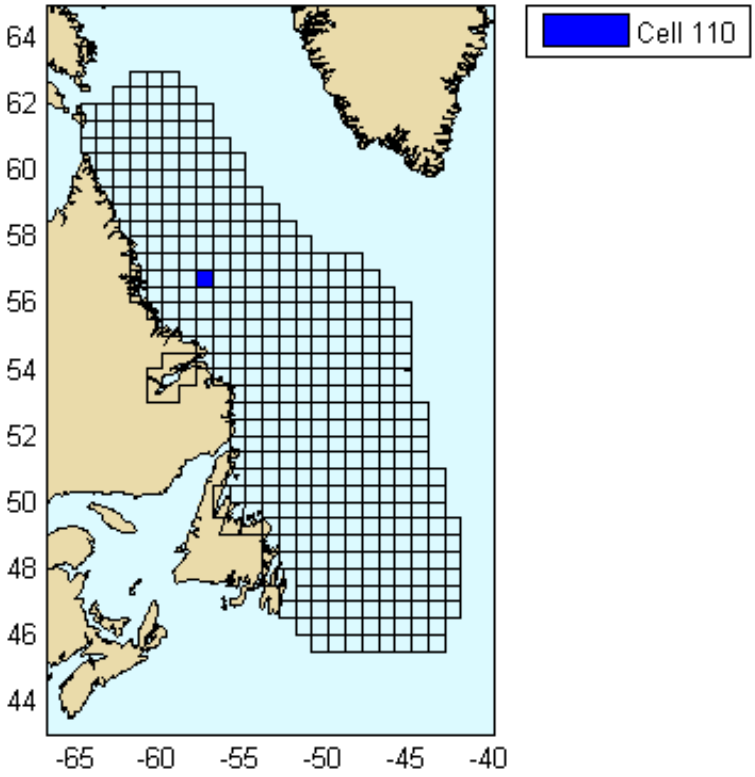

Figure 8-6. Location of sample cell (Cell 110)

8.3.1 Pack ice summary

The pack ice summary provides a monthly summary of mean and maximum concentration, dominant ice type and probability of encountering ice, for each cell during each of the 1984-1993, 1994-2003, and 2004-2013 study periods.

8.3.1.1 Pack ice concentration (when present)

The mean pack ice concentration, when ice is present, was calculated for each month from 1984-2013, with each year calculated independently. In this case when present refers to ice concentrations greater than or equal to one tenth. As a result, concentrations less than one tenth are not included in the calculation of mean concentrations. Unless explicitly stated, all future references to the mean concentration are referring to the mean when ice is present. The mean concentration for a cell was derived from the aggregate mean of each individual grid square within the cell. Mean monthly concentrations were then calculated for each of the three time periods, 1984-1993, 1994-2003, and 2004-2013. The maximum concentrations for each cell were calculated in a similar manner. Mean and maximum concentrations were plotted for each cell and month, as shown in Figure 8-7.

8.3.1.2 Dominant ice type

The dominant ice type was defined as the ice type with the largest concentration within a given region. Dominant ice type was calculated on a monthly basis for each grid square within a cell, based on the mean concentrations of each ice type. The dominant ice type for each grid square was defined as the ice type with the largest concentration in that square. Dominant ice type was calculated for each month over the three time periods discussed previously, as shown in Figure 8-7.

8.3.1.3 Probability of encountering ice

The probability of encountering sea ice was calculated on a monthly basis, for each of the 10-year time periods, and the calculation provides an indication as to how many years had ice for at least one day during a given month. For example, a 90% probability of ice indicates that nine out of 10 years had at least one day with ice in that given month. The probability of ice was calculated for each month over the three time periods discussed previously, as shown in Figure 8-7.

The interpolated concentration data were used when calculating the probability of encountering sea ice. Interpolated data provide more gradual changes between adjacent charts compared with the step pattern associated with the intermittent data. When concentrations vary sharply between consecutive charts bridging adjacent months, using interpolated data should result in more conservative probability values. For example, consider a chart on May 31 that presents sea ice with a concentration of three tenths, while the following chart on April 7 has no ice. Using the intermittent data, no ice of concentration greater than one tenth would be recorded for April, while in reality it is highly likely there was sea ice greater than one tenth for at least one day during April. Therefore, the interpolated concentration data will generally result in slightly higher probabilities when compared with the intermittent data.

The probability of encountering ice was calculated for two groupings of ice types. The first group *All Ice* includes all ice types from new ice to multi-year ice. The second group is *Old Ice* and refers to ice types that have survived at least one melt season. These old ice types fall under the category of *Old Ice, Second-Year Ice*, *or Multi-Year Ice* as defined in Table 8-1.

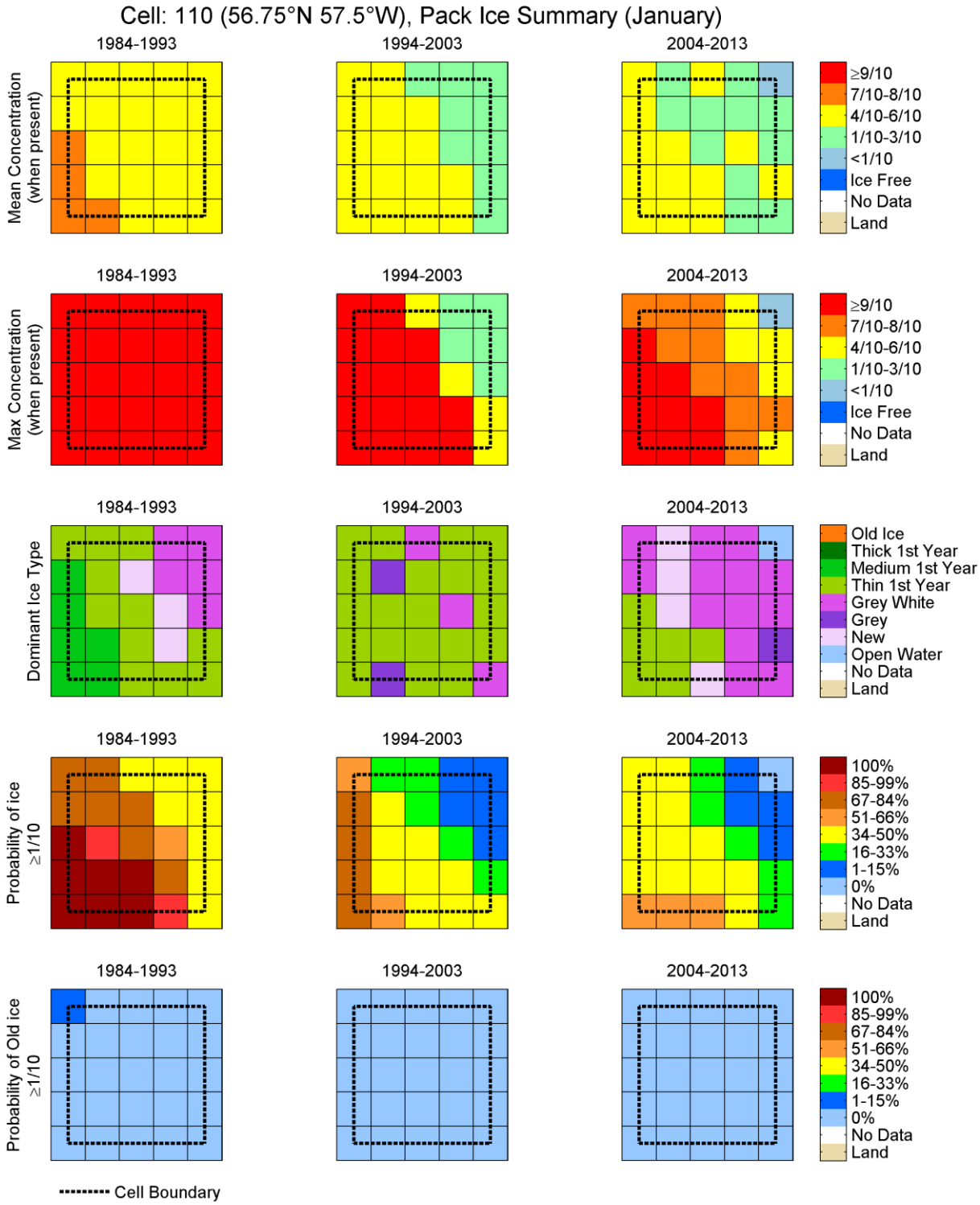

Figure 8-7. Example of pack ice summary plot (Cell 110: January)

8.3.2 Concentration and Probability Summaries

A concentration summary table, as shown in Table 8-2, was generated to help provide a quick overview of each cell. Each table includes mean concentration when present for both *All Ice* and *Old Ice* types. Additionally, calculations were performed by filtering the data according to two separate thresholds for concentrations greater than or equal to one tenth and greater than or equal to six tenths. Similarly a probability of encounter summary table, as shown in Table 8-3, was generated for each cell. Probabilities of encounter were calculated for *All Ice* and *Old Ice* types for concentrations greater than or equal to one and six tenths.

Table 8-2. Example of mean concentration when present (Cell 110)

Cell: 110 56.75°N 57.5°W	Pack Ice: Mean concentration when present											
	All Ice ≥1/10			All Ice ≥6/10			Old Ice ≥1/10			Old Ice ≥6/10		
	1984-1993	1994-2003	2004-2013	1984-1993	1994-2003	2004-2013	1984-1993	1994-2003	2004-2013	1984-1993	1994-2003	2004-2013
January	6	4	4	8	7	7	1	ND	ND	ND	ND	ND
February	6	4	4	8	7	7	1	ND	ND	ND	ND	ND
March	5	4	4	9	7	7	1	ND	ND	ND	ND	ND
April	6	3	3	9	7	7	ND	1	ND	ND	ND	ND
May	5	3	4	8	7	7	2	1	1	ND	ND	ND
June	3	2	3	7	7	7	2	1	1	ND	ND	ND
July	3	2	2	7	ND	ND	2	1	ND	ND	ND	ND
August	ND	ND	ND	ND	ND	ND	ND	ND	ND	ND	ND	ND
September	ND	ND	ND	ND	ND	ND	ND	ND	ND	ND	ND	ND
October	ND	ND	ND	ND	ND	ND	ND	ND	ND	ND	ND	ND
November	ND	ND	ND	ND	ND	ND	ND	ND	ND	ND	ND	ND
December	4	ND	3	7	ND	8	ND	ND	ND	ND	ND	ND

Table 8-3. Example of probability of encounter (Cell 110)

Cell: 110 56.75°N 57.5°W	Pack Ice: Probability of encounter											
	All Ice ≥1/10			All Ice ≥6/10			Old Ice ≥1/10			Old Ice ≥6/10		
	1984-1993	1994-2003	2004-2013	1984-1993	1994-2003	2004-2013	1984-1993	1994-2003	2004-2013	1984-1993	1994-2003	2004-2013
January	1	0.8	0.6	1	0.5	0.4	0.1	0	0	0	0	0
February	1	0.9	0.8	1	0.8	0.7	0.2	0	0	0	0	0
March	1	0.7	0.8	0.8	0.5	0.8	0.1	0	0	0	0	0
April	0.9	0.8	0.9	0.7	0.4	0.7	0	0.1	0	0	0	0
May	0.9	0.7	0.8	0.7	0.4	0.7	0.2	0.1	0.1	0	0	0
June	0.9	0.6	0.6	0.7	0.1	0.2	0.3	0.1	0.1	0	0	0
July	0.4	0.4	0.2	0.2	0	0	0.3	0.1	0	0	0	0
August	0	0	0	0	0	0	0	0	0	0	0	0
September	0	0	0	0	0	0	0	0	0	0	0	0
October	0	0	0	0	0	0	0	0	0	0	0	0
November	0	0	0	0	0	0	0	0	0	0	0	0
December	0.8	0	0.3	0.6	0	0.1	0	0	0	0	0	0

Mean concentration when present values recorded as ND corresponding to probability of encounter of zero percent indicates that no ice was present in concentrations greater than or equal to the given threshold for the time period in question. Probabilities of encounter recorded as ND indicated no data was available during the time period in question.

8.3.3 Pack Ice Concentration Time Series

A time series plot of pack ice concentration when present, as shown in Figure 8-8, was generated for each cell, and provides a quick overview of pack ice behavior throughout the calendar year for the 30-year study period. The time series plot was generated using the interpolated concentration values.

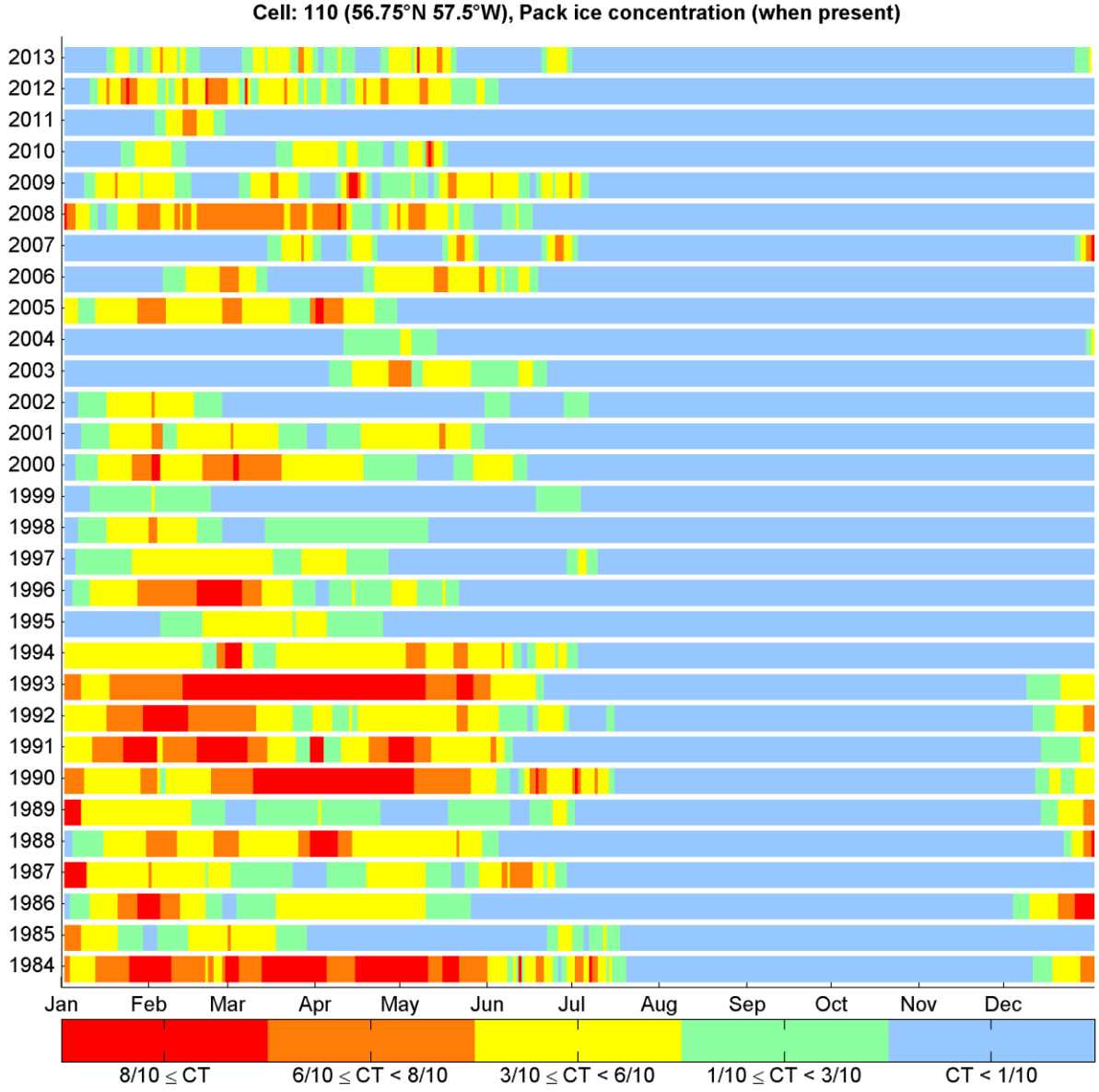

Figure 8-8. Example of pack ice concentration time series (Cell 110)

8.3.4 Open Water Season, Break-Up and Freeze-Up

The break-up and freeze-up dates, as defined in this report, are selected based on the time frame with the most consecutive charts indicating sea ice concentrations less than one tenth. This time frame is referred to as the open water season (OWS). In any given year, it is possible for ice with concentrations greater than one tenth to re-enter a region in which the concentration had previously been less than one tenth. This re-entry is referred to as an ice incursion. The occurrence of an incursion event results in a freeze-up (see point End OWS in Figure 8-9), and when this ice incursion recedes a break-up has occurred, see point Start OWS2 in Figure 8-9. In this manner, it is possible to have multiple OWSs in any given year. The break-up and freeze-up dates are considered to be the start and end dates, respectively, for the longest OWS in a given year. In the example provided in Figure 8-9, OWS2 would have been assigned as the OWS for this location, with break-up occurring at Start OWS2 and freeze-up occurring at End OWS2. The data in Figure 8-9 were generated to present the concept of multiple OWSs and are not necessarily representative of sea ice conditions at any point within the study area.

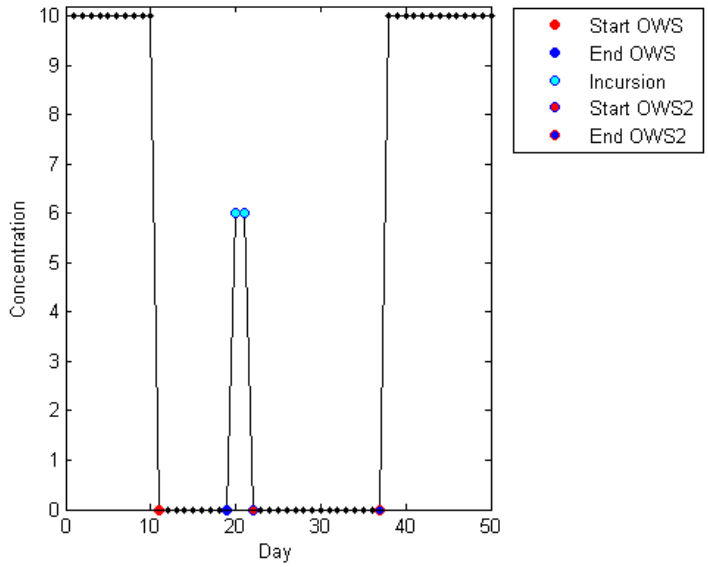

Figure 8-9. Example of OWS and ice incursion

The break-up date does not necessarily imply a decay, or a melt of the ice, but can also indicate a movement of ice out of a particular area. Similarly, the freeze-up date does not necessarily imply a growth of new ice; it can also indicate a movement of ice into a particular area. The break-up and freeze-up dates are calculated for each grid square within a cell. The break-up date for the cell as a whole is selected as the latest break-up date experience by any given grid square. Similarly, the freeze-up date for a given cell is selected as the grid square with the earliest freeze-up date. A sample table including break-up and freeze-up dates with corresponding OWS length are provided in Table 8-4.

Table 8-4. Example of break-up and freeze-up dates (Cell 110)

Cell: 110 56.75°N 57.5°W		Break-up and Freeze-up dates and Open water season length (days)		
		Break-up	Freeze-up	Open Water
Years	1984	Jul 18	Dec 8	143
	1985	Jul 16	Jan 2	170
	1986	May 25	Dec 2	191
	1987	Jun 28	Jan 3	189
	1988	Jun 3	Dec 19	199
	1989	Jul 1	Dec 12	164
	1990	Jul 15	Dec 11	149
	1991	Jun 9	Dec 12	186
	1992	Jul 14	Dec 8	147
	1993	Jun 20	Dec 7	170
	1994	Jul 2	Feb 3	216
	1995	Apr 24	Jan 3	254
	1996	May 20	Jan 4	229
	1997	Jul 9	Jan 5	180
	1998	May 10	Jan 9	244
	1999	Jul 3	Jan 4	185
	2000	Jun 13	Jan 6	207
	2001	May 30	Jan 5	220
	2002	Jul 6	Apr 4	272
	2003	Jun 21	Apr 8	292
	2004	May 12	Dec 28	230
	2005	Apr 29	Feb 5	282
	2006	Jun 18	Mar 13	268
	2007	Jul 2	Dec 24	175
	2008	Jun 15	Jan 7	206
	2009	Jul 6	Jan 20	198
	2010	May 17	Feb 2	261
	2011	Feb 27	Jan 10	317
	2012	Jun 3	Jan 15	226
	2013	Jun 30	Dec 25	178

The ninetieth (P90), fiftieth (P50 or Median), and tenth (P10) percentiles were also generated for break-up, freeze-up, and OWS length over each of the three 10-year time periods. Percentiles were calculated based on a ranking of the data over the time period of interest, with calculations being performed based on sorting the data in ascending order.

Using Cell 110 as an example, Table 8-5 demonstrates how percentiles were calculated based on the sorted data. Each column in Table 8-5 has been sorted independently; the entry of open water days equal to 199 days is not necessarily related to the July 18 break-up or the January 3 freeze-up. Percentiles were only calculated if a break-up and freeze-up event occurred during each of the 10 years within the given time frame; otherwise, the percentiles were recorded as No Data.

Table 8-5. Example of percentile calculation (Cell 110)

Break-up	Freeze-up	Open Water Days
25-May	2-Dec	143
3-Jun	7-Dec	147
9-Jun	8-Dec	149
20-Jun	8-Dec	164
28-Jun	11-Dec	170
1-Jul	12-Dec	170
14-Jul	12-Dec	186
15-Jul	19-Dec	189
16-Jul	2-Jan	191
18-Jul	3-Jan	199

P10
P50
P90

Table 8-6 shows an example of break-up, freeze-up, and OWS length percentiles for Cell 110.

Table 8-6. Example of break-up, freeze-up, and OWS length percentiles (Cell 110)

Cell: 110 56.75°N 57.5°W		Break-up, Freeze-up and Open water season percentiles								
		Break-Up			Freeze-up			OpenWater		
		1984-1993	1994-2003	2004-2013	1984-1993	1994-2003	2004-2013	1984-1993	1994-2003	2004-2013
Percentiles	P10	Jul 16	Jul 06	Jul 02	Dec 07	Jan 04	Dec 25	147	185	178
	P50	Jun 28	Jun 13	Jun 03	Dec 11	Jan 05	Jan 10	170	220	226
	P90	Jun 03	May 10	Apr 29	Jan 02	Apr 03	Feb 05	191	272	178

8.3.4.1 Open Water Season (OWS) Length

Open water season (OWS) length has been defined as the elapsed time between break-up and successive freeze-up, and is a practical means by which to define ice conditions within regions with seasonal freeze-up and break-up. However, not all regions of the study area have seasonal break-up and freeze-up, with ice occurring in some regions less than once in 10 years. The OWS in these regions can span multiple calendar years from three up to 10 years or more, or can even be undefined if no break-up and freeze-up occur during the study period. Tabulated values of OWS and OWS plots for these low ice occurrence regions are often less intuitive and provide little valuable data when compared with years experiencing annual break-up and freeze-up.

Cell 110 is an example of a region experiencing annual break-up and freeze-up events, while Cell 111 has OWS spanning multiple years and helps illustrate these less intuitive tables and plots. An OWS plot for Cell 111 is provided in Figure 8-10, and shows several occurrences of OWS lasting more than 365 days. Years without a data point indicate the OWS from the previous year is still active, and so, no OWS is recorded for that year. In regions with even lower occurrences of ice than Cell 111 (see Cell 146 in Figure 8-11), gaps within the data become even more prominent and the plots become irrelevant.

Additionally, the development of open water trend lines becomes increasingly difficult and the confidence in such trend lines declines as the number of data points decrease. Due to the conflict arising from using OWS length, as previously defined, additional methods were considered to present open water presence within each cell. These additional methods include consecutive days (CD) with open water (yearly) and the number of days with open water (yearly).

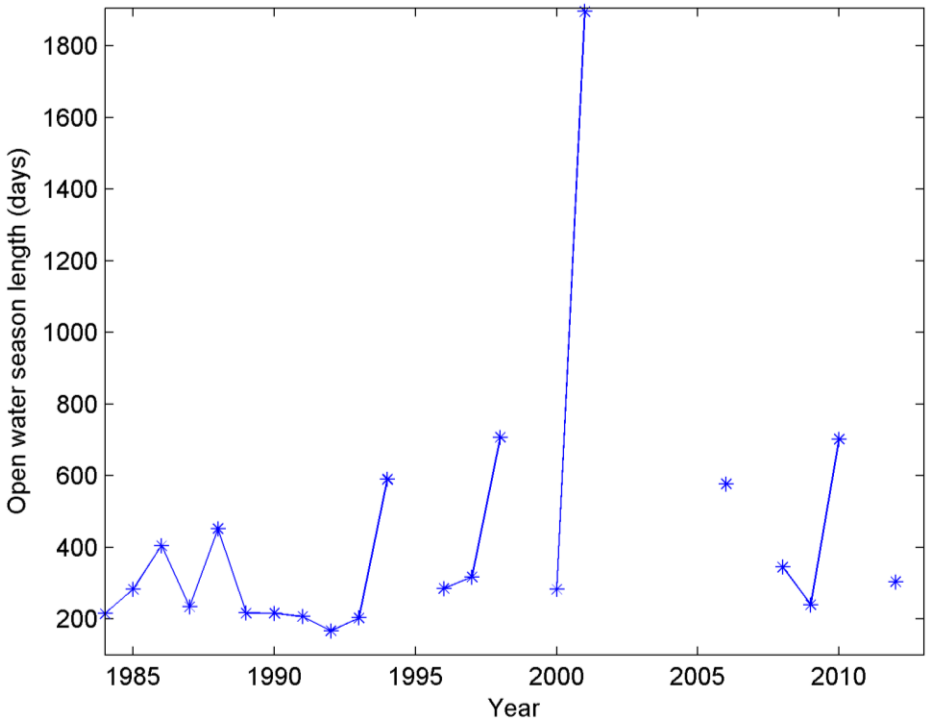

Figure 8-10. OWS length (Cell 111)

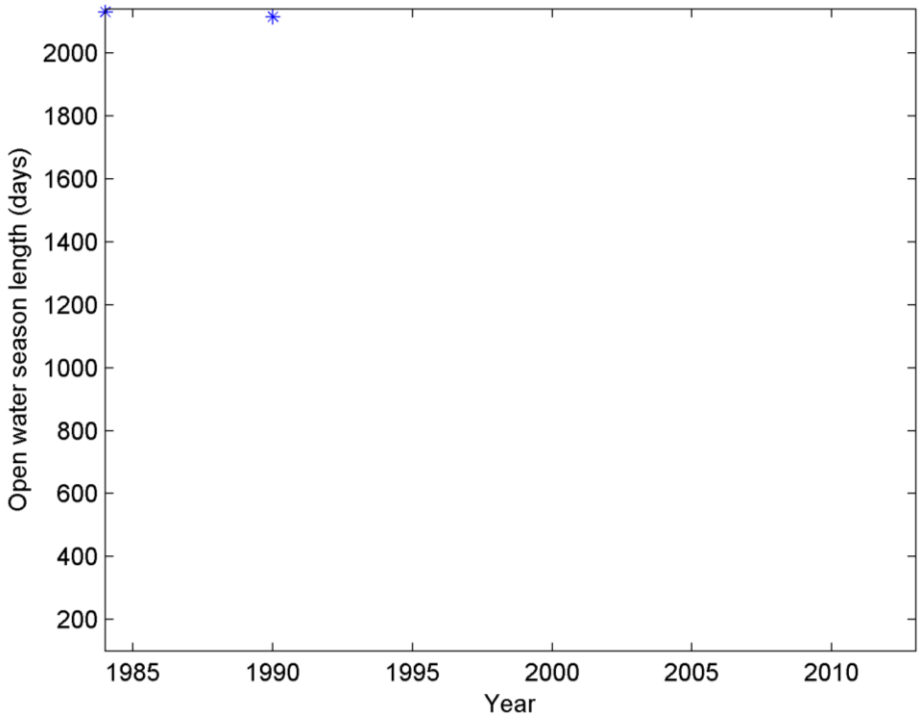

Figure 8-11. OWS length (Cell 146)

8.3.4.2 Consecutive Days (CD) with Open Water

The number of consecutive days (CD) with open water in a given year is dependent on break-up and freeze-up dates, and the relationship between freeze-up and the end of the calendar year. In general, a given year will fall into one of the following categories, which govern how CD with open water is calculated.

Break-up exists: If, in the given year, a break-up exists, the number of CD runs from date of break-up to date of freeze-up, see CD 90 (CD year 1990) and CD 91 in Example A in Figure 8-12. However, if the following calendar year experiences no break-up, the number of CD for CD 90 ends on December 31 (see Year 1991 in Example B and Example C of Figure 8-12).

No break-up exists: If no break-up exists in the given year, CD runs from January 1 to freeze-up (see Year 1991 in Example B and Example C of Figure 8-12). If the following calendar year experiences no break-up, the number of CD for CD 91 is to be capped at 365, or 366 if the year was a leap year (see Year 1992 in Example D of Figure 8-12). Note: the concentrations values presented in Figure 8-12 were generated to show how the calculation of CD can vary depending on ice conditions and are not representative of any region within the study area.

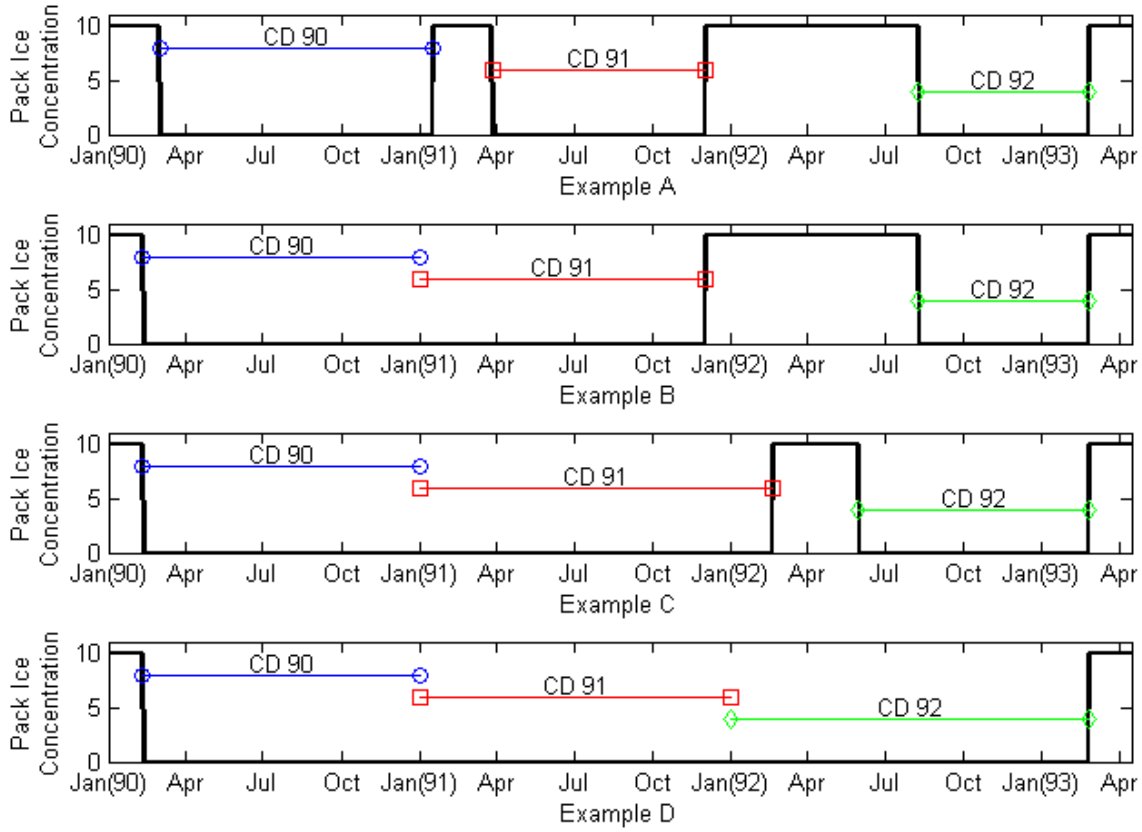

Figure 8-12. Consecutive open water days (examples)

Figure 8-13 provides an example of the use of consecutive open water days for Cell 111. In comparing Figure 8-10 and Figure 8-13, it can be seen that using CD produces a more intuitive plot.

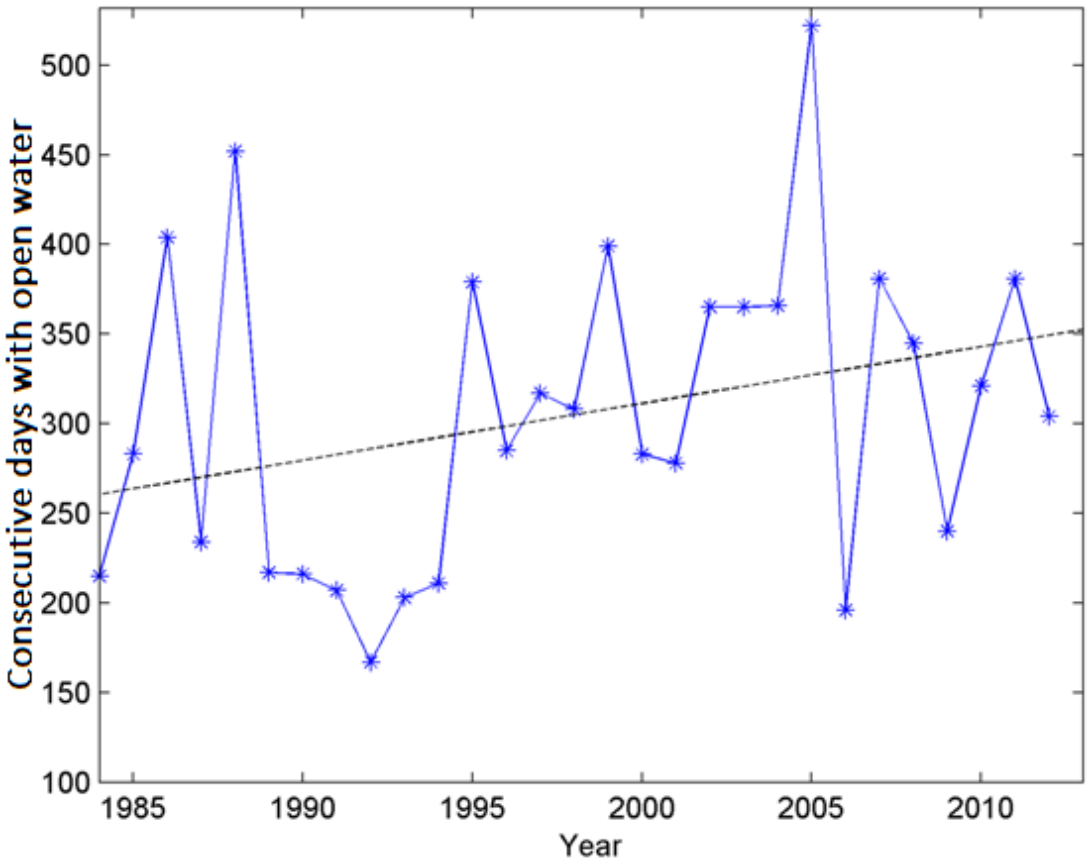

Figure 8-13. CD with open water (Cell 111)

8.3.4.3 Number of days with open water

The number of CD with open water is a very useful tool, and provides a level of detail not present when simply calculating the number of days within a calendar year experiencing open water. However, the number of days with open water is a much simpler calculation, based solely on the number of open water days within a given year, having a maximum of 365 days or 366 days for leap years. An example of the number of days with open water is provided for Cell 111 in Figure 8-14. When developing the set of cell reports detailing the pack ice conditions for each cell, the number of days with open water plot was chosen over the CD with open water for the following reasons:

1. The number of days method requires very little discussion on the calculation process, and as such is less prone to misinterpretation, and
2. Details on each OWS, including break-up and freeze-up dates, along with length of OWS, are available in tables similar to Table 8-4 for each cell and are included in each cell report.

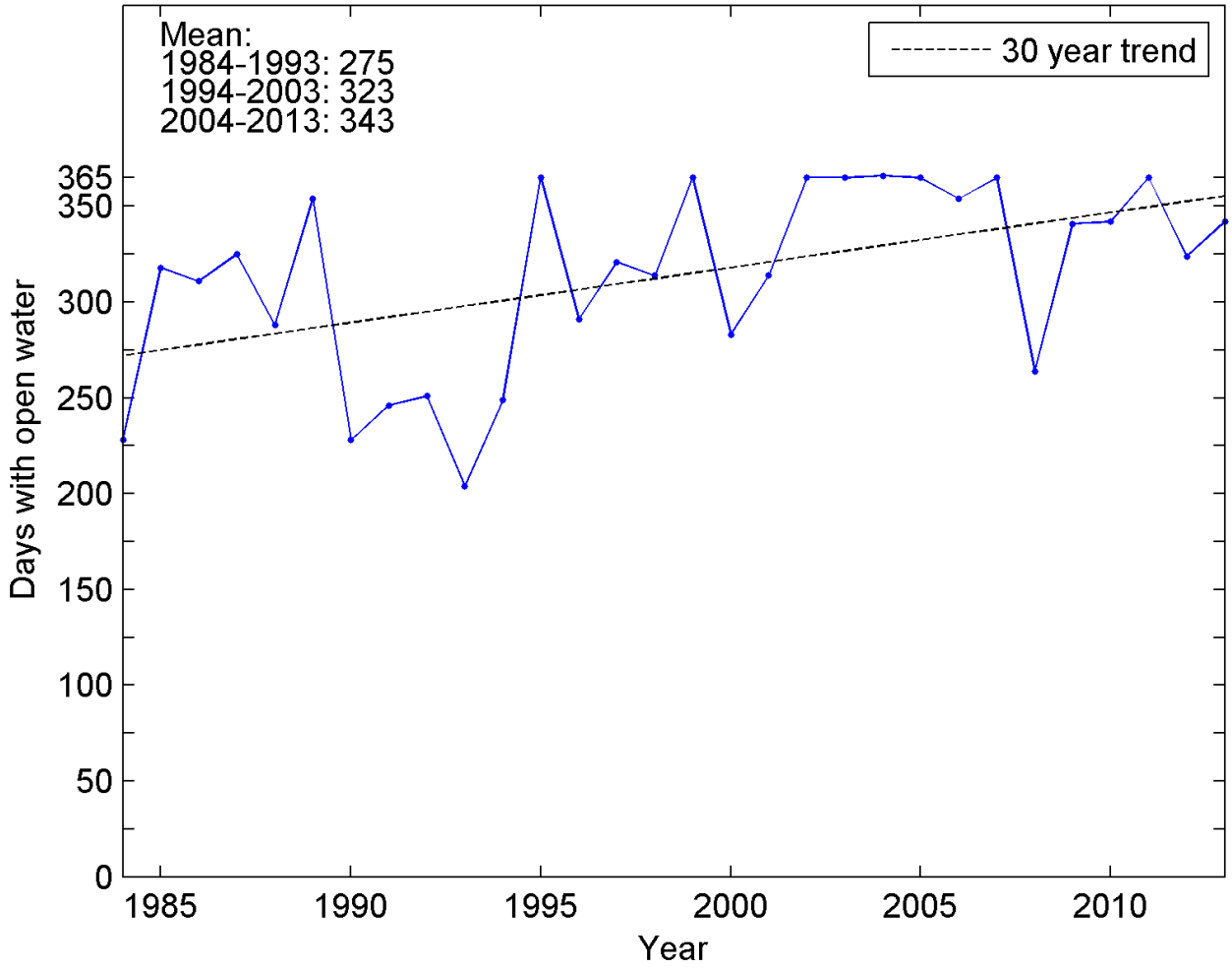

Figure 8-14. Example number of days with open water (Cell 111)

8.3.5 Probability of open water

The probability of open water (Figure 8-15) was calculated on a daily basis for the 1984-1993, 1994-2003, and 2004-2013 study periods, using the mean concentration for each cell. The term open water is used to reference waters in which the concentration of pack ice is less than one tenth. A probability of open water equal to 0.4 (40%), would indicate that four of the 10 years had open water during the time period in question.

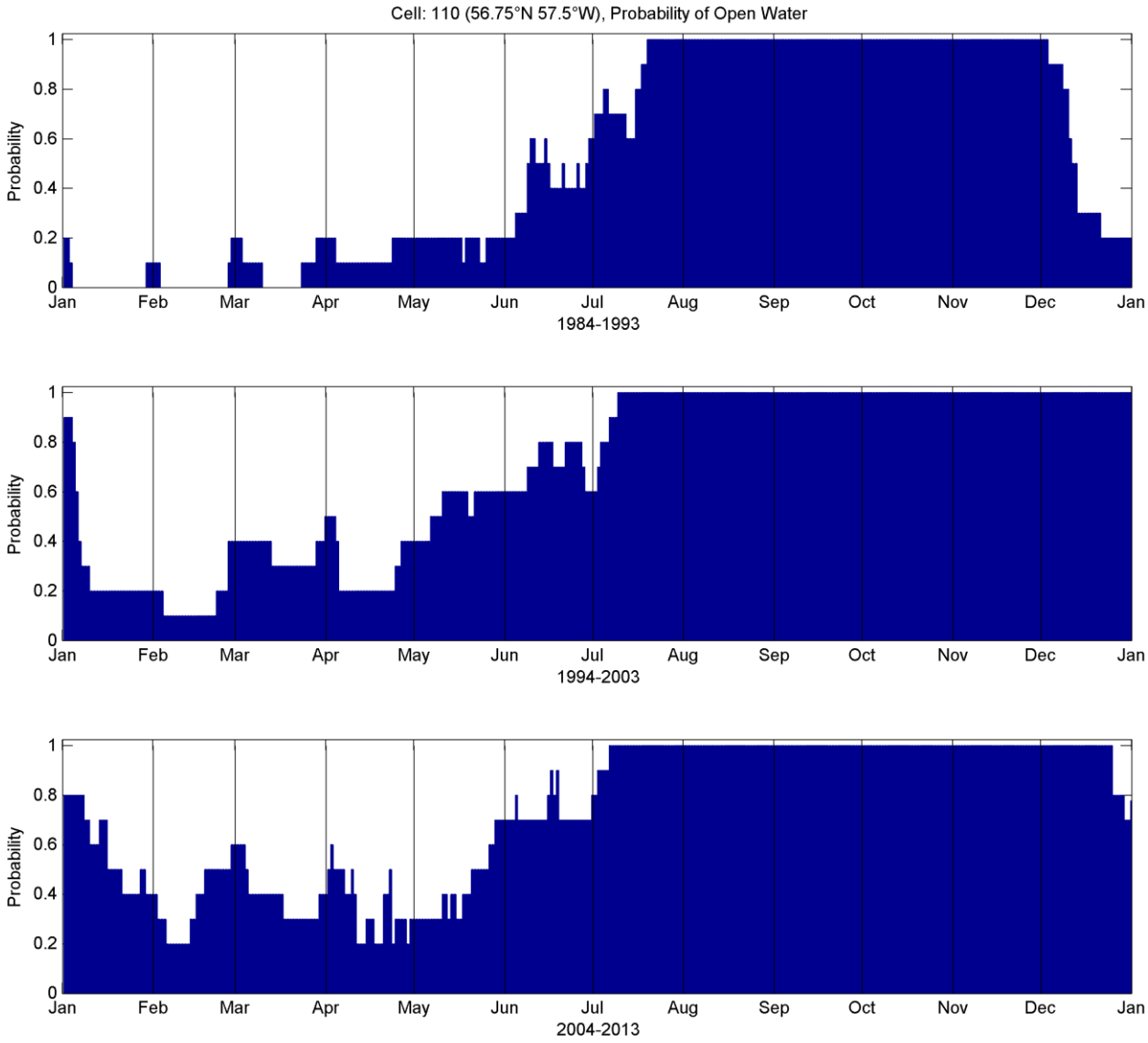

Figure 8-15. Example of probability of open water (Cell 110)

8.3.6 Number of weeks with ice

The number of weeks with ice was calculated by dividing the interpolated concentration data into seven-day bins beginning on January 1 for each year from 1984-2013, for a total of 52 bins per year. Each bin was checked for the occurrence of ice greater than or equal to one tenth. With each bin representing a week within a given year, the number of bins with at least one occurrence of ice greater than or equal to one tenth equals the number of weeks with ice for that year. The number of weeks with ice was also calculated for ice with concentrations greater than or equal to three tenths, six tenths, and eight tenths, and for old ice with concentrations greater than or equal to one tenth. The number of

weeks with ice was presented in two formats: graphically (Figure 8-16) and tabulated (Table 8-7). The number of weeks with old ice is only provided in tabular format.

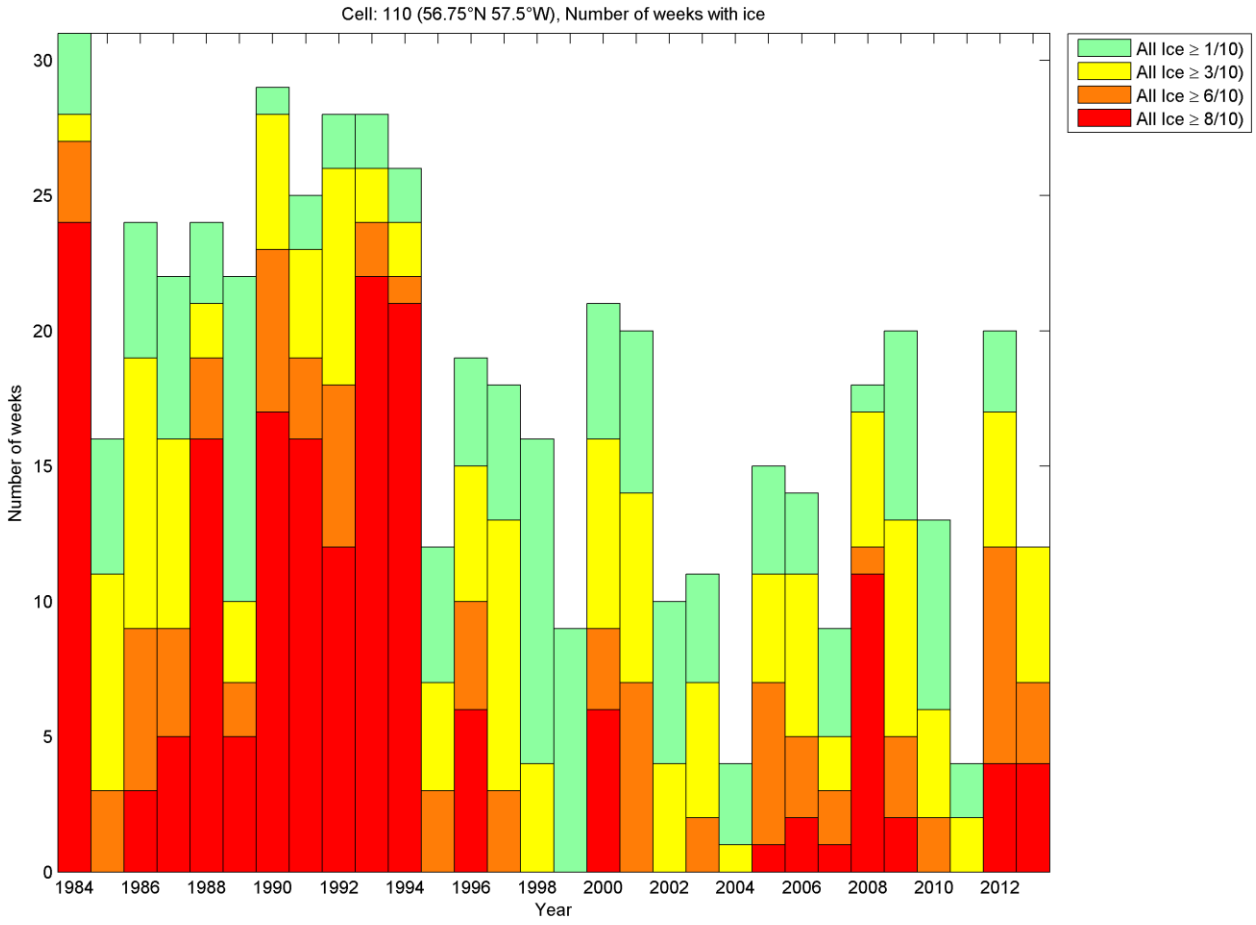

Figure 8-16. Example of graphical presentation of number of weeks with ice (Cell 110)

Table 8-7. Example of tabular presentation of number of weeks with ice (Cell 110)

Cell: 110 56.75°N 57.5°W		Number of weeks with ice				
		All Ice				Old Ice
		≥ 1/10	≥ 3/10	≥ 6/10	≥ 8/10	≥ 1/10
Years	1984	31	28	27	24	11
	1985	16	11	3	0	2
	1986	24	19	9	3	0
	1987	22	16	9	5	0
	1988	24	21	19	16	0
	1989	22	10	7	5	0
	1990	29	28	23	17	9
	1991	25	23	19	16	0
	1992	28	26	18	12	0
	1993	28	26	24	22	0
	1994	26	24	22	21	11
	1995	12	7	3	0	0
	1996	19	15	10	6	0
	1997	18	13	3	0	0
	1998	16	4	0	0	0
	1999	9	0	0	0	0
	2000	21	16	9	6	0
	2001	20	14	7	0	0
	2002	10	4	0	0	0
	2003	11	7	2	0	0
	2004	4	1	0	0	0
	2005	15	11	7	1	0
	2006	14	11	5	2	0
	2007	9	5	3	1	0
	2008	18	17	12	11	0
	2009	20	13	5	2	2
	2010	13	6	2	0	0
	2011	4	2	0	0	0
	2012	20	17	12	4	0
	2013	12	12	7	4	0
	Mean	18	14	9	6	1

8.3.7 Occurrence of land fast ice

As discussed previously, each cell has been divided into 25 grid squares, and all ice within each grid square was characterized as either fast ice or pack ice. From this characterization, the presence of fast ice was tracked for each month within the three time periods. The probability of fast ice was calculated based on the percentage of years within a given time period in which fast ice was present. An example depicting the occurrence and probability of fast ice for Cell 9 during the month of January is shown in Figure 8-17.

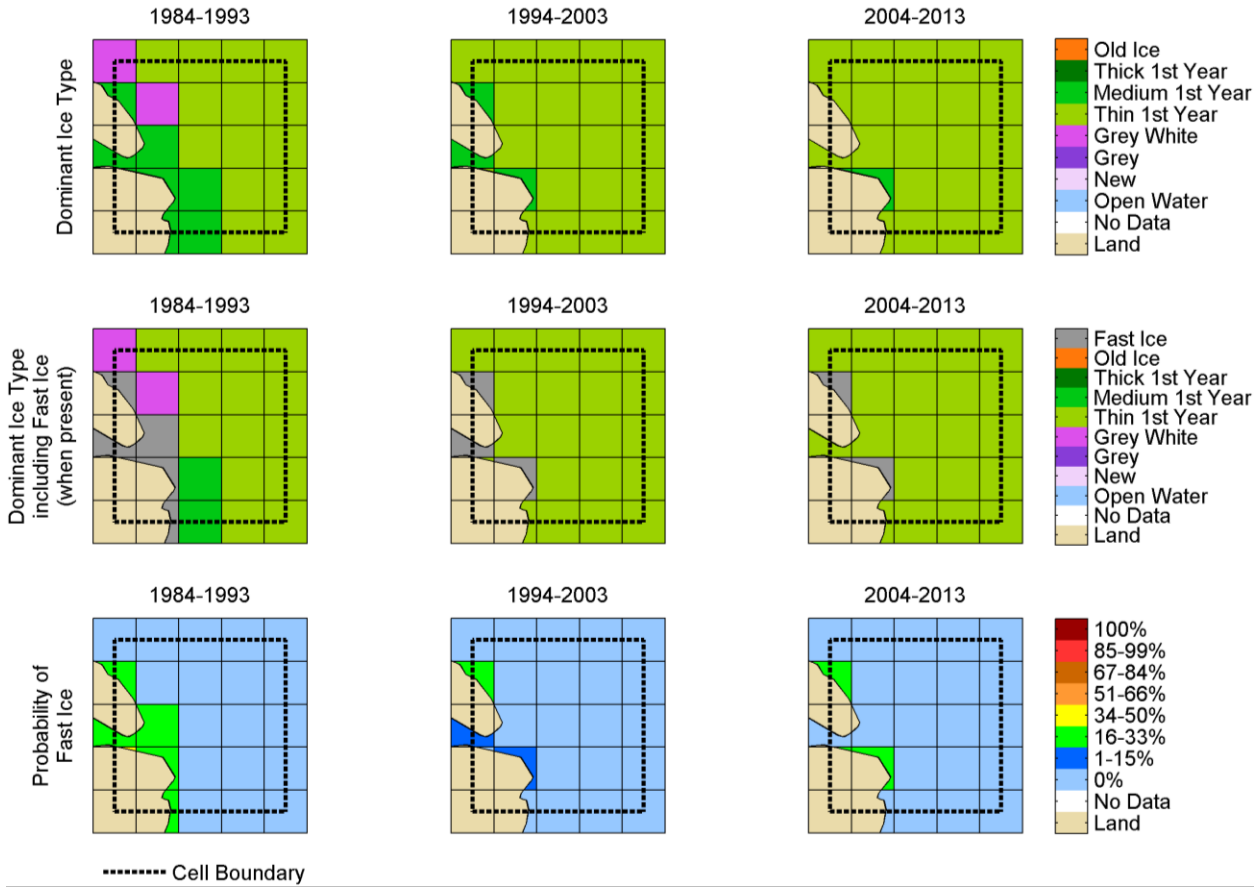

Figure 8-17. Example of occurrence of fast ice (Cell 9: January)

Grid squares registering No Data (ND) indicate that either no pack ice data were available or the available data did not contain the information necessary to characterize the ice as either fast ice or pack ice. To determine if pack ice data was available, refer to the corresponding pack ice summary plot.

8.4 Pack Ice Draft Distribution

While pack ice charts give pack ice types with approximate thickness classes, these data are not appropriate for characterizing the pack ice draft distribution, which includes rafted and ridged ice. Should any exploration or production facility be exposed to this ice, the draft distribution is required to

assess load magnitudes and associated mooring requirements or requirements for ice management. Figure 8-18 shows pack ice draft data collected by Simon Prinsenberg of Bedford Institute of Oceanography (BIO), and are available at: ftp://starfish.mar.dfo-mpo.gc.ca/pub/ocean/seaice/.

These data were collected using Upward Looking Sonar (ULS) at a site on the Makkovik Bank, referenced in Cell 140 of the study area. Maximum pack ice drafts on the order of 23 metres have been measured at this site (icebergs have been filtered from this data set). Data from 2003, 2005, 2007, 2009, and 2011 are shown.

Additional data collection is required to characterize pack ice conditions going from the shelf, with a relatively high pack ice incidence, to the less pack ice prone deep-water basins to determine if the same pack ice draft distribution is maintained in lower pack ice concentrations. Lower pack ice concentrations could potentially result in less confining stress, and therefore, there could be less potential for ridging and rafting. This would further mitigate the influence of pack ice on operations in the deepwater basins. This data collection requires the selection and instrumentation of additional sites, and data collection should be conducted annually until the required relationships have been established.

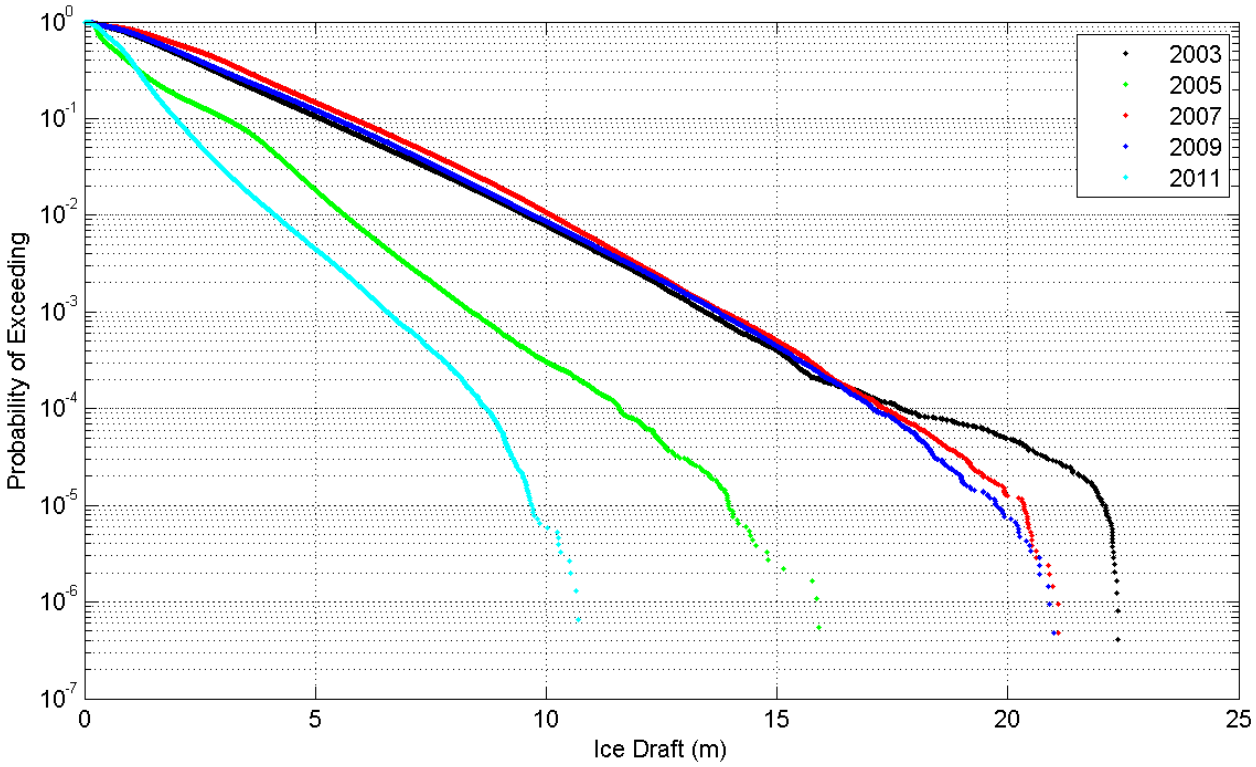

Figure 8-18. Pack ice draft distribution from ULS on the Makkovik Bank

8.5 Regional Overview

To provide a perspective of pack ice conditions on a regional scale, plots covering the whole study area were generated for mean concentration when present and the number of days with open water. The plots were generated for annual conditions and for each of the four seasons: Winter (December –

February), Spring (March – May), Summer (June – August) and Fall (September – November). The outlines of several offshore basins have been included as a reference.

8.5.1 Mean annual concentration when present

Plots showing the annual and seasonal mean concentration when present were generated covering the complete study area for the entire time period (1984 – 2013) and the last 10 years (2004 – 2013), as shown in Figure 8-19 to Figure 8-23. The *when present* designation implies that the mean annual concentration is only calculated using occurrences of ice with concentrations greater than or equal to one tenth. In the event that no ice greater than or equal to one tenth exists, the mean is calculated using occurrences of ice greater than zero but less than one tenth, concentrations (less than one tenth are often referred to as open water). If there is no ice present in any concentration, the mean is assigned a value of zero or Ice Free. Occasionally there are no data available, and those cases, the mean is assigned an *ND* designation.

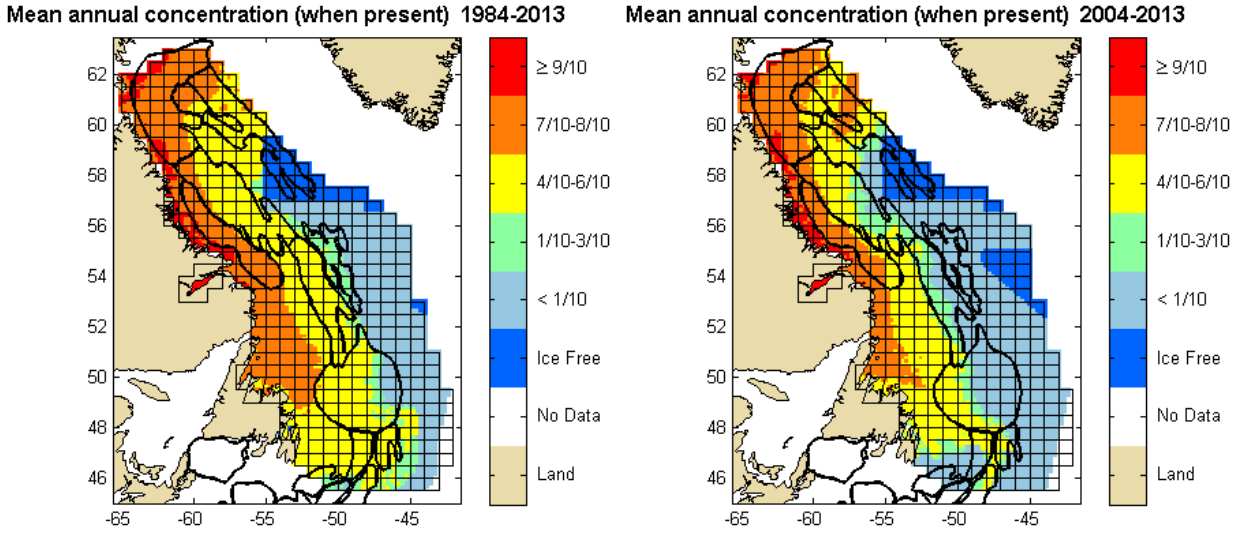

Figure 8-19. Mean pack ice concentration (Annual)

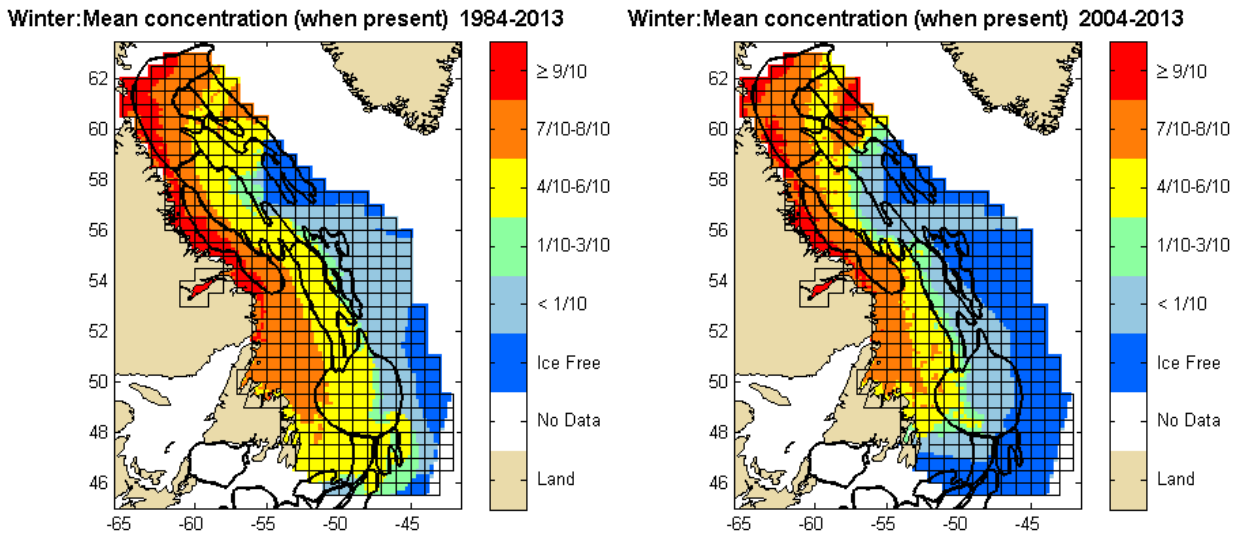

Figure 8-20. Mean pack ice concentration (Winter: December–February)

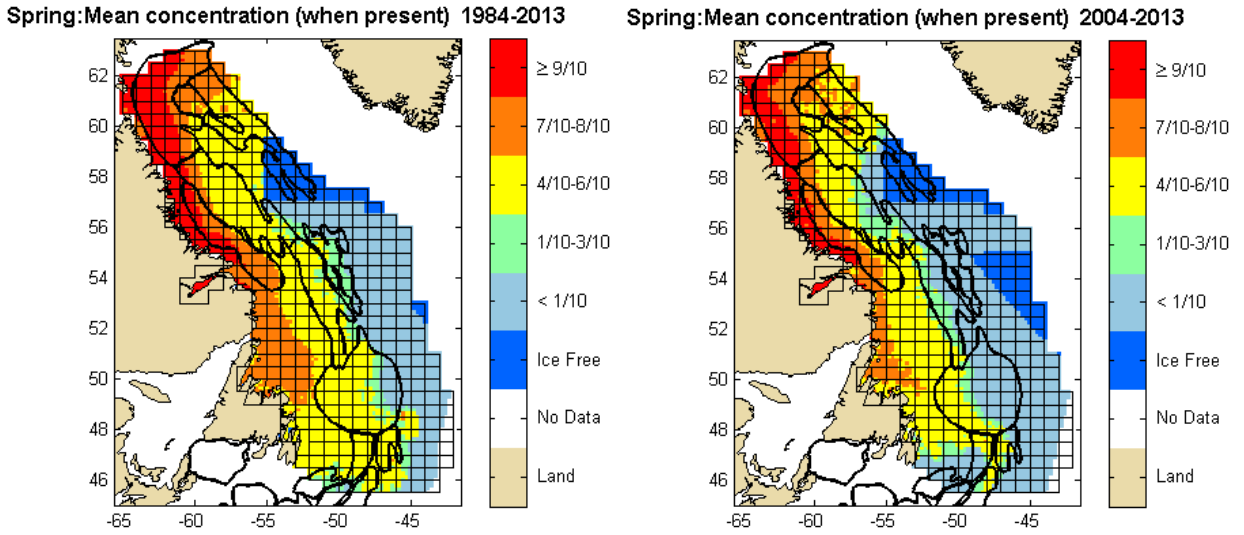

Figure 8-21. Mean pack ice concentration (Spring: March–May)

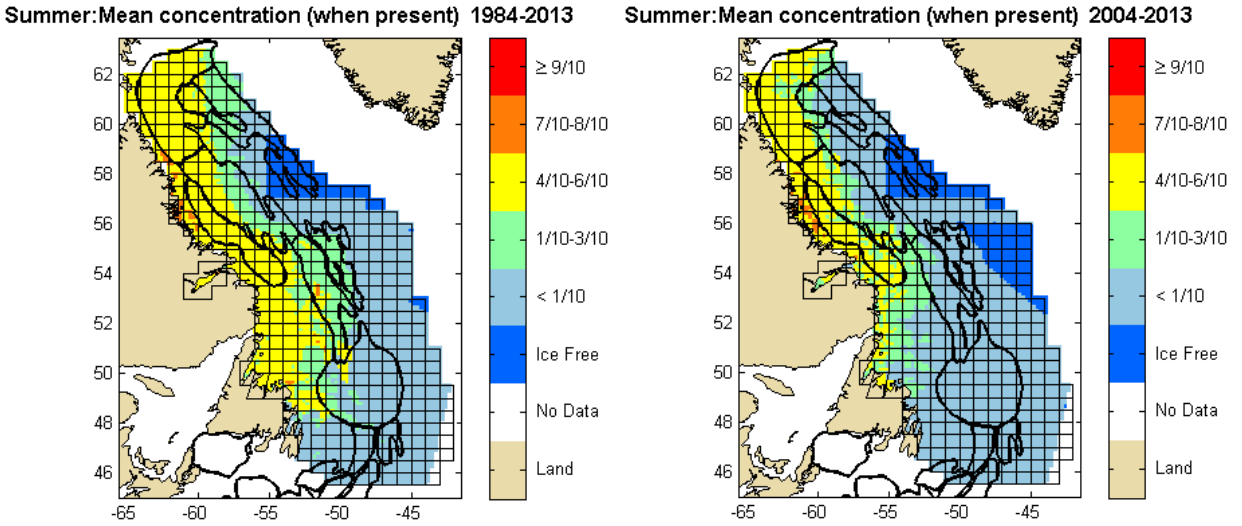

Figure 8-22. Mean pack ice concentration (Summer: June–August)

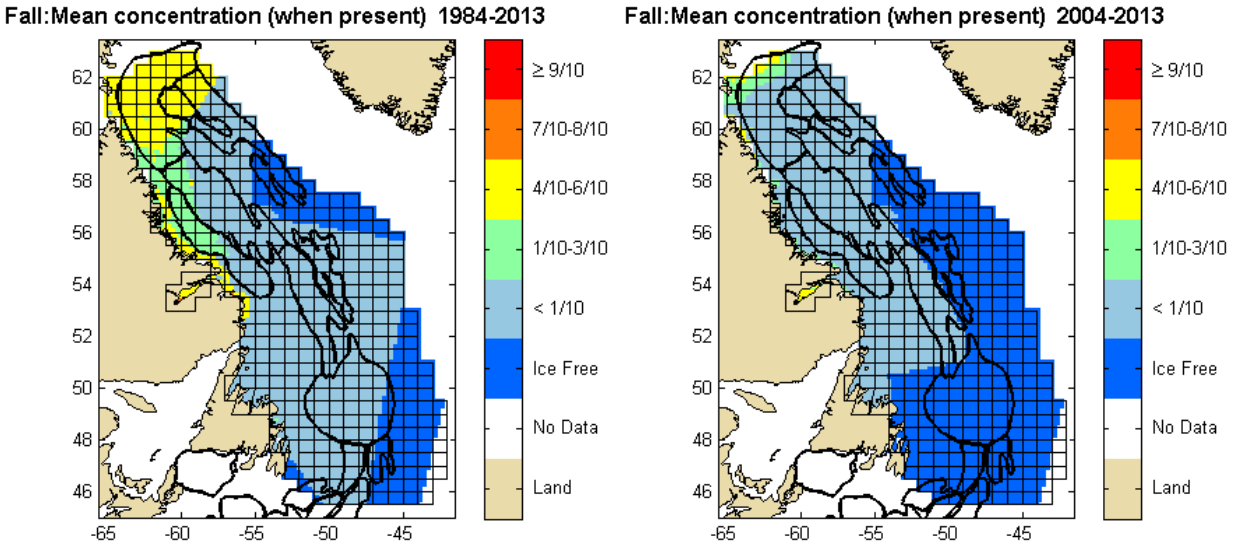

Figure 8-23. Mean pack ice concentration (Fall: September - November)

From the examination of these figures, a general trend towards lower concentrations can be seen when comparing the last 10 years to the entire 30-year period. When comparing 1984-2013 to 2004-2013, there is a general trend showing the limits of all concentration bands shifting to the north and/or west, as the heaviest coverage bands decreases while bands of 1/10-3/10, <1/10, and Ice Free concentrations begin to emerge, or increase in coverage. While this trend of the limits of various ice bands receding west and or north are present in all seasons, they are most prominent in the summer and fall.

The transition between concentrations less than one tenth and Ice Free often appears less natural than the transition between other adjacent concentration bands. The main reason behind this sharper transition is primarily due to the use of two data sources. The NIC charts rarely record concentrations

between zero and one tenth, with all concentrations less than one tenth being recorded as zero (0) or Ice Free. However, the CIS frequently uses concentrations between zero and one, and often provides a clear distinction between less than one tenth (or open water) and Ice Free waters. Therefore, as concentrations less than 1one tenth are generally not present in NIC charts there exists the possibility of experiencing a sharp transition zone when transferring from NIC to CIS coverage.

8.5.2 Number of Days with Open Water

Regional plots for the number of days with open water were generated for the complete study area for the entire study period (1984-2013) and the last ten years (2004-2013). Figure 8-24 through to Figure 8-28 were generated presenting both annual and seasonal number of days with open water. Within the last 10 years, there is an obvious increase in the annual, winter, spring, and summer OWSs when compared to the 1984-2013 time period. Between these time periods, the bands representing the number of open water days generally shift to the north and west resulting in more cells with open water days exceeding 345. When comparing 2004-2013 to 1984-2013, the winter and spring seasons see a dramatic decrease in the number of cells with open water conditions less than 15 days, the number of days with open water during the summer season experiences an increase of up to 20 days, while the fall seasons are more or less comparable.

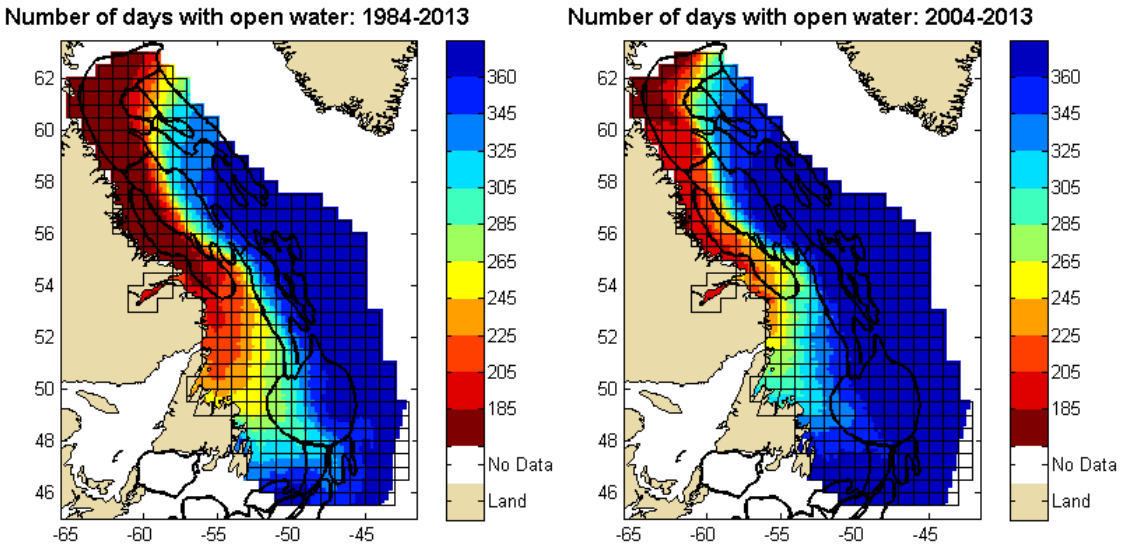

Figure 8-24. Number of days with open water (Annual)

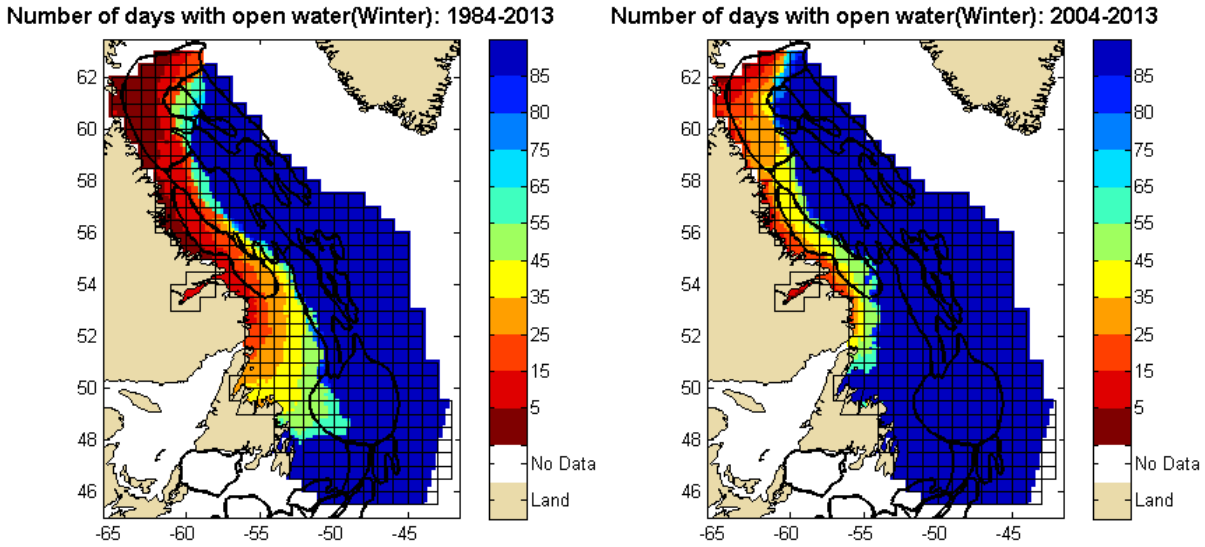

Figure 8-25. Number of days with open water (Winter: December – February)

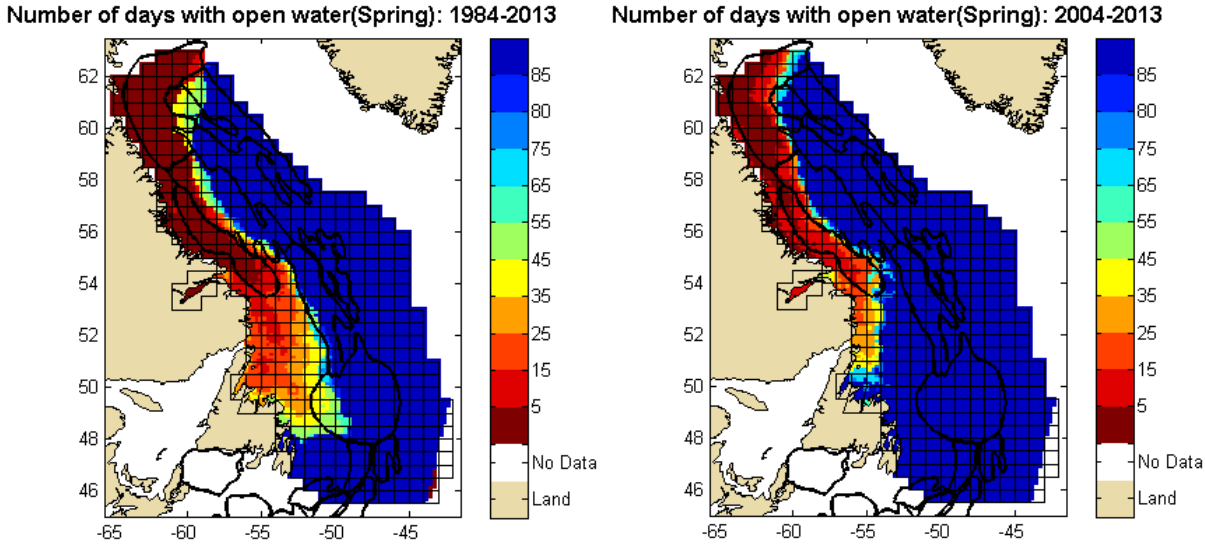

Figure 8-26. Number of days with open water (Spring: March - May)

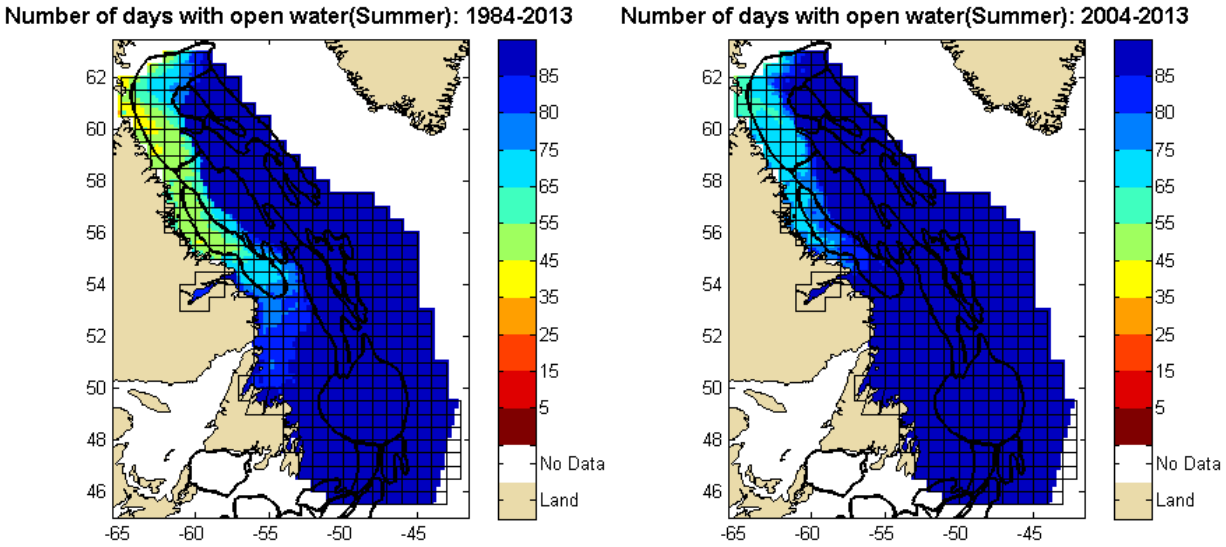

Figure 8-27. Number of days with open water (Summer: June - August)

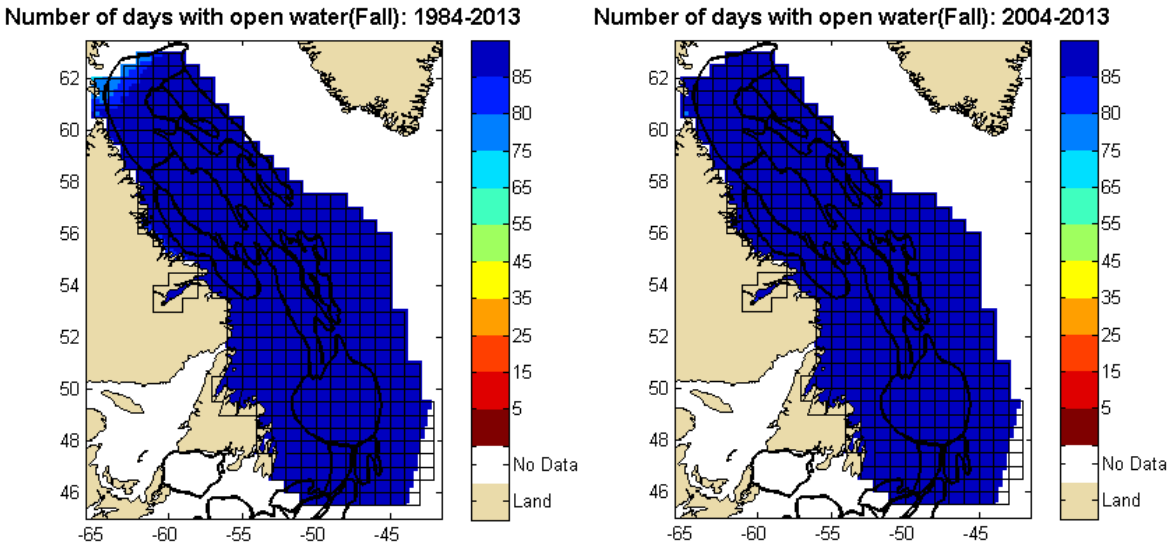

Figure 8-28. Number of days with open water (Fall: September – November)

8.6 REFERENCES

Canadian Ice Services. (2013). Weekly Regional Sea Ice Charts. Retrieved from: www.ec.gc.ca/glaces-ice.

National Snow and Ice Data Center. (2013). Weekly Regional Sea Ice Charts. Retrieved from www.natice.noaa.gov

Prinsenberg, S. (various). Pack ice draft data. Department of Fisheries and Oceans, Bedford Institute of Oceanography. Retrieved from: ftp://starfish.mar.dfo-mpo.gc.ca/pub/ocean/seaice/.

Metocean Climate Study
Offshore Newfoundland & Labrador

STUDY MAIN REPORT
Volume 1: Chapter 9 – Icebergs and Ice Islands

Prepared for:
Nalcor Energy Oil and Gas

Prepared by:
C-CORE

Reviewed & Edited by:
Bassem Eid, Ph.D.

May 2015

CHAPTER 9 ICEBERGS AND ICE ISLANDS

TABLE OF CONTENTS

LIST OF FIGURES

LIST OF TABLES

LIST OF ACRONYMS

IIP	International Ice Patrol
CIS	Canadian Ice Service
PAL	Provincial Aerospace Limited
PERD	Program of Energy Research and Development
MSC	Meteorological Service of Canada
MANICE	Manual of standard procedures for reporting and observing ice conditions
ESA	European Space Agency
ASAR	Advanced Synthetic Aperture Radar
SAR	Synthetic Aperture Radar
WSM	Wide Swath Mode
NEST	Next ESA SAR Toolbox
IDS	Iceberg Detection Software
GIS	Geographic Information System
QC	Quality Check
HBV	Husky/Bow Valley
DFO	Fisheries and Oceans Canada
GPR	Ground-penetrating Radar
GBS	Gravity Based Structure
FPSO	Floating Production Storage and Offloading
NRC	National Research Council

9 ICEBERGS AND ICE ISLANDS

9.1 BACKGROUND

The relevant parameters for defining iceberg risk to surface facilities are frequency, drift speed, and size. Iceberg frequency is very difficult to define accurately. Iceberg frequency varies considerably, both spatially and temporally (by month and year). An example of the extreme inter-annual variation possible can be seen in Figure 9-1, which shows a time series of the number of icebergs drifting south of 48°N, as assessed by the International Ice Patrol (IIP). It should be noted that values shown are affected by detection capabilities and surveillance effort, and that increased sightings would be expected in more recent decades with increased offshore activity for hydrocarbon exploration and development, and with improved detection capabilities. Iceberg surveillance efforts have focused on the Grand Banks region, both for support of Grand Banks operations and because of the proximity to international shipping lanes.

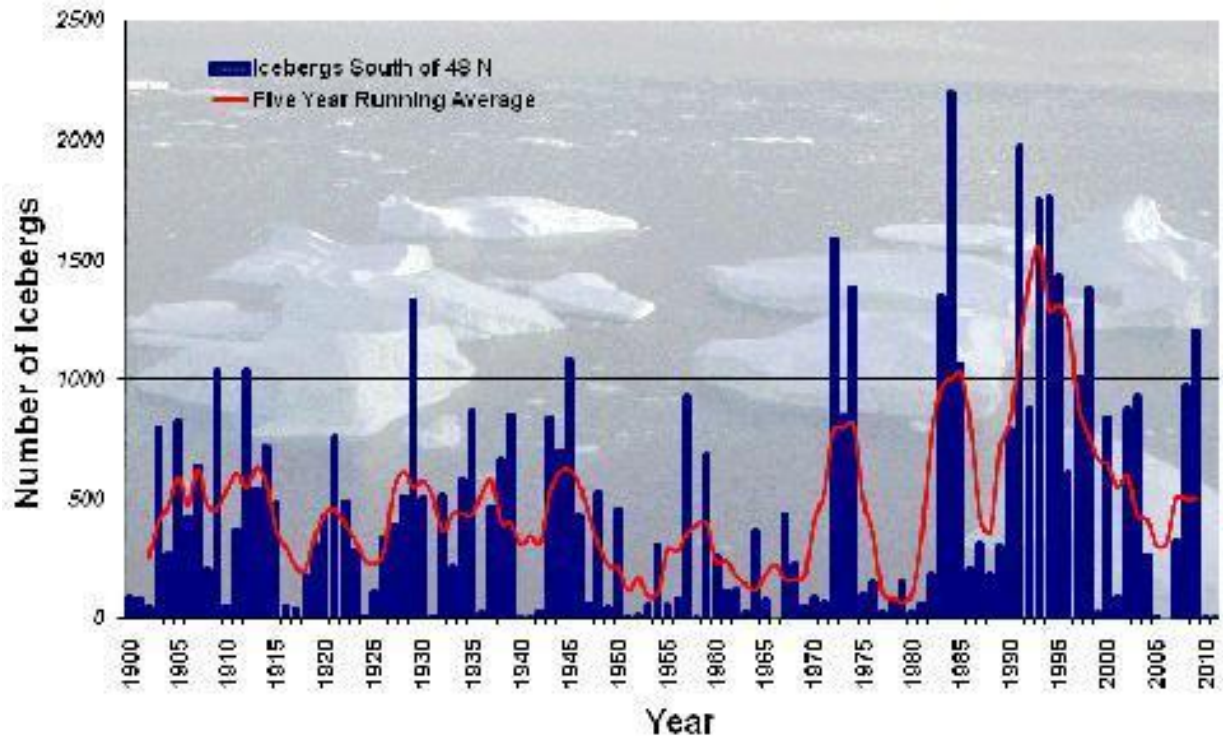

Figure 9-1. Iceberg flux across 48°N (www.navcen.uscg.gov/?pageName=IIPIcebergCounts)

Figure 9-2 shows average annual iceberg density values based on International Ice Patrol (IIP) bulletins, demonstrating the variation in iceberg densities obtained depending on the time period considered.

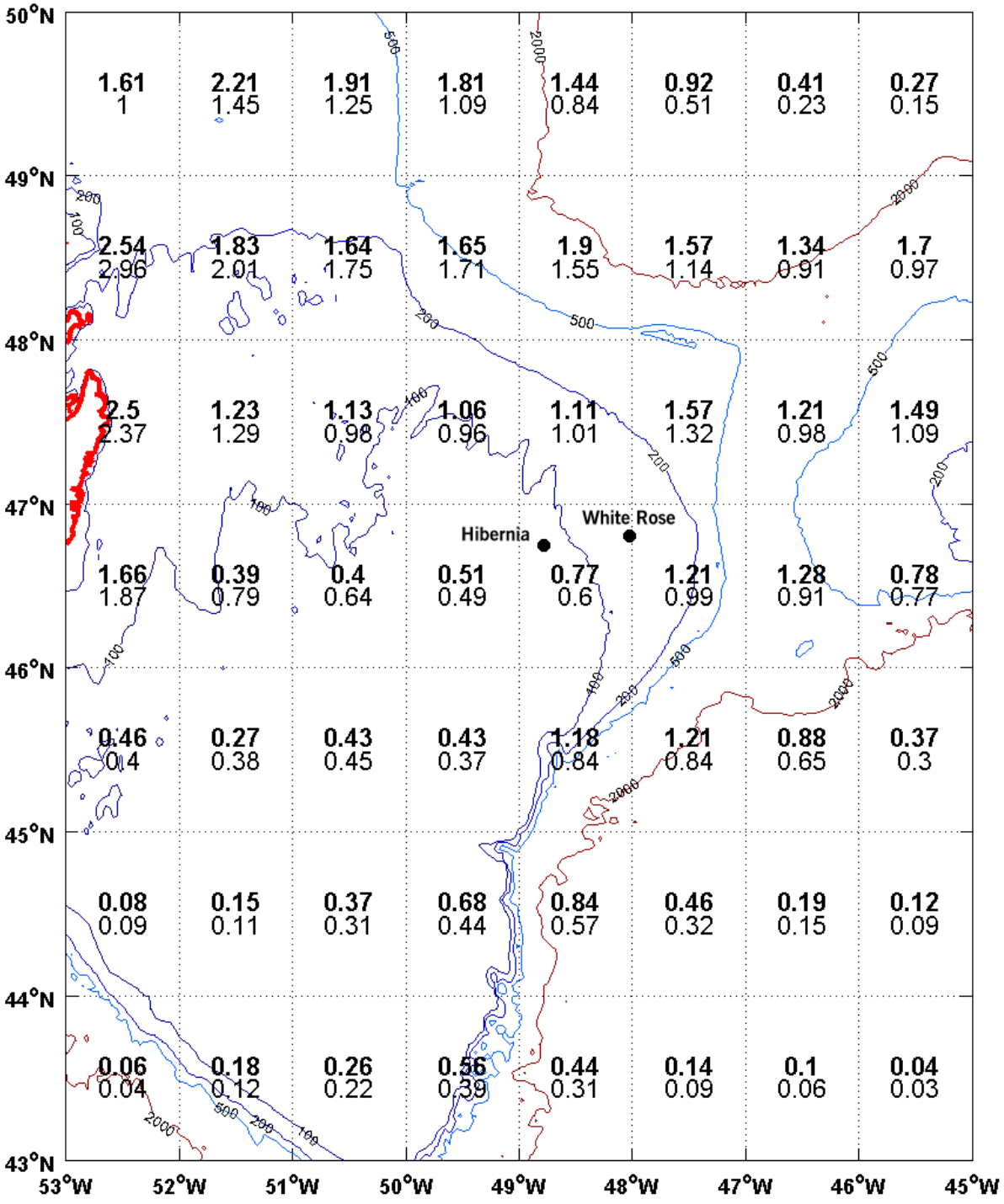

Figure 9-2. Mean annual iceberg areal density per degree square, bottom values based on IIP bulletin data from 1960-2000, top values based on data from 1981-2000 (Jordaan et al., 1999), water depths in metres (from King, 2002)

C-CORE (2007) defined iceberg frequency for a study area on the Labrador Shelf shown in Figure 9-3, using a combination of sightings from International Ice Patrol flights (no bulletins were available for this area), Canadian Ice Service (CIS) iceberg charts, and Provincial Aerospace Limited (PAL) sightings. The CIS iceberg charts make use of iceberg sightings from various sources, modeled iceberg trajectories, and deterioration rates. Icebergs are not frequently shown further north along the northern Labrador coast (i.e. 55°N and further north), presumably due to the lack of iceberg sighting data to initialize the models. Similarly, CIS charts frequently will not show icebergs inside areas covered by pack ice, although icebergs may be shown adjacent to pack ice covered areas.

Figure 9-4 shows iceberg-sighting data from the PERD (2013) Iceberg Sighting Database. These data, while useful qualitatively, are not suitable to use to develop a regional map of iceberg frequency (survey coverage area and periods with no icebergs are unknown). Sightings are from a combination of sources (i.e. ship, rigs, aircraft, lighthouses, etc.), and reflect the amount of activity and level of surveillance. It is certain that icebergs are far more numerous along the Labrador Coast than would be inferred from the density of points shown in Figure 9-4 (especially considering all icebergs observed further south have to pass through this area), and this is due to the limited surveillance in this area. There are also icebergs shown in Figure 9-4 further off the Labrador Shelf, although these are almost always random ship sightings.

The best available data are analyzed here to estimate iceberg densities in the Labrador Sea deepwater basins. This analysis will allow iceberg risk to be quantified and to benchmark these basins against other regions. This analysis will also provide a baseline that may be used for future refinement of a regional iceberg climatology using improved data collection technology, such as the ESA Sentinel satellite.

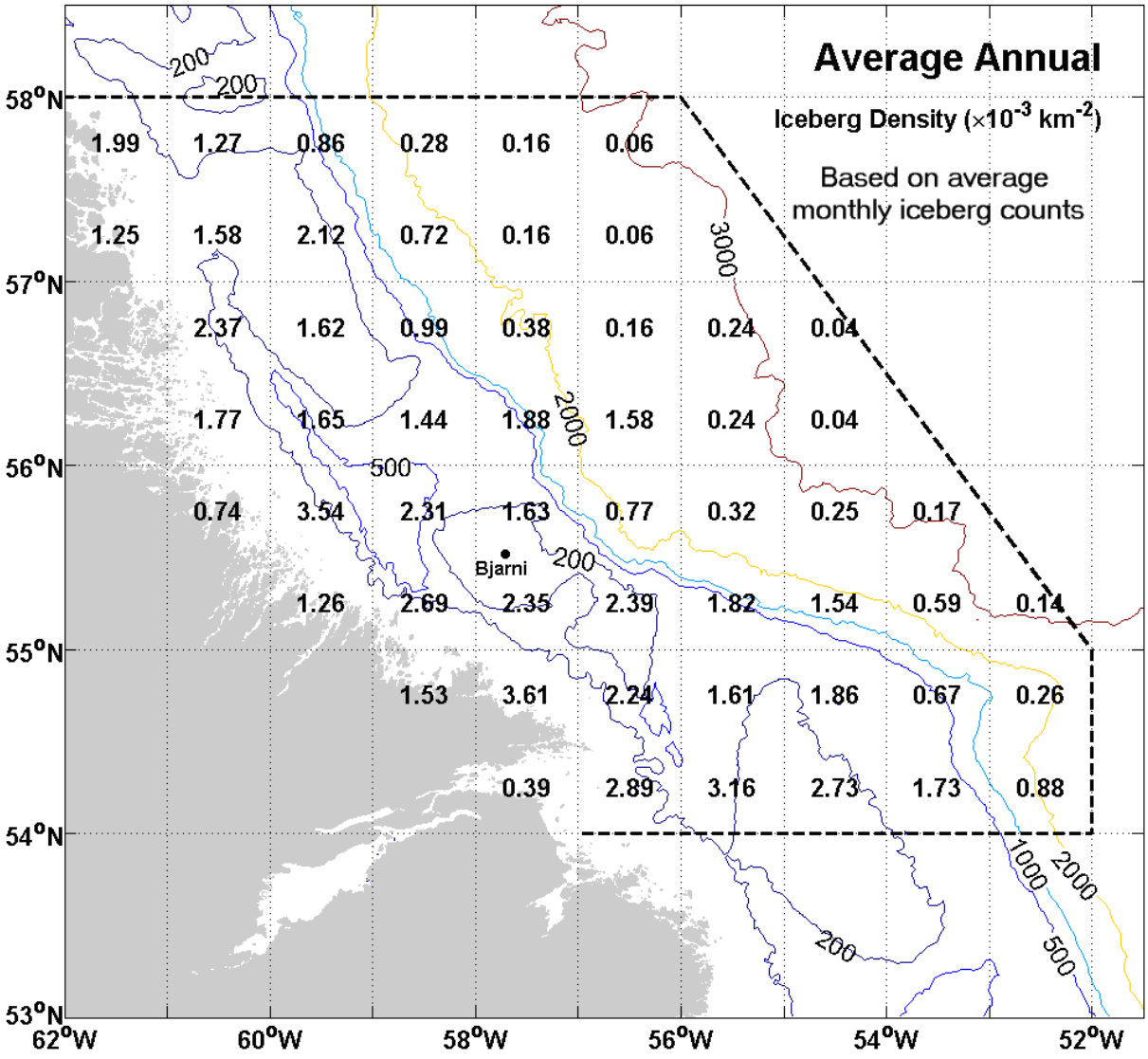

Figure 9-3. Average annual iceberg density offshore Labrador, 1988-2006 (C-CORE, 2007)

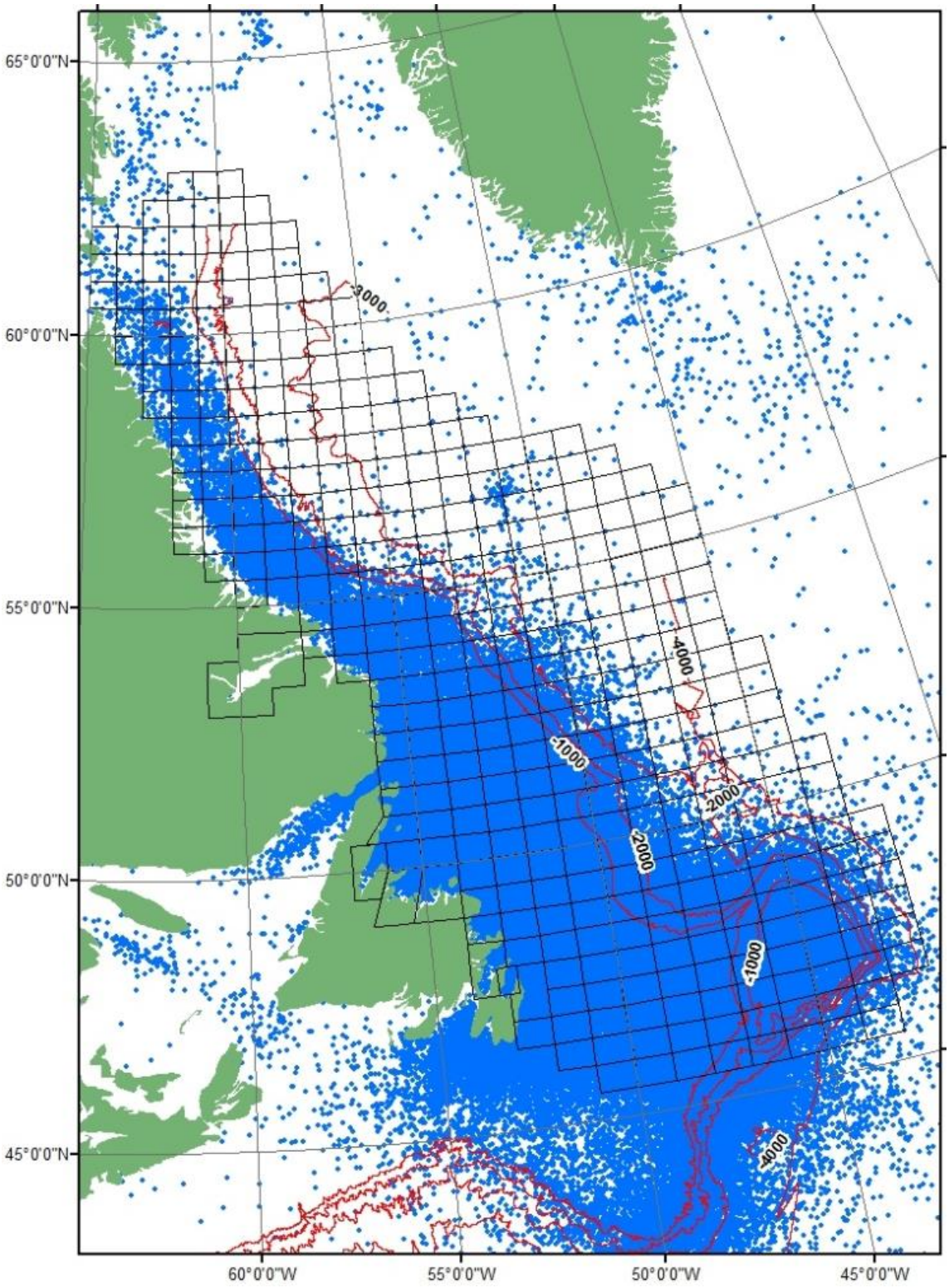

Figure 9-4. Iceberg sightings from PERD Iceberg Sighting Database (PERD, 2013)

9.2 AERIAL RECONNAISSANCE DATA ANALYSIS

9.2.1 Data Sources

Aerial reconnaissance data are one of the most reliable data sources for iceberg observations. Flights are conducted on a regular basis by IIP (International Ice Patrol) and CIS (Canadian Ice Service) to monitor the presence of icebergs and sea ice, following a standard procedure to record and report the iceberg conditions. In addition to the flight track information, the flight messages also provide the location, time, size, shape, and method of observation of the icebergs. It is also stated in the data if an iceberg is located in the sea ice. A sample aerial surveillance flight track with the radar swath and iceberg locations is shown in Figure 9-5.

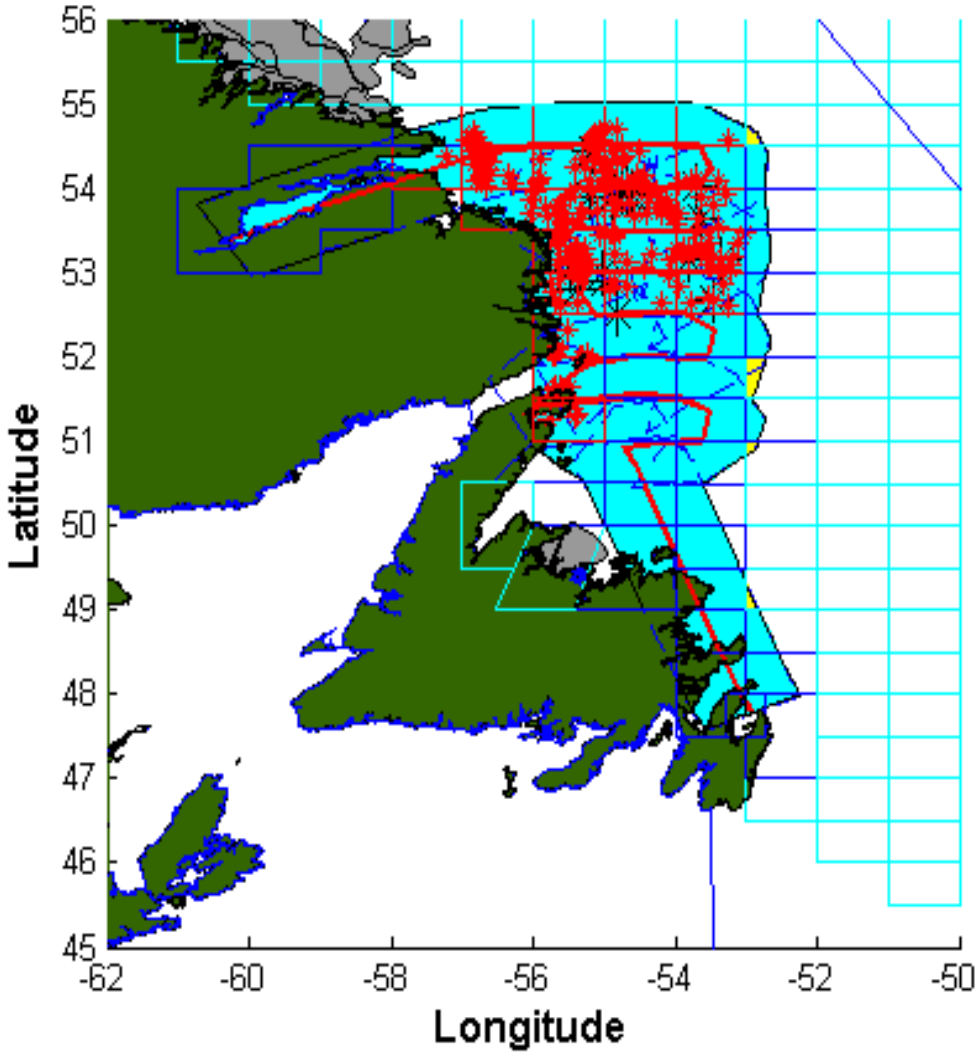

Figure 9-5. Aerial reconnaissance flight track and iceberg locations, June 1st 2008

The International Ice Patrol (IIP) is an organization, operated by US Coast Guard, to monitor and record the presence of icebergs in the Atlantic and Arctic oceans. It was established in 1912 in response to the

Titanic disaster and has operated since 1913, with the exception of the World Wars. The primary objectives of IIP are to alert ships travelling between North America and Europe of iceberg hazards and to provide iceberg limits to the maritime community near the Grand Banks area of Newfoundland. Earlier IIP area of coverage was limited to 40°N to 52°N and 39°W to 57°W, but after 2006, the area was expanded to cover 40° N to 65° N and 39°W to 57°W (IIP, 2014). Aerial reconnaissance flight messages provided by IIP from 1998 to 2014 covered mostly the southern part of the study area, with limited number of flights that covered the northern area of interest as shown in Figure 9-6.

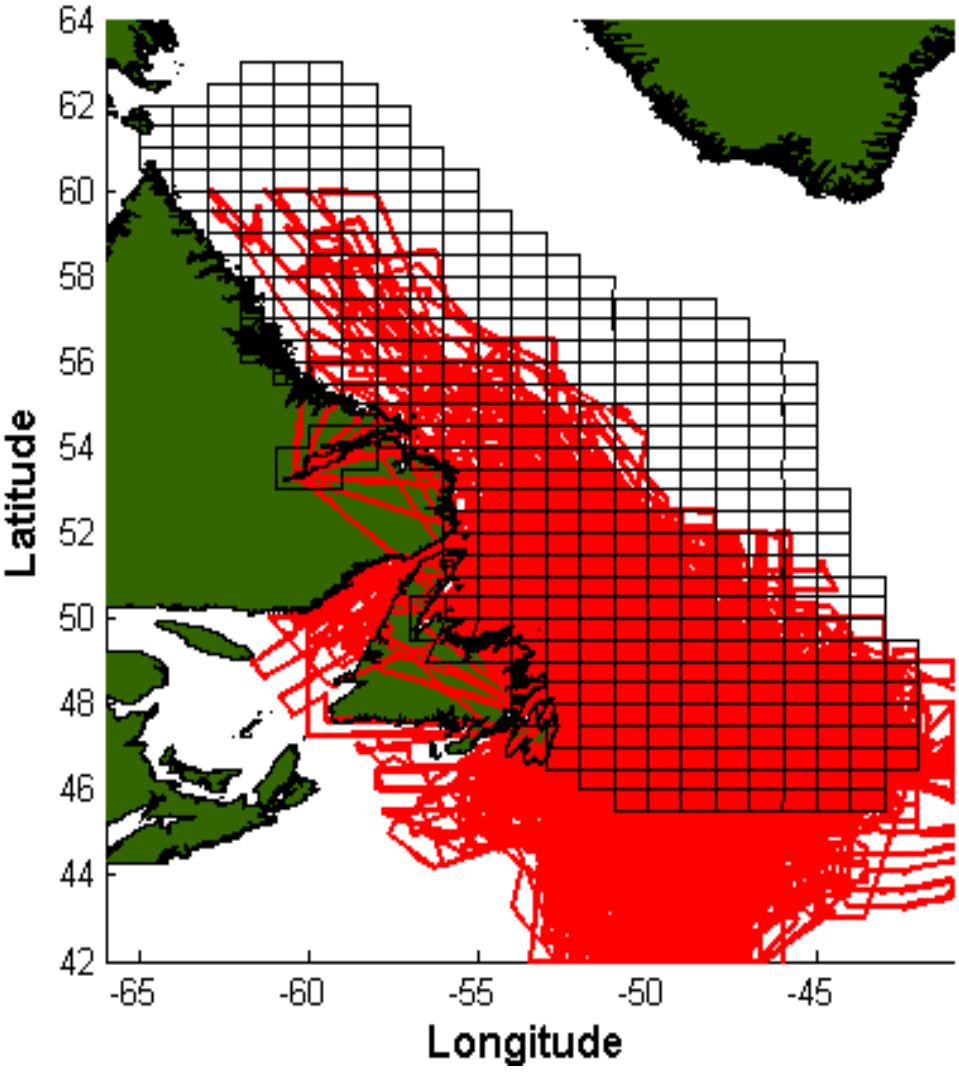

Figure 9-6. IIP flight track coverage from available files (1998-2014)

Canadian Ice Service (CIS) is a division of the Meteorological Service of Canada (MSC) and provides information about hazardous ice conditions in navigable waters of Canada. The CIS also provides information for research and development to support sound environmental policies for current and future generations (CIS, 2014). They provide direct access to ice and iceberg charts from their website

on a daily basis. Provincial Aerospace Limited (PAL) generally performs aerial iceberg reconnaissance flights for CIS. Figure 9-7 shows overall coverage by flight tracks provided by the CIS from 2000 to 2012.

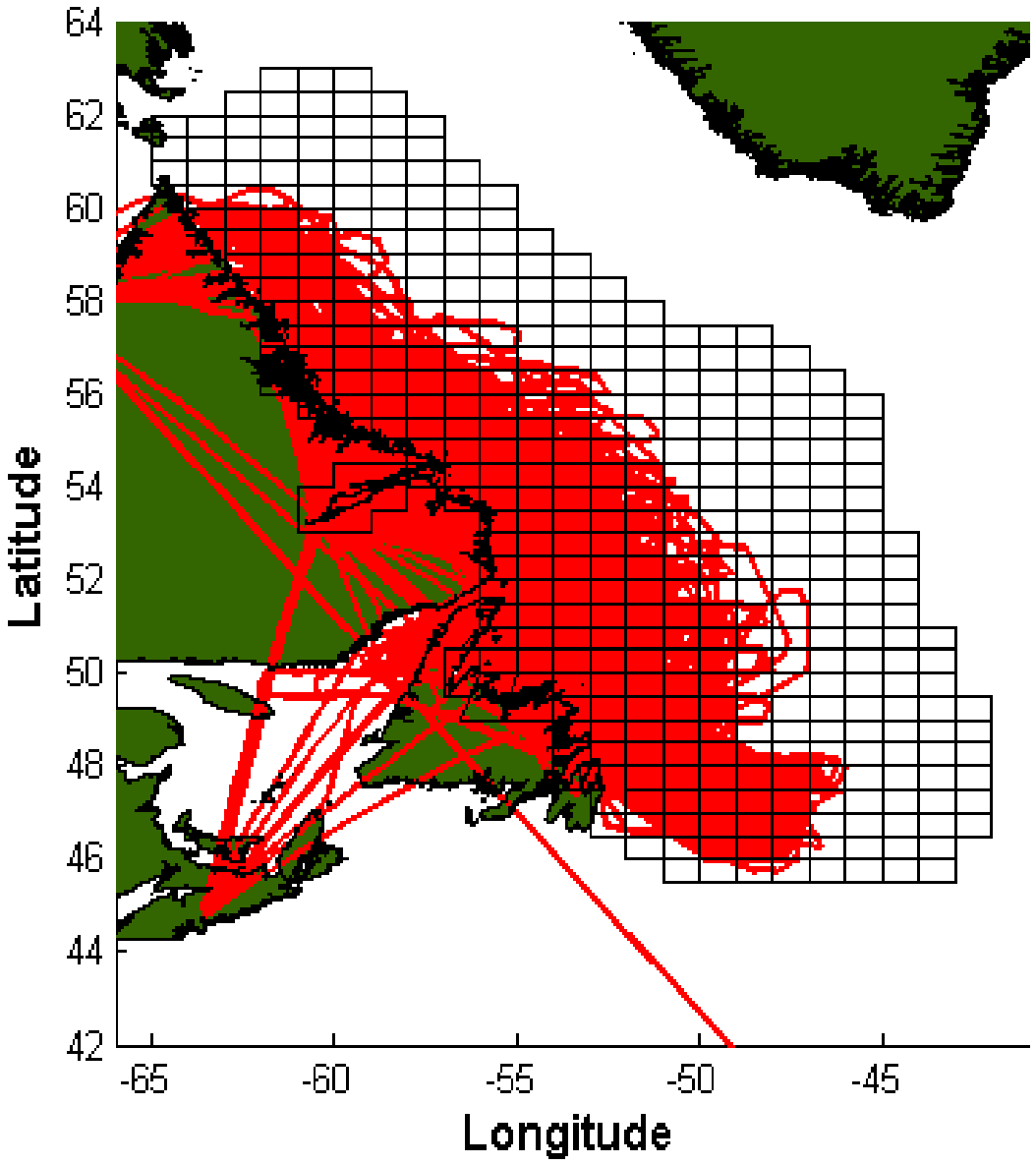

Figure 9-7. CIS flight track coverage (2000 to 2012)

In total, 923 flight surveys have been processed and analyzed for this project by combining the IIP and CIS reconnaissance flight surveys. Numbers of flights per year and per month are given in

Table 9-1. The coverage of the combined aerial reconnaissance data set is shown in Figure 9-8. As can be seen in the image, some cells of the study area were not covered by aerial reconnaissance flights in this time period.

Table 9-1. Flight data summary

	Jan	Feb	Mar	Apr	May	June	July	Aug	Sept	Oct	Nov	Dec	Total
1998	-	3	12	10	10	11	7	-	-	-	-	-	53
1999	2	-	8	4	12	2	1	-		-	-	-	29
2000	2	13	15	16	12	12	11	2	1	2	-	-	86
2001	4	-	7	13	8	4	-	2		-	-	-	38
2002	-	4	14	17	11	13	4	1	2	-	2	1	69
2003	1	1	3	9	18	14	3	-	4	-	2	3	58
2004	-	2	5	4	7	7	5	2	-	1	-	-	33
2005	3	7	8	7	4	7	2	2	3	1	-	2	46
2006	4	7	6	11	8	4	3	3	3	3	2	2	56
2007	3	3	11	9	7	11	12	5	9	3	5	2	80
2008	5	6	9	10	11	10	7	3	2	2	3	2	70
2009	5	5	12	10	12	11	9	5	3	-	2	3	77
2010	2	1	3	5	5	5	4	3	2	2	2	1	35
2011	2	-	-	-	-	-	-	-	-	-	-	-	2
2012	-	2	15	32	66	21	4	3	-	-	-	-	143
2013	-	1		3	1	4	3	-	-	-	-	-	12
2014	-	4	7	5	6	7	7	-	-	-	-	-	36
Total	33	59	135	165	198	143	82	31	29	14	18	16	923

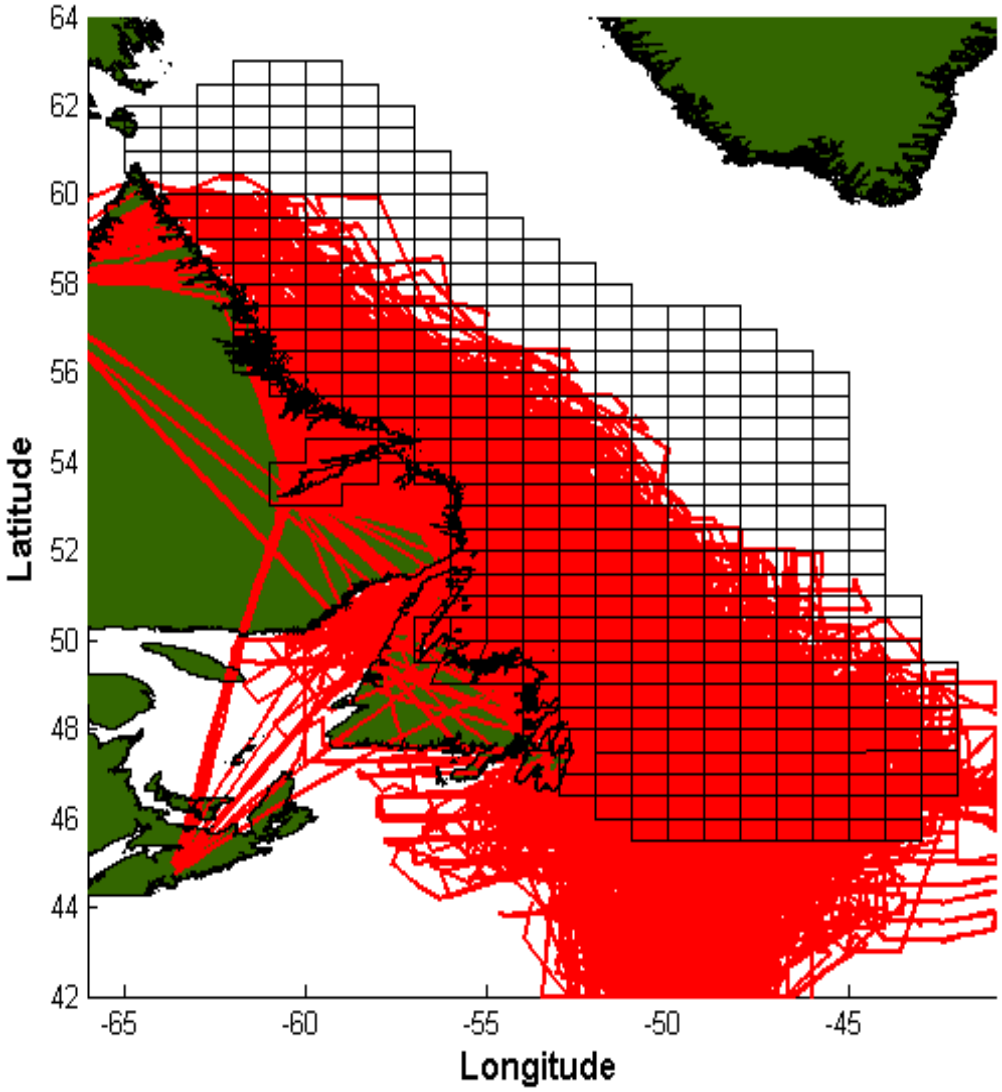

Figure 9-8. Combined flight track coverage

The total number of flights that covered the cells of the study area either fully or partially is shown in Figure 9-9. There are a considerable number of flights near Grand Banks region (from 55°W to 46°W and 46°N to 49°N), but very limited numbers of flights from 54°N to 61°N, and no coverage beyond 61°N. The processing steps of the Manice files and the adjustments to the iceberg detections are described in the following section.

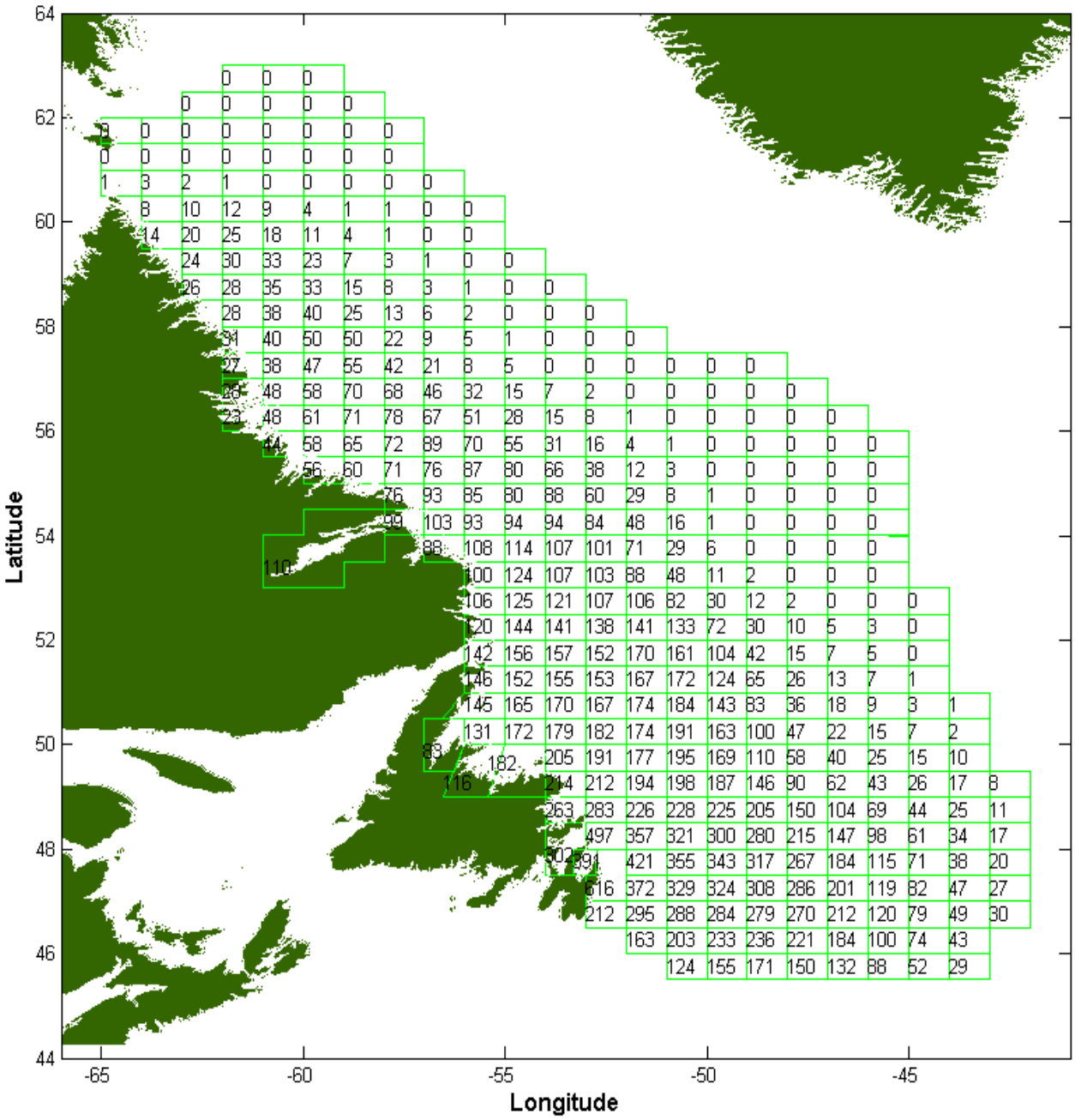

Figure 9-9. Total number of iceberg aerial surveillance flights covering each cell

9.2.2 MANICE Files

The Meteorological Service of Canada (MSC) and International Ice Patrol (IIP) have developed a universal iceberg reporting code that allows the exchange of digital iceberg information to enable computer assisted manipulation of iceberg observations into analyses (MANICE, 2005). This MANICE (Manual of

standard procedures for observing and reporting ice conditions) format provides information of all iceberg parameters, area of surveillance, and the factors influencing both visual and radar iceberg detection.

In MANICE files, the header contains the identification code, source, and platform information. It also has the information about the time, date, and consecutive message number from the platform. Track information reports the route of the flight using the location and time at the start of each leg. Data about altitude, wave and swell group, radar range, and visibility group in nautical miles are also provided with track records.

Iceberg information is provided as an individual observation or as a group. When a large number of icebergs are presented in a small area, they report it as a cluster, combination of cluster and single iceberg, grid or zone. Single icebergs have the time and location information, concentration of sea ice immediately at the iceberg position, and the size and shape of the iceberg. Cluster observations follow similar reporting: time and location of the center of the cluster along with the radius. The number of icebergs and distribution of icebergs (left of track, right of track, or both sides of track) within the cluster are also provided, but they do not include targets smaller than 15 metre in length. If they have enough time, the icebergs are also categorized based on size and shape. Grid observations follow with confidence level, defined by both radar and visual, radar only, or visual only. Time and position along the track at the start point of the grid to the end point of the grid are given with the number and distribution of icebergs. Similar to clusters, zone observations provide confidence level, time, and location with the number of icebergs, disregarding bergy bits and growlers. They also record average concentration of sea ice with size and shape of the icebergs, if time permitted. During the survey, they also record ship locations and time followed by ship identifier and confidence level.

9.2.3 Adjustments to Iceberg Detections Based on Flight Data

9.2.3.1 Radar Swath Range

The IIP currently uses the HC-130J aircraft along with the main sensor ELTA-2022 360. The X-Band radar is capable of detecting and classifying marine targets by spanning 360° around the entire aircraft. Visual observations and the APN-241 weather radar are used to expand detection performance and an AIS receiver is used to assist in distinguishing icebergs from ships. PAL uses the similar technology on the DHS-8 aircraft with 360° maritime radar. The radar facilities have the ability to change the radar range based on requirements. When the radar range was unavailable, a standard radar value was arbitrarily assigned based on the year and aircraft type. In cases of iceberg detections, radar limits were defined by the confidence that a radar return would be obtained for all icebergs of different size and shape in that range. Sometimes icebergs that are easily visible or detectable by radar, but located beyond the radar limit, are also reported. In these cases, those targets can influence the areal density of that region by underestimating the iceberg frequency if included in the calculation. In the following example, shown in Figure 9-10 from March 16, 1998, the iceberg located at 50.4°W and 47.7°N was not counted because it was far beyond the radar limit, and the area was not fully visible.

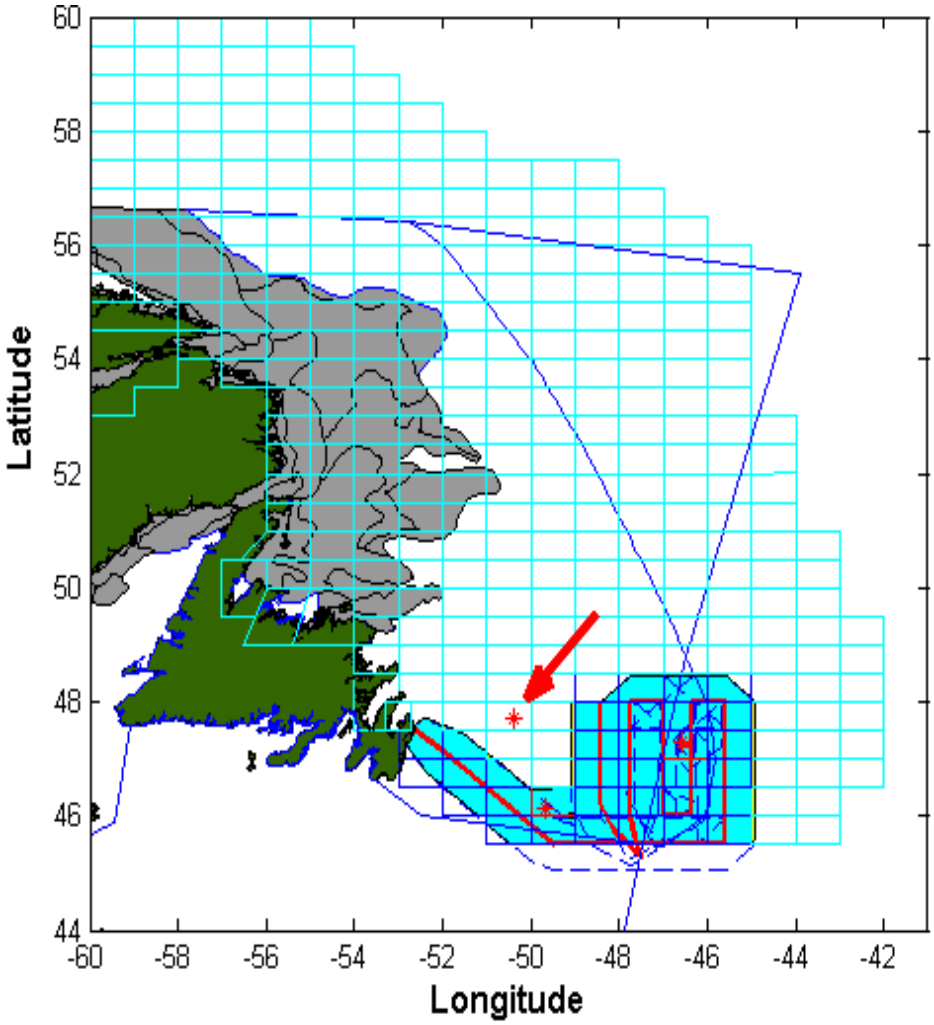

Figure 9-10. Example of an iceberg outside the radar limit

9.2.3.2 Iceberg Size

In the MANICE (2005) manual, sizes of the icebergs are grouped in seven categories. Growler and bergy bits are less than five m wide and six to 15 m length, respectively. The ranges of the length of the small, medium, large, and very large icebergs are 15-60 m, 61-120 m, 121- 200 m, and greater than 200 m. Any icebergs less than 15 metres in length were excluded from the analysis. Individual observations contain the size and shape in the message as well as cluster and zone observations. Unlike clusters and zones, grid observations do not report the total number of icebergs excluding bergy bits and growlers. Therefore, for the analysis of grid and unspecified iceberg size, all targets are assumed to be either smaller or larger. In the following example of June 30, 2004, three icebergs were located in the area shown in Figure 9-11, but two of them were growlers, with one located very near a large iceberg. Therefore, only one iceberg was considered for calculation within the region.

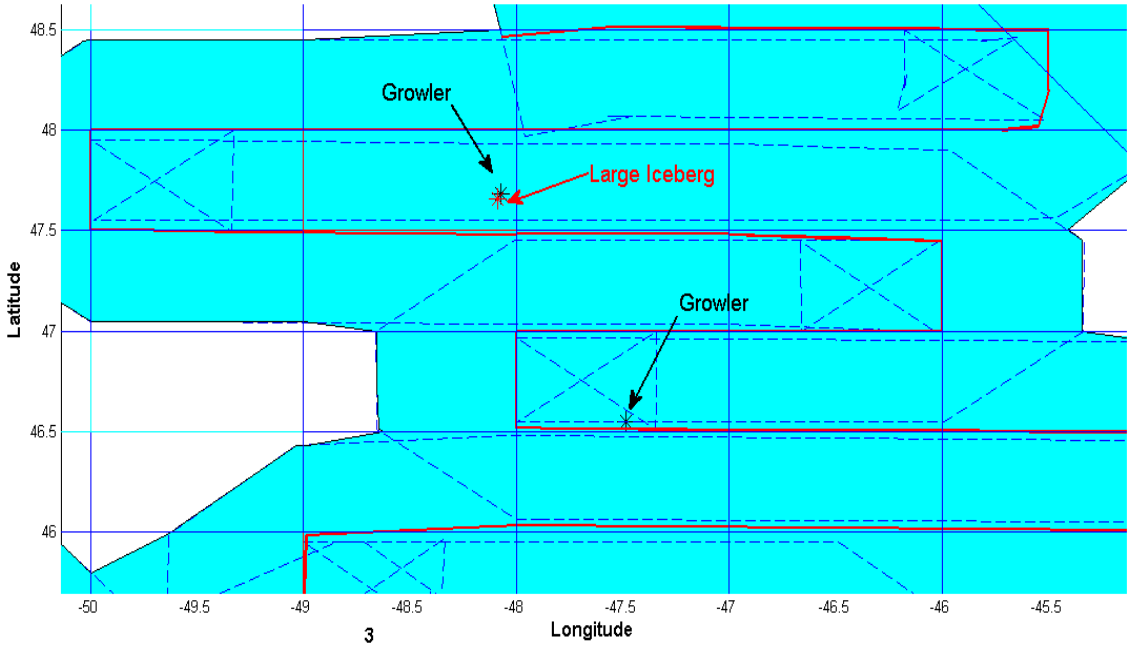

Figure 9-11. Icebergs excluded from analysis based on size

9.2.3.3 Icebergs in Pack Ice

The pack ice season on the Labrador Shelf usually starts in early November and continues to grow until May with maximum concentration near the shore. While flying over the sea ice, visual or radar confirmations of icebergs in pack ice become a challenge, which can lead to underestimation of the number of targets. As identifying icebergs in sea ice is difficult, and complications are involved in reliable detection, any iceberg located in sea ice with the concentration equal to or more than one tenth was not counted. Nevertheless, sometimes sea ice concentration is not provided for individual observations, and if time doesn't permit, sea ice concentrations are not recorded for clusters, grids, and zones. In these cases, the undetermined sea ice concentrations are considered as open water. To resolve this issue, CIS pack ice charts were compared with aerial reconnaissance data to eliminate any icebergs in sea ice from being included in the analysis. Concentrations of pack ice were also limited to ice free or open water, limiting the pack ice concentrations to less than 10%. Diagrams of ice concentrations from aerial perspectives as given in Manice (2005) are shown in Figure 9-12.

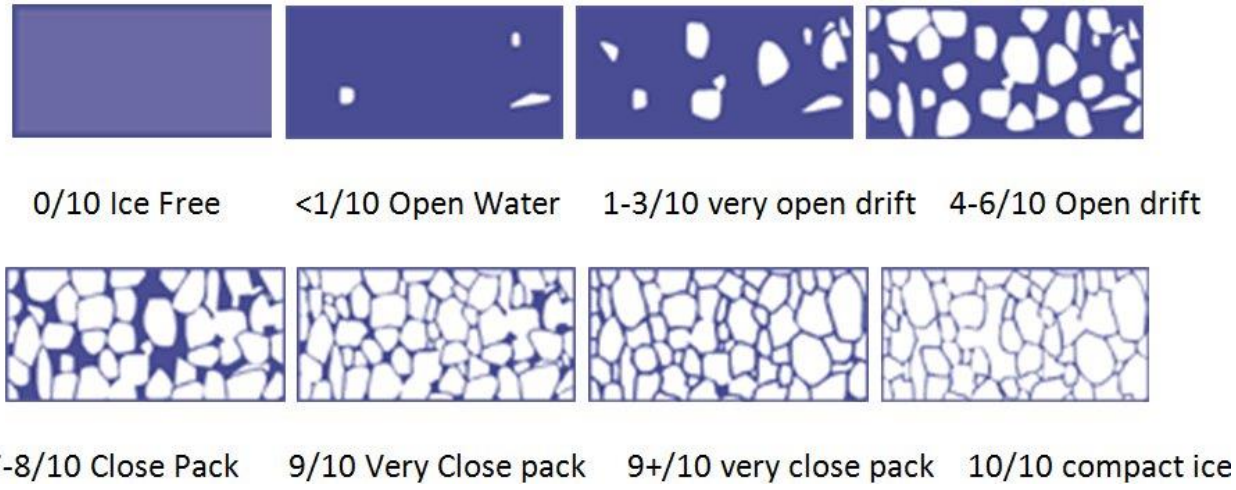

Figure 9-12. Pack ice concentration designations (MANICE, 2005)

In the following example, a total 61 icebergs were reported in the survey on March 3, 2008 (Figure 9-13.a) among which only 40 icebergs were presented in open water or reported as unidentified sea ice concentration in aerial reconnaissance data (Figure 9-13.b). Following a comparison with CIS pack ice chart for the same day, the total number of icebergs in open water was reduced to five (Figure 9-13.c).

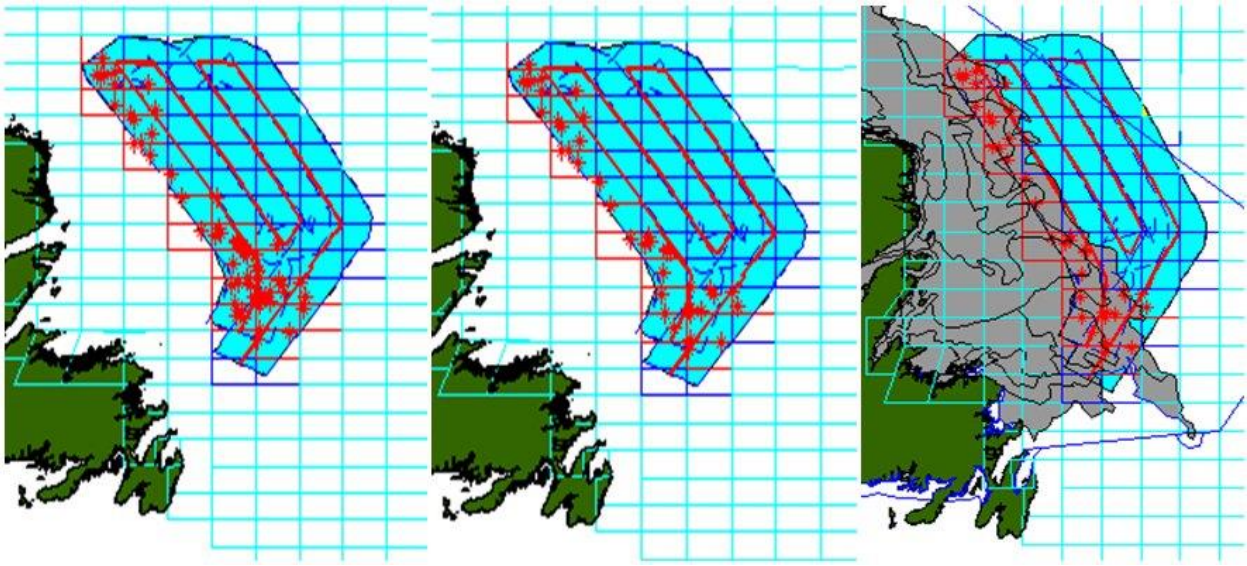

Figure 9-13. Aerial reconnaissance flight track for (a) Total icebergs, (b) Excluding the icebergs in sea ice, (c) Comparing sea ice chart and flight data

9.3 SATELLITE DATA ANALYSIS

9.3.1 Data Source

Satellite radar data were used to detect iceberg targets in ice-free waters. Radar is well suited for this study area because it is an active remote sensing technique (it emits its own source of electromagnetic radiation) allowing day and night data acquisition. The longer radar wavelengths used can penetrate most precipitation, fog, and cloud cover. Freely available European Space Agency's (ESA) Envisat (Figure 9-14) Advanced Synthetic Aperture Radar (ASAR) imagery was used as the data source (Table 9-2). Satellite data were available from January 2003 to April 2012, when the Envisat satellite went offline. The satellite had a sun synchronous polar orbit with a 35-day repeat cycle. Wide swath mode (WSM) imagery was acquired for this project using C-band frequency in HH polarization mode. Next, ESA SAR Toolbox (NEST) software was used to perform radiometric and geometric calibration on the ASAR images. The processed images have an approximate swath width of 400 km and a radar resolution of 150 m.

Figure 9-14. ESA Envisat Satellite

Table 9-2. Specification of Envisat ASAR

Parameter	Value
Orbit	Sun-Synchronous
Repeat Cycle	35-day
Frequency	C-band
Polarization	HH
Swath Width	400km
Radar Resolution	150m
Pixel Spacing	75m
Image Mode	Wide Swath Mode (WSM)

9.3.2 Data Overview and Analysis

The processed imagery was analyzed using C-CORE's Iceberg Detection Software (IDS), an automated process to detect targets from radar imagery. The software adaptively determines a threshold within a region to determine targets based on logic that target backscatter is generally brighter than ocean backscatter (Figure 9-15). Each resulting target file is exported to a shape file and overlaid on the corresponding satellite image for quality checks (QC) by satellite/GIS analysts. Target backscatter values allow analysts to omit targets not likely to be icebergs, such as sea ice pieces and vessels. Only targets in open water were included in the analysis. Sea ice polygons are extracted as part of the QC process and later removed, along with land polygons, from the satellite footprint area for iceberg density calculations (Figure 9-16). Table 9-3 tabulates the number of ASAR images analyzed each month and year and Table 9-4 tabulates the number of ASAR targets detected each month and year. Figure 9-17 shows the number of satellite footprints intersecting each cell and Figure 9-18 shows all targets detected from satellite imagery. Targets from all years were merged by month for density calculations. Using GIS techniques, the areal coverage of each satellite footprint within each Nalcor grid cell was calculated and used in the iceberg density analysis.

Table 9-3. ASAR image counts summarized by month and year

	2003	2004	2005	2006	2007	2008	2009	2010	2011	2012	Sum	Avg
Jan	21	13	14	12	11	6	6	5	11	11	110	11.0
Feb	0	14	7	4	9	6	7	3	5	10	65	6.5
Mar	4	10	6	9	6	1	10	5	3	12	66	6.6
Apr	12	7	14	4	8	3	11	4	5	10	78	7.8
May	1	8	6	12	11	5	12	3	8	NA	66	7.3
Jun	2	17	10	11	7	4	6	5	4	NA	66	7.3
Jul	8	3	5	2	3	2	8	5	5	NA	41	4.5
Aug	26	4	4	7	6	2	8	4	6	NA	67	7.4
Sep	1	4	4	0	7	2	7	3	3	NA	31	3.4
Oct	0	1	5	1	4	4	6	5	0	NA	26	2.9
Nov	1	4	8	4	3	3	5	8	9	NA	45	5
Dec	3	21	8	4	4	6	7	5	7	NA	65	7.2
Sum	79	106	91	70	79	44	93	55	66	43	726	
Avg	6.6	8.8	7.6	5.8	6.6	3.7	7.8	4.6	5.5	10.75		

Table 9-4. ASAR target counts summarized by month and year

	2003	2004	2005	2006	2007	2008	2009	2010	2011	2012	Sum	Avg
Jan	8	5	0	9	5	10	0	0	7	2	46	4.6
Feb	0	4	3	4	4	7	4	1	2	0	29	2.9
Mar	1	80	3	6	3	0	1	0	6	12	112	11.1
Apr	50	3	11	6	15	1	5	0	5	46	142	14.2
May	17	67	0	730	17	107	116	10	57	NA	1121	124.6
Jun	48	1071	116	1000	82	97	207	65	110	NA	2796	297.3
Jul	191	22	13	17	139	24	254	83	145	NA	888	100.6
Aug	410	10	23	135	61	24	73	24	15	NA	775	86.1
Sep	4	0	4	0	30	0	8	5	5	NA	56	6.2
Oct	0	2	4	0	0	3	12	1	0	NA	22	2.4
Nov	1	14	5	10	1	0	5	12	7	NA	55	6.1
Dec	4	22	4	6	0	2	9	0	4	NA	51	5.7
Sum	734	1300	186	1923	357	275	694	201	363	60	6093	
Avg	61.2	98.0	15.9	160.1	29.8	22.9	57.8	16.8	31.7	15		

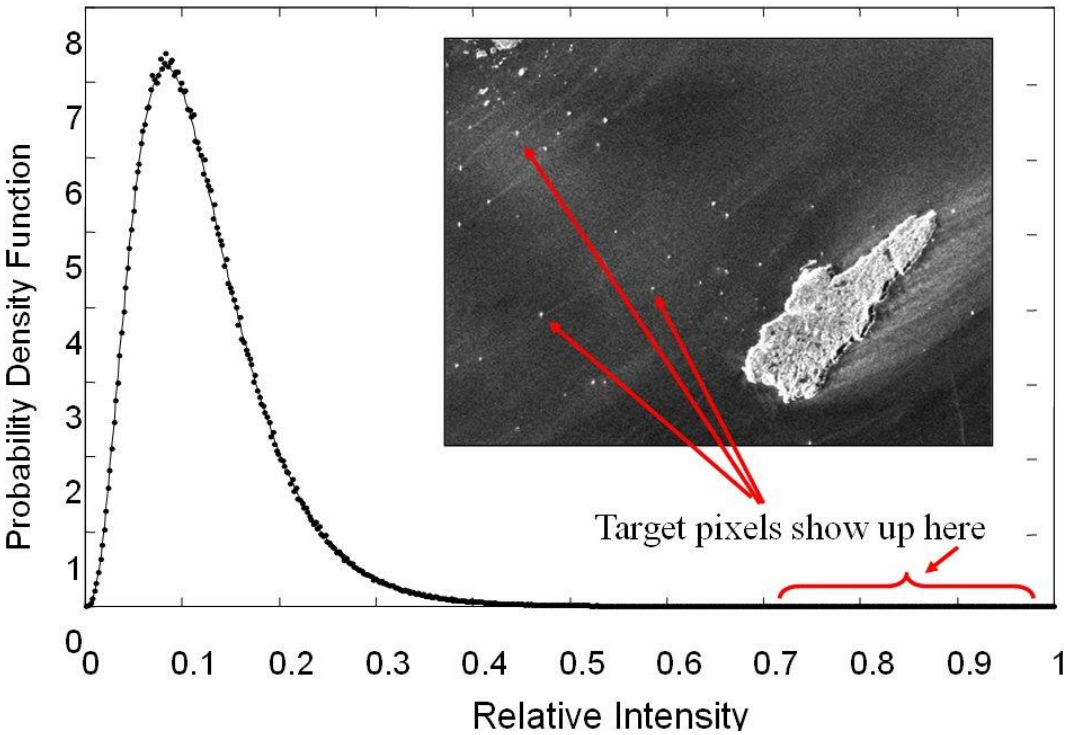

Figure 9-15. Distribution of radar backscatter and location of target pixels

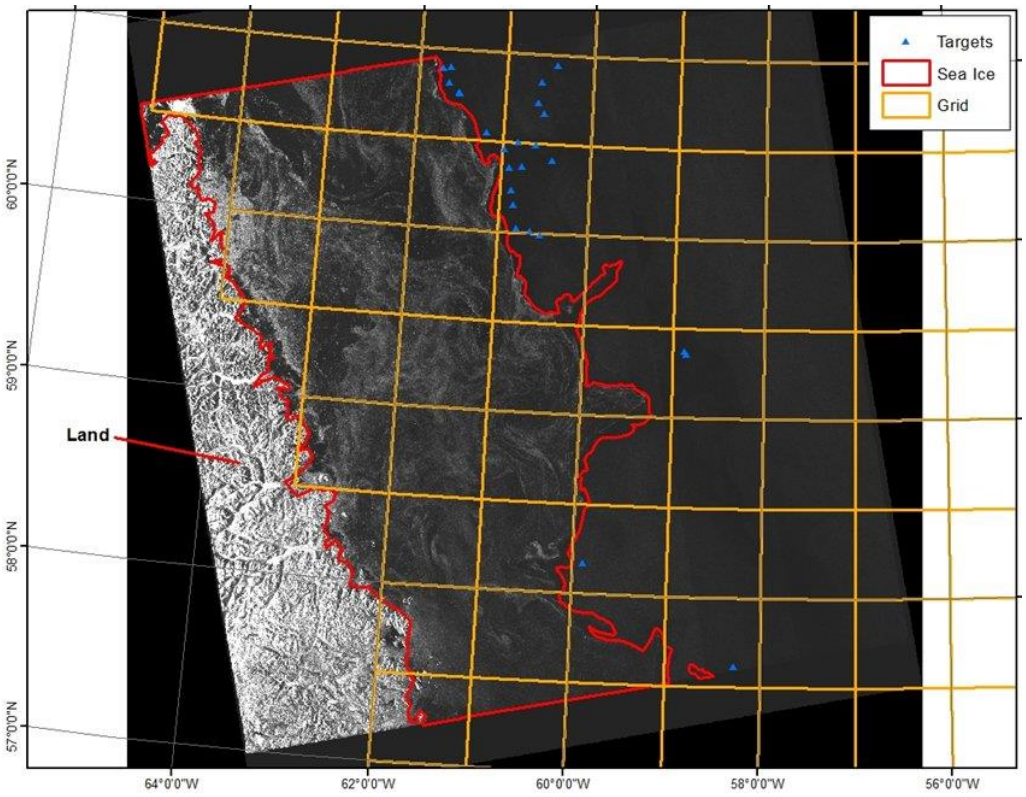

Figure 9-16. Envisat image with sea ice delineated

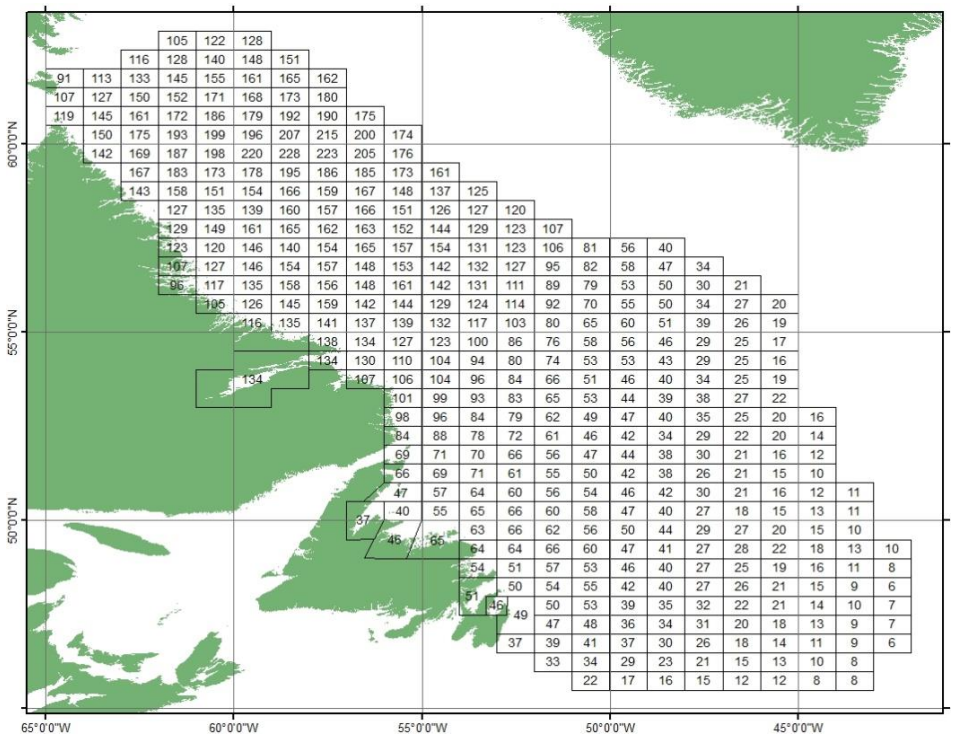

Figure 9-17. Total number of satellite footprints intersecting each cell

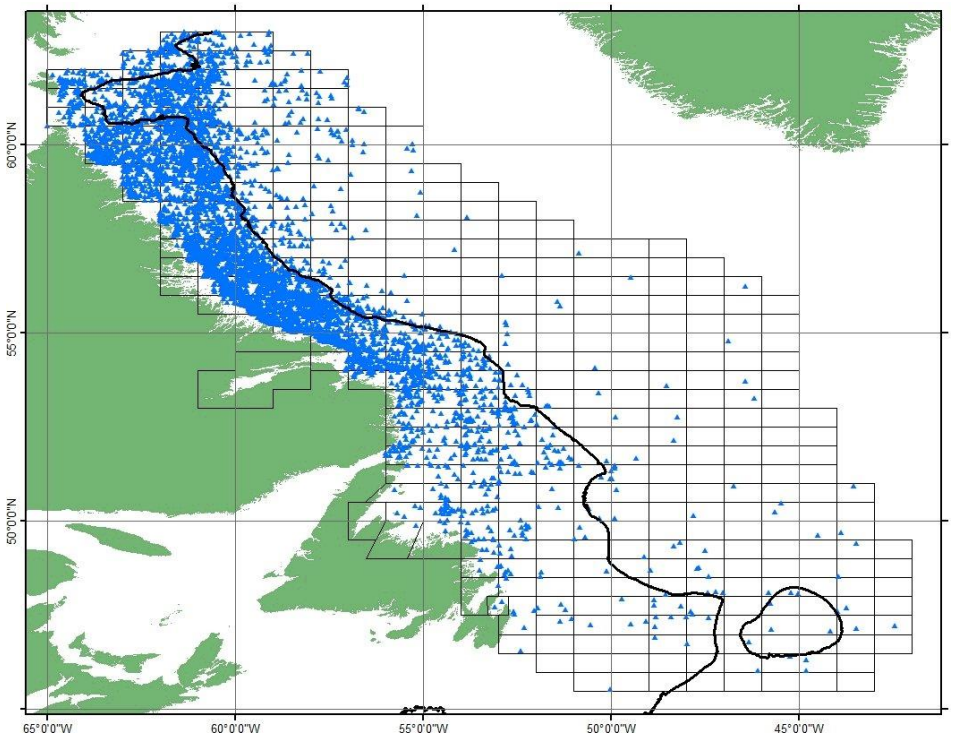

Figure 9-18. All Targets detected from satellite imagery

9.3.3 Limitations of Satellite Radar Data

There are a number of shortcomings with using satellite radar data to detect icebergs. First, radar images tend to have a near-nadir brightness zone where backscatter is too high to detect targets; however this only includes a small area of the overall image (Figure 9-19).

A simple scenario in open water with low sea state can be seen in Figure 9-20. As the sea state gets higher, ocean clutter statistics become brighter and detecting icebergs can become more challenging. Limitations become apparent with icebergs which have smaller sizes or shapes, and which produce lower backscatter returns (such as dome or tabular).

Likewise, detecting icebergs surrounded by sea ice can present comparable challenges. Returns from sea ice can also generate similar bright returns, and detecting icebergs and distinguishing them from sea ice can be difficult. This can be seen in high and low concentrations of sea ice as shown in Figure 9-21 and Figure 9-22. Figure 9-21 shows a low-resolution image containing pack ice and icebergs. In this image, the concentration of pack ice generates high background statistics and presents a challenging scenario to detect icebergs. Figure 9-22 shows a scenario of bright icebergs in an area with a lower concentration of sea ice. In this case, bright icebergs can be detected. However, the potential for false alarms can be high because of the risk of detecting bright sea ice pieces as iceberg targets.

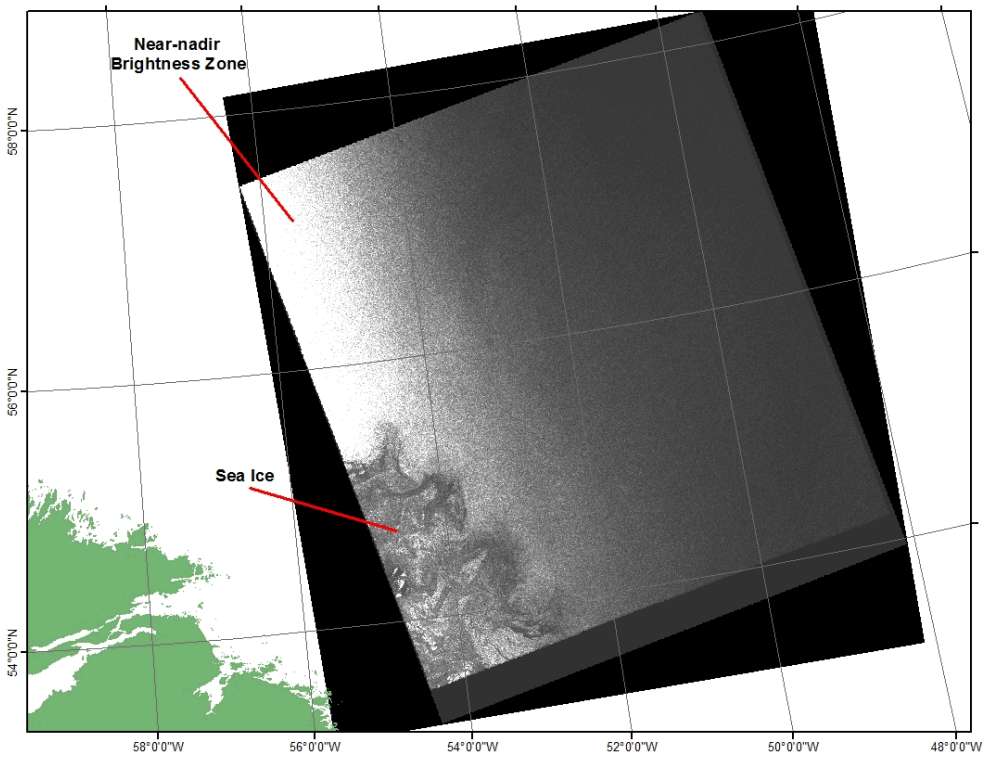

Figure 9-19. Envisat ASAR WSM image showing the near-nadir brightness region

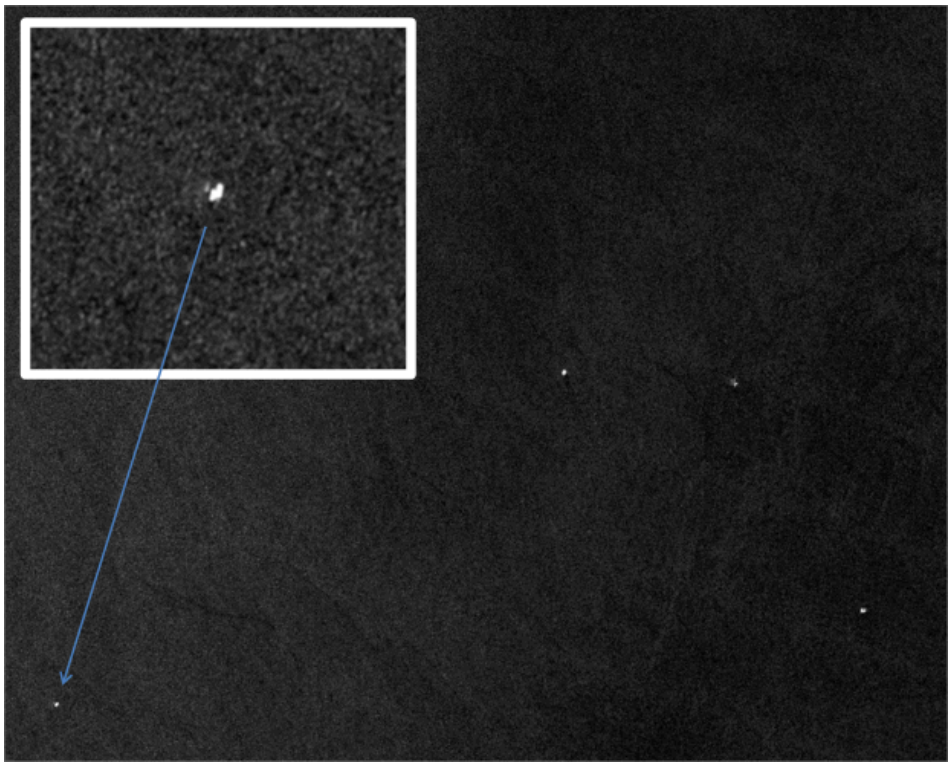

Figure 9-20. Icebergs in open water in TerraSAR-X 18 m resolution image

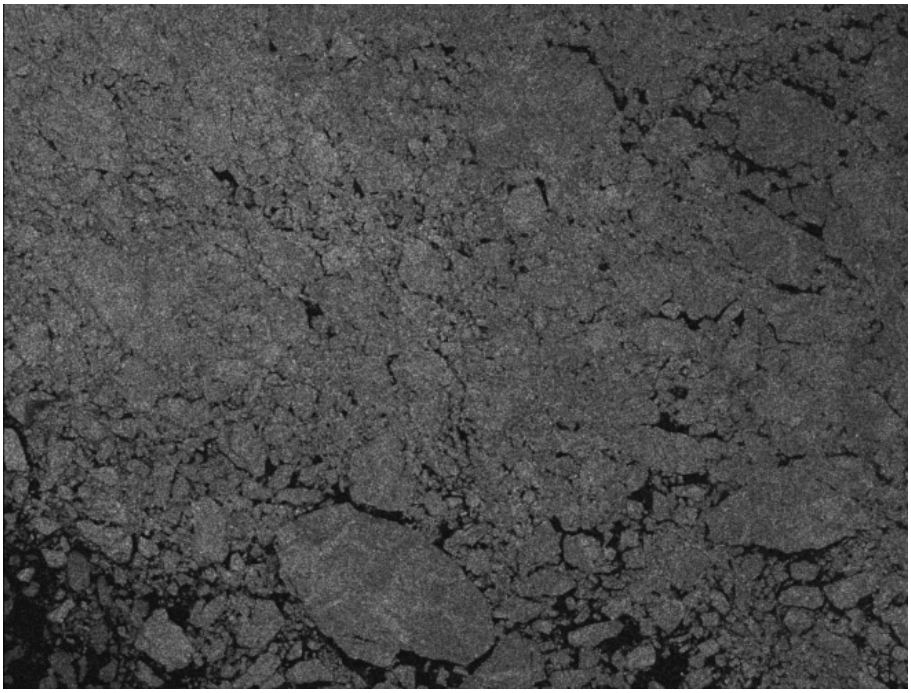

Figure 9-21. Pack ice and icebergs in a RADARSAT-2 ScanSAR Wide HH polarization 100 m resolution image

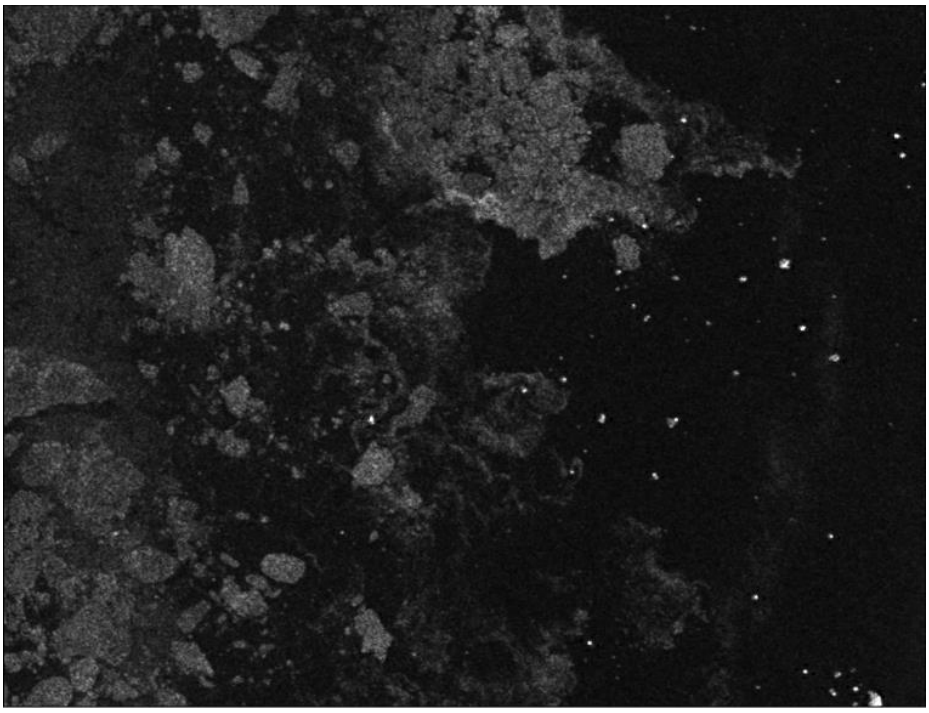

Figure 9-22. Sea ice and icebergs in a RADARSAT-2 ScanSAR Wide HH polarization 100 m resolution image

Detecting icebergs along the edge of sea ice can also present challenges. Often at the edge of sea ice, small pieces of sea ice exist, generating bright returns similar to icebergs. Discrimination between these features can be challenging with respect to representing accurately iceberg populations. Figure 9-23 and Figure 9-24 show examples of this in both low- and high-resolution SAR images respectively.

There are conditions in which icebergs can be detected quite well in sea ice. These situations include icebergs that have open water leads in the surrounding sea ice. Open water leads tend to provide higher confidence in iceberg discrimination from surrounding sea ice. Examples in low- and high-resolution SAR imagery are shown in Figure 9-25 and Figure 9-26 respectively.

Although information can be extracted from SAR data regarding sea ice and iceberg conditions, extracting accurate iceberg population statistics within the presence of sea ice can be quite challenging in some scenarios. Factors such as sea ice type and concentration, as well as iceberg size and shape, all affect the capability to represent accurately a true iceberg population. It is expected as more data and ground truth become available for more advanced satellite sensors, more accurate population statistics can be achieved in the future. For these reasons, only iceberg targets in open water were detected from the satellite radar data collected for this project. Sea ice was digitized as polygons, and any targets within sea ice were removed from the target detection results.

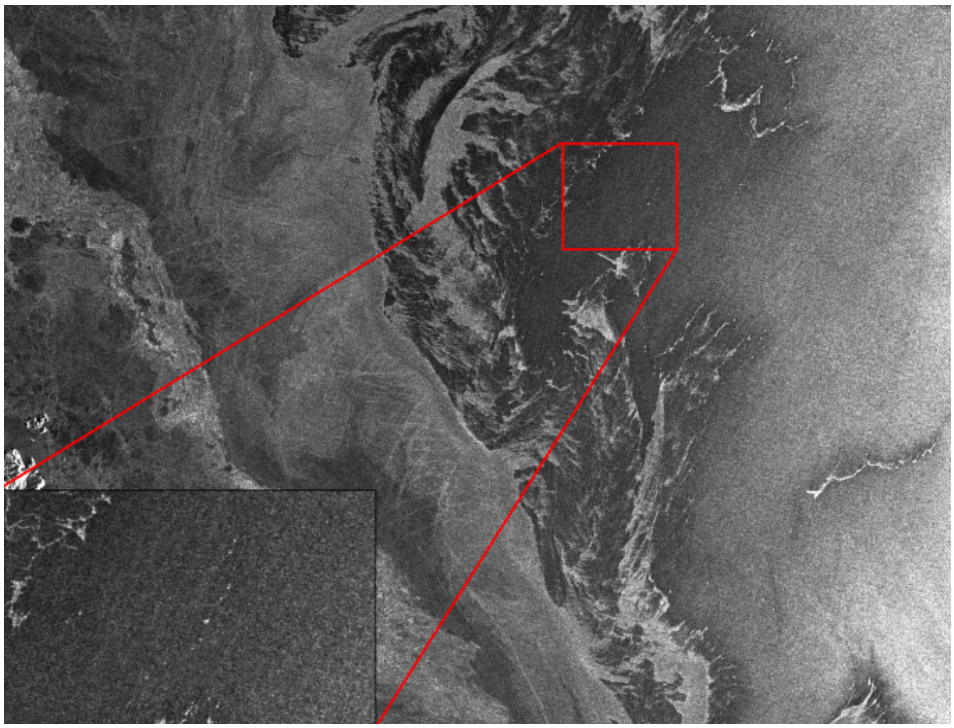

Figure 9-23. Icebergs and sea ice pieces along the edge of sea ice shown in an ENVISAT Wide Swath 150 m resolution image

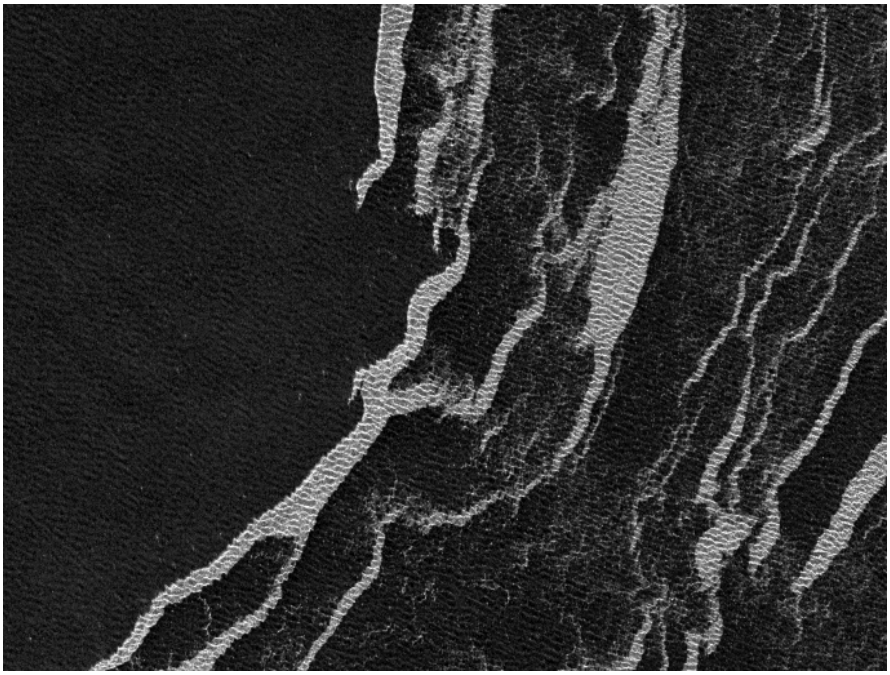

Figure 9-24. Icebergs and sea ice pieces along the edge of sea ice shown in a TerraSAR-X 18 m resolution image

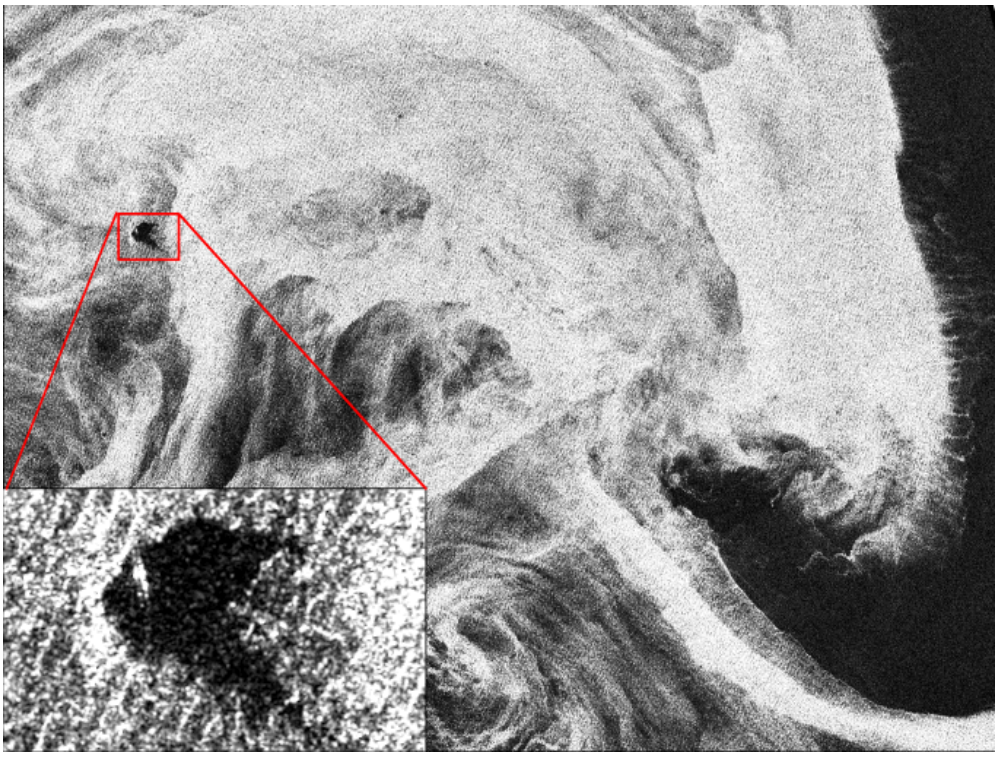

Figure 9-25. Iceberg with open water lead in sea ice in a RADARSAT-2 ScanSAR Wide HH Polarization 100 m resolution image

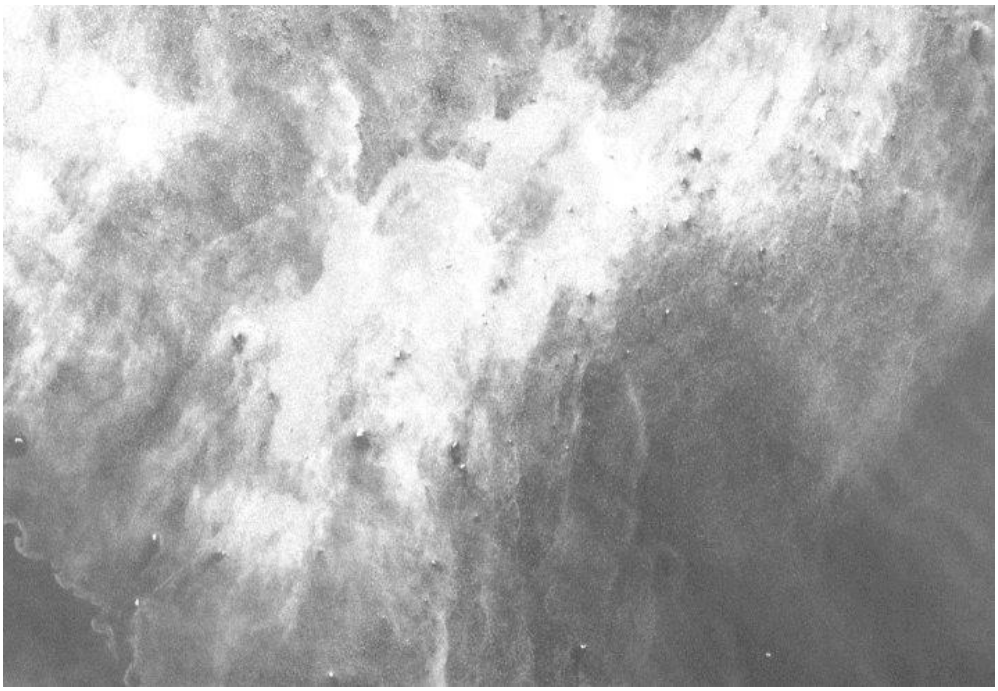

Figure 9-26. Icebergs and open water leads in sea ice in a Landsat 15 m resolution image

To compensate for smaller icebergs missed due to the 150 m resolution of the Envisat SAR, a comparison was attempted to determine a non-detection factor by comparing coincident satellite radar coverage and aerial surveys. A value of 7.5 was estimated by comparing target counts from a number of aerial and satellite data sets from the same area and date (+/- one day). Table 9-5 shows an example of total target counts from five different Envisat images and overlapping IIP MANICE targets. Total counts were only completed for cells that had complete Envisat and IIP data coverage (Figure 9-27). While it was thought to be high, this non-detection factor was not out of the realm of possibility. Subsequently, comparisons were made between iceberg densities determined for each study area cell using aerial and satellite data, and a non-detection factor of approximately four was found to be more appropriate and more in line with expected values based on experience in other regions. This lower value was adopted for correction of the satellite data and for blending of aerial and satellite data sets.

Table 9-5. Target counts from both IIP MANICE and Envisat detections. Each row represents an Envisat image and any IIP targets within the image.

Date IIP (YMD)	Date Envisat (YMD_HMS)	Total Count IIP	Total Count Envisat	Ratio
20070616	20070616_010852	47	5	9.40
20070616	20070616_010752	16	2	8.00
20070615	20070616_010752	7	3	2.33
20070510	20070509_010326	3	0	N/A
20070510	20070509_010224	6	0	N/A
Total		79	10	79 / 10 = 7.9

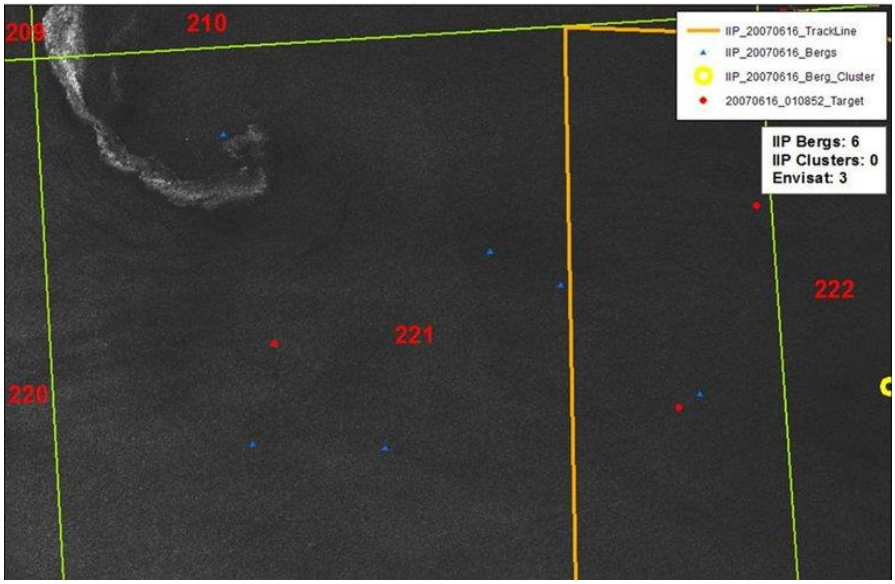

Figure 9-27. Example of IIP MANICE targets (June 16, 2007) overlaid on an Envisat ASAR image (June 16, 2007) for Cell 221.

9.4 ICEBERG FREQUENCY FOR STUDY AREA

The calculation of iceberg densities followed the same procedure for both the aerial reconnaissance and Envisat data. For each cell, the first step was to calculate average iceberg densities on a monthly basis. This was accomplished by going through each year from 1998 to 2014, determining the total number of icebergs observed in the cell for that month and year, as well as the total area surveyed, and calculating the density of icebergs. If no surveys (aerial reconnaissance flights or satellite swaths) covered the cell for that month and year, then that year was ignored in the calculation Note: this can potentially lead to conservative results, if there was a decision not to perform surveillance because it was a very light iceberg season. After going through the range of years, the final list of monthly iceberg densities was averaged to give an overall mean monthly density. This process was repeated for each month. The monthly means were then averaged to give an annual mean iceberg areal density. If any month had no data, then this month was left out of the calculation (again, conservative if iceberg surveillance is typically not performed during certain times of the year).

Figure 9-28 shows annual mean iceberg areal densities based on aerial reconnaissance data. The NaN values (Not a Number) on the northern and northeastern edges of the study area are cells without aerial reconnaissance data. Iceberg aerial reconnaissance is typically conducted on a seasonal basis, and therefore, these results are somewhat distorted as a result. For example, in cell 368 containing the Hibernia, Terra Nova, and White Rose developments (indicated with magenta dots on Figure 9-28) there were no aerial surveillance flights from August to December. Thus, if it were assumed that iceberg densities in those months were zero (a reasonable assumption), the average annual iceberg areal density would be reduced by a factor of seven-twelfths. However, this assumption, while valid over the Grand Banks, cannot be assumed to be valid on the Labrador Shelf where the iceberg season is longer and aerial reconnaissance is less frequent (or in some cases non-existent). Figure 9-29 shows annual mean iceberg areal densities based on Envisat data. Note that sufficient coverage was obtained over the entire study area so that no NaNs were produced. Results shown here do not include any non-detection factor.

Figure 9-30 shows the combined aerial reconnaissance and Envisat data. The calculation process was the same as outlined previously, except that the total number of icebergs used in the calculation was the total of the aerial reconnaissance sighting plus the number of Envisat sightings multiplied by the non-detection factor (four). The total area surveyed was the sum of the area covered by the aerial and satellite surveys. This approach weighted the final result to the data source providing the most information. In the case of the Grand Banks aerial analysis results discussed previously, this blending of sources provided values for the later part of the year when aerial reconnaissance is typically lacking.

Figure 9-31 gives an alternate presentation of Figure 9-30, with the iceberg density presented using a color-coded logarithmic scale. Figure 9-32 normalizes the iceberg densities by the iceberg density in cell 368 (Jeanne d'Arc Basin), giving iceberg densities relative to a known location with existing operations. This figure clearly shows that a majority of the cells in the deep-water basins have iceberg densities lower than cell 368.

Figure 9-33 shows iceberg densities for each season. Breaking the limited available data down by season produces coarser results than those shown in Figure 9-31. The influence of using only icebergs in open water can be seen in results for spring, north of 58°N, and near shore, where presumably no open water occurs during the spring. The patchy results for the fall and winter seasons reflect both the limited

number of icebergs as well the heavy reliance on low-resolution satellite data, due to limited aerial reconnaissance data during these seasons.

Figure 9-34 shows a comparison of iceberg densities obtained from the C-CORE (2007) analysis, which considered a combination of CIS charts, PAL surveillance flights, and IIP sightings (the last used to break degree square densities to half degree squares), against the average annual open-water iceberg areal densities derived from the analysis of aerial reconnaissance and Envisat data. It can be seen that near the coast, the areal density values are in fair agreement. When further away from shore, the densities in the more recent analysis decrease more rapidly than the earlier analysis.

This could be due to any number of reasons, but the control of the data sources and the analysis in the present study were better than the 2007 study, and therefore, the confidence in the more recent results is higher. It should also be noted that the C-CORE (2007) study drew on earlier data, and the more severe ice environment noted in the pack ice analysis may to some extent influence the differences in results.

Table 9-6 shows a data summary and an example areal density assessment for cell 368. The annual value is the mean of the monthly values, excluding months without data. If average densities for September and October were assumed to be zero, which is a reasonably safe assumption for this region, the annual average iceberg density would be reduced to 7.4 × 10-5 km-2. Ignoring null data in the iceberg density calculations represents conservatism in the approach.

Table 9-6. Data summary and calculation example for cell 368

Cell 368	Aerial Reconnaissance				Envisat ASAR				
Month	Years Data	No. Surveys	No. Counts	Total Area (km^2)	Years Data	No. Surveys	No. Counts	Total Area (km^2)	Combined Areal Density (km^2)
Jan.	1	1	0	3672	4	5	0	14752	0
Feb.	4	8	0	14883	4	5	0	13432	0
Mar.	11	32	2	44173	4	4	0	7160	4.55E-05
Apr.	12	67	29	47747	4	5	0	8638	5.15E-04
May	12	98	8	40794	0	0	NaN	NaN	1.87E-04
Jun.	13	51	2	43434	1	1	0	1477	3.41E-05
Jul.	8	22	0	29376	2	2	1	5921	1.13E-04
Aug.	0	0	NaN	NaN	2	2	0	6890	0
Sept.	0	0	NaN	NaN	0	0	NaN	NaN	NaN
Oct.	0	0	NaN	NaN	0	0	NaN	NaN	NaN
Nov.	0	0	NaN	NaN	2	2	0	8495	0
Dec.	0	0	NaN	NaN	3	4	0	12742	0
Annual									8.96E-05

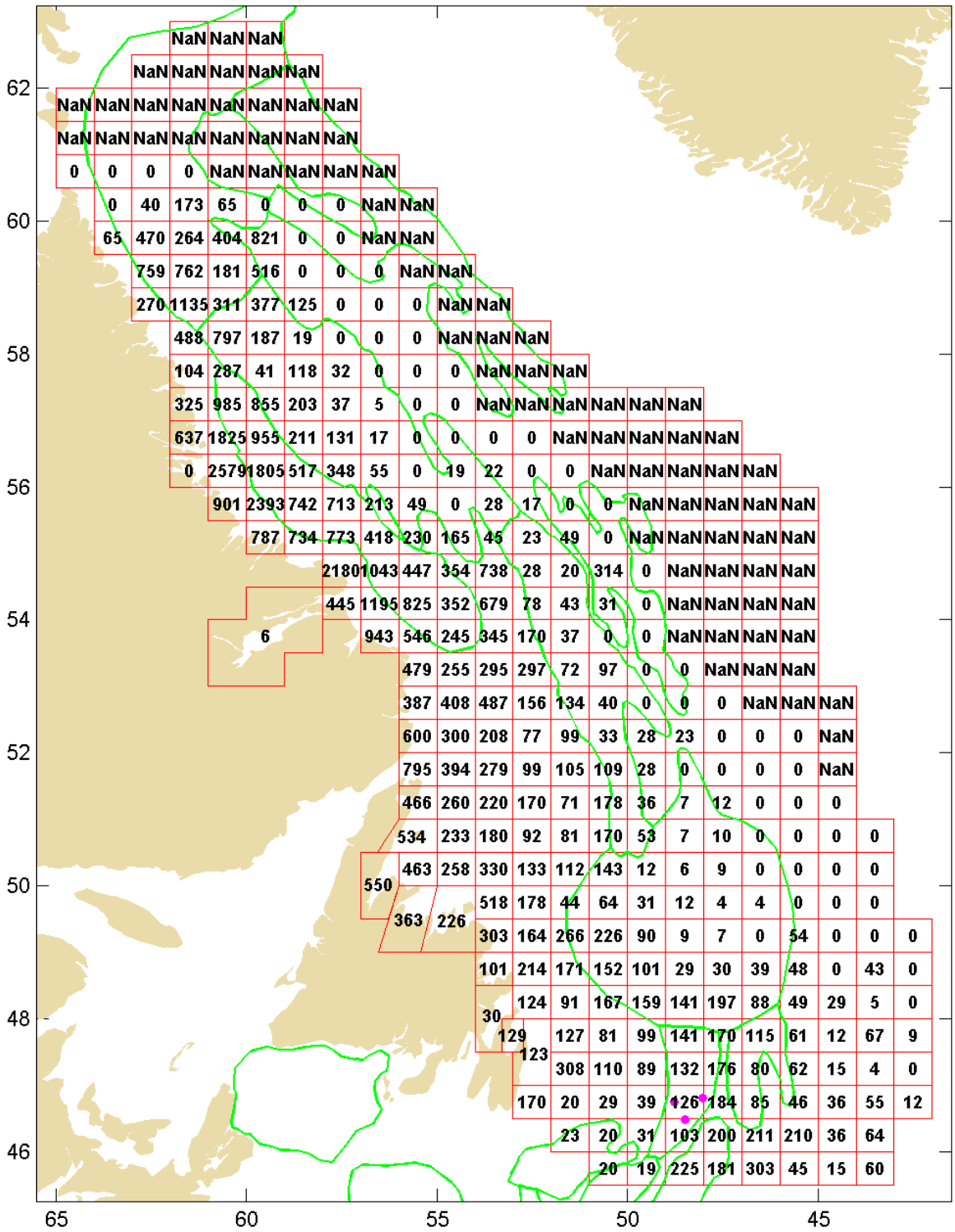

Figure 9-28. Average annual open-water iceberg areal densities based on the analysis of aerial surveillance data (density values ×10-6 km-2)

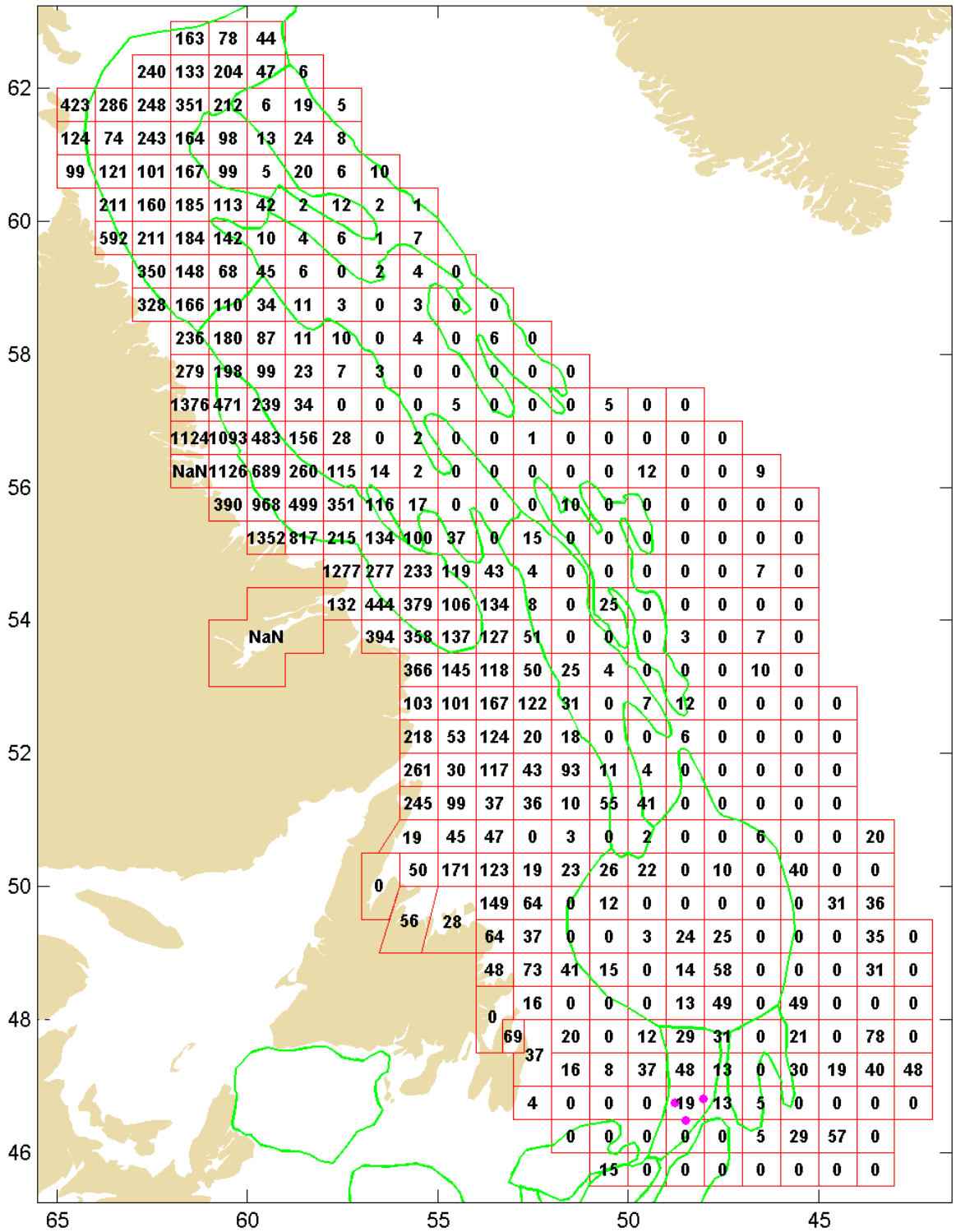

Figure 9-29. Average annual open-water iceberg areal densities based on the analysis of Envisat data (density values ×10-6 km-2), no non-detection factor applied

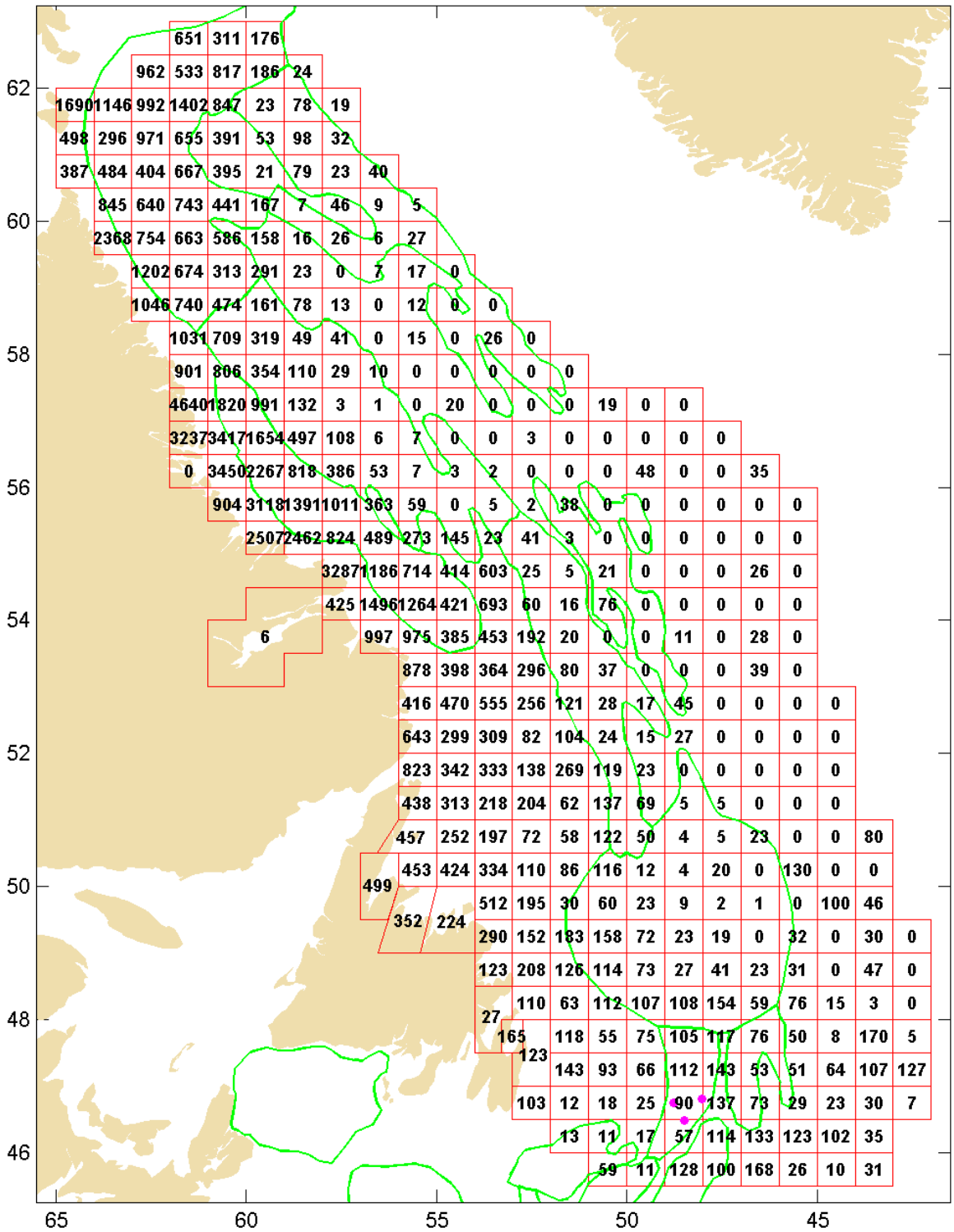

Figure 9-30. Average annual open-water iceberg areal densities based on combined aerial and Envisat data (density values ×10-6 km-2)

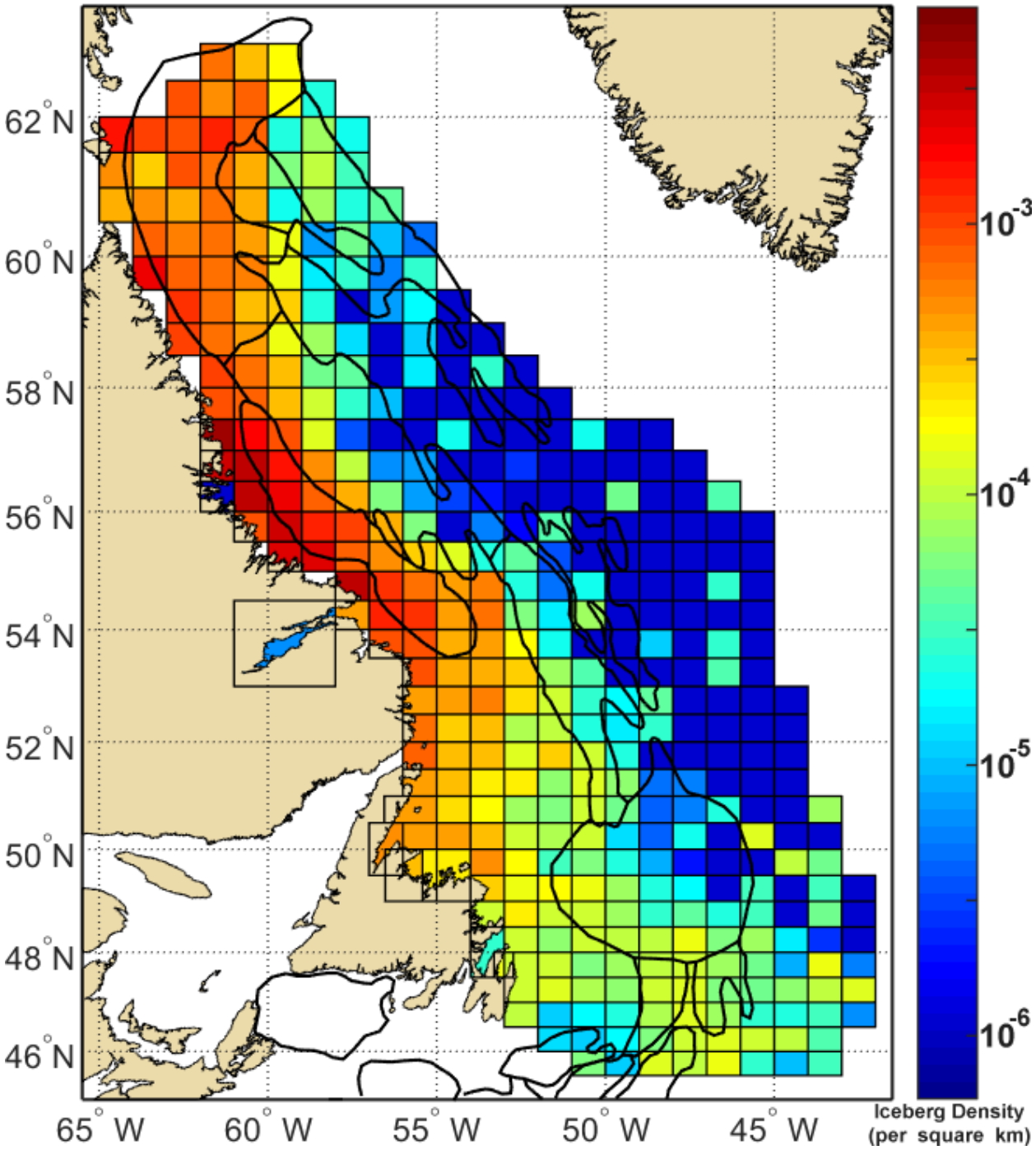

Figure 9-31. Average annual open-water iceberg areal densities based on combined aerial and Envisat data

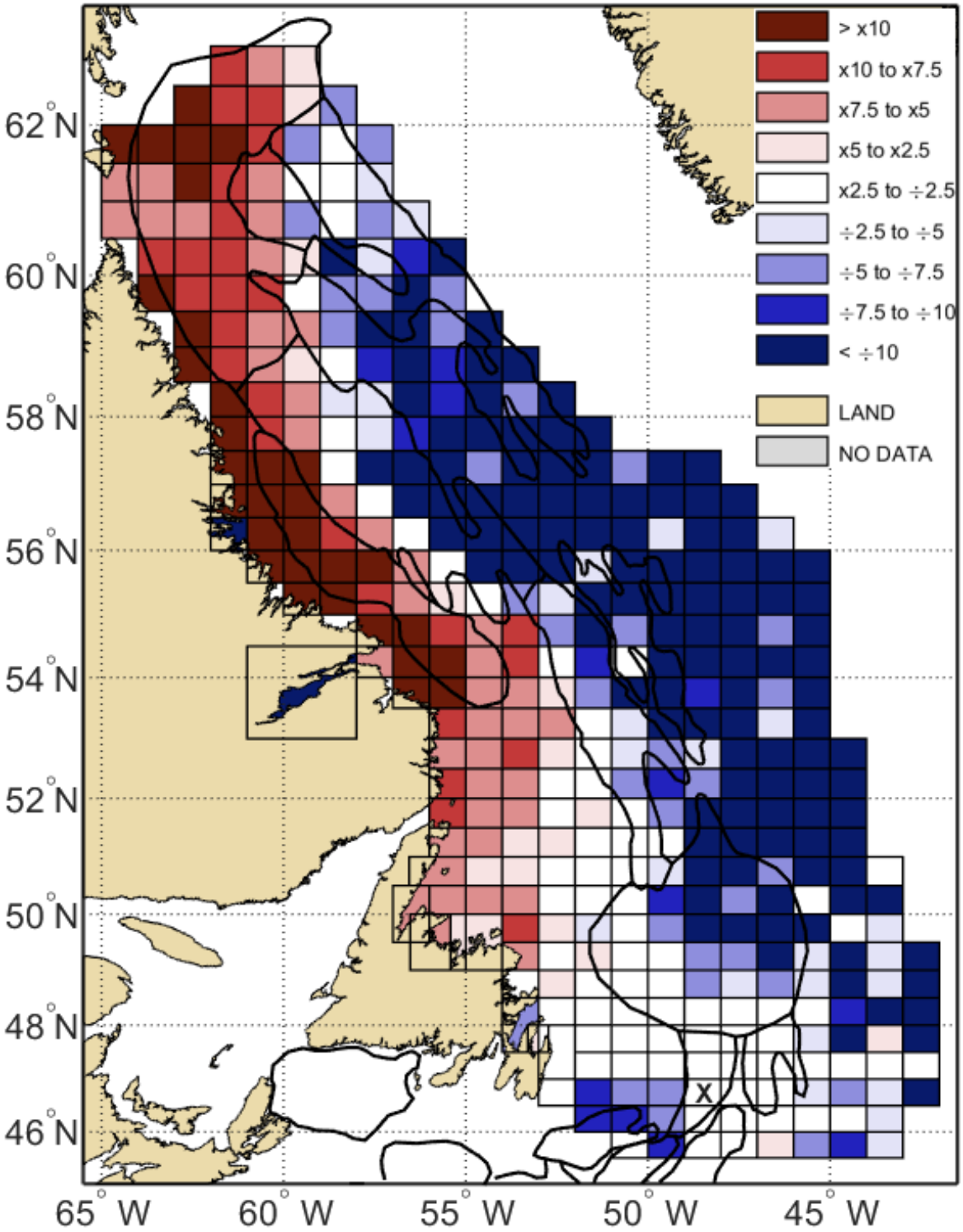

Figure 9-32. Average annual open-water iceberg areal densities normalized by value in cell 368 (containing Hibernia, Terra Nova and White Rose)

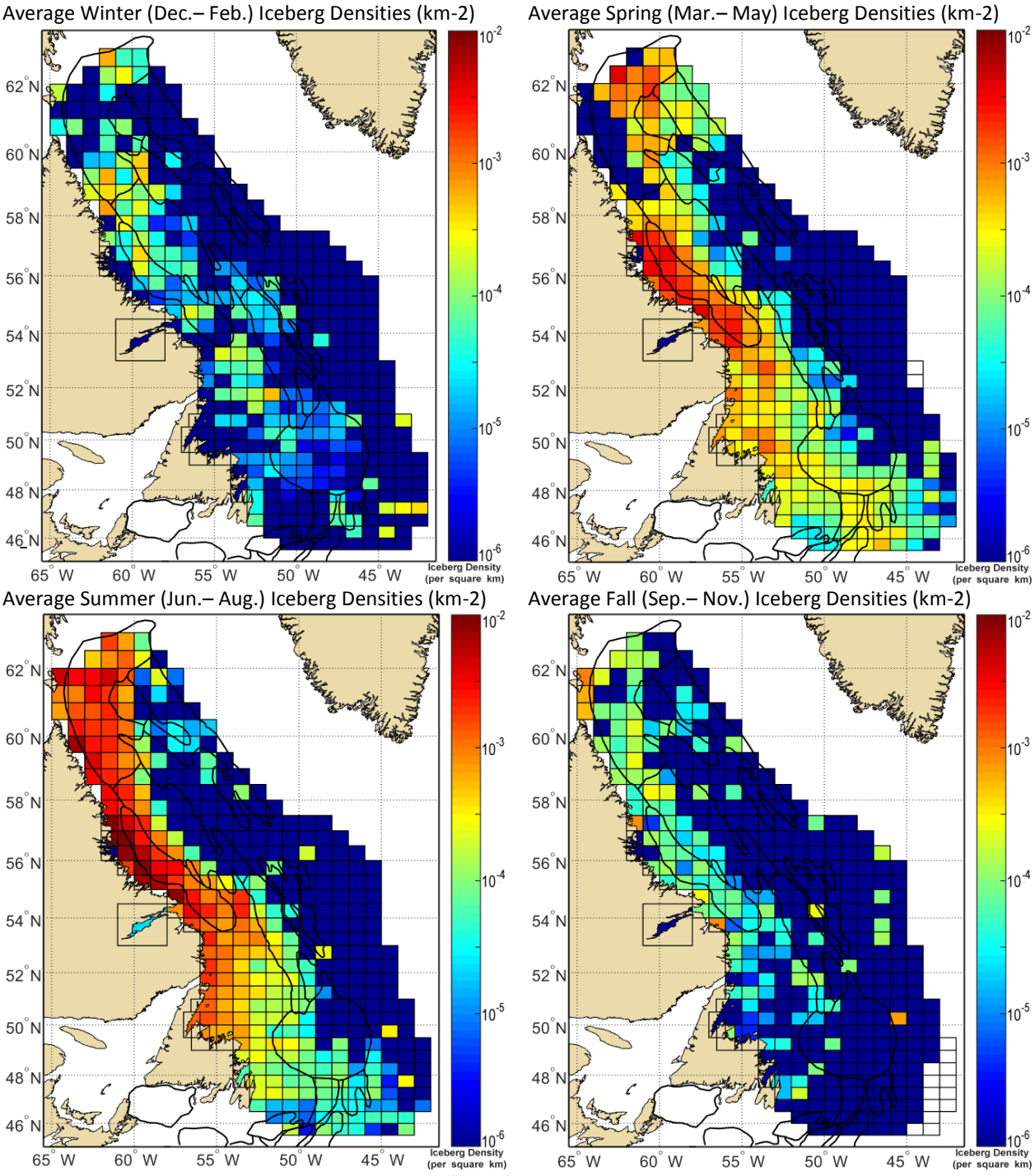

Figure 9-33. Mean seasonal iceberg densities (km-2)

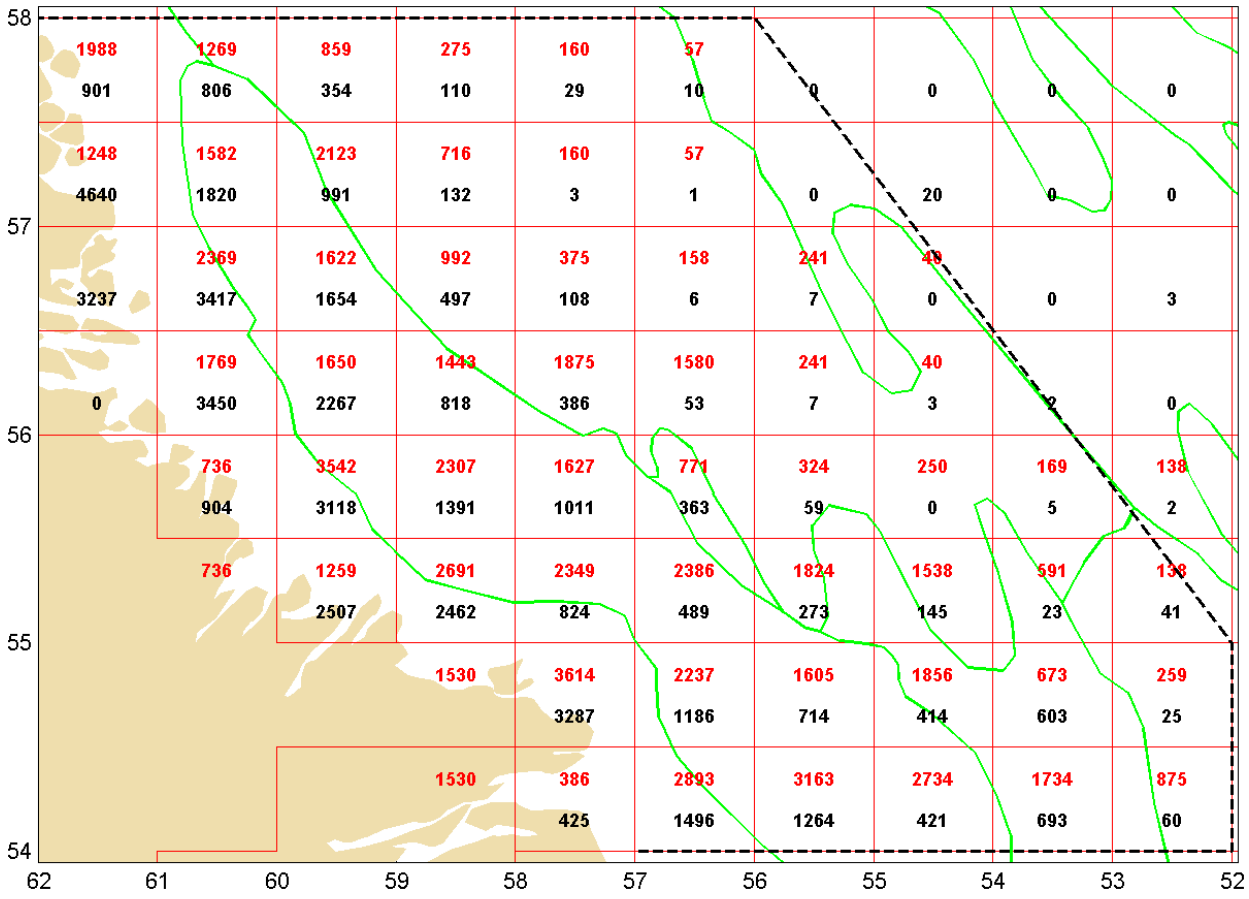

Figure 9-34. Comparison of average annual open-water iceberg areal densities from analysis of aerial reconnaissance and Envisat data (black values, bottom) with results from C-CORE (2007) analysis (red values, top), iceberg density values ×10-6 km-2

9.5 ICEBERG SIZE DISTRIBUTION

9.5.1 Introduction

Icebergs size is usually characterized in terms of waterline length, primarily because of the ease with which waterline lengths can be measured or estimated. Waterline length is defined as the maximum plan dimension of the iceberg at the waterline. The mean iceberg waterline length is used in the calculation of impact rates with surface structures. The waterline length (as well as mass, etc.) is also used in iceberg load calculations.

9.5.2 Grand Banks Iceberg Waterline Lengths

A relatively large data set, which includes some small ice pieces, is summarized in Fenco Newfoundland (1987). These data were collected on the Grand Banks during the period 1984 through 1987 as part of the routine ice observation and ice management procedures for the Husky/Bow Valley (HBV) East Coast

Project. A correlation, goodness of fit test revealed the HBV data are best represented using an exponential distribution with λ = 59 (Jordaan et al., 1995), see Figure 9-35. It is reasonable to assume the HBV data is representative of small, medium, and large icebergs (i.e. L ≥ 16 m), but this underestimates the frequency of bergy bits and growlers. Excluding the observed ice islands, recent iceberg data collected on and around the Grand Banks have continued to support this assessment

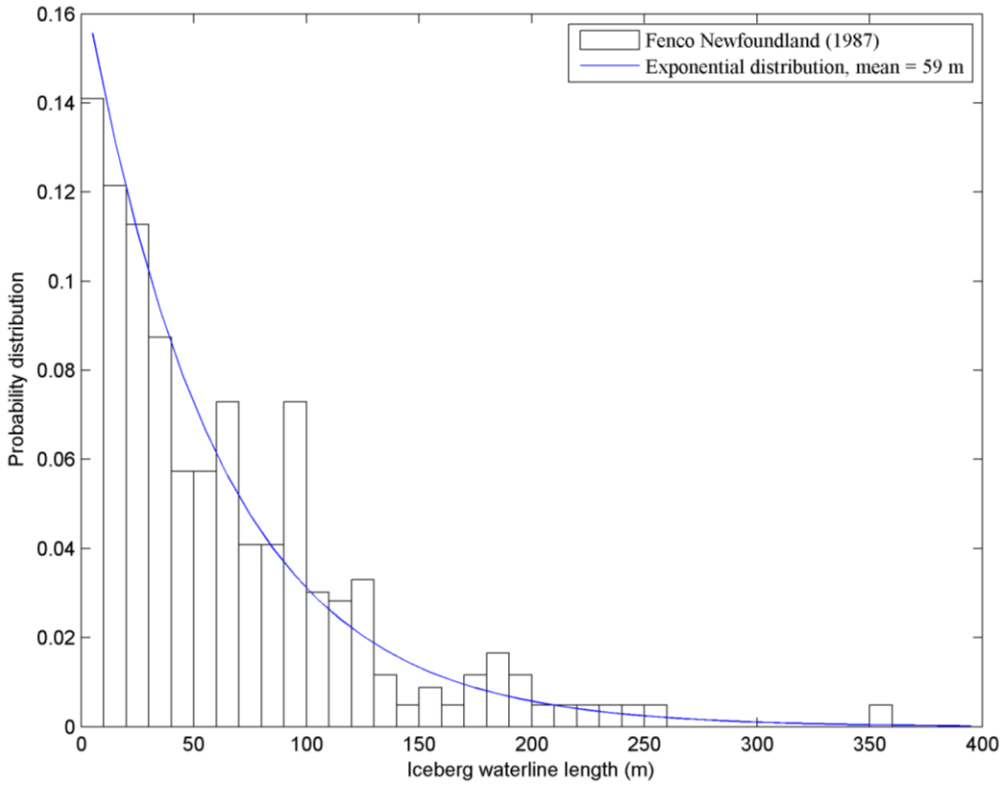

Figure 9-35. Husky/Bow Valley waterline length data with best fit exponential distribution

9.5.3 Offshore Labrador Iceberg Waterline Lengths

While an iceberg size distribution has been established for use in the Grand Banks region, an iceberg length distribution for use on the Labrador Shelf has not been firmly established. Several iceberg surveys have been conducted offshore Labrador, including:

- The 2006 Labrador iceberg survey program was conducted as part of an evaluation of the capabilities of dual-polarization synthetic aperture radar (SAR) for the detection and classification of icebergs (King et al., 2009)
- Above-water dimensions for 607 icebergs were obtained from aerial surveys over the Labrador Sea during the spring of 1979 (Petro-Canada, 1983)
- Observations collected during drilling operations (PAL, 2005)
- An iceberg survey performed in support of Voisey's Bay operations (C-CORE, 1998).

These various data sets are described in King et al., (2009), with locations of surveys and distributions shown in Figure 9-36. To summarize, iceberg size surveys of Labrador have exhibited extraordinary variation. Very high quality, unbiased surveys along predetermined survey lines taking stereo aerial photographs (Petro-Canada, 1983) have produced iceberg data sets with small mean waterline lengths (37 m), while other surveys have produced mean waterline lengths on the order of 95 m (PAL, 2005). If iceberg size class designations given by the IIP are considered (Figure 9-36, right) the result is very similar to the distribution developed for the Grand Banks. A similar result is reached if data sets are combined. Until better data are available, the Grand Banks values may be used, but additional data collection is recommended.

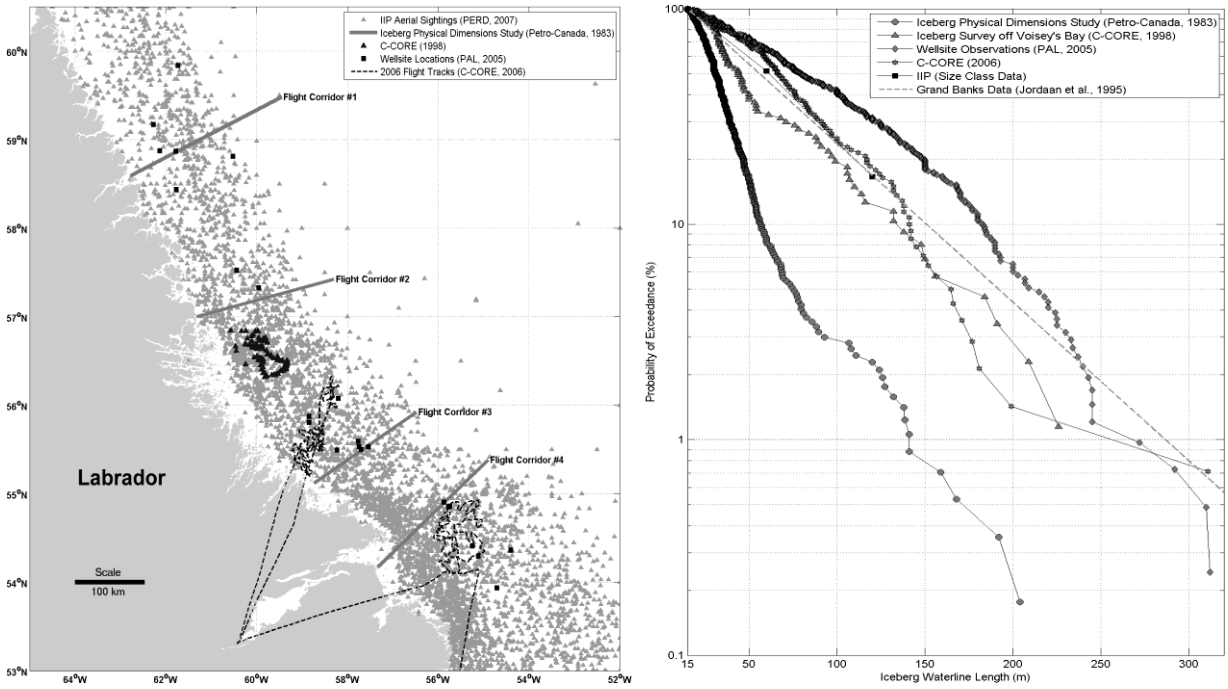

Figure 9-36. Labrador Iceberg size data (locations left, distributions, right) from King et al., 2009

9.5.4 Iceberg Size Distribution from Aerial Reconnaissance Data

In the Manice (2005) manual, sizes of the icebergs are grouped in seven categories. Growlers and bergy bits are the smallest icebergs, as they are less than five metres and 15 metres in length, respectively. Small icebergs vary from 15 m to 60 m waterline length. Medium icebergs range from 61 m to 120 m waterline length and large icebergs from 121 m to 200 m. Any icebergs beyond 200 m waterline length are classed as very large. For visual comparison, the size of bergs compared to everyday structures is illustrated in Figure 9-37. Based on all available data, the percentage of very large icebergs is very low compared to the other categories. Therefore, the large and very large icebergs are grouped together as large icebergs in this analysis. As before, growlers and bergy bits are excluded from the size distribution analysis as only single icebergs (individual observation) were considered, there being very limited numbers of cluster or zone observations with iceberg size information.

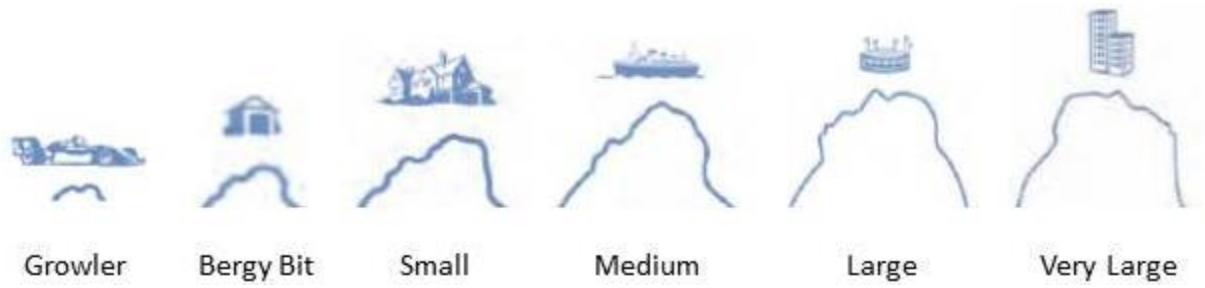

Figure 9-37. Iceberg size class comparisons (Manice, 2005)

Initially, the iceberg size distribution was analyzed from two perspectives: change of iceberg size according to location and time of the year. In the case of size distribution based on location, water depth of the iceberg position was considered as an input as well as sea ice concentration. If the water depth of the iceberg location was less than 100 m or located in sea ice, the iceberg was not considered. The focus was to consider targets located in deeper water free of pack ice, as large icebergs are unlikely to reach shallow water. Iceberg size distributions, as percentage and total number of icebergs, are plotted against latitude in Figure 9-38. Most iceberg observations are between 46°N and 56°N. In this range, the proportion of medium size icebergs decreases from north to south, whereas the proportion of small icebergs is highest around 51°N. As expected, from north to south the proportion of large icebergs decreases, but south of 52°N, the proportion increases. It is assumed that the observed variations are due to the deterioration process, but the exact mechanisms leading to the observed trends are unknown at this point.

All open water icebergs were considered for monthly analysis of iceberg size distribution. As shown in Figure 9-39, there is sufficient number of icebergs from April to July to compare confidently the distributions during these months. The medium icebergs show a clear trend from February to August. In this period, the proportion of medium size icebergs increases linearly. In April and May, higher numbers of large bergs are observed, but the number decreases abruptly in June. In the same month, the number of small icebergs increases significantly compared to May, but the percentage of small bergs decreases again in July. This is believed to be the result of breakage of large bergs into smaller bergs in June and deterioration processes that melted away smaller bergs in July. However, it is unclear why the percentage of large icebergs increased in July.

The iceberg size class data were given additional consideration to determine whether it would give any further insight into the mean iceberg size over the study area. Excluding those identified as radar targets, 9,577 icebergs in the available aerial reconnaissance data were assigned to the various iceberg size classes. Of the 391 study area cells, 177 (45%) have no size class data and roughly one-third of the cells have 10 or more size class records. Figure 9-40 shows the number of icebergs with class sizes assigned per cell and Table 9-7 gives the total number of records for each size class and the percentages of the total. Also shown are the proportions that would be expected for an exponential distribution with a mean of 59 m (Jordaan et al., 1995). The exponential distribution, typically used for iceberg waterline length, gives decreasing proportions of icebergs with increasing iceberg size; however, the iceberg size class data from the aerial data have substantially more in the medium size class than the small, which is inconsistent with the exponential distribution. This may be due to a systematic bias in observations (i.e., small icebergs being missed or misclassified as medium).

Table 9-7. Total iceberg size classifications from aerial surveillance data

Size Class	Number	Percentage of Total	Percentage for Exponential Distribution with Mean of 59 m
Small (15 to 60 m)	2,995	31.3	54.1
Medium (61 to 120 m)	4,311	45.0	29.2
Large (121 to 200 m)	2,109	22.0	12.4
Very Large (> 200 m)	162	1.7	4.3
Total	9,577	100	100

An attempt was made to fit the observed iceberg size data to an exponential distribution by generating large (106) samples with varying mean values, determining the numbers falling in the various size categories (excluding growlers and bergy bits). The sum of the differences between modeled and observed percentages for each size class was calculated as shown in Figure 9-42, showing a minimum total error (sum of absolute values) for a mean iceberg waterline length of 99 m, compared with the 59 m estimate from Jordaan et al. (1995). Considering data south and north of the Strait of Belle Isle separately gave very similar results. Figure 9-43 shows a comparison of the observed and simulated results per size category. All of the simulated results give similar proportions for the medium size bin, yet are still significantly lower than the observations, again suggesting some sort of bias in the observations. Figure 9-43 shows the estimated mean iceberg size (mean waterline length) per cell using exponential distribution fit.

An alternate approach is to combine results by assigning the mean waterline length for each size class, using 37.5 m for small icebergs, 90.5 m for medium icebergs, and 160.5 m for large icebergs. Very large icebergs with no upper size are excluded, which is a minor issue as these are relatively rare compared to the other size classes. Using the combined data shown in Table 9-7, this gives a mean iceberg length of 89 m, which is still high compared with the Jordaan et al., (1995) estimate, but could conceivably be used as a conservative number for facility impact calculations. Results obtained for study area cells using this approach are shown in Figure 9-44.

Both approaches shown here for estimating mean iceberg size from the aerial reconnaissance iceberg size class data give values generally ranging from 80 m to 100 m. Cells that deviate from this range generally have lower numbers of iceberg size class data to use in the estimation process. The available size class data does not allow mean iceberg size to be estimated on a cell-by-cell basis. For areas that are well characterized, such as the northeast Grand Banks and surrounding area, a mean of 59 m is reasonable. For areas with limited data, a more conservative value (i.e., 100 m) may be used for impact rate calculations.

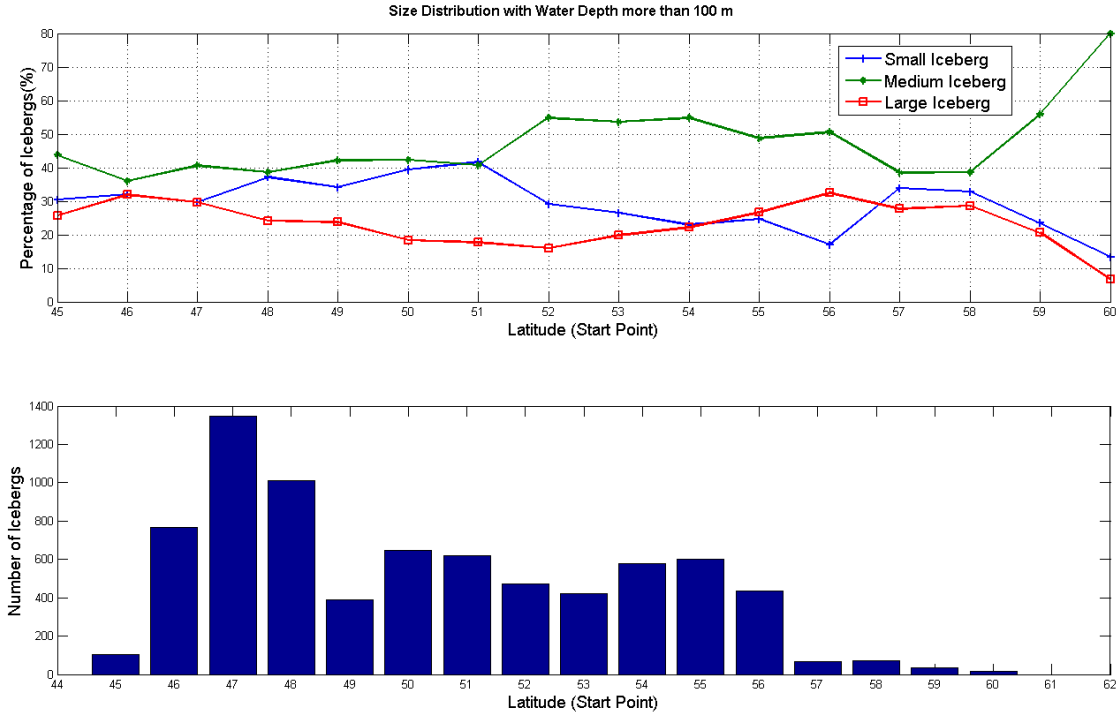

Figure 9-38. Iceberg size distributions and total number of icebergs per latitude with water depths > 100 m

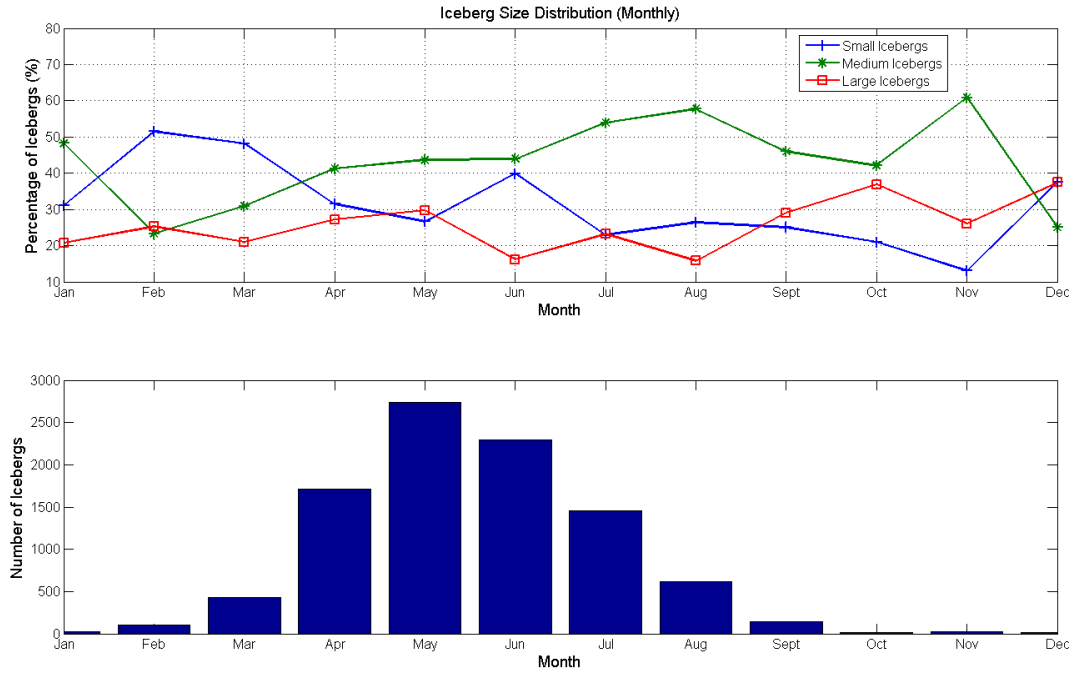

Figure 9-39. Monthly iceberg size distributions and total number of icebergs per month

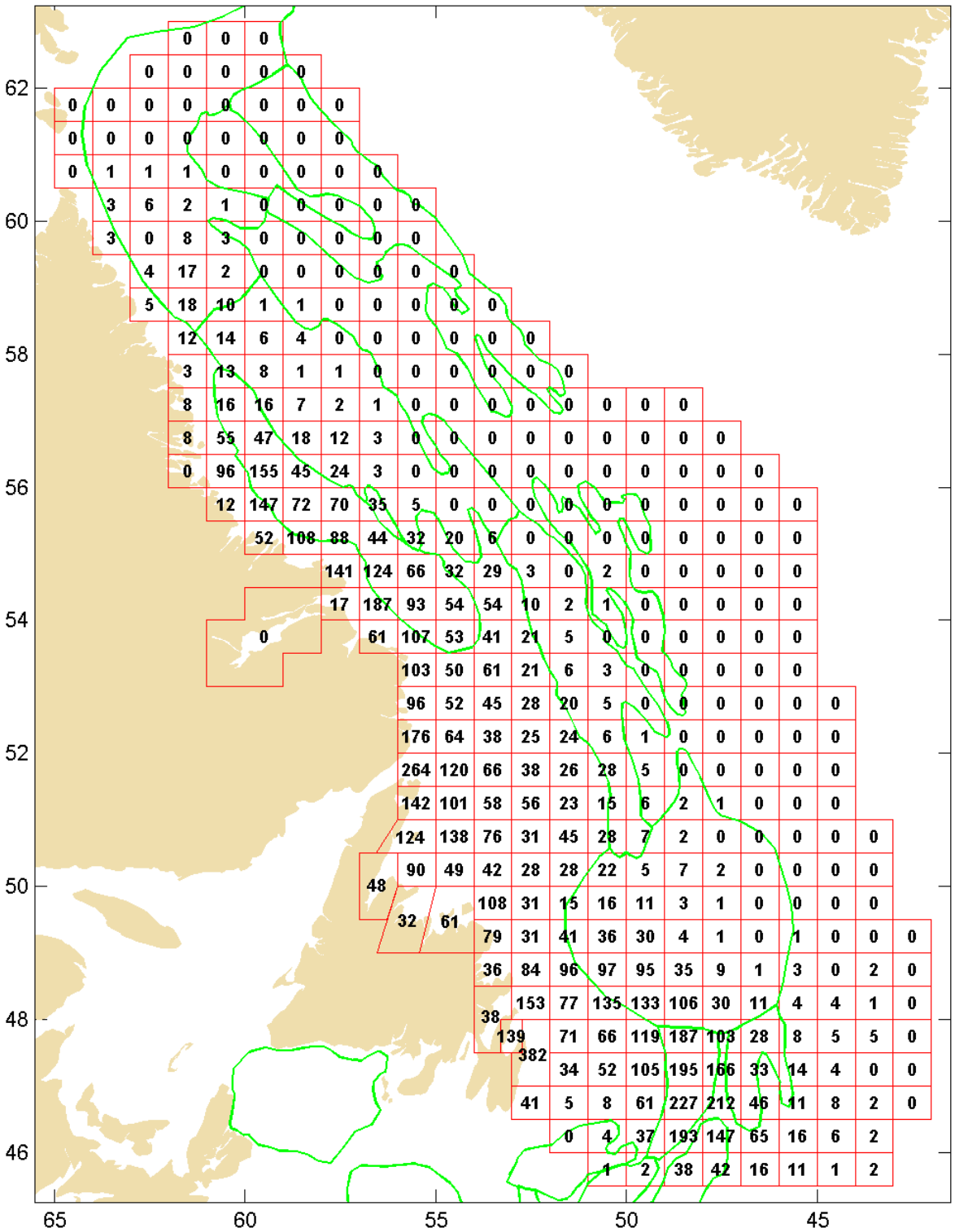

Figure 9-40. Number of icebergs assigned size classes per cell in aerial reconnaissance data

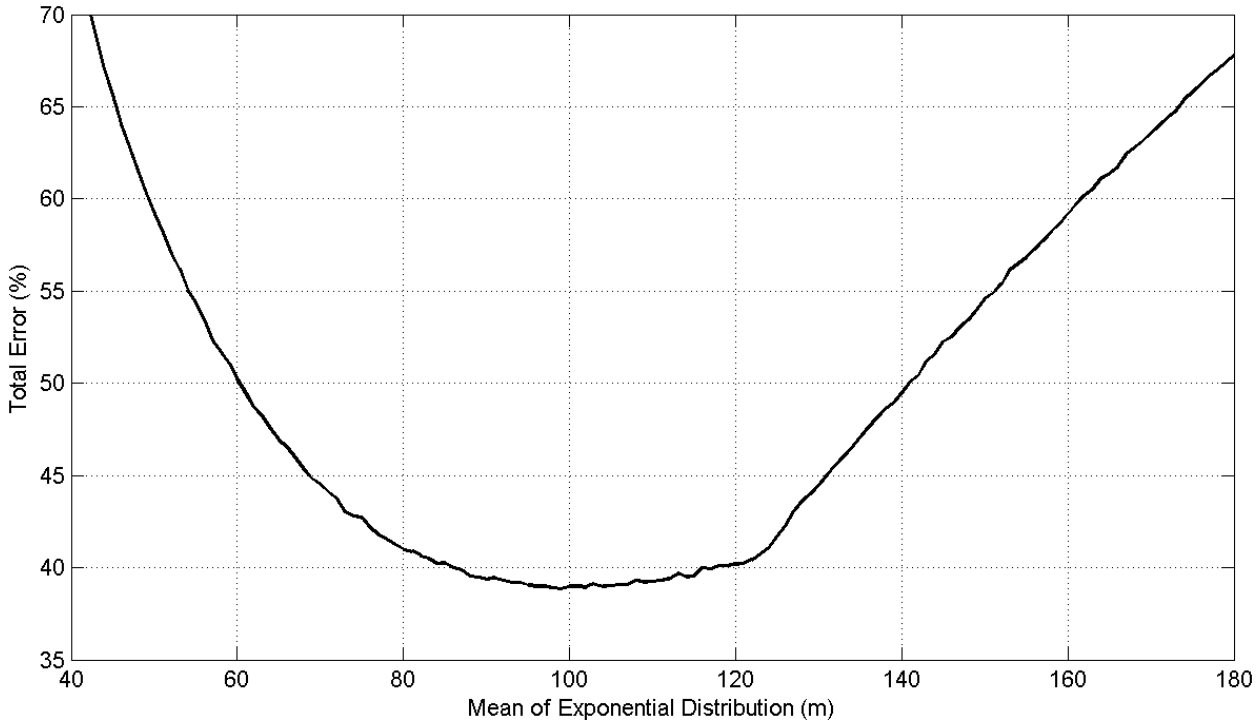

Figure 9-41. Number of iceberg size classifications per cell from aerial reconnaissance data

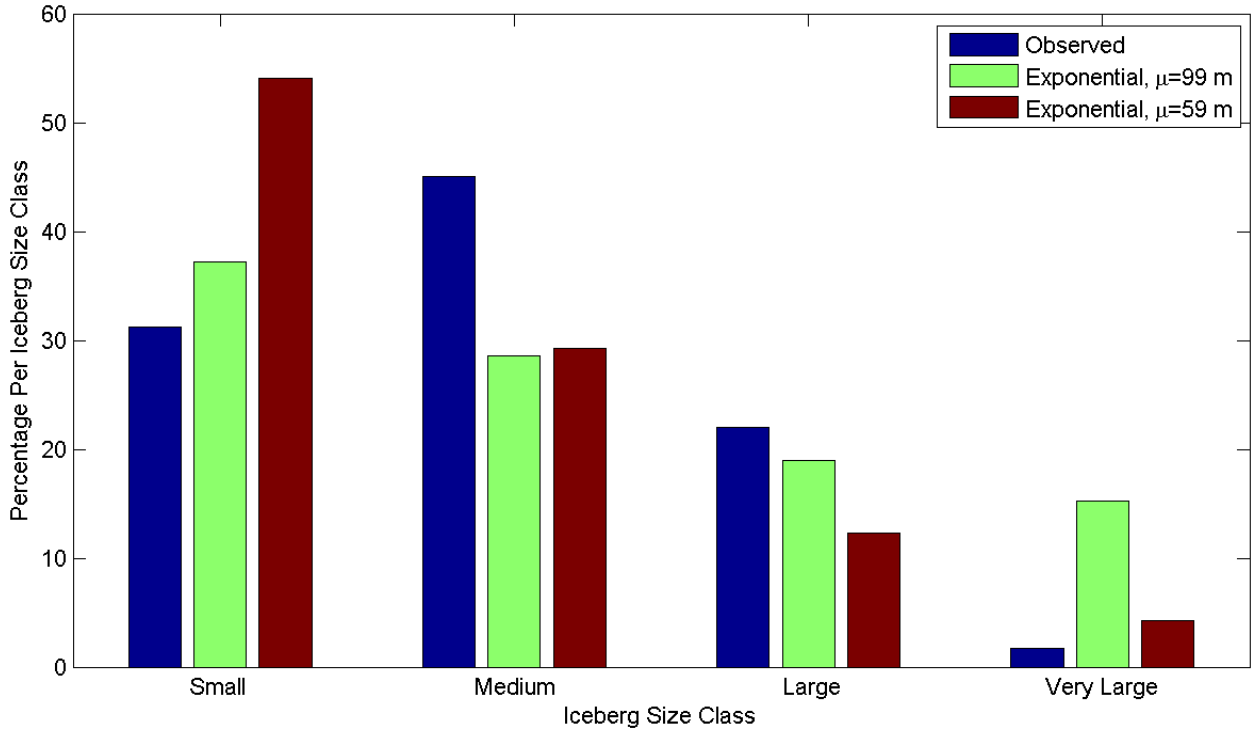

Figure 9-42. Comparison of observed percentage per size class with exponential distributions of waterline length with means of 99 and 59 m

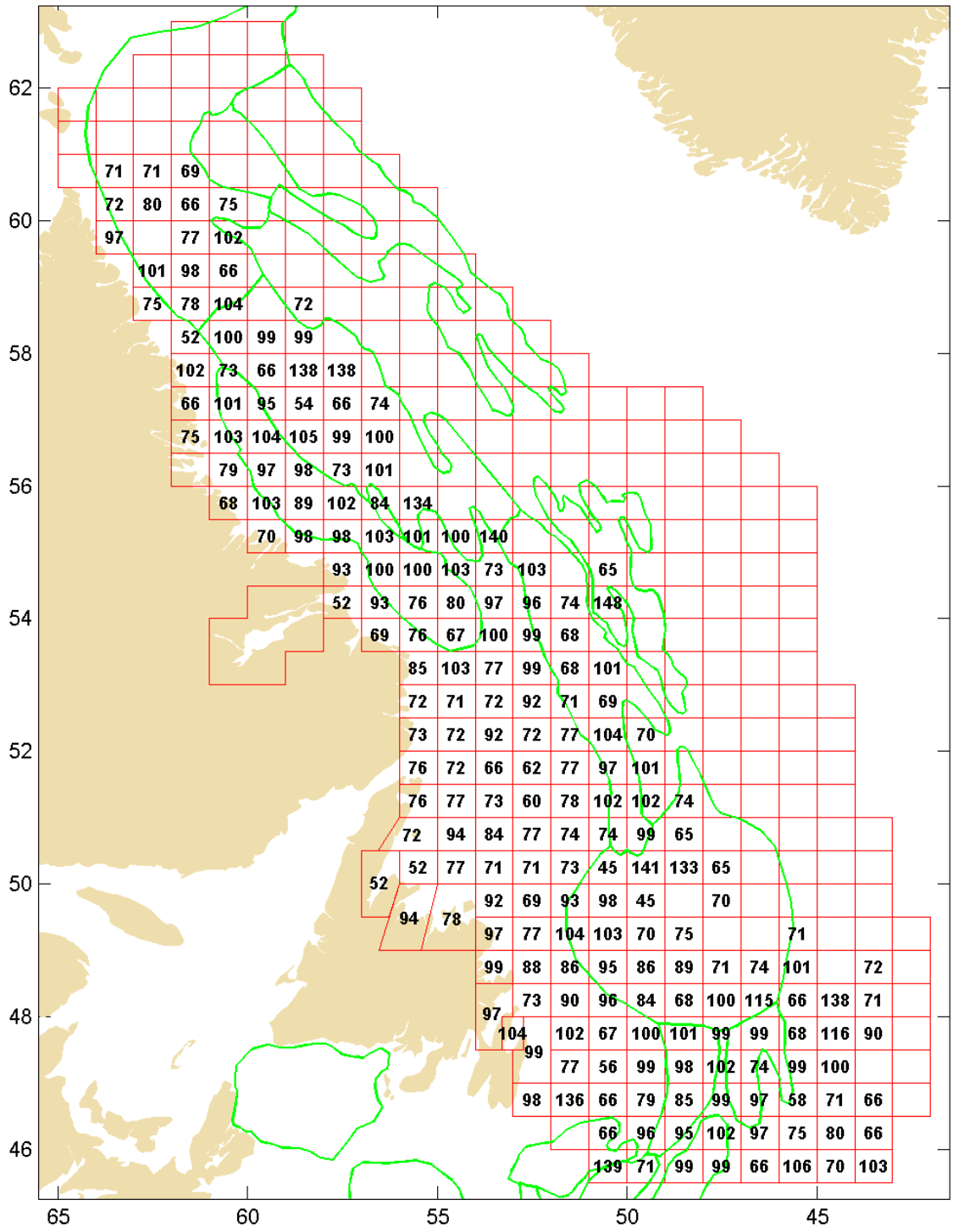

Figure 9-43. Mean iceberg size per cell estimated using exponential fit to aerial reconnaissance ice class data

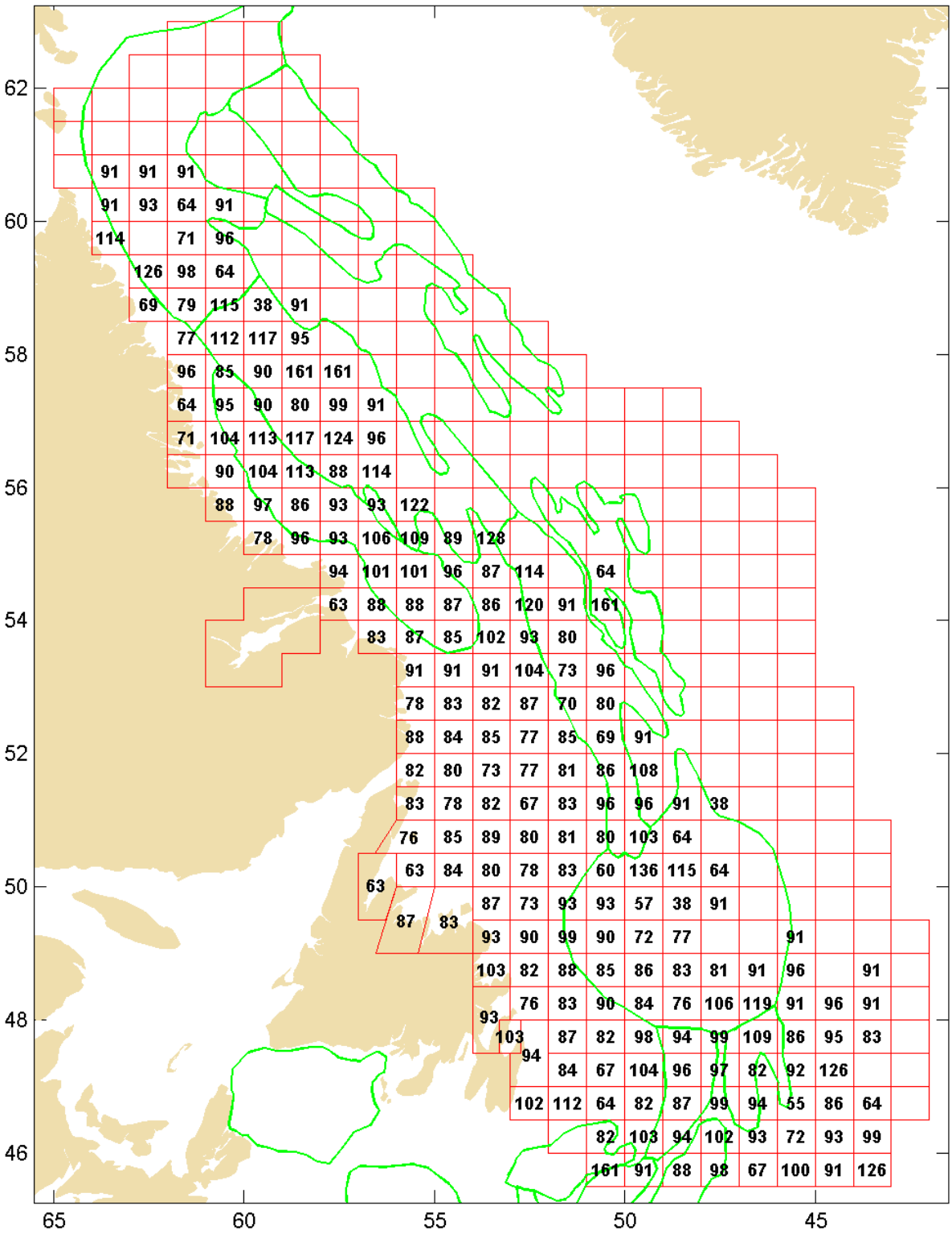

Figure 9-44. Mean iceberg size per cell estimated using mean waterline length per iceberg size class

9.6 MEAN ICEBERG DRIFT SPEED

The mean iceberg drift speed, along with the structure diameter, mean iceberg waterline length, and the mean iceberg areal density, are used to calculate iceberg impact rates with structures and to estimate downtime and required ice management resources. Thus, a best estimate of this parameter is a requirement for the various cells in the study area.

While a fairly substantial quantity of iceberg drift data has been collected in some areas, such as the Jeanne d'Arc Basin on the northeast Grand Banks and Makkovik Bank on the Labrador Shelf, there are very limited data available to define iceberg drift in the Labrador Sea deepwater basins of interest here. To address this gap, modeled iceberg drift data were used. The iceberg drift model used by the National Research Council (NRC) and the CIS for forecasting iceberg drift is described in detail by Savage (1999), Sayed (2000), Carrieres et al (2001), Kubat et al. (2005), and C-CORE (2013). The model accounts for water and air drag forces, wave radiation stress, water pressure gradient, and added mass. Forcing is provided by ocean currents from the CIS coupled ice-ocean model and by winds and waves from the Canadian Meteorological Centre. The model accuracy and requirements for further development were addressed in a study funded by Petroleum Research Newfoundland and Labrador (C-CORE, 2013).

Iceberg drift tracks of two days duration were generated in hindcast mode at weekly intervals for a period covering 2000 to 2006 (the period for which archived currents were available for use in the driving model). Initial iceberg locations were on a grid spacing of 0.5° longitude and 0.25° latitude over a majority of the study area. Note: this modeled data set was generated for use in a previous project summarizing metocean conditions in a more limited region on the Labrador Shelf (C-CORE, 2007), but it was not possible to regenerate this data set over a larger area for this study. The model output available covers about 90% of the study area (Figure 9-45). Extrapolation from the available data is considered acceptable for cells with insufficient model coverage (i.e., cells 1-24 in the northern part of the study area). Vectors indicating mean iceberg drift direction, calculated from the means of the easterly and northerly drift components, have been included for illustration, but do not factor into encounter rate calculations; therefore, they are not considered further except for comparison with observed drift.

Monthly variations in the mean drift speeds were noted (Figure 9-46) in the model output, but monthly changes in net drift direction were negligible. If considering a typical iceberg season for the Grand Banks (March to June) the mean drift speed is just seven percent lower than the annual value. Given that the iceberg season differs according to region (and is essentially undefined in areas with minimal or no data), and that the model output is calibrated against observed data, the model output from the full year was used. Note: the iceberg drift model output would not be expected to produce representative results closer to land or in bays, as currents would not be expected to be modeled as accurately as in the open ocean. Also, there is no tidal component for the ocean currents used in the iceberg drift modeling. Also, icebergs in shallow water or bays are often grounded, typically for extended periods. Thus any model not capturing these effects would not produce representative mean iceberg drift speeds.

Figure 9-47 shows a comparison of the observed and modeled iceberg drift speeds for cell 368 on the northeast Grand Banks. The observed iceberg drift speeds are from offshore operations, and include data collected during exploration dating back to the 1980s. The mean observed iceberg drift speed is 0.32 m/s, with a standard deviation of 0.20 m/s. The mean modeled iceberg drift speed is 0.20 m/s with a standard deviation of 0.12 m/s. In both cases, the data follow a gamma distribution.

Figure 9-48 shows a comparison of observed and modeled iceberg drift speeds for the northeast Grand Banks on a per cell basis. Figure 9-49 shows a similar plot using data compiled for the Makkovik Bank (King, 2002). Results are shown only for cells with a sufficient number of observed iceberg drift data points for a meaningful comparison (several hundred) with model results. Overall, the mean observed iceberg drift speeds exceed the modeled values by about 12%. However, when results are considered by region a different picture emerges, with the average of the mean observed drift speeds exceeding modeled values by about 20% for the Grand Banks (11 cells), and the average of the mean observed drift speeds about 12% lower than modeled values for the Makkovik Bank (four cells). At this point, no explanation can be offered for the difference between the regions. Future data collection and/or drift model development may offer a better basis for characterizing regional iceberg drift speeds.

For the purpose of estimating mean iceberg drift speeds for each cell, the mean modeled iceberg drift speed for each cell was used with a correction factor, which was a linear function of the latitude, having a value of 1.216 at 47°N and 0.877 at 55.5°N. North of 55.5, a constant value of 0.877 was applied. For cells in the upper portion of the study area with minimal or no data, values are assigned from cells immediately south of that cell. The resulting mean iceberg drift speed per cell is shown in Figure 9-50 (values are given in centimetres per second or cm/s for clarity).

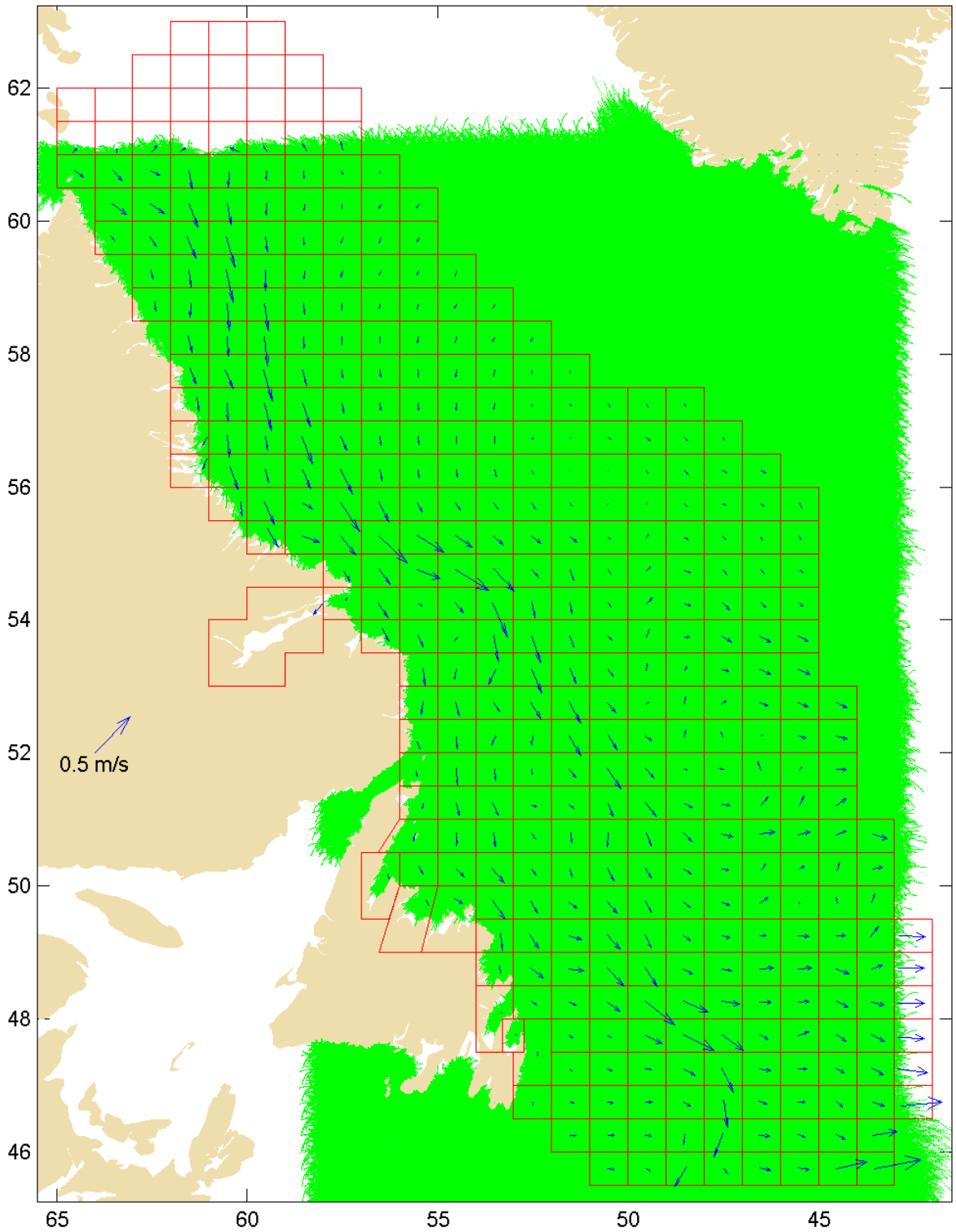

Figure 9-45. Model data output from iceberg drift model, along with vectors showing net drift direction calculated using means of easterly and northerly drift components

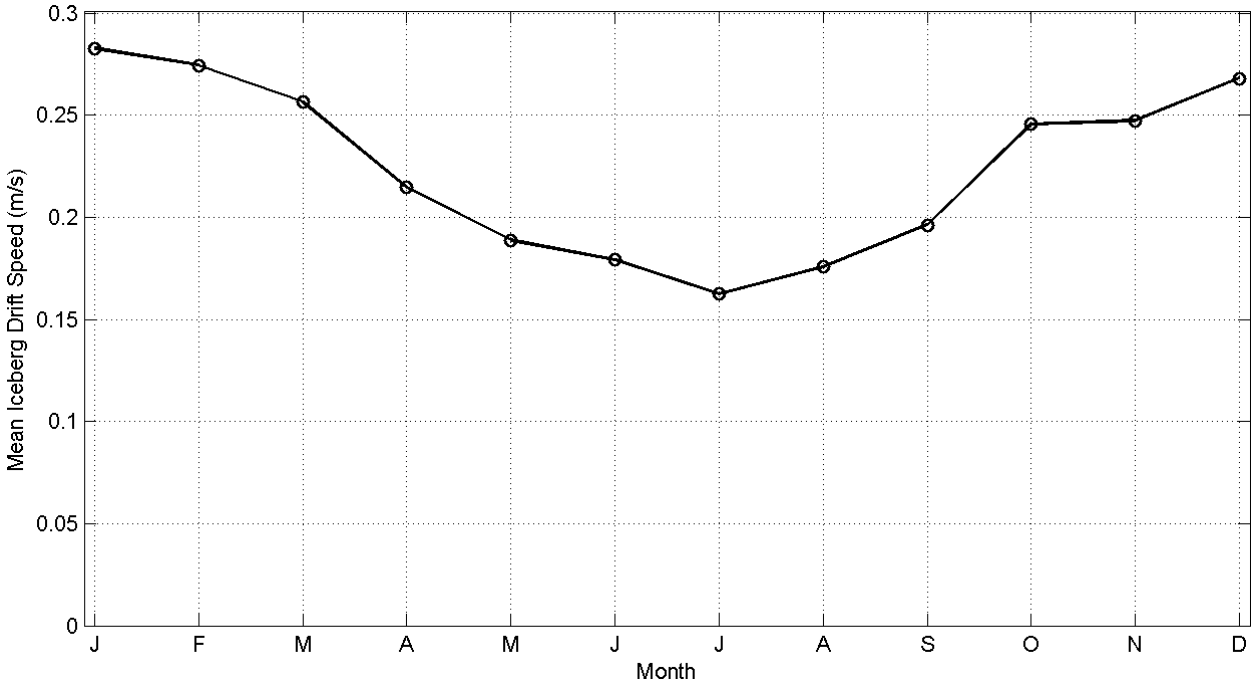

Figure 9-46. Monthly mean iceberg drift speed produced by iceberg drift model over study area

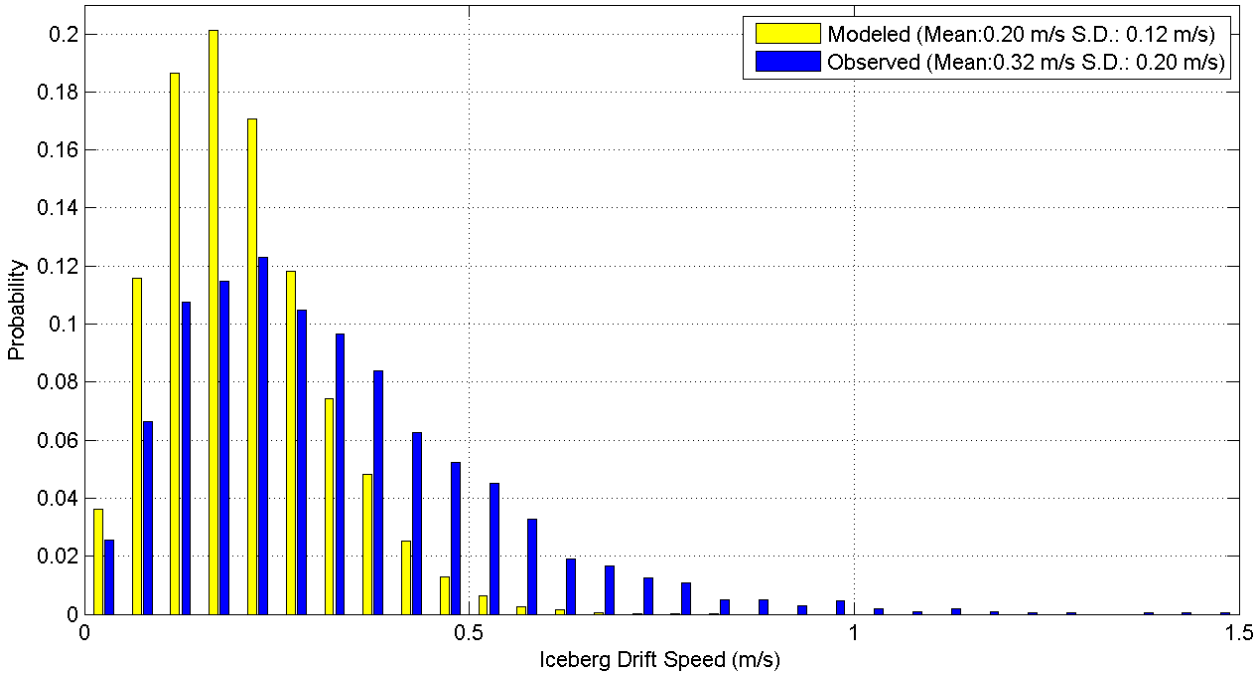

Figure 9-47. Modeled and observed drift speed distribution comparison, cell 368

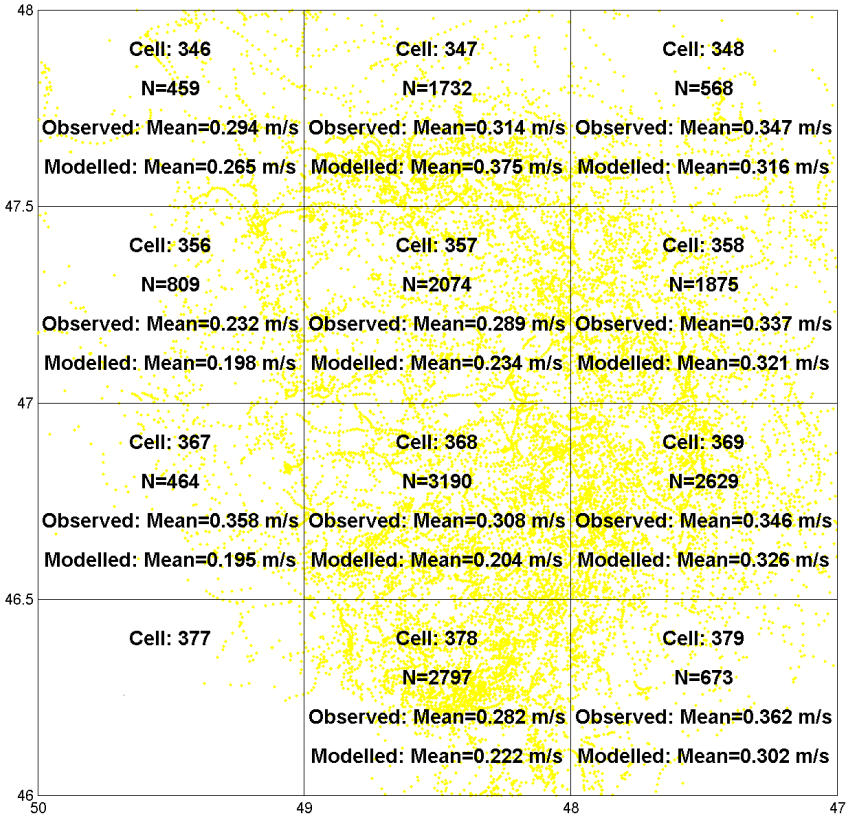

Figure 9-48. Modeled and observed iceberg drift speeds per cell, northeast Grand Banks

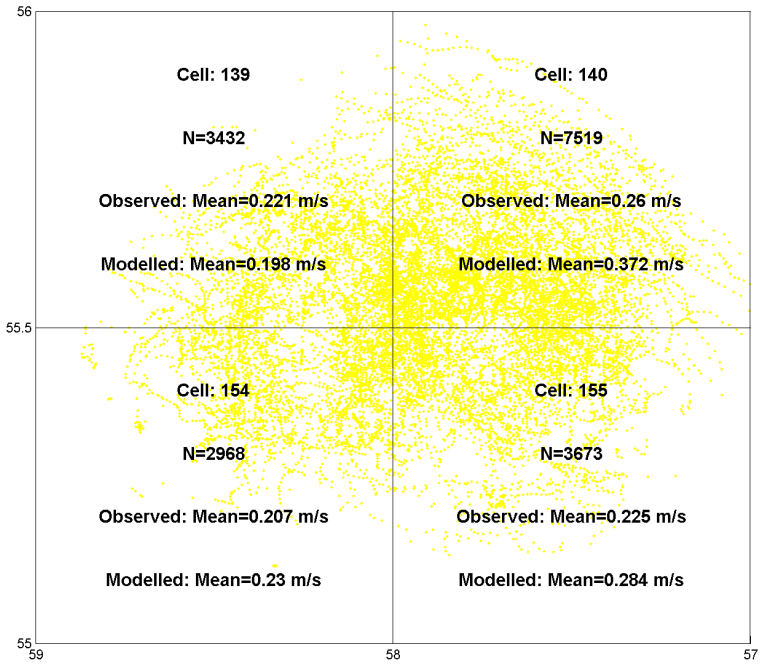

Figure 9-49. Modeled and observed iceberg drift speeds per cell, Makkovik Bank

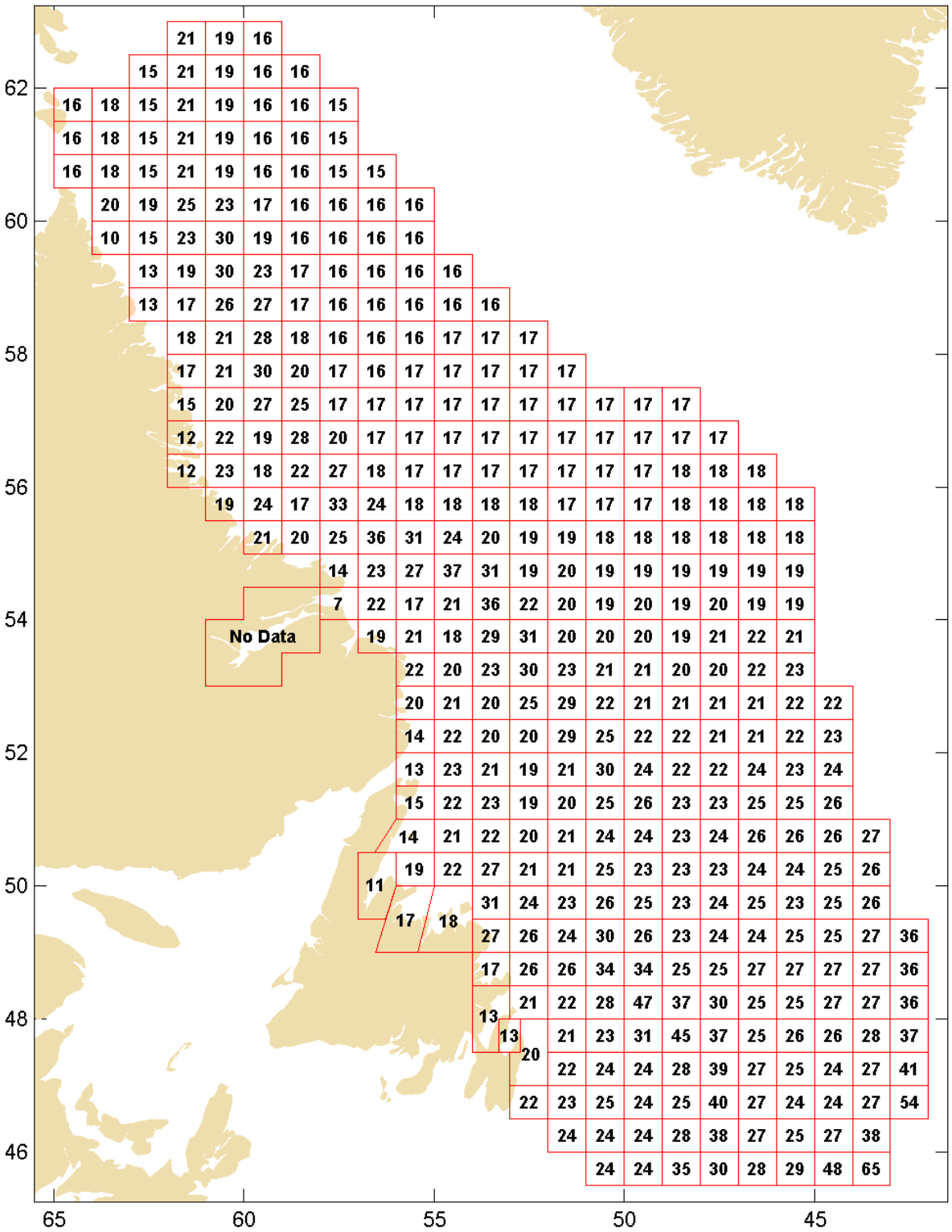

Figure 9-50. Mean iceberg drift speeds per cell (cm/s)

9.7 ICE ISLANDS

9.7.1 Introduction

On occasion, ice islands are sighted off the coast of Newfoundland and Labrador (Figure 9-51). Ice islands are a special class of tabular icebergs characterized by their large size (ranging from hundreds of metres to several kilometres), low freeboard (generally less than 20 metres), and undulating surface. Bowditch (2002) defines an ice island as a piece of glacial ice that rises roughly 10 metres above the ocean surface, having an overall thickness of about 50 metres, often having a wave-like surface, and a surface area ranging from a few thousand square metres to hundreds of square kilometres. An alternate description put forward by Newell (1993) defined Atlantic ice islands as very large, low, flat topped icebergs having a length that exceeds 500 metres if north of latitude 50^{o}N, or exceeding 300 metres if south of that latitude, and emanating from the ice shelves of Northern Ellesmere Island or the east coast of Greenland.

Figure 9-51. 480 m long ice island off Grand Banks in 2003 (image source: PAL)

There are a number of reasons why ice islands are of interest. Their large size means that it is difficult, if not impossible, to tow them, so it may not be possible to deflect an ice island from approaching an offshore platform. Ice islands may have relatively low drafts, compared with other conventional large icebergs, thus allowing them to drift into relatively shallow waters such as those in the Jeanne d'Arc Basin. While usually obvious in open water, ice island fragments can be difficult to detect in heavy seas because of their low freeboard, and they pose a particular hazard for shipping. From the air, they can be mistaken for pack ice and, if actually accompanied by pack ice, they can be very difficult to detect.

9.7.2 Historical Ice Island Sightings in the Labrador Sea

The earliest known report of an ice island in the region is from 1884. In its October 4 issue, *Harper's Weekly* reported an ice island sighted near St. John's, Newfoundland. The article included a sketch of an ice island sighted on September 9, 1884 from a signal station 10 miles northeast of St. John's (Figure 9-52). Reports indicated the ice island was six to eight miles long, with varying height and breadth. There

were also 51 other icebergs following in the wake of the ice island. While not unheard of, September is an unusual time to spot an iceberg off Newfoundland, since icebergs are typically observed in the spring and early summer.

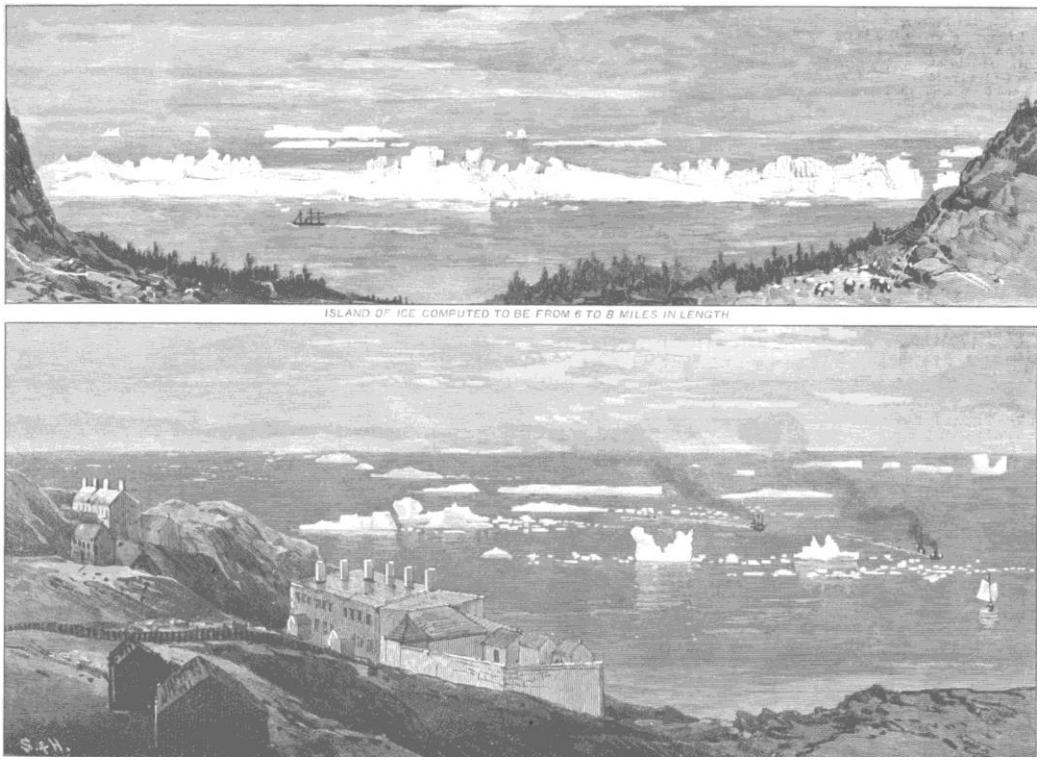

Figure 9-52. Ice island off St. John's (Harper's Weekly, October 4, 1884)

The PERD iceberg database (PERD, 2013) contains a number of sightings of ice islands south of 50°N, following Newell's definition (> 300 m). The largest waterline lengths given in the specified region are 19,308 m (height 46 m) in 1891, 19,300 m (height 183 m) in 1899, and 19,312 m in 1901 (no height specified). The large height on the 1899 iceberg is puzzling and suggests a need for more study of historical records (or a possible issue with units). Figure 9-53 shows this as a time series, which does not include either 1884 or more recent sightings. These have not been filtered by height or reported shape, so some sightings in the 300 to 1000 m class may simply be very large icebergs. A review of the data indicates the majority are ice islands.

Newell (1993) gave a review of larger icebergs and ice islands sighted from 1900-1992 (see Table 9-8). Some sightings noted in the PERD (2013) database are missing and some of the sightings in Table 9-8 (e.g., 1928, 1953, 1976, 1978, and 1991) are missing from the PERD (2013) database.

The PERD (2013) database also lists an ice island (length 1370 m, width 1005 m) sighted in 1945 in the southern Flemish Pass. This iceberg caused damage to 21 vessels in a convoy that encountered it in a thick fog (Stoermer and Rudkin, 2003) and it was one of several large tabular icebergs reported in the region that year. The estimated freeboard of this ice island was 15 m.

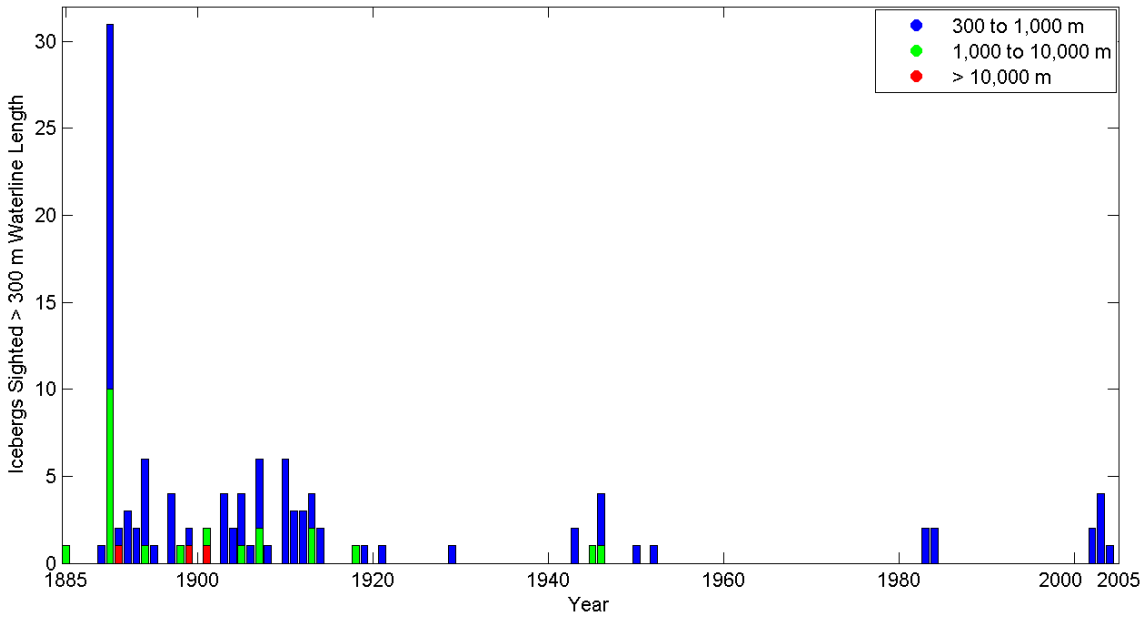

Figure 9-53. Time series, icebergs > 300 m waterline length south of 50°N (PERD, 2013)

Table 9-8. Summary of large icebergs and ice islands 1911-1991 (Newell, 1993)

Year/Month	Lat. (N) Long. (W)	Length (km)	Ht.† (m)	Source
1991/7	48.8, 53.3	2.81	15	Rudkin (pers. comm. 1991)
1991/7	49.3, 53.1	0.91	76	Rudkin (pers. comm. 1991)
1978/5	48.9, 51.5	0.70	?	IIP (1978)
1976/5	49.3, 49.6	0.75	5	IIP (1976)
1976/6*	47.5, 49.1	0.65	Low	IIP (1976)
1975/5	81.0	2.00	Low	Dunbar (1978)
1974/7	54.6 55.5	0.57	61	MAREX (1974)
1967/7	82.5	1.60	?	Lindsay *et al.* (1968)
1964/6	57.2 60.5	6.50	Low	Nutt (1966)
1964/2	61.2 63.8	0.61	3	IIP (1964)
1964/4	50.4 52.5	0.46	12	IIP (1964)
1963/7	81.0	20.4	Low	Nutt (1966)
1960/9	70.5	9.30	Low	Dunbar (1962)
1959/5	42.8 49.5	0.30	84	IIP (1959)
1957/7	46.5 48.0	0.27	38	IIP (1957)
1955	75.0 60.0	1.40	24	Polar Times (1955)
1953/3	47.6 52.2	0.30	30	IIP (1953)
1953/5	48.2 51.9	0.59	74	IIP (1953)
1953/5	81.0	7.40	Low	Greenaway (1953)
1952/5	51.9 55.1	0.93	12	IIP (1952)
1952/6	49.4 53.7	0.30	43	IIP (1952)
1950/6	52.4 52.7	1.40	Low	IIP (1950)
1950/7	49.9 49.7	0.45	?	IIP (1950)
1950/9	52.6 51.1	0.93	?	IIP (1950)
1950/10	60.6 46.5	1.40	61	IIP (1950)
1950/9	74.5	3.70	11	Canada, DOT (1951)
1945/5	43.1 49.3	1.40	15	IIP (1945)
1943/4	49.3 48.0	0.46	60	IIP (1943)
1940/8	58.2	1.90	?	IIP (1940)
1940/9	70.7 67.8	9.30	14	IIP (1940)
1940/9*	70.7 67.8	4.30	14	IIP (1940)
1940/9	75.0 60.0	0.56	101	IIP (1940)
1938/7	64.6 59.0	0.92	?	IIP (1938)
1934/7	62.6 60.7	13.0	?	Hennessy (1935)
1933/7	54.7	1.85	?	Wyatt (1934)
1928/6	47.5 52.5	1.40	?	IIP (1928)
1928/7	62.5 70.5	1.40	18	McLean (1929)
1928/8	52.0	7.40	24	Smith (1931)
1928/6	52.0	12.0	30	Hennessy (1932)
1928/7	52.0	1.80	?	Hennessy (1932)
1914/7	55.0	0.90	46	Wilson (1975)
1911/6	53.0	3.70	18	Amy (1912)
1911/7*	53.0	1.40	18	Amy (1912)

*Indicates second sighting.
†In some cases an exact height is not given but the iceberg or ice island is referred to as low, medium or high; these cases are coded as such.

The International Ice Patrol observed an ice island (Robe et al., 1977) during May and June 1976 as it drifted near the Grand Banks (see Figure 9-54). The reported freeboard for this iceberg was four to five metres, which, if accurate, is quite low. The waterline length was not reported, but using the scale on Figure 9-54 (inset) shows that the waterline length varied from about 700 m to 600 m. The total surface area decreased from 190,000 m2 to 110,000 m2 over the observation period, and when combined with the reported freeboard, this indicates a mass reduction from 5.7 to 3.5 million tonnes. This ice island was not included in the PERD (2013) database.

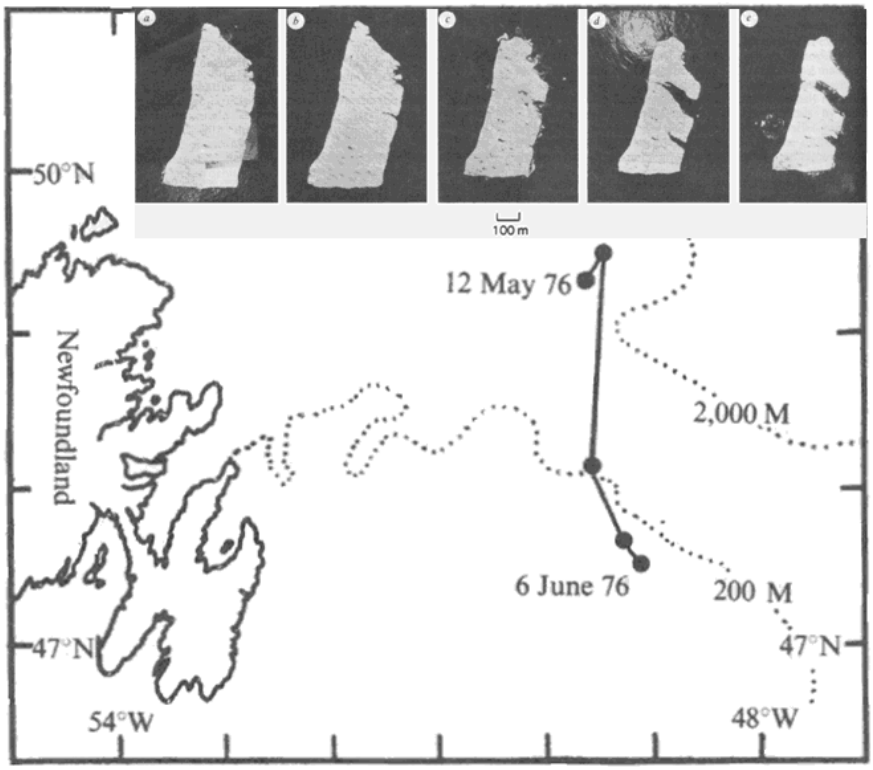

Figure 9-54. Aerial photographs of large tabular iceberg (inset) from May 12 to June 6, 1976 and sighting locations (from Robe et al, 1977)

Nutt (1966) documented the case of ice island WH-5 which calved from the Ward Hunt Ice Shelf during the winter of 1961-1962, and fragments of the ice island reached the Grand Banks in 1964 (see Figure 9-55). The initial dimensions of WH-5 were approximately 18 km by eight km. The course of the ice island was reconstructed by sightings from a variety of sources, including ship and aerial sightings by Canadian and American agencies. In some cases, pieces of the ice island were marked using oil drums and flags for later identification. The ice island broke into numerous fragments along the way, and about 50 fragments of WH-5 were identified in April 1964 in the Grand Banks vicinity near 46°N, 51°W. The sizes of these fragments were not reported. The transit time from the Nares Strait to the Grand Banks was less than one year.

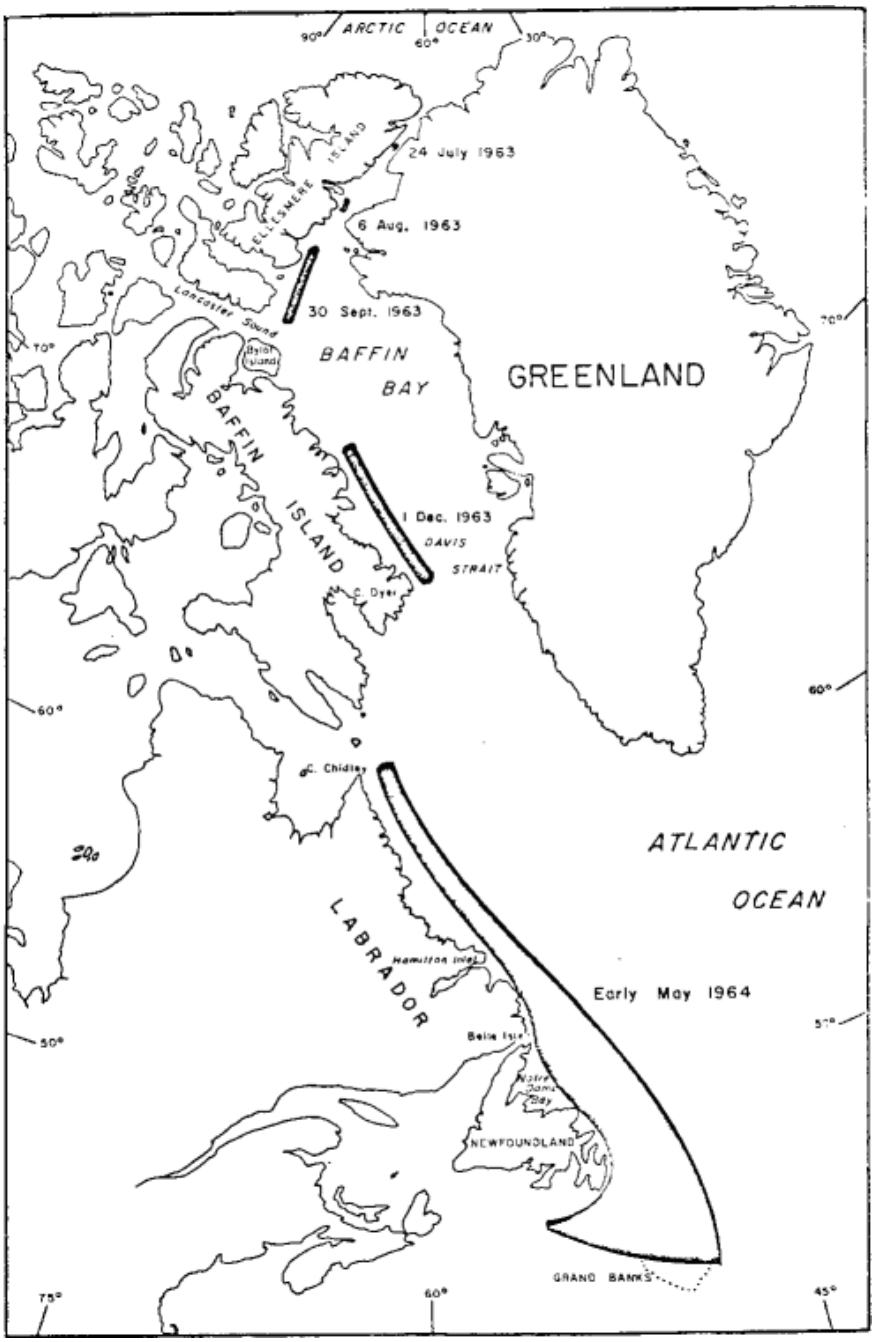

Figure 9-55. Drift of large ice island and fragments from Ward Hunt ice shelf to Grand Banks (Nutt, 1966)

9.7.3 Recent Ice Island Sightings in the Labrador Sea

Ice islands were observed on or near the Grand Banks in 2002, 2003, and 2004, with the peak occurring in 2003. Table 9-9 gives a list of the largest ice islands and ice island fragments spotted between 2002 and 2004 off the northeast Grand Banks during surveillance in support of offshore operations. The ice islands sighted in 2002 likely originated from a single ice island which was estimated to be seven km in length (Stoermer and Rudkin, 2003) when sighted north of the Grand Bank (≈ 51°N) by the Department of Fisheries and Oceans (DFO).

Table 9-9. Ice islands sighted in Grand Banks region 2002-2004

Year	Iceberg ID	Length (m)	Width (m)	Height (m)	Estimated Mass (tonnes)
2002	02077	500	290	12	6,200,000
2002	02076	355	206	9	2,300,000
2002	02086	300	300	10	3,200,000
2002	02095	280	90	20	1,800,000
2002	02091	260	130	15	1,800,000
2002	02087	250	150	7	900,000
2003	HG03-027	212	154	17	2,000,000
2003	HG03-015	213	142	9	1,000,000
2003	HG03-061	270	100	10	900,000
2003	HG03-101	307	235	10	2,600,000
2003	HG03-017	333	152	9	1,600,000
2003	ER03-039	350	250	10	3,100,000
2003	ER03-011	380	300	8	3,300,000
2003	HG03-033	480	230	10	3,900,000
2004	2004-11	422	314	9	4,200,000
2004	2004-16	250	200	10	1,800,000

An analysis of the 2002 – 2004 trajectory data indicates that ice islands have higher drift speeds than the general iceberg population. The analysis excludes periods when the icebergs or ice islands/fragments were under tow, or the interval between sightings was less than 45 minutes or greater than eight hours. The influence of water depth is given in Table 9-10. Overall, the mean ice island (and larger fragments) drift speed is greater than smaller icebergs by approximately 10%. Based on the available information, it seems reasonable to conclude that ice islands tend to move at higher drift speeds than the general iceberg population. This would be expected due to the increased influence of surface currents and

winds, as well as the decreased influence of the typically slower deeper currents that would slow down deeper-keeled blocky icebergs.

Table 9-10. Ice island drift speed as a function of water depth compared with icebergs with waterline length < 200 m (2002-2004)

Water Depth	Ice Islands & Fragments	Data Points	Drift Speed (m/s)		Icebergs (W.L.< 200m)	Data Points	Drift Speed (m/s)	
			Mean	Std. Dev.			Mean	Std. Dev.
All	21	532	0.39	0.22	223	3574	0.36	0.25
≤ 200	17	431	0.40	0.22	181	2959	0.34	0.24
≤ 150	13	296	0.37	0.24	170	2667	0.33	0.23
≤ 125	11	177	0.39	0.25	155	2334	0.33	0.23
≤ 100	7	67	0.43	0.24	116	1461	0.34	0.25

A significant calving event of the Petermann Glacier on northeast Greenland occurred in early August 5, 2010, and produced an ice island with a surface area in excess of 250 km^2. Figure 9-56 shows the Petermann Glacier before the calving event. Figure 9-57 shows a larger regional image with the newly calved ice island and five large ice islands (all greater than 20 km^2) at the Ryder Glacier further north.

On September 17, 2010, the CIS dropped a beacon on ice island PII-A. This beacon functioned until June 3, 2011, when the ice island was just north of the Makkovik Bank on the Labrador Shelf. For a brief period, tracking of PII-A was performed using satellite imagery. On June 17 and 18, 2011, C-CORE placed a number of beacons on PII-A when it was on the Makkovik Bank. Two beacons fell off PII-A approximately August 1, 2011, when PII-A was just off St. Anthony. PII-A grounded just north of St. Anthony, a few kilometres offshore at Great Brehat, from August 7 to August 13.

After resuming free-floating, PII-A moved south towards White Bay and collided with Bell Island (one of the Grey Islands) on August 20; it split into two large pieces (PII-A-b and PII-A-c, 19.0 and 14.2 km^2, respectively) and a significant number of smaller pieces, many of which qualified as ice islands according to accepted definitions. The remaining fragments of PII-A moved into Notre Dame Bay and deteriorated into smaller fragments. Figure 9-58 shows a relatively complete plot of the PII-A ice island trajectory.

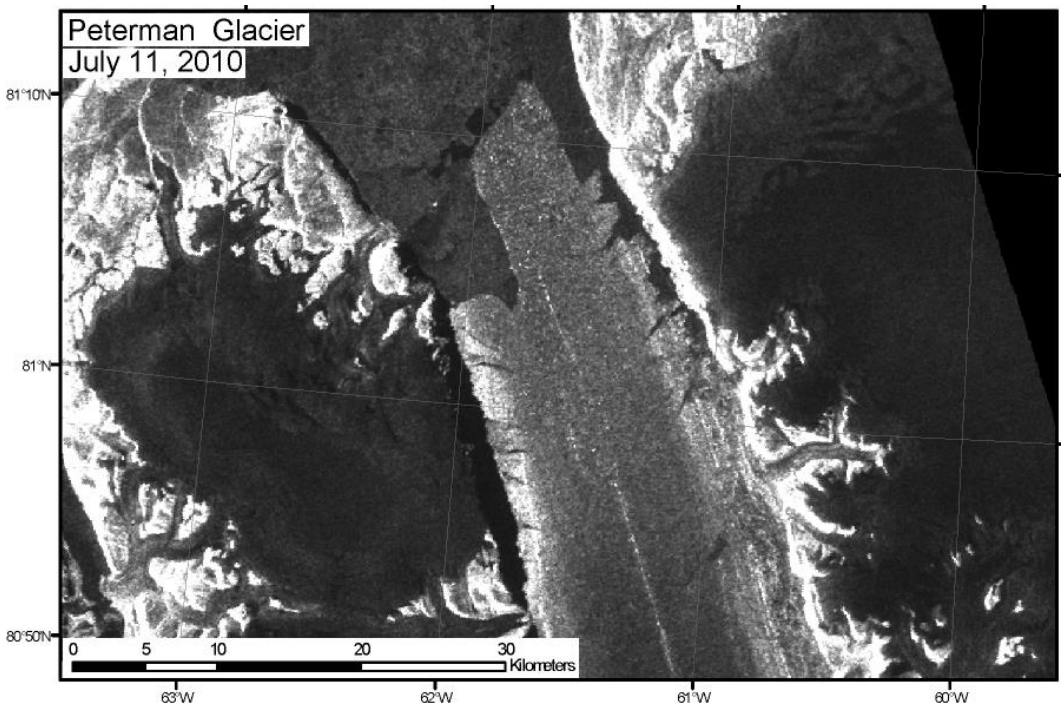

Figure 9-56. Petermann Glacier before 2010 calving event

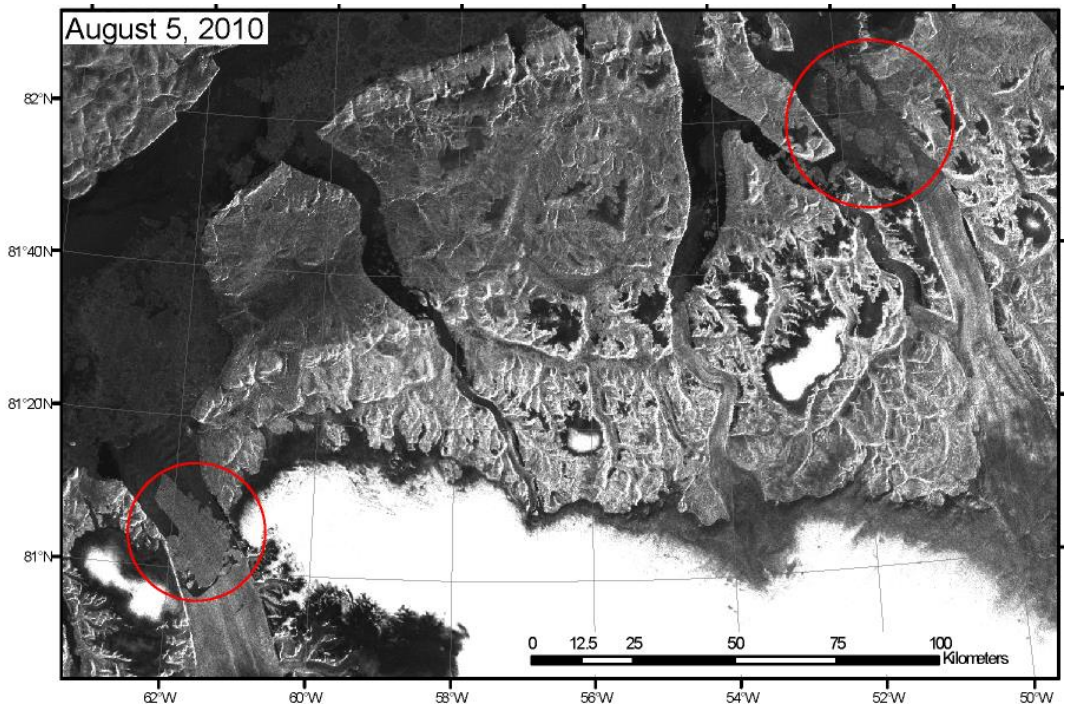

Figure 9-57. Regional image showing additional ice islands calved from Ryder Glacier

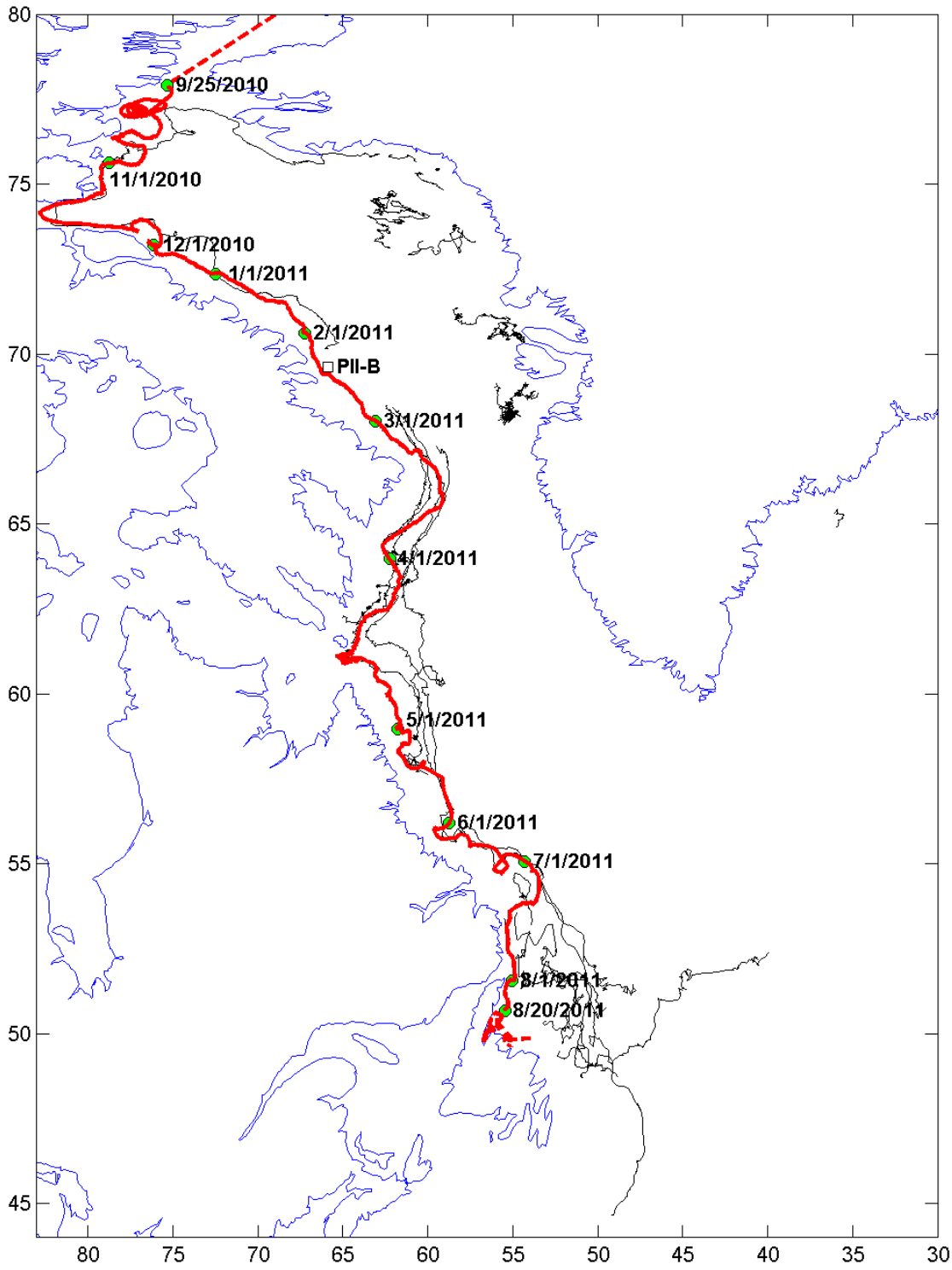

Figure 9-58 Trajectory plot of PII-A ice island and current location of PII-B ice island. Black lines are iceberg tracks from IIP data buoy program.

In 2011, C-CORE executed a three-day field program on the Petermann Ice Islands, PII-A and PII-A-a, from June 17 to June 19 (Halliday et al., 2012). At this time PII-A and PII-A-a (recently calved from PII-A) were situated offshore Labrador, Canada, about 100 km northeast of the town of Rigolet. Geophysical survey methods, including Ground Penetrating Radar (GPR) and Seismic Reflection, were used to identify the base of the islands and obtain ice thickness measurements at various locations. Eight satellite tracking beacons were deployed on PII-A and one was deployed on PII-A-a. Ablation data, photographs, and video footage were also obtained during the program.

ArcticNet researchers on the Canadian Coast Guard vessel Amundsen revisited PII-A on July 22, 2011 while it was off the southern Labrador coast. GPR measurements were acquired at the pre-existing stations; the measurements allowed for the calculation of deterioration rates, due to surface and basal melting of PII-A. Results of the field measurements indicate ice thickness varied between 50 to 80 m on PII-A; the thickness of PII-A-a was 30 m at a single survey location. Surface melt rates of 2.7-6.3 cm day-1 were observed over a one-day period in June. For the 35-day period between June and July visits, average surface and basal melt of 5.0 cm day-1 and 3.4 cm day-1, respectively, were calculated. Figure 9-59 shows an aerial photograph of the ice island. Based on an average thickness of 62 m for ice island PII-A measured using GPR, and an area of 62 km^2 determined on June 20 using satellite imagery, the mass of PII-A at the time of the survey was approximately 3.5 billion tonnes.

Figure 9-59. PII-A Ice Island (seals visible on surface)

In July 2012, another major calving event (approximately 120 km^2) occurred at the Petermann Glacier. The majority of this ice is still in Baffin Bay and the Canadian Ice Service regularly produces bulletins updating interested parties on the status of ice islands in that region. These bulletins, issued by Luc Desjardins from October 2010 to November 2013, and by others at the CIS since then, are a valuable source of data to the research community. Figure 9-60 shows the distribution of ice islands in Baffin Bay as of April 9, 2015, which includes a number off the coast of Labrador.

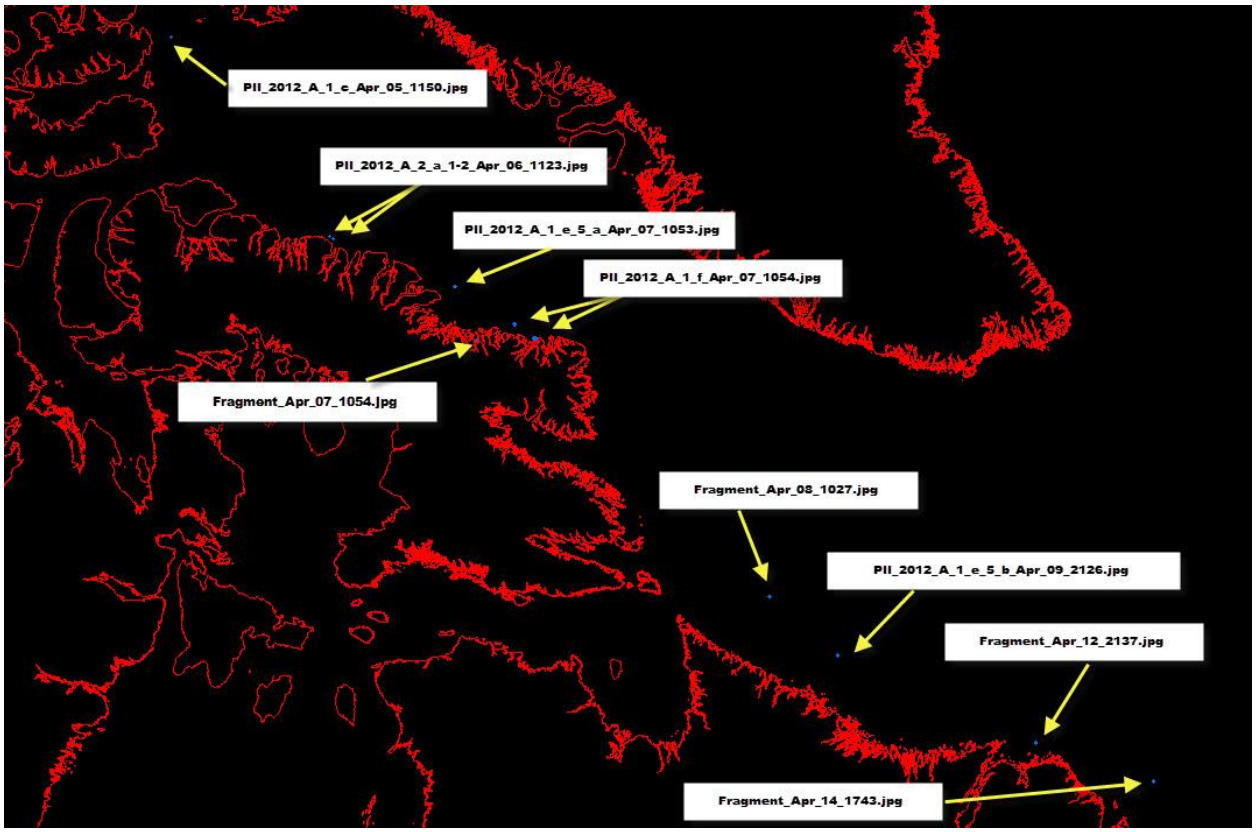

Figure 9-60. CIS ice island bulletin, April 9, 2015

9.7.4 Implications for Activities in the Labrador Sea

The appearance of ice islands in the Grand Banks region early in the previous decade was a surprise to many as historical records of ice islands were largely dismissed as rare events that were unlikely to recur. While the design of the Hibernia Gravity Based Structure (GBS) did not consider ice island impacts, the conservatisms in the design (i.e., six MPa ice crushing strength) resulted in a design adequate for this scenario. More recent designs of GBS structures for the Grand Banks (e.g., Hebron and Husky Wellhead Platforms) have incorporated ice islands into the ice design basis. To date, there have been no disconnection events for the Terra Nova or White Rose FPSOs in response to ice island (or iceberg) threats.

Many ice islands were observed at the beginning of the twentieth century and have occurred periodically since at approximately 20-year intervals. Given that the Petermann Glacier has retreated substantially, and is therefore not likely to produce additional significant calving events in the near term, ice island incursions into the Labrador Sea (such as those observed over the last decade) are likely to subside. That said, ice islands from other sources may become a factor.

While smaller ice islands have been successfully managed (towed), many ice islands are too large and cannot be managed with current ice management technology. Work by Crawford (2013) and Fuglem et al., (2012) have addressed ice island deterioration mechanisms and risk analysis frameworks. Due to the water depth in the Labrador Sea deepwater basins, any facilities likely to be employed for exploration or production would be floating, and as with floating facilities on the Grand Banks, disconnection capabilities would be incorporated. The key to addressing potential ice island threats will be upstream monitoring so appropriate risk mitigation measures can be implemented.

9.8 REFERENCES

Bowditch, N. (2002). American Practical Navigator, Pub No. 9, 2002.

C-CORE (1998). Analysis of Pack Ice and Iceberg data from the 1997 CCGS Henry Larson Probe to Voisey's Bay. Contract Report prepared for Canadian Coast Guard, Fisheries and Oceans Canada, June, C-CORE Publication 98-C7.

C-CORE (2007). Location, Environmental and Other Factors Influencing Exploration and Development of Labrador Gas, C-CORE Report R 06 088-525 V2, Prepared for Atlantic Canada Opportunities Agency (ACOA), May.

C-CORE. (2013).Needs Analysis and Project Development for Enhanced Iceberg and Sea Ice Drift Forecasting – Final Report, C-CORE Report R-12-120-999 (Revision 4), Prepared for Petroleum Research Newfoundland and Labrador (PRNL).

Carrieres, T., Sayed, M., Savage, S. and Crocker, G. (2001). Preliminary verification of an operational iceberg drift model. POAC '01, Proceedings of the 16th International Conference on Port and Ocean Engineering under Arctic Conditions, August 12-17, Ottawa, pp. 1107-1116.

CIS (2014). Retrieved from: https://www.ec.gc.ca/glaces-ice

Crawford, A.J. (2013). Ice Island Deterioration in the Canadian Arctic: Rates Patterns and Model Evaluation. Masters submitted to Carleton University, Ottawa, Ontario, 127 pp.

Fenco Newfoundland Ltd. (1987). Husky/Bow Valley East Coast Environmental Data Archive. Contract Report for Husky/Bow Valley East Cost Project, December.

Fuglem, M., Richard, M., Kennedy, A., King, T. and Cater, N. (2012). "Modelling risks to offshore facilities associated with ice islands off Canada's east coast." ICETECH 2012, September 17-20, Banff, Alberta, Canada.

Halliday, E.J., King, T., Bobby, P., Copland, L., and Mueller, D. (2012). "Petermann ice island 'A' survey results, offshore Labrador" (OTC 23714). Arctic Technology Conference, Houston, Texas, December 3-5.

International Ice Patrol. (2014). http://www.navcen.uscg.gov

Jordaan, I.J., Fuglem, M., Crocker, G., and Olsen, C. (1995). Canadian Offshore Design for Ice Environments, Volume 1, Environment and Routes, Prepared for Department of Industry, Trade and Technology, Canada-Newfoundland Offshore Development Fund, Government of Newfoundland and Labrador, September, 1995.

Jordaan, I., Press, D., and Milord, P. (1999). Iceberg Databases and Verification. Prepared for National Research Council Canada, Canadian Hydraulics Centre, March 1999.

King, A.D. (2002). Iceberg Scour Risk Analysis for Pipelines on the Labrador Shelf. M.Eng. Thesis, Memorial University of Newfoundland, St. John's, Newfoundland, Canada, 212 p.

King, T., Howell, C., Youden, J. and Lynch, M. (2009). 2006 Labrador iceberg survey. POAC '09, Lulea, Sweden.

Kubat, I., Sayed, M., Savage, S. and Carrieres, T. (2005). An operational model of iceberg drift. International Journal of Offshore and Polar Engineering, Vol. 15, No. 2, June, pp. 125-131.

MANICE manual (2005). https://ec.gc.ca/glaces-ice/default.asp?lang=En&n=4FF82CBD-1

Newell, J.P. (1993). Exceptionally large icebergs and ice islands in eastern Canadian Waters: a review of sightings from 1900 to present. Arctic, Vol. 46, No. 3, September, pp. 205-211.

Nutt, D.C. (1966). The Drift of Ice Island WH-5. Arctic, 19(3), pp. 244-262.

Provincial Aerospace Environmental Services (2005). Comprehensive Iceberg Management Database. PERD/CHC Report 20-72, March

PERD (2013). PERD Iceberg Sighting Database Update 2013. Prepared by BMT Fleet Rechnologu Limited for National Research Council Canada, Reference: 7909FR (Rev 00), March.

Petro-Canada (1983). Bjarni/North Bjarni Production Perspectives Study. Prepared by Petro-Canada Resources – Frontier Development Group for The Labrador Group of Companies. 10 volumes.

Robe, R.Q., Maier, D.C. and Kollmeyer, R.C. (1977). Iceberg Deterioration. Nature, Vol 267, June 9th, pp. 505-506.

Savage, S. (1999). State of the Art Review – Prediction of Iceberg Deterioration and Drift. Contract Report to Canadian Ice Service.

Sayed, M. (2000). Implementation of Iceberg Drift and Deterioration Model. Technical Report HYD-TR-049, Canadian Hydraulics Centre, March, 39 pp.

Stoermer, S.A, and Rudkin, P. (2003). Tabular icebergs: ice season 2002 and the past. Mariners Weather Log, Vol. 47, No. 2, December.